Fluorescent Probes for Lipid Droplet and Lipid Membrane Imaging in Cells and Models

---

Darragh O' Connor, B.Sc. (Hons)

A thesis submitted to Dublin City University for the award of PhD.

School of Chemical Sciences,
Dublin City University
Glasnevin,
Dublin 9.

September 2019

Supervisor: Prof. Tia E. Keyes

Declaration

I hereby certify that this material, which I now submit for assessment on the programme of study leading to the award of PhD. is entirely my own work, that I have exercised reasonable care to ensure that the work is original, and does not to the best of my knowledge breach any law of copyright, and has not been taken from the work of others save and to the extent that such work has been cited and acknowledged within the text of my work.

Signed: _____

ID No: 15212943

Date: _____

Acknowledgements

Firstly, I would like to express my gratitude to my supervisor Prof. Tia E. Keyes for giving me the opportunity to continue my education through this PhD. I would like to thank you for your wealth of knowledge, expertise and advice along the way.

I would like to thank all the technical staff in the Chemical Sciences department for continuously helping not only me but everyone around them and keeping the department running smoothly.

I also would like to thank Dr. Aisling Byrne, Dr. Ciarán Dolan, Dr. Nirod Sarangi, Guilherme Berselli, Carolin Müller and Prof. Conor Long for their hard-work, expertise and contributions to this thesis.

I would like to thank the Keyes research group for all their support throughout my project. Thank you to Dolan for telling it like it is, and Chris for all the tips/hints/tricks taught in the lab and advice along the way. I greatly appreciate all the help by everyone in the Keyes group and discussions which always helped to either clarify or solve the problem. I would like to thank the many fellow chemistry friends in DCU; Eadaoin, Ivan, Steve (soft boi), Monty and everyone else I met along the way. Thank you for the many choffs, pints, laughs and especially rants. No-one could relate to this journey as much as you guys. I wish you all the best in the future!

To my friends from home, I want to thank you all for all the encouragement, support and words of kindness. Thank you for keeping me grounded. Thank you all for all the mid-week pints, Sunday night football, day-dranks on Saturdays, chats, trips and nights out. Lisa, thank you for always thinking of me and my brother and for always being there for tea and chats. The main hon herself Eads, for all the chats, rants and pints. Jake, Ian, Fagan, Grall, Greer, Flan, Bullet, Karl, O' Toole and our newest addition from across the pond Gilham. You are all my brothers, much love.

To all my family I say thank you for your never-ending love and support. A special thanks to my brother Seán, you are the reason I have gotten through these past few years, I strive to be better for you. Ros you are my rock, a mother/best-friend/aunt all in one. With your continued love and support I know there is no obstacle I can't overcome. Gill, I can't thank you enough for all the love, support, advice and motivation you give me, you help

keep me focused and grounded. Granda, you continue to be the greatest role model, I can only hope I am one day half the man you are.

To my better half, Ais, never did I expect to find you, least of all in a lab. I would never regret choosing to do this PhD as I never would have met you. Thank you for your continued support, guidance and words of wisdom. Thank you for bringing balance to my life in and out of the lab. I would never have made it without your help, expertise and work ethic in the lab, but also all the good times, laughs and memories outside it. I can't thank you enough.

To my nanny Roseleen, you told me to go and become a doctor…I got there in the end, just not the kind of doctor you had in mind. I know you were looking down on me all along this journey. Finally, I say thank you to my mother Laura. I know you have been looking down on me and helping me every step of the way. I hope I can say I have made you proud over these past few years. Everything I have accomplished and will hopefully accomplish in the future is because of the way you raised me. Love you always.

'Two roads diverged in a wood and I - I took the one less travelled by, And that has made all the difference'

Robert Frost

Research Output

Publications

O'Connor, D.; Byrne, A.; Dolan, C.; Keyes, T. E. Phase Partitioning, Solvent-Switchable BODIPY Probes for High Contrast Cellular Imaging and FCS. *New J. Chem.* **2018**, *42* (5), 3671–3682.

O'Connor, D.; Byrne, A.; Berselli, G.; Long, C.; Keyes, T. E. Mega-Stokes Pyrene Ceramide Conjugates for STED Imaging of Lipid Droplets in Live Cells. *Analyst.* **2019** ,144, 1608-1621

O'Connor, D.; Byrne, A.; Keyes, T. E. Linker Length in Fluorophore-Cholesterol Conjugates directs Phase Selectivity and Cellular Localisation in GUVs and Live Cells. *RSC Adv.*, **2019**, 9, 22805-22816

O'Connor, D.; Sarangi, N.; Müeller, C.; Byrne, A.; Keyes, T. E. pH Dependence of Dimethylaniline Functionalised Pyrene Fluorophores; Dual Colour Switching in Solution and SAMs. *PCCP* **2019**. Submitted (September 2019)

Posters

Phase partitioning, solvent-switchable BODIPY probes for high contrast cellular imaging and FCS. Darragh O' Connor, Aisling Byrne, Ciarán Dolan, Tia E. Keyes. The 41st Microscopy Society of Ireland Symposium, 23rd -24th April 2018, IT Sligo.

Pyrene charge transfer compounds: robust fluorophores for stimulated emission depletion microscopy (STED) of lipid droplets. Darragh O' Connor, Aisling Byrne, Guilherme B. Berselli, Conor Long and Tia E. Keyes. 44th Annual Congress of the Institute of Chemistry of Ireland 'Molecular Sensing and Imaging', 20th May 2019, NUI Maynooth.

Awards

Awarded best poster prize 1st Microscopy Society of Ireland Symposium, 24th April 2018, IT Sligo.

Awarded best poster prize 1st, 44th Annual Congress of the Institute of Chemistry of Ireland 'Molecular Sensing and Imaging', 20th May 2019, NUI Maynooth.

Thesis Outline

Chapter 1

This chapter introduces the background to this thesis, describing the cell membrane with a focus on the role of lipids and the importance of artificial lipid models for understanding the biophysical impacts of lipid domains in terms of lipid order and membrane fluidity. The photophysical and optical properties of BODIPY and pyrene dyes are discussed, and their current applications as lipid stains in live cellular imaging and sensing. Microscopy techniques that are the focus of the probes developed here such as confocal laser scanning microscopy, stimulated emission depletion (STED) microscopy and fluorescence lifetime imaging microscopy (FLIM) are discussed and how they are used alongside luminescent probes for cellular imaging.

Chapter 2

This chapter describes two novel BODIPY derivatives, one with a lipophilic Dppz pendant and one with a naphthyridyl unit conjugated to a cholesterol moiety. The photophysical properties of both Dppz-BODIPY and Naphthyridy-BODIPY-2-Cholesterol are examined and compared, as well as their uptake by live CHO and HeLa cells, examined by confocal microscopy. Their ability to partition into lipid phases is examined using giant unilamellar vesicles (GUVs) and their suitability as new FCS probes is investigated. The 'switch-off' ability of these dyes in aqueous environments results in high contrast imaging of lipid regions in both artificial membrane models and live cells.

Chapter 3

Chapter 3 outlines two novel BODIPY-cholesterol derivatives with varying linker length between the BODIPY core and the cholesterol unit in order to investigate liquid-ordered domain partitioning. The number of available fluorescent probes capable of selectively staining liquid-ordered domains in artificial membrane models is very limited compared to their liquid-disordered staining counterparts. By incorporating an amino-hexanoic acid linker, BODIPY-Ahx-Chol can selectively partition into Lo domains in phase separated GUVs, and its use as a cell-imaging dye is investigated using confocal microscopy and

FLIM. The design and synthesis of this simple but effective dye increases the understanding of what is structurally needed in order to selectively target Lo domains.

Chapter 4

This chapter focuses on the design and synthesis of a novel pyrene dye PyLa and its ceramide derivative PyLa-C_{17}Cer for use as a super-resolution lipid droplet stain. High resolution images of lipid droplets in HeLa cells treated with TNF-α are captured and the number of lipid droplets present is successfully resolved. The diffusion values of PyLa-C_{17}Cer successfully obtained on supported lipid bilayers using FCS resulting in data that is used to distinguish lipid order and phase. We believe that PyLa-C_{17}Cer is the first example reported in literature of a pyrene derivative being used for super resolution STED microscopy as well as FCS.

Chapter 5

This body of work explores the photophysical properties of PyLa and its thiol derivative PyLaOT, specifically their ability to detect changes in pH and act as fluorescent ‘on-off-on’ switches. A visiting student provided computational studies to explore the effect of protonation of the 3,4-dimethylamino substituents on the photophysics and compared to experimental data. The pH sensing capabilities of both probes is compared in both aqueous and organic media. The thiol functional group on PyLaOT allows for surface chemistry to be applied to gold surfaces and the pH effects studied when bound to this substrate.

Author Contribution to Publications

Chapter	Title	Publication Status*	Authors	Contribution by Candidate
2	Phase Partitioning, Solvent-Switchable BODIPY Probes for High Contrast Cellular Imaging and FCS	*New J. Chem* 2018, ***42*** (5), 3671–3682.	O'Connor, D.; Byrne, A.; Dolan, C.; Keyes, T. E.	Manuscript primary author. Primary contributor to experimental design and execution.
3	Linker Length in Fluorophore-Cholesterol Conjugates directs Phase Selectivity and Cellular Localisation in GUVs and Live Cells.	*RSC Adv.*, 2019, ***9***, 22805-22816	O'Connor, D.; Byrne, A.; Keyes, T. E.	Manuscript primary author. Primary contributor to experimental design and execution.
4	Mega-Stokes Pyrene Ceramide Conjugates for STED Imaging of Lipid Droplets in Live Cells.	*The Analyst.* 2019, **144**, 1608-1621	O'Connor, D.; Byrne, A.; Berselli, G.; Long, C.; Keyes, T. E.	Co-author of manuscript with Dr. A. Byrne. Designed and synthesised dyes. Carried out structural and photophysical characterisation. Conducted FLIM experiments. Conducted confocal and FCS experiments in partnership with G. Berselli.
5	pH Dependence of Dimethylaniline Functionalised Pyrene Fluorophores; Dual Colour Switching in Solution and SAMs.	*PCCP* *Submitted September* 2019	O'Connor, D.; Müeller, C.; Sarangi, N.; Byrne, A.; Keyes, T. E.	Manuscript primary author. Primary contributor to experimental design and execution.

Signed:   

Candidate Principal Supervisor Co-author

ID No: 15212943

Date: 9/09/19 Date: 9/09/19 Date: 9/09/19

Table of Contents

Table of Figures

Table of Schemes

Table of Tables

Abbreviations

AC –Alternating Current

AcCOOH – Acetic acid

ACN – Acetonitrile

ATP – Adenosine Triphosphate

BHK – Baby hamster kidney

BODIPY- Boron dipyrromethene

BODIPY-PC - 2-(4,4-difluoro-5,7-dimethyl-4-bora-3a,4a-diaza-s-indacene-3-pentanoyl)-1-hexadecanoyl-sn-glycero-3 phosphocholine

BSM – Brain sphingomyelin

CD_3OD – Deuterated methanol

$CDCl_3$ – Deuterated chloroform

CHO – Chinese hamster ovary

Chol - Cholesterol

DC – Direct current

DCC – *N*,*N*'-dicyclohexylcarbodiimide

DCM – Dichloromethane

DDQ - 2,3-Dichloro-5,6-dicyano-1,4-benzoquinone

DHU – Dicylcohexylurea

DiD - (1,1'-Dioctadecyl-3,3,3',3'-Tetramethylindodicarbocyanine, 4-Chlorobenzenesulfonate Salt)

DMAP – 4-dimethylaminopyridine

DMF – Dimethylformamide

DNA – Deoxyribonucleic acid

DOPC - 1,2-dioleoyl-sn-glycero-3-phosphocholine

Dppz – Dipyridophenazine

EDC - 1-Ethyl-3-(3-dimethylaminopropyl) carbodiimide

ER – Endoplasmic Reticulum

eDHFR - Escherichia coli dihydrofolate reductase

FCS – Fluorescence correlation spectroscopy

FLCS – Fluorescence lifetime correlation spectroscopy

FLIM – Fluorescence lifetime imaging microscopy

GTP – Guanosine Triphosphate

GUV – Giant unilamellar vesicle

HA - Hemagglutinin

HeLa – Human cervical cancer cell

HPLC – High performance liquid chromatography

IRF – Instrument response function

ISC – Intersystem crossing

ITO – Indium tin oxide

LD – Lipid droplet

Ld – Liquid-disordered

Lo – Liquid-ordered

MADLI - Matrix-assisted laser desorption/ionisation

MS – Mass spectrometry

NADH - Nicotinamide adenine dinucleotide

NaOH – Sodium Hydroxide

NHS - N-Hydroxysuccinimide

NIR – Near infrared region

NMR – Nuclear magnetic resonance

PDMS – Polydimethylsiloxane

PDT – Photodynamic therapeutics

PeT – Photoinduced electron transfer

RT – Room temperature

SE – Steryl esters

SiO_2 – Silicon dioxide

SM – Sphingomyelin

SUV – Small unilamellar vesicle

TAG - Triacylgycerols

TCSPC – Time correlated single photon counting

TFA – Trifluoroacetic acid

THF – Tetrahydrofuran

TLC – Thin layer chromatography

TMP - Trimethoprim

TR-DPPE - Texas Red 1,2-dihexadecanoyl-sn-glycero-3-phosphoethanolamine

Units of Measurement

cm – Centimetre

cm^{-1} – Reciprocal wavelength

℃ - Degrees celcius

ε – Molar absorption coefficient

g – Gram

Hz – Hertz

IC_{50} – Concentration causing 50 % inhibition

K – Kelvin

L – Litre

m – metre

M – Molar

MHz - Megahertz

mL – Millilitre

mM – Millimolar

Mol – Mole

ng – Nanogram

nm – Nanometre

nM – Nanomolar

ns – Nanosecond

s – Second

V – Volt

v/v – Volume per volume

v/w – Volume per weight

μg – Microgram

μL – Microlitre

μm – Micrometre

$\mu m^2/s$ – Micrometre squared per second

μM – Micromolar

Darragh O' Connor

Fluorescent Probes for Lipid Droplet and Lipid Membrane Imaging in Cells and Models

Thesis Abstract

Cell membranes are believed to be laterally ordered into micro and nano-domains comprising of more fluid liquid-disordered (Ld) and more viscous liquid-ordered (Lo) phases. The latter subphases contain high concentrations of cholesterol and glycosphingolipids. These so call lipid rafts are experimentally distinguishable on the basis of their resistance to detergent solubilisation and are believed to play important roles in membrane function including in protein trafficking and signalling as they can drive protein-protein interactions through sequestering of proteins to these domains. Membrane domains in living cells are difficult to interrogate as they are dynamic and at sub-microscopic length scales they are outside the range of most conventional microscopies. However, they can potentially be imaged using recently developed super-resolution methods and as they are dynamic structures their diffusion can be measured using correlation methods. Therefore, new fluorescent probes are needed that can (a) partition selectively to membranous regions, (b) target the Lo and Ld phases selectively (c) that have appropriate photophysical properties compatible with the above techniques. These include large Stokes shift, high selectivity, excellent photostability, high molecular brightness, low cytotoxicity and high quantum yields. A key aim of this thesis was to design and synthesise new fluorescent probes that sequester specifically to lipid rich regions of cells or models and can distinguish Lo/Ld regions or lipid droplets, using confocal microscopy, fluorescence correlation spectroscopy (FCS), fluorescent lifetime imaging (FLIM) and the relatively new technique of super resolution microscopy, specifically, STimulated Emission Depletion (STED) microscopy.

Chapter 1: Introduction

1.1 The Cell Membrane

The first proposed model of the cell membrane was described by Danielli *et al* in 1935. This model described the cell membrane as a phospholipid bilayer which is between a protein layer.[1] Following this the 'fluid mosaic model' was proposed by Singer and Nicolson in 1972.[2] They suggested that the cell membrane was more complex than first described by suggesting it behaved more like a two-dimensional fluid that inhibited lateral diffusion of components and consisted of regions of lipids and proteins that promoted the formation of 'lipid-rafts'. Since then, the understanding of the cell membrane has been greatly expanded on. It is now widely accepted that the cell membrane is a fluid lipid bilayer consisting of glycolipids, sterols and phospholipids. It also contains a range of proteins, ~50 % by dry weight. This mixture of various lipids and proteins are compartmentalised into heterogeneous phases or domains. These specialised regions are dynamic, microdomains which aid in the compartmentalisation of proteins that help organise molecular assembly and enable cellular processes such as endocytosis and signalling. This is known as the "raft-hypothesis" and remains somewhat controversial and is under significant investigation.[3–5] There is great interest in the phase separation of lipids into liquid-ordered and liquid-disordered regions. The liquid-ordered phase is a region more tightly-packed and ordered than the surround bilayer which contains high concentrations of sphingolipids and sterols and can flow freely in the lipid membrane bilayer. These domains are believed to be platforms for proteins involved in cell-signalling.[3,6]

Lipid molecules account for approximately 40 % in dry weight of most animal cell membranes, with phospholipids accounting for the majority of membrane lipid content. They are critical to cell function for two main reasons. Phospholipids are amphipathic comprising a polar head group with hydrophobic tails. They spontaneously form bilayer structures in aqueous environments and this bilayer plays a critical role in cell permeability where they

present a semi-permeable barrier between the cell and its environment. Phospholipids contain two fatty acid tails that can differ in length (between 14-24 carbon atoms). Phospholipids that contain one or more double bonds in their fatty acid tails can result in a 'kink' orientation due to unsaturated carbon bonds. This 'kink' causes the hydrophobic tails to be more loosely packed together resulting in a flexible or more fluidic membrane. These are the main components of liquid-disordered phases. The most abundant lipids in biological membranes are glycerophospholipids, which can be sub-categorised into lamellar and nonlamellar according to phase behaviour. 1,2-dioleoyl-sn-glycero-3-phosphocholine (DOPC) is a representative of the lamellar lipid family and is one of the most commonly used lipids within our group. DOPC is a neutral lipid which comprises of a choline head group, consisting of three terminal methyl (CH_3) substituents (Figure 1.1). DOPC has a preference to self-assemble in the lamellar phase.[8] The lamellar phase can be described as the packing of long chain hydrophobic tail compounds consisting of a polar head group in a predominantly polar liquid environment. In giant unilamellar vesicles (GUVs), DOPC is the most common lipid used, which contributes to the formation of the liquid-disordered (Ld) phase.

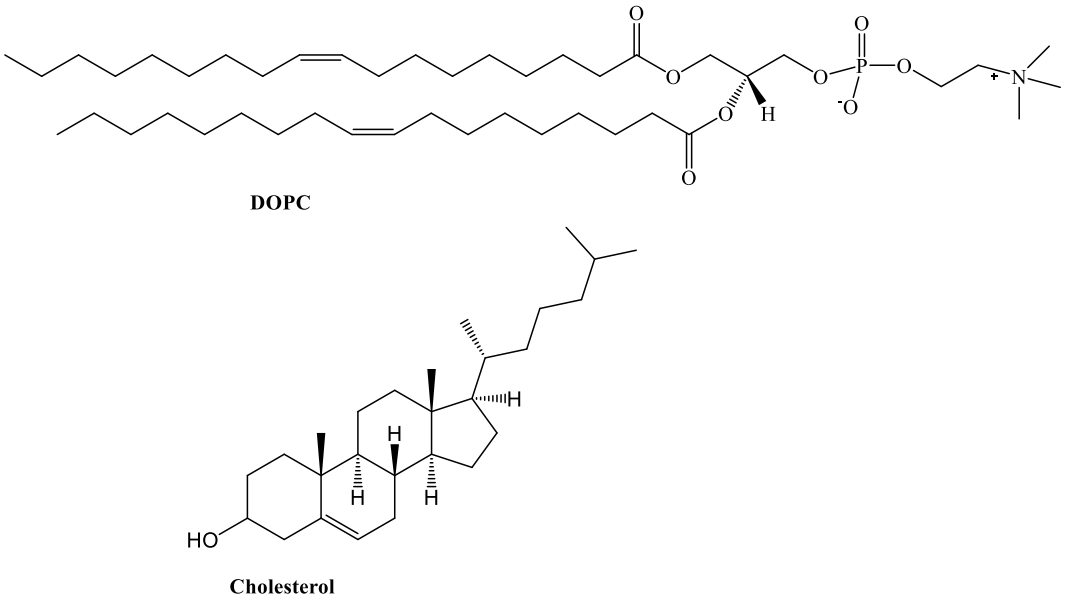

Figure 1.1 Chemical structure of 1,2-dioleoyl-sn-glycero-3-phosphocholin (DOPC) and cholesterol.

Cholesterol is a sterol that plays a distinct role in the cell membrane of eukaryotes. The key driver for the formation of liquid-ordered domains is cholesterol. The structure of cholesterol consists of a hydrophobic polycyclic core to which an acyl chain tail and hydroxyl polar head group is attached. Cholesterol cannot form a membrane by itself but inserts into phospholipid bilayers with the polar head group forming hydrogen bonds with the polar phosphate head groups. At physiological temperatures cholesterol reduces the mobility of the phospholipid tails due to the rigidity of its structure, which also extends the tails of the lipid bilayer. Cholesterol plays a key role in the formation of liquid-ordered (Lo) domains along with sphingolipids of long acyl chains such as sphingomyelin (Figure 1.2).[9]

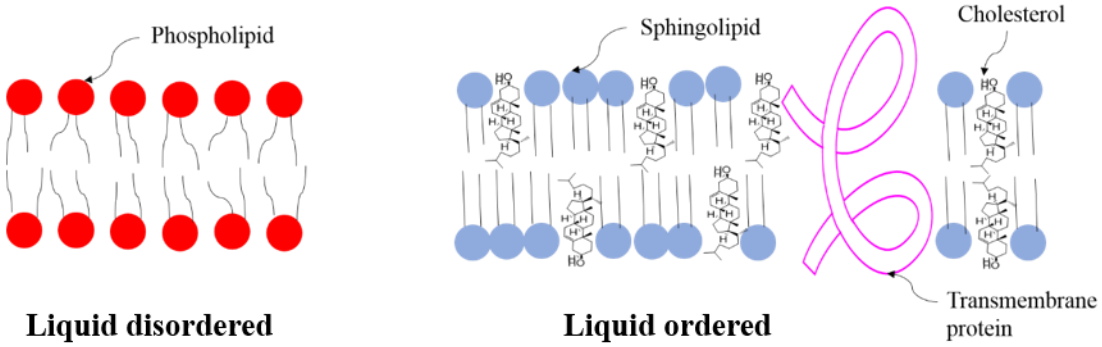

Figure 1.2 Diagram distinguishing between liquid-disordered and liquid-ordered domains within the cell membrane.

1.1.1 Lipid Droplets

Lipid droplets (LDs) are dynamic intracellular organelles that regulate the storage of neutral lipids and recently have been discovered to be involved in many physiological processes, metabolic disorders and diseases. Lipid droplets were first discovered in the nineteenth century by light microscopy, however they were initially ignored due to the premise that they had little to no function other than fat storage. The main function of lipid droplets are the storage of neutral lipids such as triglycerides, sterols, steryl esters and retinyl esters.[10–12] Lipid droplets also play an important role in protecting the cell from lipid toxicity as they safely sequester toxic lipids such as fatty acids, toxic glycerolipids and sterols which can disrupt the integrity of the cell membrane.[13–15] The discovery of the protein perilipin on the surface of lipid droplets in 1991 kick-started the interest in this organelle. Perilipin acts as a protective barrier against lipases which can break down triglycerides, fatty acids and sterols,

and therefore acts as a lipid storage regulator. Over expression of perilipin in both animals and humans is a factor of obesity.

In eukaryote cells it is thought that lipid droplets are formed from triacylglycerol (TAG) and steryl esters (SE) in the endoplasmic reticulum (ER).[16–18] This was long hypothesised to be due to the presence of enzymes localised in the endoplasmic reticulum associated with synthesising neutral lipids (TAG and SE) for lipid droplet formation.[19] The formation of an oil lens in the membrane of the endoplasmic reticulum followed by budding and then growth of lipid droplets by acquisition of proteins is one of the most widely cited models for lipid droplet formation, however it has been far from fully validated.[20]

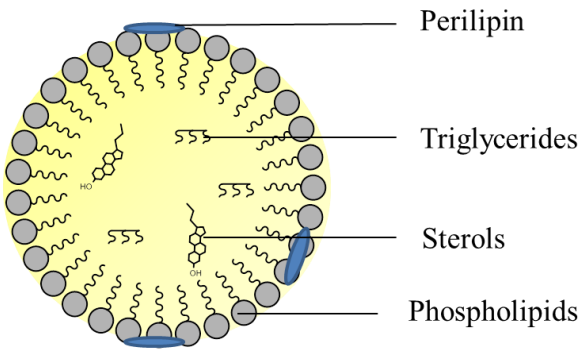

Figure 1.3 Schematic diagram of the structure of a lipid droplet. The outer membrane contains phospholipids (phosphatidylcholine (PC), phosphatidylethanolamine (PE), phosphatidylinositol, lysoPC and lysoPE) and perilipin family proteins. The inner core contains sterols (cholesterol), steryl esters (cholesterol ester) and triglycerides.

Commonalities between cell membranes and lipid droplets have now been realised. Although not a bilayer, lipid droplets contain a protein-decorated phospholipid monolayer abundant in phosphatidylcholine that separates the hydrophobic core from aqueous cellular environments.[21,22] Similarly to the cell membrane, lipid droplets are now being described as dynamic and have been found to be involved in many physiological processes including membrane synthesis, trafficking[23,24] and inflammation[25] as well as pathologies including atherosclerosis and diabetes[26], the hepatitis C virus[27], and cancer.[28,29] It is for this reason that we developed a novel pyrene dye for specific labelling of LDs which could be used as an accurate quantification tool using stimulated emission depletion spectroscopy (STED).

1.2 Artificial Lipid Models and Self-Assembled Monolayers

1.2.1 Giant Unilamellar Vesicles (GUVs)

Due to the complex nature of the cell membrane it is necessary to be able to create artificial structures that can mimic the structure and phases present. Liposomes offer the means to create fluidic artificial systems mimicking physiological conditions with varying degrees of complexity. Within this work giant unilamellar vesicles (GUVs) were created using both homogeneous and heterogeneous lipid compositions. Models such as GUVs can employ a wide variety of lipids (phospholipids, sphingolipids and cholesterol) and can also incorporate proteins or molecules such as ganglioside GM1. Liposomes can be defined as spherical vesicles containing at least one lipid bilayer. Giant unilamellar vesicles are liposomes that have a diameter above one micron (1 μm). Unilamellar refers to a single bilayer while multilamellar consists of two or more. Liposomes can be formed by a number of methods and techniques. For this work it was desirable to create GUVs to enable clear visualisation of phase separated domains by microscopy methods. The principle of GUV formation has not been fully elucidated however, in literature there have been many techniques employed to prepare GUVs e.g. solvent evaporation[30], gentle hydration[31] and more commonly, electroformation[32]. Electroformation results in the formation of a disperse population of giant unilamellar vesicles. In the 1980s Angelova and Dimitrov were the first to produce GUVs using a DC electric field.[32] This method was later updated by Angelova *et al* to produce GUVs using an AC electric field.[33] The method consists of dissolving lipids in either chloroform, or sometimes a chloroform/methanol mixture, followed by deposition of this lipid mixture onto an electrode surface. A counter electrode is then positioned perpendicular to a cell assembled between two electrodes. This cell is then filled with buffer and an electric field is applied between the electrodes. Over a number of hours GUVs start to form in large 'clusters' containing hundreds of congregated GUVs. These clusters can remain bound to the electrode, however by applying a low frequency electric field this can be avoided, and GUVs can be collected in solution by carefully removing the buffer after electroformation is complete. Within this thesis, electroformation is the method used to form GUVs.

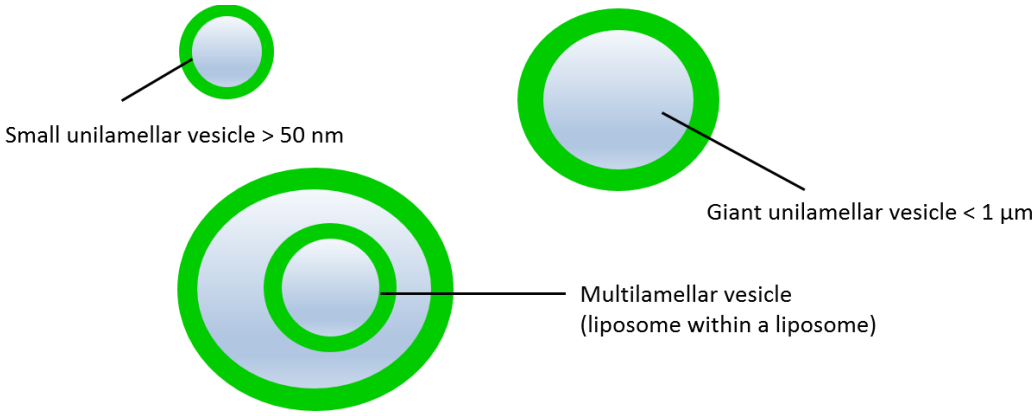

Figure 1.4 Diagram depicting the various sizes and morphologies of liposomes.

By incorporating a phospholipid such as DOPC it is possible to create GUVs that contain predominantly liquid-disordered regions. The formation of liquid-ordered domains is driven by adding cholesterol in high concentration (<20 mol %). Therefore, by adding a mixture of lipids such a DOPC, sphingomyelin (SM) and cholesterol, it is possible to create GUVs which contain both liquid-disordered and liquid-ordered domains. Fluorescence imaging can then be used for studying lipid membranes and artificial lipid membranes such as GUVs by incorporating a fluorescent dye into the lipid mixture prior to electroformation. Most fluorescent lipid membrane markers show strong preferential partitioning into the liquid-disordered phase.[34] The ability to label such lipid bilayers allows for the identification of lipid phases and also the ability to obtain environmental information using fluorescence lifetime imaging spectroscopy (FLIM) and fluorescence lifetime correlation spectroscopy (FLCS).

In recent years, interest in developing new dyes to study complex membrane components has increased due to the growing understanding of their role in signalling and also advances in modern microscopy.[34–37] Therefore, a need for probes capable of distinguishing lipid domains has risen. Today there are many commercially available probes with known partitioning behaviours such as Texas Red 1,2-dihexadecanoyl-sn-glycero-3-phosphoethanolamine (TR-DPPE), 2-(4,4-difluoro-5,7-dimethyl-4-bora-3a,4a-diaza-s-indacene-3-pentanoyl)-1-hexadecanoyl-sn-glycero-3 phosphocholine (Bodipy-PC) and as mentioned (1,1'-

Dioctadecyl-3,3,3',3'-Tetramethylindodicarbocyanine, 4-Chlorobenzenesulfonate Salt) (DiD). Such probes can now be used to identify the varying physical forms of lipid phases by exploiting their preferential phase partitioning. Using fluorescence microscopy, GUVs can be used to investigate physical processes such as phase separation.[38] A commonly used fluorescent lipid label is DiIC18(5) solid (1,1'-Dioctadecyl-3,3,3',3'-Tetramethylindodicarbocyanine, 4-Chlorobenzenesulfonate Salt) (DiD), which is known to selectively partition into the liquid-disordered phase.[34] The use of DiD to fluorescently label the liquid-disordered phase of GUVs can be seen in the reference below in Figure 1.5. Despite the availability of commercial probes there is always the need to design more efficient probes with enhanced photophysical properties. Dyes that are highly emissive, non-toxic, that can be used in low concentrations, that exhibit high quantum yields, show preferential partitioning to liquid-disordered domains or in particular to liquid-ordered domains, that are eligible for FLCS measurements and that can behave like a 'switch' i.e. only display fluorescence when partitioned into regions of interest are highly desirable.

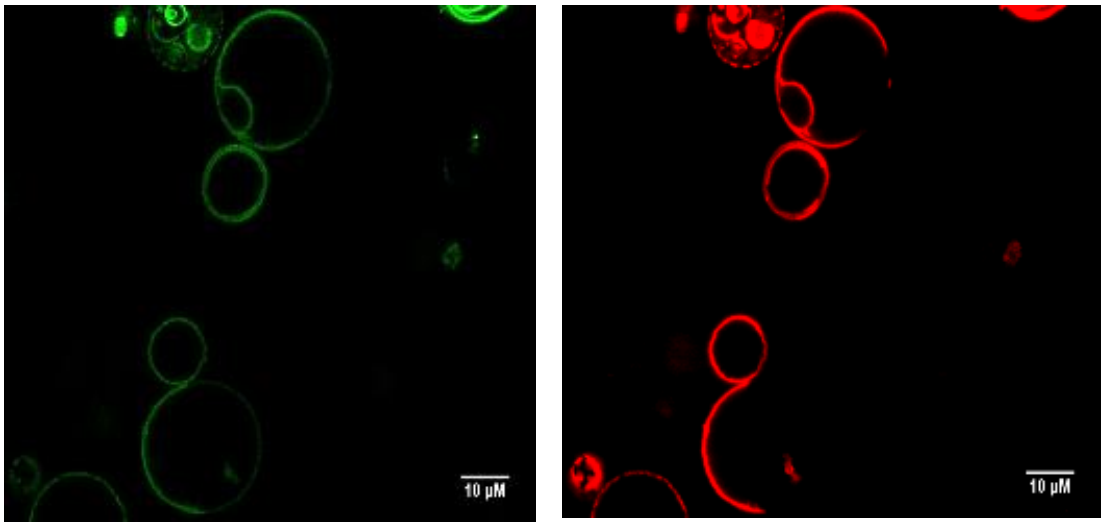

Figure 1.5 GUVs of composition DOPC/SM/Chol 4:4:2 mol % labelled with DiD (right) which is excluded from cholesterol rich liquid-ordered domains (shadowed regions). GUVs of composition DOPC/SM/Chol 4:4:2 mol % labelled with Dppz-Ar-BODIPY (left).

1.2.2 Supported Lipid Bilayers (SLBs)

Another commonly used biomimetic system is a supported lipid bilayer (SLB). SLBs are planar lipid bilayers which are most commonly formed on top of solid transparent substrates such as glass and less often, polydimethylsiloxane (PDMS).[39–41] These supported bilayers are extremely versatile, as they can be synthesised using a wide range of lipid compositions.

Within this body of work a supported lipid bilayer micro-cavity array on PDMS was used to carry out diffusion studies using the dyes outlined in chapter 4. A sophisticated method for preparing micro-cavity supported lipid bilayers involves a modified version of the Langmuir Blodgett technique by transferring a lipid monolayer from an air water interface to the array surface. The first step is to form a monolayer on the chosen substrate using the Langmuir-Blodgett technique. Using this technique, the monolayer forms as the lower leaflet of the bilayer, which lipid vesicles can then be absorbed and fused onto, creating the upper leaflet and completion of the supported lipid bilayer. The major advantage offered by this technique is it allows for the transfer of a highly complex lipid monolayer, defect free. The fusion of lipid vesicles over the monolayer results in a lipid bilayer formed across a buffer filled pore.

One of the drawbacks of SLBs is the close proximity of the supporting substrate from the bilayer which frequently results in surface interactions that can affect protein and lipid diffusion studies. These limitations can be overcome by spanning a bilayer across a buffer filled micro-cavity array. In chapter 4 this technique is used to prepare supported lipid bilayers of mixed compositions. One containing only DOPC 100 mol %, therefore forming a more fluidic bilayer containing only the Ld phase, and another bilayer rich in sphingomyelin and cholesterol (DOPC/SM/Chol 4:4:2 mol %), resulting in a more rigid bilayer that contains both Ld and Lo domains. This technique also allows biomimetic asymmetry to be built into the membrane model.

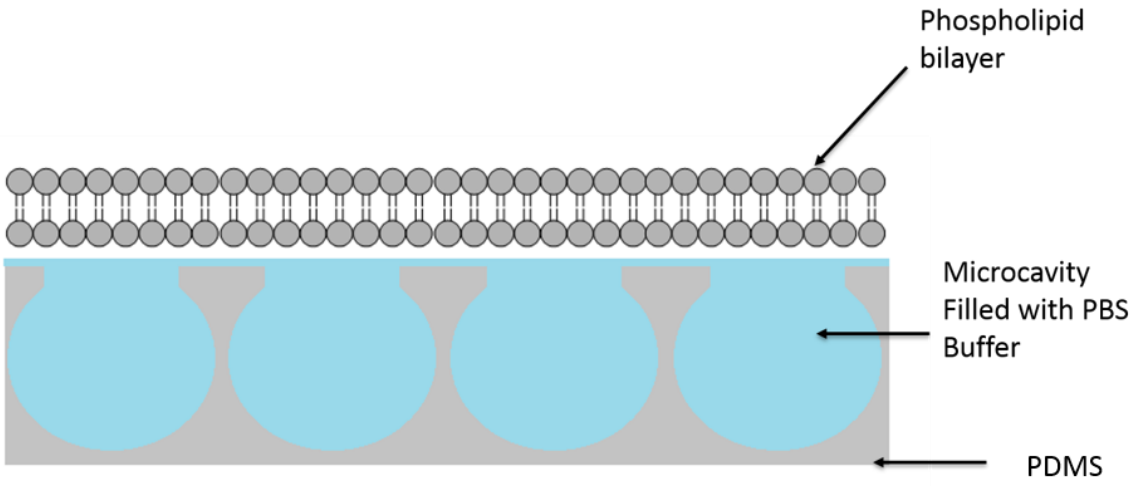

Figure 1.6 Schematic diagram of PDMS supported lipid bilayer microcavity array.

1.2.3 Fluorescent Self-Assembled Monolayers

Self-assembled monolayers (SAMs) are molecular assemblies adsorbed on solid substrates which can be spontaneously formed from the vapour phase or more commonly, from solution. SAMs provide a versatile way of controlling both the chemical composition and physical structure of the substrate surface. Fluorescent SAMs constructed on metal surfaces such as gold, silver and copper as well as oxides such as ITO and SiO_2 are attractive in applications across various domains as sensors and in optical devices.[42–44] By forming fluorescent SAMs on nanostructured substrates or nanoparticles, the photophysical properties of the fluorophore can be combined with the physiochemical properties of the substrate.

As shown in Figure 1.7, the building blocks of SAMs consist of three main constituents; the head group (linking group), the tail (backbone) typically consists of a hydrocarbon chain and the functional (active) group.[45] The head group is what drives the absorption onto the substrate linking the tail and substrate through strong bonds. The packing and stability of the monolayer can be affected by the bond angle between the head group and the substrate, length of the hydrocarbon tail and the interactions between tails (hydrophobic forces and weak Van der Waals).

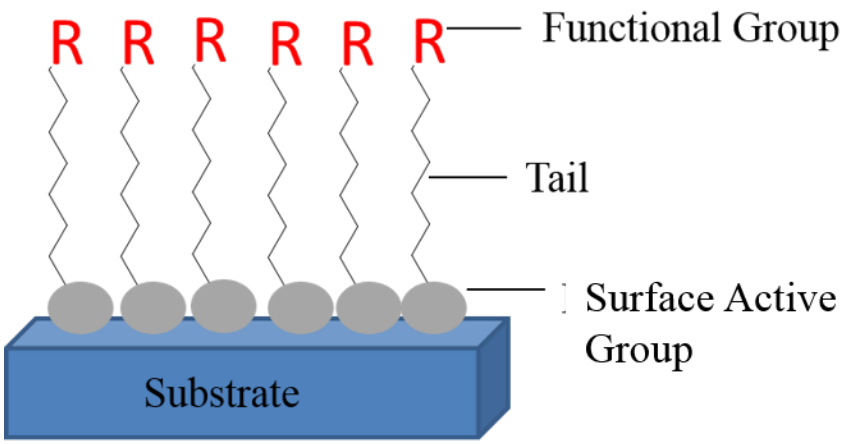

Figure 1.7 Schematic representation of a self-assembled monolayer (SAM).

The immobilisation of a fluorophore on a solid substrate can impact the photophysics in a number of ways. Close-packing of the self-assembly can result in fluorescence concentration quenching. When bound to the substrate surface the mobility of the fluorophore can be restricted. This may reduce rotational and vibrational effects that can reduce non-radiative decay pathways therefore increasing fluorescence polarisation. Immobilisation on a surface can also lead to inaccessibility, leading to limited access of quenchers (O_2), solvent and ions. Therefore, the fluorophore must be carefully selected or designed based on properties that can overcome the impacts of surface immobilisation and that also suit the target application.

The choice of surface-active group depends on the substrate being used. It is well known that thiols and disulfides bond to gold and silver subtrates.[47] While carboxylic acids and trialkoxysilanes are used to form SAMs on metal oxides.[45] Alkanethiols are one of the most commonly utilised surface-active groups, as in its reduced state thiol has a high affinity for metal surfaces, particularly gold substrates. The formation of fluorescent SAMs on gold substrates allows for fluorescence detection of fluorophore-analyte interactions as well as the ability to carry out electrochemical studies on gold electrodes. Many PAHs have been used in fluorescent SAMs including pyrene[46]. As shown in Figure 1.8, chapter 5 discusses the application of a fluorescent SAM for multimodal pH sensing using a newly synthesised pyrene derivative (PyLaOT). The dye incorporates dimethylamino groups which not only result in a red-shift of emission but also provide pH sensitivity through protonation of the nitrogen atoms. PyLaOT was also designed to overcome the surface immbolisation effects

mentioned above. The C_8 alkyl chain reduces the likelihood of quenching effects as the linker length decreases the probability of close-packed SAMs. At the surface the dye is more concentrated than it would be in solution, thus it is prone to self-quenching, however this is overcome in compounds with large Stokes shifts because the emitted photons do not lie within the absorbance tail of the compound.

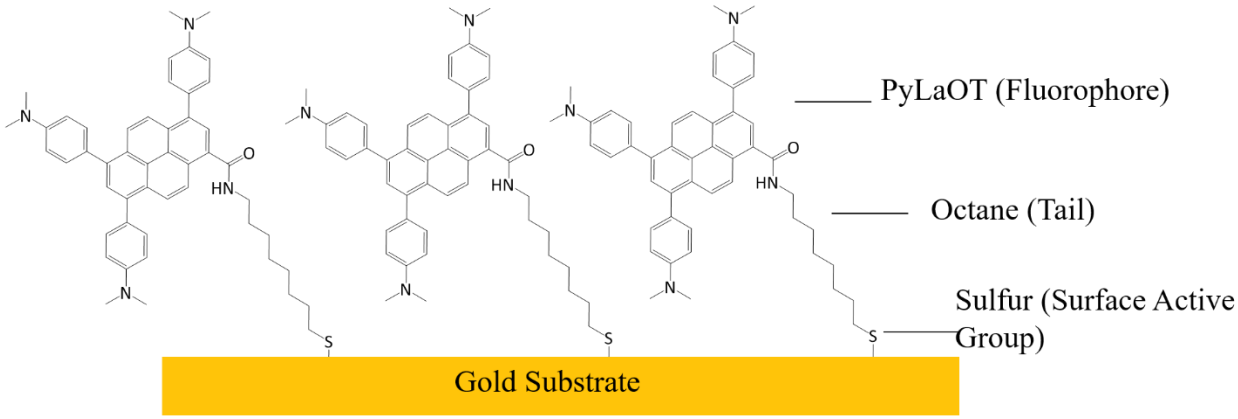

Figure 1.8 Schematic representation of a fluorescent SAM using PyLaOT formed on a gold substrate. (Diagram for visual purposes and not an accurate representation of bond angles).

1.3 Introduction to Molecular Photophysics

Figure 1.9 shows a Jablonski diagram that illustrates the photophysical deactivation pathways that an excited state molecule can undergo when it loses its excess energy and returns to the ground state. Figure 1.9 illustrates how fluorescence occurs for most organic fluorophores. Typically, a chromophore absorbs photonic energy leading to a transition from the ground state (S_0) to a higher vibronic level within a singlet excited state (Sn). It then rapidly relaxes to the lowest vibrational level of S_1 through vibration of the molecule and its surrounding solvent shell, known as vibrational cascade.

In condensed media fluorescence occurs when the molecule deactivates from this lowest vibrational level of the first singlet excited state to the ground state. The fluorescent lifetime of this emission is typically very short, of the order of 10^{-9} to 10^{-8} s. As fluorescence is spin allowed it typically occurs as the molecule transitions from singlet-to-singlet states. Fluorescence will always occur at lower energy (i.e. higher wavelengths) than absorption,

which is a result of the energy loss incurred during vibrational relaxation in the excited state. This is explained by Stokes Rule which states that the emission wavelength will always be at longer wavelengths than the initial absorption.

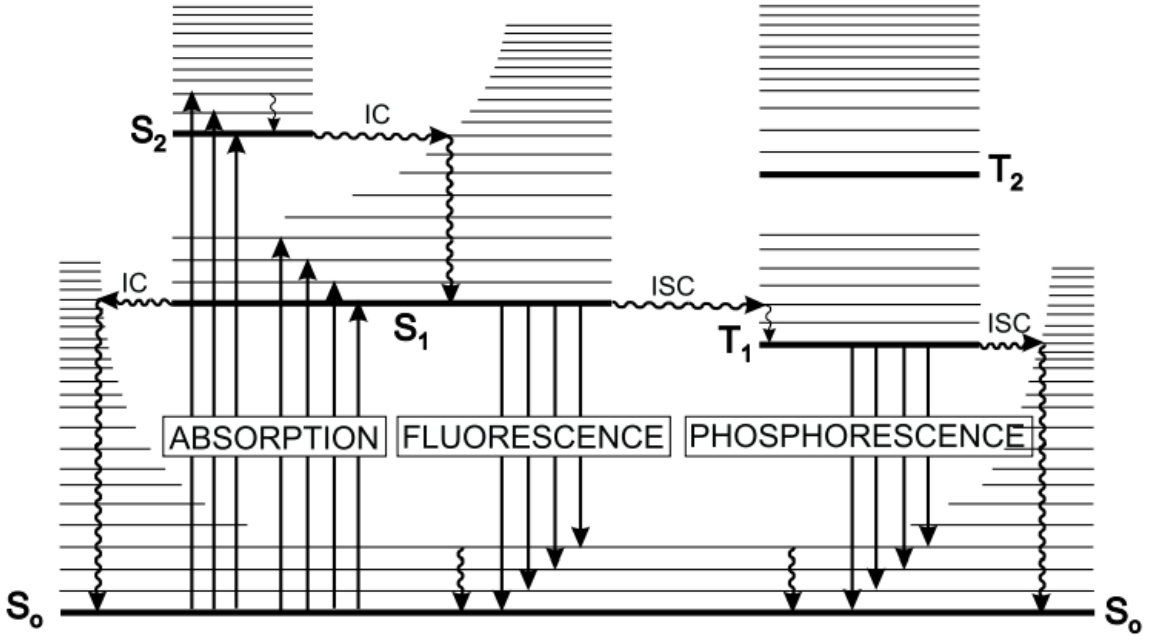

Figure 1.9 Jablonski diagram illustrating the radiative and non-radiative processes involved in the absorption and resultant deactivation of a molecule following excitation by a photon of light.[48]

Internal conversion is a non-radiative process described as the non-radiative transition between states of the same multiplicity (i.e. $S_2 \rightarrow S_1$). This process occurs when there is an isoenergetic crossover between vibronic states, then rapid vibrational relaxation to the lowest vibrational level of that electronic state. As seen in Figure 1.9 the vibrational relaxation to the lowest vibrational state of S_1 directly follows.

Phosphorescence is a radiative deactivation process which is observed when an excited state molecule emits a photon during the deactivation process between energy states of different multiplicities ($T_1 \rightarrow S_0$). Phosphorescence occurs when a molecule is excited from the ground state S_0 to the singlet excited state S_1 and then undergoes intersystem crossing (ISC), i.e. from the singlet excited state S_1 to the triplet state T_1.

ISC is an iso-energetic non-radiative deactivation process that occurs between states of different multiplicities (i.e. $S_1 \rightarrow T_1$). This process, in principle, is forbidden due to the electron in the excited state having parallel spin to the ground state, however may occur due to spin-orbit-coupling due to heavy atoms such as Br which increase spin-orbit-coupling and thus increase the likelihood of intersystem crossing. The phosphorescence lifetime is longer than the fluorescence lifetime due to these forbidden transitions and is usually of the order of 10^{-3} to 10^{-1} s. Fluorescence, however, is a higher energy process as it occurs at shorter wavelengths than phosphorescence.

1.3.1 Quantum Yield (Φ) and Lifetime (τ)

The luminescent quantum yield and the luminescent lifetime are two important photophysical properties of a fluorophore as they can be used to quantitatively assess the emission efficiency. Obtaining the lifetime is important as it determines how much time is available for the fluorophore to interact with or diffuse through its environment.[49] There are a number of factors that can affect the lifetime, such as the solvent used, oxygen concentration, pH and the presence of heavy atoms. Typically, the lifetime is independent of the fluorophore concentration, which makes it a useful analytical parameter. The luminescence lifetime (τ) of the fluorophore can be described as the average time an excited species spends in the excited state before photon emission. It can be expressed in terms of the radiative rate constant (k_r) and the non-radiative rate constant (k_{nr}) indicated by Equation 1.1

$$\tau = \frac{1}{k_r + k_{nr}} \qquad \text{Equation 1.1}$$

The luminescence quantum yield (ϕ_{lum}) can be simply expressed as the ratio of the number of absorbed photons to those emitted. It can be related to the lifetime and rate constants which are proportional to the absorbed and emitted photon, therefore ϕ_{lum} can be expressed in terms of k_r, k_{nr} and τ shown by Equation 1.2.

$$\phi_{lum} = \frac{k_r}{k_r + k_{nr}} = \tau . k_r = \qquad \text{Equation 1.2}$$

Thus, fluorophores with high quantum yields display bright emission, and if the rate of radiative rate constant (k_r) is greater than the rate of non-radiative decay (k_{nr}), then the quantum yield will be high. The luminescent quantum yield is a key parameter in calculating quenching rate constants, energy transfer rates and radiative/non-radiative decay rate constants.[50]

1.4 Fluorescent Dyes and Probes

1.4.1 General Introduction

There are thousands of fluorescent probes known today, with many being commercially available. Fluorescent probes, also known as fluorophores, are molecules which can absorb light at a specific wavelength and then re-emit that light at a longer wavelength. The development and characterisation of fluorescent probes is an ever-increasing area of interest due to the wide range of applications for fluorescent sensors and the abundance of information they can provide. Due to the strides made in synthetic chemistry and an increased understanding of photophysics, there has been an increase in the number of fluorescent probes in the literature which have been used to investigate biological, biochemical and physiochemical systems. Organic probes have a number of common structural and photophysical characteristics. They typically contain several combined cyclic or planar molecules with several pi (π) bonds. Other characteristics include: lambda max, luminescent lifetime, luminescent quantum yield, Stokes shift and molar extinction coefficient. Each of these characteristics will vary depending on the structure of the fluorophore and its chemical environment. The size, shape and polarity of the fluorophore in ground and excited state, along with its likelihood to photobleach are all important factors to be considered when creating or choosing a fluorescent probe particularly for biological imaging applications.

When applied to life sciences fluorophores can be divided into two main categories, intrinsic and extrinsic. Intrinsic fluorescent probes are those that occur naturally, examples are nicotinamide adenine dinucleotide (NADH), chlorophyll, flavins, the aromatic amino acids and green fluorescent proteins (GFPs). Extrinsic fluorescent probes include modified biochemical and synthetic dyes that are then added to a sample to produce a specific fluorescent profile. There is a great need for extrinsic fluorescent probes in the fields of

biological investigation of DNA and lipids as they generally do not contain any intrinsic fluorescence. Disadvantages of intrinsic fluorophores are that many need to be genetically modified which can be difficult and expensive. Many intrinsic fluorophores tend to excite and emit in the blue-region. It is often desirable to label the molecule with an extrinsic fluorophore in order to meet the requirements of modern fluorescence microscopy techniques.

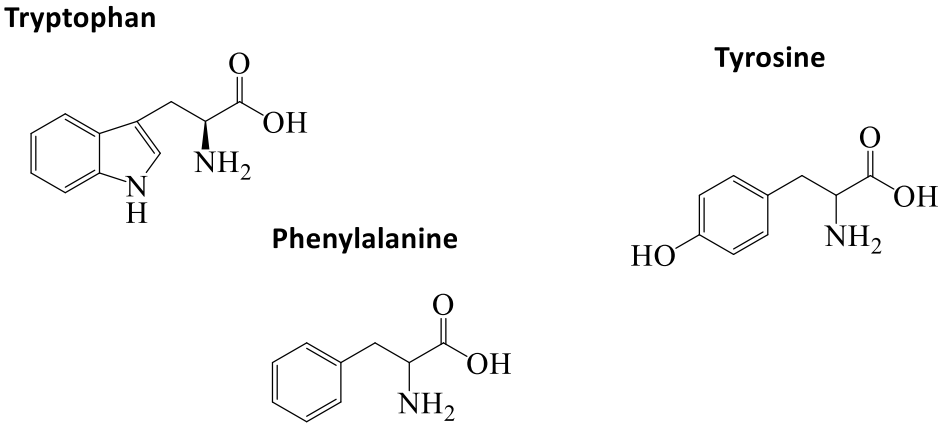

Figure 1.10 Structure of intrinsically fluorescent aromatic amino acids, tryptophan, tyrosine and phenylalanine.

Dansyl chloride is a commonly used fluorophore for labelling proteins and is a good example of an extrinsic fluorescent probe. It is capable of forming covalent bonds with amines and histidines present in proteins.[51] The dansyl groups can be excited at 350 nm which is well resolved from protein absorption and can emit in the region of 520 nm therefore possessing a large Stokes shift. Other commonly used commercial probes include rhodamines and fluoresceins, which are available in several derivatives. Fluoresceins are widely used for labelling as they have high molar extinction coefficients usually near 80'000 M^{-1} cm^{-1}, high quantum yields (fluorescein, ϕ = 0.90, 0.1 M NaOH)[52] and have a large emission range typically between 500-600 nm.[53] Several drawbacks of fluoresceins and many commercially available fluorophores is their small Stokes shift, poor photostability and their tendency to self-quench.

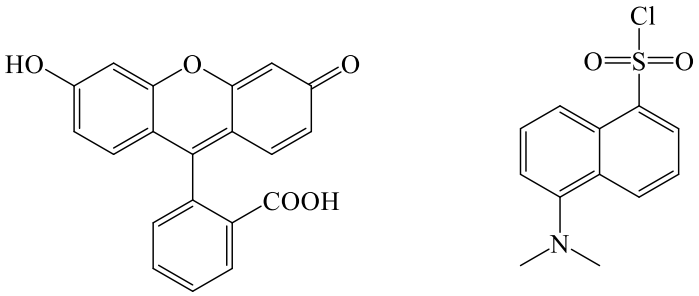

Fluorescein Dansyl Chloride

Figure 1.11 Chemical structure of fluorescein and dansyl chloride.

1.4.2 Properties of Ideal Fluorescent Probes for Imaging

When selecting a fluorescent probe for labelling, there are certain properties and characteristics to take into consideration:

Selectivity: When designing a new fluorescent probe or choosing a commercial probe for a specific study, it is vitally important to determine the ability of the probe to selectively target and emit a fluorescent response when in the presence of the studied analyte or environment. In the case of this study it important to design a probe that can selectively label liquid-ordered or liquid-disordered domains.

Robustness: Fluorescent probes should ideally possess good photostability as well as chemostability. Probes that have a low tendency to photobleach (destruction of the fluorophore due to over exposure to high fluorescent intensity, such as high laser power) are highly desirable.

Photophysical Traits: It is very important that the probe displays a high level of fluorescent brightness. For the probe to possess this quality it must have a high luminescent quantum yield and a high molar extinction coefficient. A large Stokes shift (possessing a large gap between the excitation maxima and the emission maxima) is also desirable, as it decreases the likelihood of the probe self-quenching. Narrow excitation and emission bands eliminates the likelihood of cross-talk with other probes when carrying out dual-labelling experiments.

The successful labelling of biological systems and living samples require the probes to possess good cell permeability, solubility and absorption and emission profiles in the near-infrared region (NIR).

Cell Permeability: the cells environment is largely made up of cytoplasm and plasma, therefore making aqueous solubility an important factor for the use of fluorescent probes in biological applications. A completely non-aqueous fluorescent probe may have trouble entering the cell and may accumulate in the cell membrane. It is important to have a good balance between hydrophilicity and lipophilicity so that the probe is capable of entering the cell, as well as then localising in subcellular units such as the nucleus and mitochondria.[6,54]

For biological studies, it is desirable to have a probe that emits in the near-infrared region (NIR, < 600 nm) as these probes can exploit the 'biological window', therefore penetrating deeper into tissues and are also less likely to cause photodegradation to live tissues and cells.[55,56]

It is important to note that although these are ideal properties for fluorescent probes in the use of fluorescence imaging, there are few probes that display all the characteristics mentioned above. For a given application it is desirable to design a probe which exhibits as many of these properties as possible.

1.5 Introduction to Microscopy Techniques

1.5.1 Principle of Fluorescence Confocal Microscopy

Within this work, fluorescence microscopy is used to image the novel fluorophores within artificial lipid membranes and cells. This technique uses a pinhole in front of the detector eliminating signal from out-of-focus planes. Only fluorescence very close to the focal plane is detected. This results in high resolution images of greater quality and detail. However due to much of the light being blocked by the pinhole, there is a decrease in signal intensity which must be overcome by long exposure times, bright fluorophores and sensitive detectors. In a confocal fluorescent microscope, the sample is excited using an excitation laser. Shown in Figure 1.12 is a schematic diagram of a confocal microscope system. This technique directs a beam of light at a desired wavelength through an aperture, which is then focused by the

objective lens into a cone shape so that the maximum intensity of the beam is focused on a single spot. The luminescence from the sample is then reflected by a dichroic mirror and directed onto a pinhole aperture. It is this pinhole system that differs confocal from conventional wide field microscopy. This aperture eliminates out-of-focus light, only allowing light from the selected focal plane. Therefore, the light from this selected optical region is picked up by the detector and converted to an electrical signal.[57]

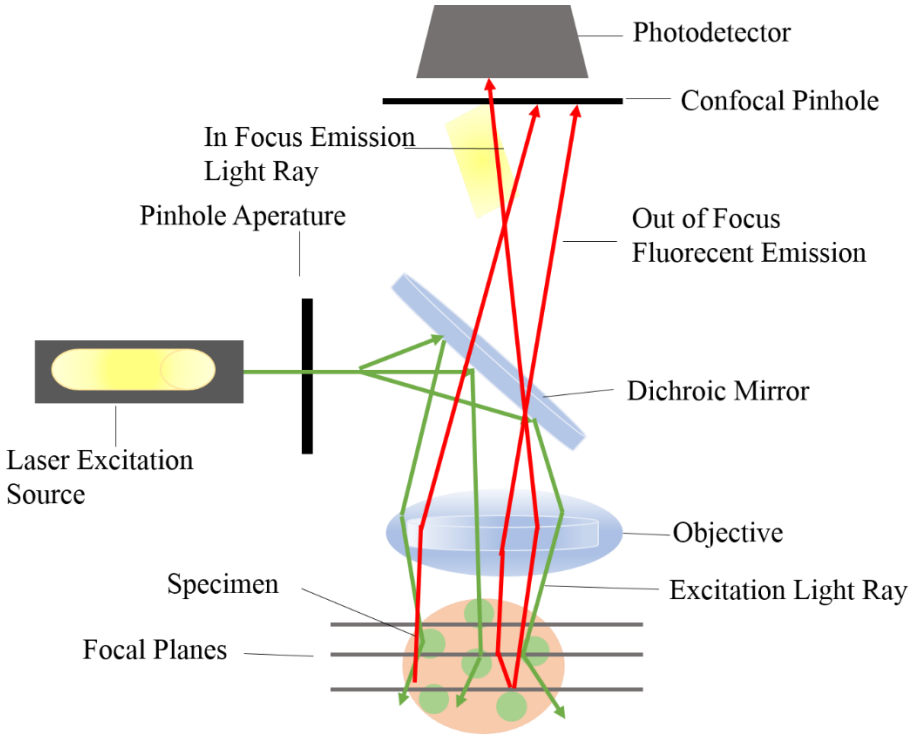

Figure 1.12 Schematic diagram of the components and optical pathway in a laser scanning confocal microscope.

1.5.2 Fluorescence Lifetime Imaging Microscopy (FLIM)

Fluorescence lifetime imaging microscopy (FLIM) is an imaging technique that can be applied as a confocal method that produces an image based on the differences in the excited state decay rate of a fluorescent sample. Image contrast is therefore based on the emission lifetime of the probe rather than emission intensity. Fluorescent lifetime measurements are robust as they can be independent of concentration as well as other factors such as excitation intensity, however it can be greatly affected by the environment, pH, oxygen concentration

and molecular binding. For these reasons, FLIM is one of the most reliable methods for obtaining information about the environment of the probe.

FLIM usually employs time correlated single photon counting (TCSPC) in order to determine the fluorescence lifetime. This method uses short pulses of light to excite the sample which then emits a photon. The lifetime decay is obtained by measuring the time taken between the excitation of the sample and the arrival of an emitted photon at the detector. This is the main principle behind TCSPC.[58] The decay time, which is represented by τ, is calculated by getting the slope of the plot *log (I) t versus t.* The measurement is repeated, and each detected photon contributes to a histogram or decay curve which overtime, builds to give the lifetime. In FLIM, the detected photons are sorted into pixels based on their arrival time of detection. In the resulting FLIM image, each pixel is made up of the detected photons in that region, making up a false-colour lifetime image.[59] TCSPC FLIM gives the highest time resolution with the best lifetime accuracy of the time resolved fluorescence imaging methods.[60] Each pixel of a FLIM image is the fluorescent lifetime decay and not the intensity. The data acquired from a FLIM image is analysed by fitting it to a decay model, typically either a mono- or bi-exponential decay.[61] Mono-exponential (single exponential) is when there is only one contributing fluorophore (or fluorophore environment) in the sample. Bi-exponential or indeed multi-exponential emission decays can occur, for example, where a single fluorophore occupies different environments that impact the photophysics of the probe distinguished by their individual lifetimes. An example of this is if there are multiple fluorophores present, they can be distinguished based on their lifetime. Martin *et al* synthesised a ruthenium-BODIPY dyad which was bi-exponential. In aerated methanol a lifetime of 306 ns was attributed to the ruthenium and a second lifetime of 24 ns was attributed to the appendant BODIPY.[62]

1.5.3 Stimulated Emission Depletion Spectroscopy (STED)

As discussed in section 1.5.1 confocal fluorescent microscopy is a widely used imaging technique and a key tool for the detection of proteins, structures and processes in cells, tissues and organisms. However, the spatial resolution that can be obtained by this technique is limited due to the restraints caused by the diffraction limit of light. The successful resolution of sub-wavelength structures using confocal microscopy is impossible and can be described by the Ernst Abbe equation (Equation 1.6). This equation states that light of a specific wavelength λ, travelling in a medium with a refractive index *n* that converges with a spot of half-angle θ will result in a minimal resolvable distance (d) given by Equation 1.6, where $dnsin\theta$ is also expressed as the numerical aperture (NA) of the lens.

$$d = \frac{\lambda}{2n\sin\theta} = \frac{\lambda}{2NA} \qquad \text{Equation 1.6}$$

Thus, a microscope cannot resolve features that are located closer to each other than λ/2NA. If blue light at wavelength 450 nm is taken with a numerical aperture (NA = 1), then the Ernst Abbe diffraction limit will be 225 nm (0.225 μm). This is small when compared to cells that can range in size from (1100 μm), however considerably larger than regions of interest such as proteins (10 nm) or organelle components.

A technique that has been able to overcome the diffraction limit is super resolution microscopy. The first super resolution microscopy to emerge was stimulated emission depletion microscopy (STED).[63] The development of this technique led to Stefan W. Hell, William E. Moerner, and Eric Betzig being awarded the Nobel Prize for Chemistry in 2014.

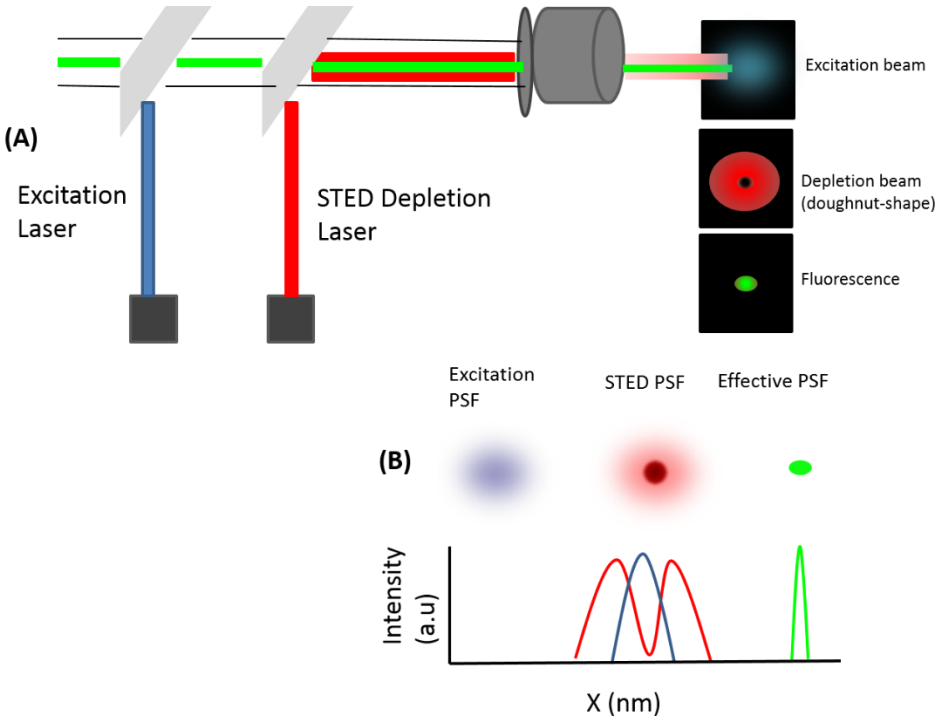

Figure 1.13 (a) Schematic diagram of an optical STED microscope with excitation laser (blue) and STED depletion beam (red). The depletion laser (red) overlaps the excitation laser (blue) resulting in a 'donut-shape' in the focal plane and the resulting effective detected fluorescence emission (green). (b) The principles of STED: A laser light is used to excite (blue) fluorescence emission (green) in the area of focus. The STED laser (red) is used to selectively turn off emission in the outer periphery, allowing for better separation of fluorescent entities. This results in a smaller point spread function (green) which in turn results in much more effective fluorescence being achieved and higher resolution.

In confocal fluorescence microscopy, fluorescence occurs by exciting the sample from S_0 to a higher excited state $S_{1,}$ which after relaxation to the ground state of $S_{1,}$ emits a photon by falling from the ground state of S_1 to a higher vibrational level on S_0. As shown above in Figure 1.13 STED uses a pair of synchronised lasers to interfere with this process. The first laser depicted in blue (Figure 1.13 (a)) is used to excite the sample. Following this a depletion laser, typically red-shifted in comparison to the emission of the fluorophore is used to interrupt the fluorescence process by forcing the excited electron to relax into a higher vibrational level than the fluorescence transition, resulting in a red-shifted photon release of lower energy. By lowering the energy gap, a higher wavelength photon shifted to the red is observed. This increase in wavelength can then be used to differentiate between photons, allowing stimulated emission to be ignored. The STED laser is spatially arranged in a

'doughnut-shape' designed to overlap with the excitation as shown in Figure 1.13 (b). Fluorescence from molecules at the periphery of the excitation focus are quenched by the stimulated emission as explained above, resulting in a reduction of spot size of the incident laser below the diffraction limit. The application of STED for imaging a sample can be seen in the schematic representation (Figure 1.14). A sample labelled with a fluorophore is excited with an excitation laser which fluoresce and result in the imaging of the sample (Figure 1.14 (a)). Using STED, the fluorescence by some of the fluorophores present in the sample is quenched resulting in a more effective point spread function and higher resolution (Figure 1.14 (a)). This improved optical resolution can be explained by Equation 1.7.

$$d = \frac{\lambda}{2NA\sqrt{1+\frac{I_{max}}{I_{sat}}}} \qquad \text{Equation 1.7}$$

Where λ is the emission wavelength, NA is the numerical aperture of the objective lens, I_{max} is the peak intensity of the STED laser within the depletion zone, and I_{sat} is the applied STED laser threshold intensity, in other words the intensity that depletes 50 % of the probe's emission intensity. The intensity of the laser is proportional to the effective depletion. This results in the need for dyes with high photostability, able to withstand intense laser power and photobleaching, while maintaining a high quantum yield. Therefore, choosing a STED dye with the right characteristics is very important.

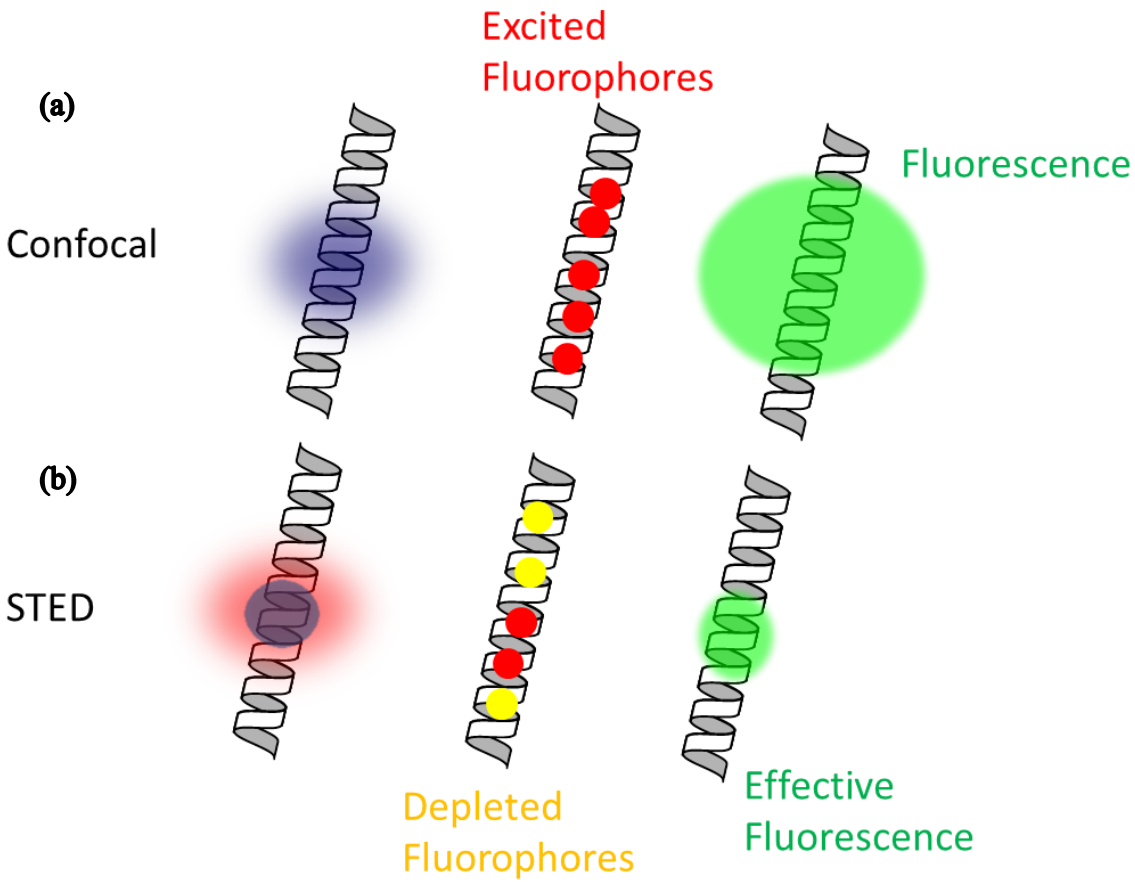

Figure 1.14 Schematic of confocal fluorescent microscopy (a) Sample is excited with an excitation laser (blue). The fluorophores present within the sample are excited (red). The fluorophores present then emit photons resulting in fluorescence (green). Schematic of stimulated emission depletion spectroscopy (STED) (b) The sample is excited with an excitation laser (blue). A depletion laser (red) is used to suppress emission in the outer periphery resulting in a 'donut-shaped' focal plane. This results in some fluorophores being excited (red) while others are depleted (yellow). This depletion results in a more effective fluorescence and increases resolution.

1.5.4 The Characteristics of a Good STED Dye

The development of STED super resolution microscopy means there is now a requirement for dyes compatible with the technique. Many fluorescent dyes used in microscopy are organic based. The commercially available dyes recommended for STED imaging include Atto[64–66] and AlexaFluor[65,67]. Both sets of probes are widely used due to their high photostability. One of the main disadvantages of organic fluorophores for use as STED dyes is their small Stokes shift. This can result in the STED depletion laser re-exciting the probe due to spectral overlap between the absorption profile of the dye and the depletion laser line.

In chapter 4 this problem was overcome by synthesising a fluorescent pyrene derivative which exhibited a mega-Stokes shift in most solvents and cell samples. Dyes with large Stokes shifts can avoid re-excitation by the depletion laser and thus avoid transitions to dark states which can cause photo bleaching.[68] Mega-Stokes shifted dyes such as PyLa-C_{17}Cer described in chapter 4 also aid multicolour and dual-stain imaging. Multicolour imaging is the ability to image more than one fluorophore at the same time.[66] This requires the dyes in question to absorb and emit in different regions of the UV-Vis spectrum.

As previously mentioned, it is desirable for STED dyes to have high photostability to withstand the high intensity of the depletion laser and avoid photo bleaching or degradation. The emission profile of the dye must overlap well with the depletion laser to stimulate effective depletion emission. When carrying out cell and molecular biology experiments it is desirable to have dyes with high molecular brightness and quantum yields, able to be stimulated at low concentrations. If a dye can be used effectively at low concentrations, cytotoxic effects during imaging experiment time-frames can be avoided. Many commercial probes only address photostability and high quantum yields.

1.6 BODIPY Based Fluorescent Probes

1.6.1 Structure and Spectroscopic Properties

One of the main aims of this study is to synthesise and characterise BODIPY and pyrene dyes containing different ligands and cholesterol conjugated derivatives to enable imaging and dynamic studies of the natural and artificial cell membranes. The difluoro-boroindacene family (4,4-difluoro-4-bora-3a,4a-diaza-s-indacene), abbreviated (BODIPY) has gained popularity as fluorescent probes for imaging in recent years, mainly due to their versatility and tunability. They were first reported by Treibz and Kreuzer in 1968.[69] BODIPY dyes contain a 4,4-difluoro-4-bora-3a,4a-diaza-s-indacene core structure which can be functionalised at a number of positions as shown in Figure 1.15. Many derivatives have several advantages including good photostability, high molar extinction coefficients ($<$ 80,000 M^{-1} cm^{-1}), exhibit quantum yields as high as 0.90, emit in the visible region ($\geq$ 500 nm), have sharp narrow absorption bands, good solubility and tend not to self-aggregate in solution. BODIPY dyes typically exhibit an intense narrow band absorbance peak at

approximately 500 nm which is due to a S_0-S_1 (π-π^*) electronic transition and a shoulder at 480 nm due to S_0-S_1 (π-π^*) vibrational transition. A broad transition of weaker intensity at 360-370 nm can be attributed to a S_0-S_2 (π-π^*) transition from the dipyrromethene ligand.[70,71] BODIPY dyes tend to have lifetimes, typically in the region of 0.8-10 ns.[72]

The BODIPY core has eight positions that can be readily functionalised. Functionalisation at these positions can have a profound effect on the photophysical properties, enabling optical tuning. Some of the reactions include nucleophilic substitutions at positions 3, 5, 4 and 8, electrophilic substitutions at positions 2 and 6, condensation reactions at 3, 5 and 2, 6. Palladium catalysed coupling reactions such as Sonogashira and Suzuki–Miyaura which is utilised in this study, can be used at all positions except the 4–position.[73]

Substituents at the 1 and 7-positions of 1,7-dimethyl-8-aryl-substituted BODIPY dyes can result in increased quantum yields. Studies have shown that a 1, 3, 5, 7-tetramethyl BODIPY core compared with a 3,5-dimethyl core results in an increase in quantum yields due to steric constraint, by reducing the loss of energy from non-radiative decay by preventing free rotation of the aryl groups at the *meso*-position.[74] The inclusion of *ortho*-substituents on phenyl rings positioned on the 8– or *meso*–position can also increase fluorescent quantum yields. This is due to the prevention of free rotation of the external phenyl group which can be caused by either the *ortho*-substituents on the phenyl group or due to steric effects caused by substituents at positions 1-and 7, which lead to a reduction in energy loss form excited states.

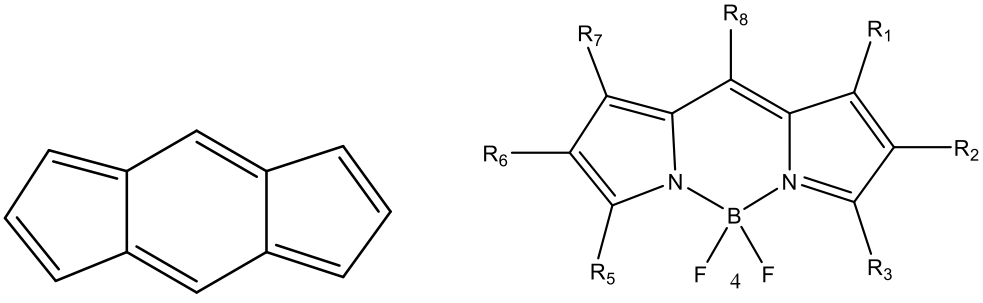

S-indacene BODIPY core

Figure 1.15 Structure and numbering of BODIPY core derived from s-indacene.

The BODIPY core does not show emission at long wavelength or NIR fluorescence. However, modifications to the core can result in red-shifted BODIPY derivatives and many have been reported with emission ranges between 480-700.[72,75–77] By incorporating aromatic rings, double and triple bonds through the electrophilic positions of the BODIPY core, large red-shifts can be obtained by extending the π-system. *Vincente et al* reported a series of 3, 5-diiodo-BODIPY complexes that had emission maxima's ranging from 579-686 nm, the largest Stokes shift reported being 0.092 eV.[78] Our group has also previously reported a naphthyridyl-BODIPY derivative which exhibited a mega-Stokes shift of 0.52 eV and an emission maximum of 740 nm.[76] Another successful approach to shifting the emission profile of BODIPY to the NIR-region is the synthesis of aza-BODIPYs. These BODIPY derivatives containing a nitrogen atom at the 8-position and aryl substituents at the 1, 3, 5 and 7-positions result in longer wavelength absorption and emission profiles shifted to the far-red.[79,80] The photophysical properties of aza-BODIPYs make them advantageous for biological labelling, however the dependence on hydrophobic aryl substituents tends to cause aggregation in aqueous media. In order to increase hydrophilicity, aryl substituents containing sulfonyl groups have been used to great effect.[81]

1.6.2 Synthesis of Symmetrical BODIPY Dyes

Like many significant chemical discoveries, BODIPY was synthesised by accident when 2, 4-diemthylpyrrole was reacted with acetic anhydride while in the presence of boron trifluoride diethyl etherate ($BF_3{\cdot}OEt_2$). Many years passed until its potential, especially in the field of fluorescent imaging was realised in the 1980s, and it wasn't until the 1990s that research in creating BODIPY derivatives greatly increased. The most commonly synthesised BODIPYs are 8-position or *meso*-substituted BODIPYs due to their relative ease of synthesis. They can be prepared via condensation reactions of acyl chlorides with pyrroles followed by the addition of $BF_3{\cdot}OEt_2$ and Et_3N. The reaction scheme can be seen below, Scheme 1.1.

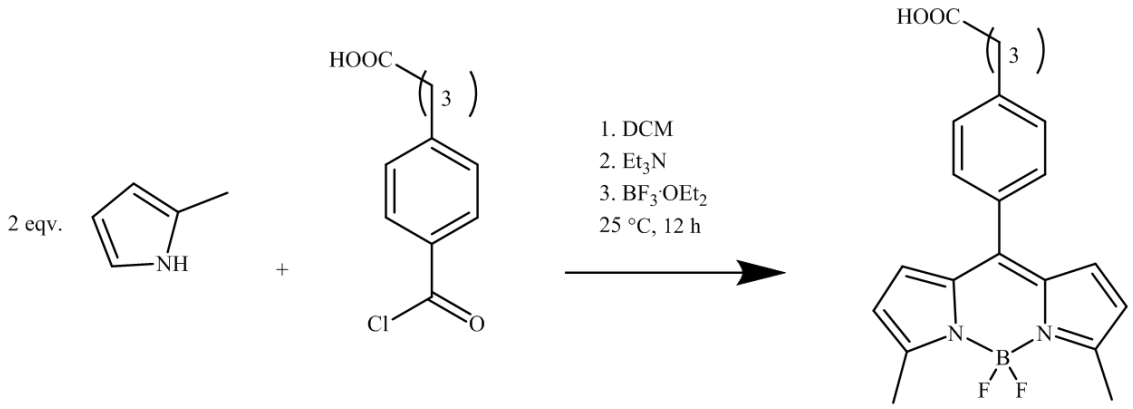

Scheme 1.1 Reaction scheme for the synthesis of BODIPY via the condensation of acyl chlorides and pyrroles.[73]

Another common synthetic route, and the method which is used by our group, is to synthesise BODIPY dyes using an aromatic aldehyde and two equivalents of a substituted pyrrole. Similar to the reaction shown in Scheme 1.1, BODIPY dyes can be formed via a knoevanegal type condensation reaction of aromatic aldehydes and pyrroles as shown in Scheme 1.2. This route requires an oxidation step and the two commonly used oxidants are p–chloranil and 2,3-dichloro-5,6-dicyano-1,4-benzoquinone (DDQ). This reaction can be carried out in two steps or one. An 8–position substituted dipyrromethane derivative can be formed by reacting an aromatic aldehyde and pyrrole in the presence of TFA catalyst. This dipyrromethane complex can then be purified and then oxidised to form dipyrromethene or the reaction can be continued by directly adding either p–chloranil or DDQ as an oxidant and then treating with $BF_3{\cdot}OEt_2$ and Et_3N. The use of either oxidant results in the formation of unwanted by-products which require tedious purification, often needing two column chromatography purification steps of column chromatography followed by a recrystallisation step, in order to isolate the desired BODIPY product. However, this route has a clear advantage as the use of substituted pyrroles and benzaldehydes broaden the scope of the reaction and allow for further elaboration of these groups. The advantage of the acyl chloride route is that there is no oxidation step required therefore requiring less purification steps and larger yields.

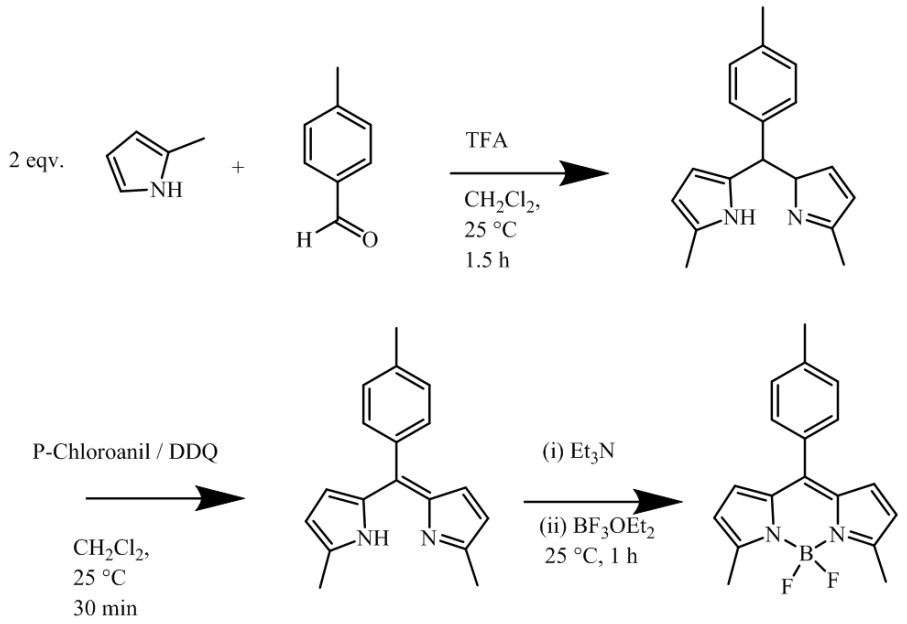

Scheme 1.2 General reaction scheme for the synthesis of BODIPY via condensation type reactions of aldehydes and pyrroles.

The resulting products of these types of reactions are BODIPY dyes with aryl groups at the 8- or *meso*–position. It would be expected that the addition of aromatic groups to an extended π–system would increase the electron conjugation, resulting in significant alterations of the absorption and emission wavelength. However, these aryl groups are typically orientated perpendicular to the BODIPY core, therefore modifications at this position generally do not result in noticeable changes in the absorption and emission wavelengths.[69,82] The extent of rotation of the 8–position substituents are also important for the overall fluorescence of the complex. Substituents at the 1, 7–positions as well as *ortho*-substituted groups on a *meso*–positioned phenyl ring prevent free rotation of the *meso*–group which in turn increases the fluorescent brightness.[82] The *meso*–group is important for structural versatility as it provides the route to structurally unique derivatives, as many BODIPY dyes are linked to other moieties through this position. For example, BODIPY dyes synthesised via the acyl chloride route have a free carboxylic acid terminal which can be readily linked to lipids, DNA and peptides.[83,84] One area of research that has successfully exploited the *meso*- position is the design and synthesis of molecular rotors. Work carried out by the Kuimova group has used one of the most widely used lifetime-based rotors phenyl-BODIPY and its derivatives to probe lipid membrane viscosity.[85–87] The dyes contain a hydrophobic alky chain attached to

a *meso*- phenyl-BODIPY which increases the likelihood of lipid partitioning. Changes in the lifetimes and quantum yields of these dyes due to rotation of the phenyl group at the *meso*-position can be attributed to the rigidity and viscosity of the membranes.

1.6.3 Synthesis of Unsymmetrical BODIPY Dyes

Condensation of acyl chlorides and aldehydes with pyrroles are two good synthetic pathways for synthesising symmetrically substituted BODIPYs. However, in order to synthesise unsymmetrically substituted BODIPYs, a Lewis acid mediated condensation of ketopyrroles must be carried out with another pyrrole molecule, as shown in Scheme 1.3.[88]

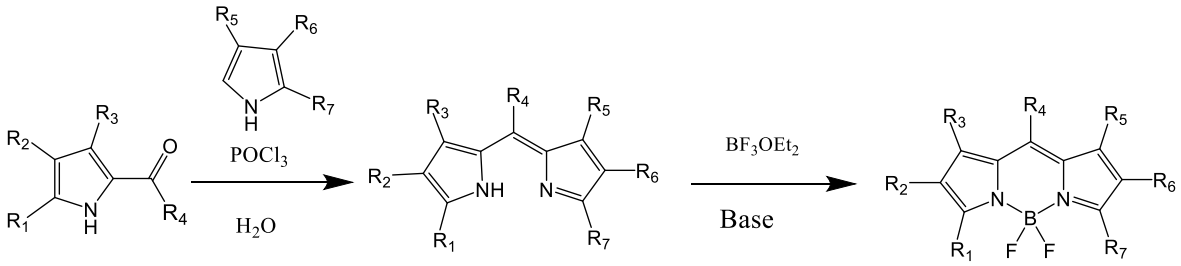

Scheme 1.3 Common procedure for the synthesis of asymmetric BODIPYs from ketopyrroles.

This reaction results in higher yields when electron–rich pyrroles are used and is a useful means to obtain BODIPY probes with different functional groups on the left and right side of the core. However, if electron–deficient pyrroles are used, a self–condensation side reaction can occur, resulting in the formation of unwanted symmetric BODIPY, thus lowering the yield.

1.6.4 Functionalisation at the 2,6- positions of the BODIPY Core

Due to our interest in designing BODIPY derivatives with polycyclic ligands at the 8- or *meso*-position to promote membrane partitioning, all BODIPY derivatives outlined in chapter 2 and 3 of this thesis were synthesised using aromatic aldehydes and substituted pyrroles as described in Scheme 1.2. It was therefore necessary to find another route to the functionalisation of the BODIPY core. The most facile option was to carry out functionalisation reactions at the 2,6-positions. It is well established in literature that the 2, 6-positions bear the least positive charge, this is clearly shown by the resonance structures in

Figure 1.16.[38] Therefore they readily undergo electrophilic substitution reactions, including halogenation (Br, Cl and I), sulfonation, nitration and formylation.[50,58,89–9

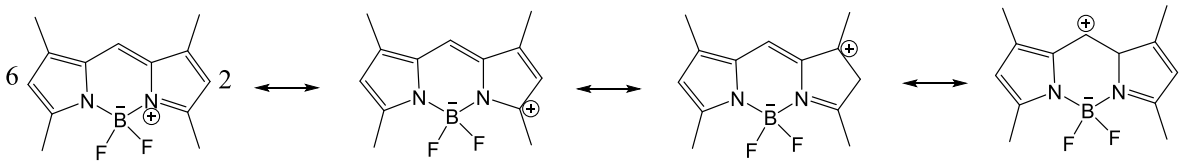

Figure 1.16 Illustration of the resonance delocalisation of the positive charge on the BODIPY core.

Halogenation, particularly bromination and iodination, have been the most common electrophilic substitution reactions employed at the 2- and 6-positions. For example, bromination at the 2,6-positions can be easily achieved by slowly adding bromine at room temperature to 1, 3, 5, 7-tetramethyl substituted BODIPYs. This reaction has been previously used by our group to synthesise brominated BODIPY derivatives.[62]The addition of heavy atoms such as bromine and iodine at positions 2- and 6- can result in a bathochromic shift in the absorption and emission profiles, while decreasing the quantum yield by increasing the rate of intersystem crossing by facilitating strong spin-orbital coupling between singlet and triplet states..[50] These 2,6–bromo and iodo-BODIPY dyes can also be used as intermediates in coupling reactions such as Suzuki–Miyaura, Sonagashira and Heck-coupling. Our group has previously synthesised a naphthyridyl-BODIPY complex with two diaminobenzene groups attached at the 2,6–positions by carrying out a Suzuki-Miyaura coupling of the brominated intermediate.[76]

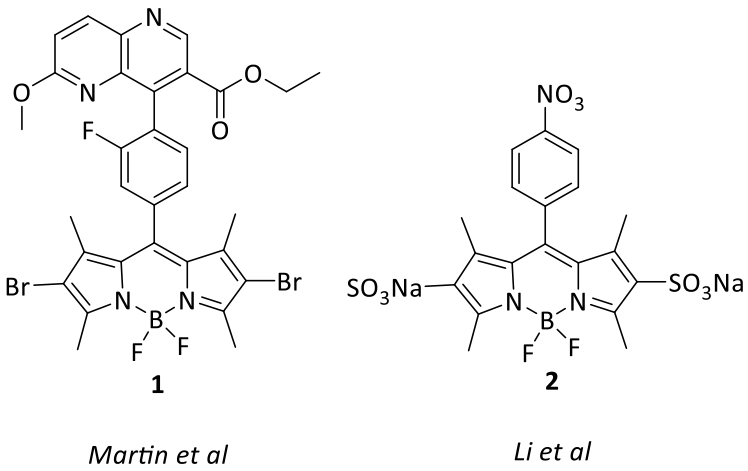

Figure 1.17 2,6-substituted BODIPY dyes from literature, **1**[76], **2**[84].

Another important electrophilic substitution reaction that has recently been reported for BODIPY derivatives is formylation via the Vilsmeier-Haack reaction.[89] It involves treating BODIPY derivatives unsubstituted at the 2,6-positions with Vilsmeier-Haack reagent, which is generated by adding phosphorous oxychloride ($POCl_3$) with dimethylformamide (DMF) at 0 °C. This reaction is employed in the synthesis of naphthyridyl-BODIPY-2-Cholesterol and is discussed in chapter 2 in greater detail.

1.6.5 Biological Applications of BODIPY

The BODIPY fluorophore has been described as the 'El Dorado' of fluorescence tools[92], with its desirable photophysical properties and outstanding chemical versatility leading to widespread applications, including light-harvesting arrays[93,94], photodynamic therapies[95–97], laser dyes[98,99] ion/metal-sensing[100–102] and hydrogen production[103]. One area of research that has seen extensive use of BODIPY is the field of bio-imaging. Their ease of synthesis and modification allows for tuning of optical properties, solubility and targeting, all of which play a vital role when imaging biological samples.

To date BODIPY derivatives have been widely applied to cellular imaging, targeting a wide range of organelles. Despite its overall hydrophobic structure BODIPY has been used to image cytosol by substituting mono-alkoxy groups onto the boron atom, resulting in increased water solublitiy.[104] By adding the positively charged moieties triphenylphosphine and triethylamine to a phenyl-BODIPY core, Gao *et al* successfully labelled HeLa cells with

no cytotoxic effects by using the cationic groups to guide the BODIPY to the mitochondria.[105] As well as specific cell organelles, BODIPY derivatives tagged with peptides or proteins have been used to label target proteins. Miller *et al* synthesised a trimethoprim (TMP) conjugated BODIPY capable of tagging *Escherichia coli* dihydrofolate reductase (eDHFR) fusion proteins on the plasma membrane or nucleus of wild-type mammalian cells.[106] Further work carried out by Wu *et al* modified eDHFR with a thiol group so it would covalently bond to a similar BOIDPY-TMP derivative.[107]

By functionalising fluorophores with moieties that provide an optical response to certain stimuli, changes in cellular environments can be detected. One of the most important biological parameters is pH, as it plays a role in many vital physiological processes, including cell growth, metabolism and ion transport. For this reason, many pH-sensitive BODIPY dyes have been synthesised capable of 'Off-On' fluorescent switching.[108,109] The pH-sensitivity usually occurs through a photoinduced electron transfer (PeT) mechanism. Switching is usually dependent on the protonation of amino or phenol groups, resulting in detection of reversible pH changes. Work carried out by the O' Shea group demonstrated a sophisticated pH-sensor based on aza-BODIPY.[110] The dye consisted of an aza-BODIPY core resulting in NIR emission allowing for penetration of biological tissues. A polyethylene glycol (PEG) group was added to increase water solubility and promote uptake. The pH-sensitive moiety was an *ortho*-nitro phenolic group which upon protonation in the acidic environment of lysosomes exhibited a 'switch-on' fluorescence, easily detected through fluorescence microscopy.

The popularity of the BODIPY fluorophore across a wide range of scientific fields including bio-imaging and sensing, combined with regular reports of new derivatives in literature like the examples given above, has led to a significant increase in the number of commercially available BODIPY dyes. Thermo Fisher Scientific is one of the largest commercial sellers of BODIPY dyes worldwide and they provide many probes with a range of biological applications, some of are shown in Table 1.1 and 1.2.

Some of the dyes they sell include BODIPY FL conjugates of adenosine triphosphate (ATP) and guanosine triphosphate (GTP) which can be used as structural probes for nucleotide-protein binding. BODIPY FL Histamine is used to label acidic organelles in living cells. They also sell two of the longest wavelength amine-reactive BODIPY dyes commercially available, BODIPY 630/650-X and BODIPY 650/665-X. Thermo Fisher Scientific provide numerous excellent cellular stains for specific organelle labelling, two of which are commonly used to stain the golgi apparatus and endoplasmic reticulum, the red fluorescent BODIPY TR-glibenclamide and BODIPY TR-ceramide.

Table 1.1 Near – IR Commercial BODIPY probes available from Thermo Fisher Scientific for biomolecular conjugation.

Dye	**Chemical Structure**	**Absorption Maximum (nm)**	**Emission Maximum (nm)**
BODIPY 630/650-X	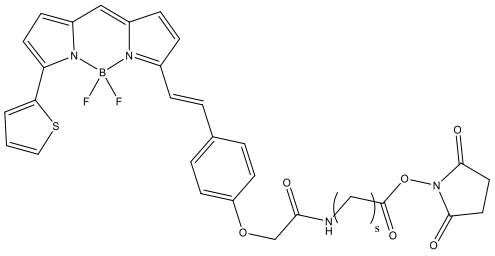	625	640
BODIPY 650/665-X	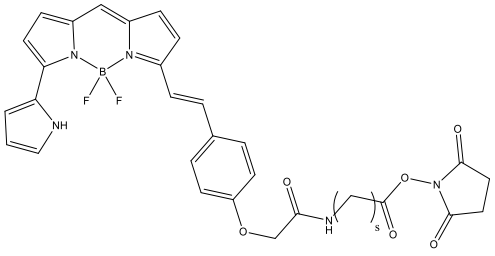	646	664

Table 1.2 Commercial BODIPY probes available from Thermo Fisher Scientific for cellular staining.

Dye	Chemical Structure	Absorption Maximum (nm)	Emission Maximum (nm)
BODIPY TR - glibenclamide	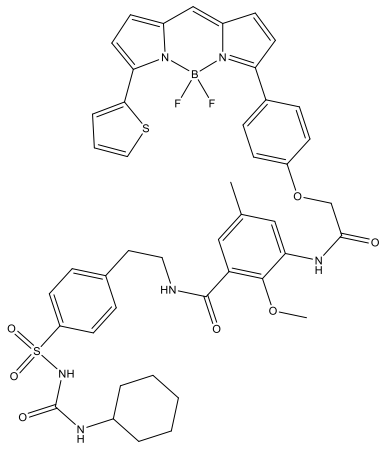	587	615
BODIPY TR - ceramide	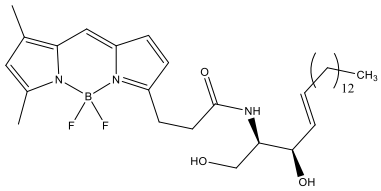	505	520
BODIPY 630/650-X	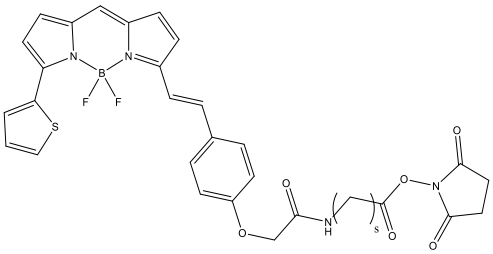	625	640
BODIPY 650/665-X	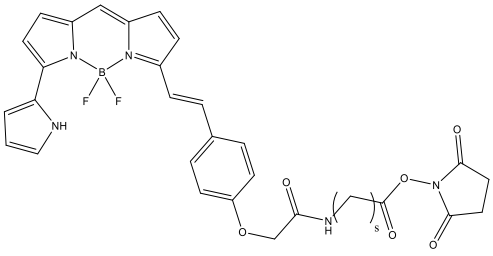	646	664

1.6.6 The Use of BODIPY Probes for Lipid Labelling

One of the drawbacks of BODIPY for biological imaging is the hydrophobic nature of its derivatives, however an ever-expanding area of research where hydrophobicity is desirable is lipid membrane imaging, which is the prime focus of this study.[35,36,111] As mentioned in previous sections, the coexistence of different lipid phases is a hotly debated topic and in order to investigate lipid bilayer membranes, in particular those that contain coexisting lipid domains, probes whose partitioning behaviour is well distinguished is needed. Lipid-rafts' were originally identified as regions of cell membranes that were resistant to detergent. Also called liquid-ordered domains, these regions contain a high concentration of cholesterol and sphingolipids.[9] This physical state is said to be the liquid-ordered phase and tends to be more compact and rigid. Although experimentation seems to suggest evidence of the existence of nanodomain 'lipid-rafts', the ability to visually detect them in living cells still causes controversy.

Within cells, it is believed that 'lipid-rafts' are nanometer scale in length, therefore resulting in difficult characterisation. Modern day imaging techniques capable reaching such low resolutions are mainly non-fluorescent such as atomic force microscopy. De Wit *et al* developed interferometric scattering microscopy (iSCAT) which saw them image a single protein molecule label free.[112] Work carried out by Moss and Boxer also used a non-fluorescent technique, nano-secondary ion mass spectrometry nano(SIMS) to probe the distance in lipid assemblies achieving a <50 nm imaging length.[113]

Despite the greater success of non-fluorescent techniques to achieve sub-diffraction limit imaging, there is still great interest in developing dyes that can successfully visualise phase partitioning, with many researchers in the field using artificial lipid models which can be used to create domains on micron scale. GUVs can be created in sizes of (<20 μm) resulting in liquid-ordered regions that are microns in length and therefore easily visualised by fluorescence spectroscopy. It is therefore desirable to develop fluorescent probes to be used for lipid membrane labelling, with emphasis on probes that can selectively differentiate between the liquid-ordered (Lo) and the liquid-disordered (Ld) phases.

In recent times research into the use of BODIPY probes for lipid membrane labelling has gathered much interest due to the photophysical properties previously mentioned and the

overall lipophilic nature of the BODIPY core. To date there has been two approaches to labelling domains; labelling domain components such as cholesterol, sphingolipids, ceramides and gangliosides with fluorescent molecules or by creating molecules that can mimic domain components, therefore partitioning into liquid-disordered or liquid-ordered domains.[35,36,111,114]

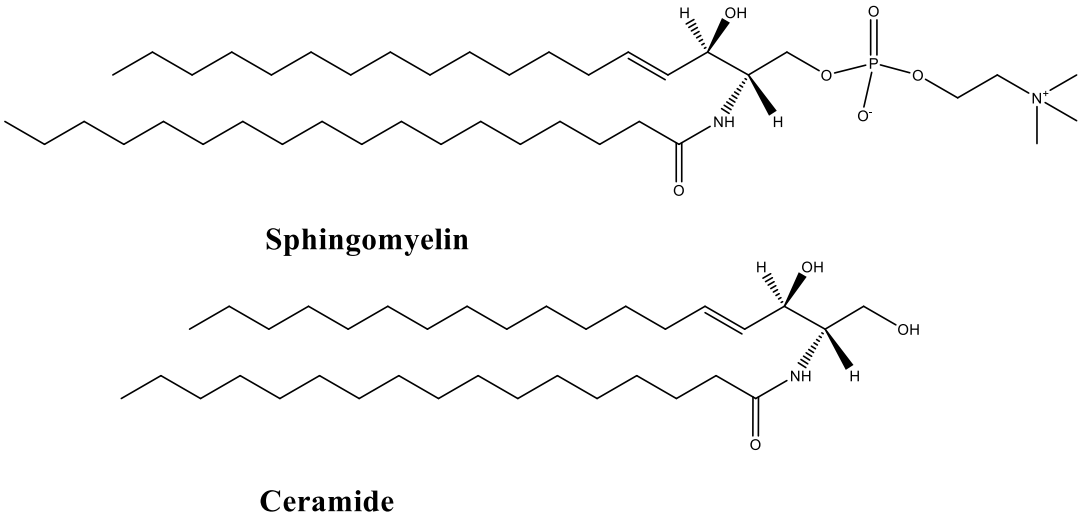

Figure 1.18 Chemical structure of sphingomyelin and ceramide.

A number of BODIPY lipid probes have been developed which have been applied to lipid domain labelling and some are commercially available. They differ depending on whether the BODIPY moiety is linked to the alkyl chains or closer to the head group of common membrane components. Thermo Fisher Scientific provides a range of BODIPY dye-labelled sphingolipid derivatives that include fatty acids, glycerophosphocholines and cholesteryl linked probes. BODIPY-PC and BODIPY-Cer are commonly used BODIPY probes for lipid membrane imaging, with BODIPY-PC being widely applied for general membranes as well as a liquid-disordered marker.[115–117] Within the literature many research groups have published BODIPY-lipid conjugates and investigated their preference for both liquid-disordered and liquid-ordered phases. Three acyl chain modified lipid-BODIPY derivatives of phosphatidylcholine (PC) and sphingomyelin (SM) have been reported. 5-BODIPY-PC, 5-BODIPY-SM and 12-BODIPY-SM.[34,118] They all contain the BODIPY core attached to

one of the fatty acid tails of PC and SM with varying chain length, and all three probes were shown to be excluded from the liquid-ordered region of GUVs and strongly partition into the liquid-disordered region.[119] The idea that PC labelled probe would show preference for the liquid-disordered region is no surprise, since the liquid-disordered region has a high content of PC lipids such as DOPC, however the results of the SM labelled BODIPY derivatives is surprising.

Liquid-ordered domains tend to be rich in sphingomyelins, and Marks *et al* presented data that showed 5-BODIPY-SM labels sphingomyelin rich domains in cell membranes.[111] Sezgin *et al* also reported the fluorescently labelled ganglioside GM1 derivative (5-BODIPY-GM1) that showed preference for the liquid-disordered phase, despite evidence of GM1 being present in liquid-ordered regions.[118] Samsonov *et al*, however, showed that BODIPY-GM1 selectively partitioned to the liquid-ordered region of phase separated GUVs.[120] The structural difference resulting in different partitioning behaviours is that 5-BODIPY-GM1 has the BODIPY core attached to one of the ceramide tails of GM1, whereas the BODIPY fluorophore is attached to one of the sugar groups in BODIPY-GM1. This suggests that having unhindered long chain fatty acid tails are important for partitioning into the liquid-ordered phase. BODIPY-Cholesterol (TF-Chol) synthesised by Li *et al* is a BODIPY-sterol conjugate that was shown to partition into the liquid-ordered phase of GUVs.[121] The BODIPY core is attached directly to the acyl chain of the cholesterol, leaving the hydroxyl tail free as seen in Figure 1.19. It is expected that within liquid-ordered domains TF-Chol orientates in the bilayer with the BODIPY core incorporated adjacent to the fatty acid tails of neighbouring phospholipids, while the lone hydroxyl group is exposed at the bilayer interface. Interestingly, within chapter 3 of this thesis, a BODIPY-cholesterol conjugate was synthesised exploiting the free hydroxyl group to form an ester bond between a carboxylic acid BODIPY derivative and a cholesterol moiety. Similar to TF-Chol, BODIPY-Ahx-Chol also showed preference for liquid-ordered domains. This suggests that cholesterol will still orientate into liquid-ordered domains despite the physiochemical changes to the cholesterol by esterification of the hydroxyl group.

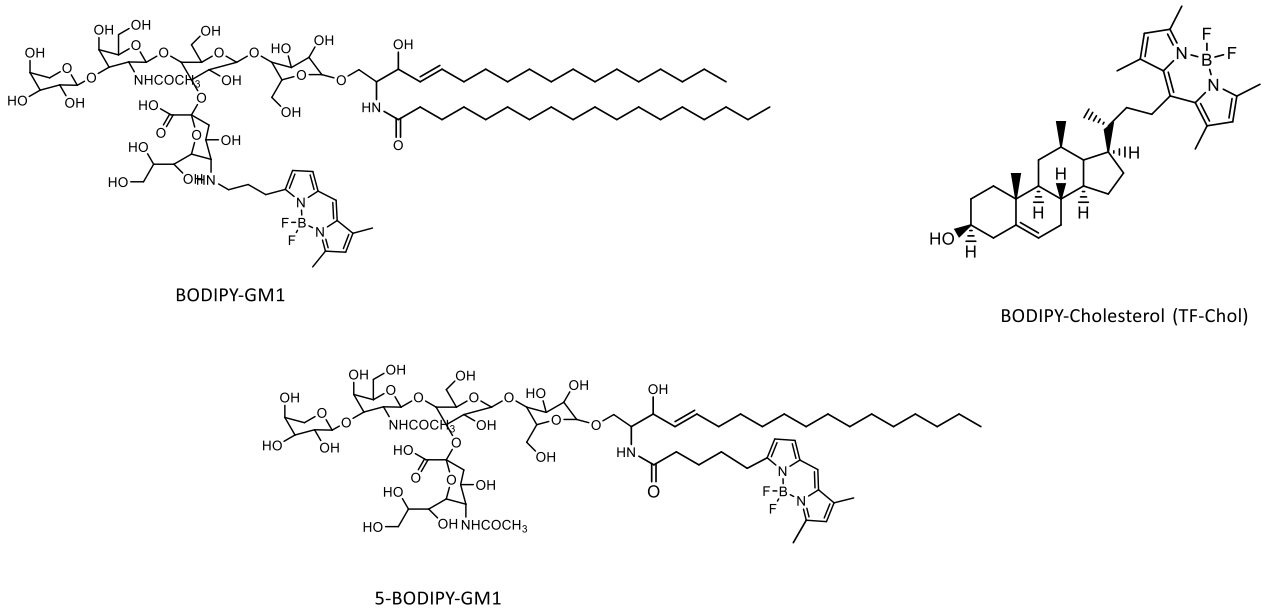

Figure 1.19 Chemical structures of BODIPY-lipid conjugates, BODIPY-GM1, BODIPY-Cholesterol (TF-Chol) and 5-BODIPY-GM1.

In summary, the literature suggests that BODIPY-lipid conjugates, show great promise for use as lipid membrane labels. The site at which the BODIPY is conjugated to the lipid seems to be very important in driving partitioning into either the liquid-disordered or liquid-ordered phase. To target the liquid-ordered phase, which is the goal for many researchers in this area, it seems necessary to conjugate the fluorescent label to lipids or molecules that are present in lipid rafts within the cell membrane, such as cholesterol, sphingomyelin, ceramides or ganglioside GM1. For the lipids that contain long chained fatty acid tails, partitioning studies seem to suggest it is important to leave these tails unblocked. To create a probe that partitions into the liquid-ordered phase without conjugation to one of the mentioned molecules, structures that mimic either cholesterol (cyclic and planar) or have a synthetic long chained aliphatic region appear necessary, however tuning their optical properties to suit modern microscopy techniques without hindering their partitioning abilities remains challenging.

1.7 Pyrene Based Fluorescent Probes

1.7.1 Structure and Spectroscopic Properties

Pyrene is a polycyclic aromatic hydrocarbon (PAH) consisting of four fused benzene rings resulting in a conjugated aromatic system. Since its discovery in 1837 it has become one of

the most widely studied PAHs due to its interesting photophysical and electronic properties including long lived singlet excited states[122,123], high quantum yields and its ability to form excimers via π-π interactions in both the solid state and in solution[122]. Due to possessing these qualities, pyrene has been used in many applications such as organic light emitting diodes (OLEDS) [122,124], DNA[125] and nucleic acid[126] binding, detection of lipid domain and membrane formation[127–129] as well as sensing solvent polarity[130] and pH[131–133].

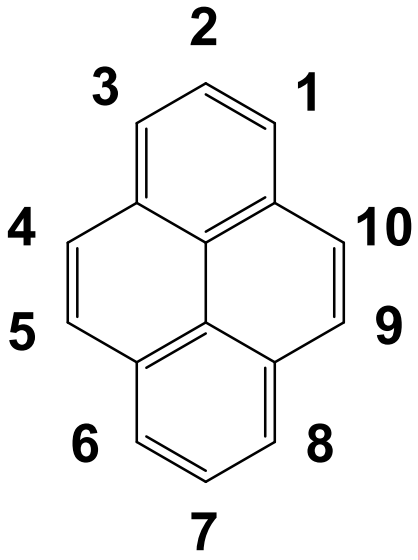

Figure 1.20 Chemical structure of the pyrene core with positions labelled.

The photophysical properties of pyrene have been well characterised.[122,134,135] It has unusually long lifetimes[136,137], moderate to high extinction coefficients and high quantum yields. A typical pyrene absorption spectrum shows two intense shoulders at approximately 320 nm and 335 nm with a weaker shoulder at 306 nm as show in Figure 1.21. Pyrene monomer emission can exhibit five vibronic bands designated I-V. These five emission peaks can occur between ~375-420 nm and are attributed to π-π* transitions. Like many organic fluorophores, pyrene emission can become quenched with an increase in molar concentrations. At higher concentrations, the likelihood of a ground state pyrene and excited state pyrene coming into close proximity with one another is increased, resulting in the formation of a dimer or 'excimer'. The formation of excimers that can lead to a bathochromic shift in the emission profile with a decrease in luminescent intensity.[122,138,139] The excimer emission appears as a broad structureless band between 420-550 nm, typically centred ~ 450

nm.[140] Although undesirable for the applications outlined within this body of work, pyrene excimer fluorescence has been widely used to investigate inter- and intra-molecular interactions in both photophysical and biological studies.[141–143]

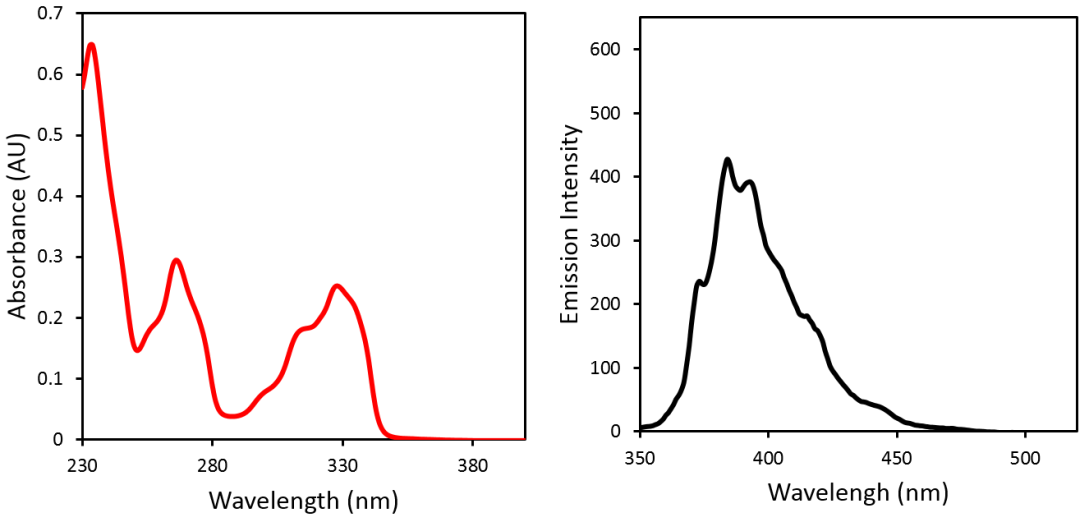

Figure 1.21 Absorbance spectrum of pyrene (10 μM) in hexane (left) and subsequent monomer-emission spectrum (right).

1.7.2 Synthesis of Pyrene Charge-Transfer Derivatives

Many groups have focused on carrying out synthetic modifications to optimise the electronic and photophysical properties of the core, to avoid aggregation and quenching due to π-π interactions. The main strategy employed to achieve this has been to create conjugated π-systems substituting the pyrene core with donors (D) and/or acceptors (A) that can provide energetically high lying occupied orbitals (HOMO) and low-lying unoccupied orbitals (LUMO), respectively. Some of the substituents used to extend π-conjugation include thiophene, piperdine, pyridine and ethynyl-bridged phenyl groups.

Several pyrene-based charge-transfer fluorophores have been found to have different distinctive emission profiles, due to functionalisation and substitution of the pyrene core.[144,145] With respect to this thesis, the core itself was not thought useful for spectroscopic techniques such as fluorescent confocal microscopy, FCS or STED due to its blue region absorption and emission. For these reasons the pyrene core alone has not commonly been reported in literature as a cell imaging dye. The synthesis of highly emissive pyrene

fluorophores has focused on adding substituents at the 1, 3 ,6 and 8-positions[122] as these positions are more active than the remaining positions (4, 5, 9, 10 and the 2 and 7-positions), which are more difficult to directly substitute. The 1, 3, 6, and 8-positions of pyrene are preferentially suitable for electrophilic aromatic substitution (S_EAr) reactions. The relative ease of brominating both K-region (4, 5, 9 and 10-positions) and non-K-region (1, 2, 3, 6, 7 and 8-positions) sites on the pyrene core has led to many donor-acceptor pyrene derivatives being synthesised by utilising palladium-catalysed coupling reactions including Suzuki-Miyaura[145,146] and Sonogashira[147] coupling. By brominating the pyrene core via electrophilic aromatic substitution (SEAr) reactions, 1, 3, 6, 8-tetrabromopyrene can be obtained in high yield (90 %). It is a common precursor widely used for designing star-shaped pyrene-based OLEDs/OFETs material by Suzuki/Sonogashira cross-coupling.

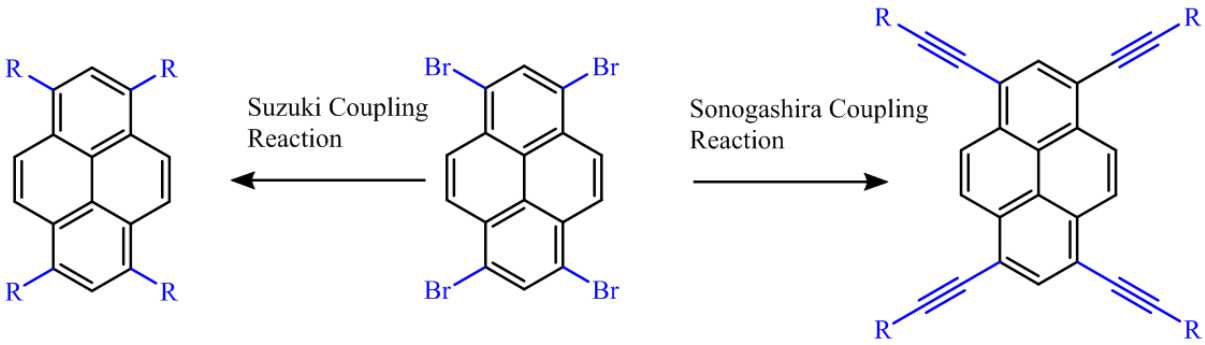

Scheme 1.4 Synthetic route to tetra-substituted pyrenes using Suzuki-Miyuara and Sonogashira coupling reactions.

Within this body of work, the highly tuneable 1,3,6 and 8-positions were exploited using palladium catalysed coupling chemistry.[147,148] The synthesis of highly emissive, longer wavelength pyrene fluorophores was achieved by adding electron donating groups to non-K-region sites, thus creating an electron charge transfer from these substituents to the pyrene core. These derivatives have shown to possess high quantum yields, moderate to high extinction coefficients, good photostability and display large Stokes shifts.[148–150]

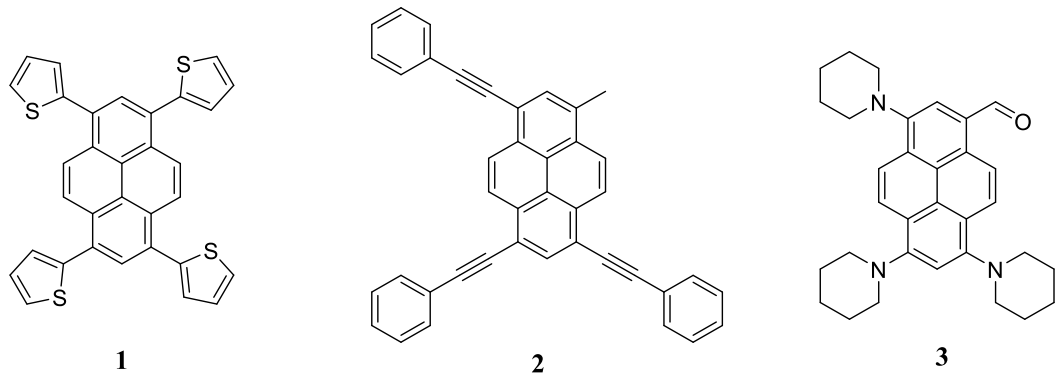

1 **2** **3**

Figure 1.22 Chemical structures of pyrene derivatives **1**[151], **2**[147], and **3**[149] which were synthesised using palladium catalysed coupling strategies at the 1, 3, 6 and 8-positions.

1.7.3 Use of Pyrene for Lipid Labelling

Nearly two decades ago, Tanhuanpää *et al* used pyrene-phospholipid conjugates to obtain fluorescent images of the plasma membrane in BHK (baby hamster kidney) cells.[152] However, to obtain good quality images, quenching strategies and background subtraction techniques needed to be employed. The pyrene-phospholipid was excited at 345 nm and emission collected at 395 nm which is not compatible with modern imaging techniques (e.g. super resolution) and is also undesirable for biological studies due to potential damage caused by UV excitation. Since then there has been very few reported pyrene derivatives used for cell-imaging. Jana *et al* synthesised pyrene-carbamate derivative to be used as phototriggers for realising alcohols, phenols and adenosines into live cells.[153] These derivatives stained the cell with no apparent selectivity and required blue-region excitation. Another study carried out by Zhang *et al* reported a pyrene derivative containing an formaldehyde reactive moiety in order to sense formaldehyde in living cells.[154] Similarly this work focused more on the sensing capabilities rather than the cell-imaging application and once again, the pyrene derivative showed no selectivity for any specific cellular regions and required 390 nm excitation

In recent times synthetic strategies have been employed not only to tune the optical properties of the pyrene core but also to add groups to aid specific targeting. Only recently has a 'push-pull' pyrene derivative been reported as an effective lipid probe for labelling lipid domains in phase separated GUVs.[127] This derivative called PA localised in both Ld and Lo domains

in GUVs, exhibiting photophysical changes in the emission profile based on phase difference. The dye exhibited a mega-Stokes shift in a range of different solvents and lipid compositions and excellent quantum yields were reported, 0.96 and 0.93 in toluene and hexane respectively. Photostability testing showed that PA outperformed the commercially available 'push-pull' probe Laurdan, as the fluorescence intensity retention was ~70 % higher after 1 h photoexcitation.

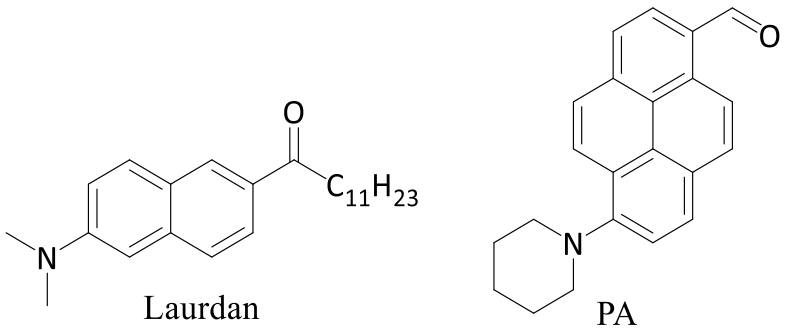

Figure 1.23 Chemical structures of the solvatochromatic fluorescent probes Laurdan and PA.

The synthetic tunability of the 1,3,6 and 8-positions of the pyrene core along with the ability of the fluorophore PA to distinguish lipid phase led to the design of PyLa in chapter 4. PyLa exploits the readiness for the 3,6 and 8-positions to undergo Suzuki-Miyaura coupling as well as the 1-position being easily functionalised to allow future conjugations. By incorporating red-shifting substituents, mainly 4-dimethylaminophenyl groups to pyrene-1-carboxylic acid, the resultant fluorophore PyLa obtained a mega-Stokes shifted emission, high quantum yields and excellent photostability.

1.8 Conclusions

Over the past number of years, research into cell membrane composition and cellular lipid content has grown considerably across a range of areas from biophysics to health and disease. Due to the size of lipid domains (nm), lipid droplets (<1 μm) and membrane proteins (nm) within cells, the need for fluorescent dyes capable of illuminating these regions of interest that are compatible with techniques which can provide structural information and biophysical information on membrane interactions (e.g. lipid, protein or toxin) such as super resolution

microscopy and FCS, are of vital importance for the progression of this scientific field. It is therefore necessary to design dyes that have the desired biological properties (cell permeability, low cytotoxicity and high selectivity for lipid regions in particular liquid-ordered domains) as well as the photophysical properties (mega-Stokes shift, high quantum yield and molecular brightness in the nanomolar range and high photostability) required to be compatible with super-resolution microscopy, FLIM, FCS and more recently multi-modal techniques such as STED-FCS.

This thesis focuses on two fluorophores, BODIPY and pyrene for use in bio-imaging applications due to their desirable photophysical properties including intense fluorescence, high extinction coefficients and high quantum yields at low nanomolar to micromolar concentrations, as well as good photostability and relatively low cytotoxicity. As a result, there are now many commercially available BODIPY dyes and BODIPY-lipid conjugates targeted specifically for imaging. Pyrene and its derivatives have also found widespread use in many applications including nucleic acid binding, as organic light emitting diodes (OLEDS) and supramolecular photosensors, however is far less common in bio-imaging due to many derivatives exhibiting UV-region excitation, which incompatible for many modern imaging techniques. This thesis explores the design, synthesis and bio-imaging applications of novel BODIPY and pyrene-based dyes and their respective sterol/lipid conjugates to provide information and images of lipid environments in both model lipid membranes and live cells, with particular focus on lipid membranes, lipid droplets and phase separation of lipid domains. Across this body of work the approach of extending π-conjugation and conjugating sterols/lipids to the respective dyes was used in order to create lipid imaging probes that were highly selective to lipid regions and possessed desirable photophysical properties compatible with the techniques outlined above, resulting in high quality, low background images. This thesis provides an insight into lipid membranes, the artificial models that mimic them and the structural and photophysical requirements of successful lipid membrane probes.

1.9 References

(1) Eeman, M.; Deleu, M. From biological membranes to biomimetic model membranes. *BASE* **2010**, *4*, (14), 719-736.

(2) Singer, S. J.; Nicolson, G. L. The Fluid Mosaic Model of the Structure of Cell Membranes. *Science* **1972**, *175* (4023), 720–731.

(3) Binder, W. H.; Barragan, V.; Menger, F. M. Domains and Rafts in Lipid Membranes. *Angew. Chem. Int. Ed Engl.* **2003**, *42* (47), 5802–5827.

(4) Simons, K.; Ikonen, E. Functional Rafts in Cell Membranes. *Nature* **1997**, *387* (6633), 569–572.

(5) Edidin, M. The State of Lipid Rafts: From Model Membranes to Cells. *Annu. Rev. Biophys. Biomol. Struct.* **2003**, *32*, 257–283.

(6) Pike, L. J. The Challenge of Lipid Rafts. *J. Lipid Res.* **2009**, *50 Suppl*, S323–S328.

(7) Alberts, B.; Johnson, A.; Lewis, J.; Raff, M.; Roberts, K.; Walter, P. *Molecular Biology of the Cell*, 4th ed.; Garland Science, 2002.

(8) Ding, W.; Palaiokostas, M.; Wang, W.; Orsi, M. Effects of Lipid Composition on Bilayer Membranes Quantified by All-Atom Molecular Dynamics. *J. Phys. Chem. B* **2015**, *119* (49), 15263–15274.

(9) Pike, L. J. Lipid Rafts Bringing Order to Chaos. *J. Lipid Res.* **2003**, *44* (4), 655–667.

(10) Walther, T. C.; Farese, R. V. Lipid Droplets and Cellular Lipid Metabolism. *Annu. Rev. Biochem.* **2012**, *81* (1), 687–714.

(11) Brasaemle, D. L. Thematic Review Series: Adipocyte Biology. The Perilipin Family of Structural Lipid Droplet Proteins: Stabilization of Lipid Droplets and Control of Lipolysis. *J. Lipid Res.* **2007**, *48* (12), 2547–2559.

(12) Bickel, P. E.; Tansey, J. T.; Welte, M. A. PAT Proteins, an Ancient Family of Lipid Droplet Proteins That Regulate Cellular Lipid Stores. *Biochim. Biophys. Acta* **2009**, *1791* (6), 419–440.

(13) DeVries-Seimon, T.; Li, Y.; Yao, P. M.; Stone, E.; Wang, Y.; Davis, R. J.; Flavell, R.; Tabas, I. Cholesterol-Induced Macrophage Apoptosis Requires ER Stress Pathways and Engagement of the Type A Scavenger Receptor. *J. Cell Biol.* **2005**, *171* (1), 61–73.

(14) Koliwad, S. K.; Streeper, R. S.; Monetti, M.; Cornelissen, I.; Chan, L.; Terayama, K.; Naylor, S.; Rao, M.; Hubbard, B.; Farese, R. V. DGAT1-Dependent Triacylglycerol Storage by Macrophages Protects Mice from Diet-Induced Insulin Resistance and Inflammation. *J. Clin. Invest.* **2010**, *120* (3), 756–767.

(15) Listenberger, L. L.; Han, X.; Lewis, S. E.; Cases, S.; Farese, R. V.; Ory, D. S.; Schaffer, J. E. Triglyceride Accumulation Protects against Fatty Acid-Induced Lipotoxicity. *Proc. Natl. Acad. Sci. U. S. A.* **2003**, *100* (6), 3077–3082.

(16) Choudhary, V.; Ojha, N.; Golden, A.; Prinz, W. A. A Conserved Family of Proteins Facilitates Nascent Lipid Droplet Budding from the ER. *J. Cell Biol.* **2015**, *211* (2), 261–271.

(17) Jacquier, N.; Choudhary, V.; Mari, M.; Toulmay, A.; Reggiori, F.; Schneiter, R. Lipid Droplets Are Functionally Connected to the Endoplasmic Reticulum in Saccharomyces Cerevisiae. *J. Cell Sci.* **2011**, *124* (Pt 14), 2424–2437.

(18) Kassan, A.; Herms, A.; Fernández-Vidal, A.; Bosch, M.; Schieber, N. L.; Reddy, B. J. N.; Fajardo, A.; Gelabert-Baldrich, M.; Tebar, F.; Enrich, C.; et al. Acyl-CoA Synthetase 3 Promotes Lipid Droplet Biogenesis in ER Microdomains. *J. Cell Biol.* **2013**, *203* (6), 985–1001.

(19) Buhman, K. K.; Chen, H. C.; Farese, R. V. The Enzymes of Neutral Lipid Synthesis. *J. Biol. Chem.* **2001**, *276* (44), 40369–40372.

(20) Walther, T. C.; Farese, R. V. The Life of Lipid Droplets. *Biochim. Biophys. Acta* **2009**, *1791* (6), 459–466.

(21) Bartz, R.; Zehmer, J. K.; Zhu, M.; Chen, Y.; Serrero, G.; Zhao, Y.; Liu, P. Dynamic Activity of Lipid Droplets: Protein Phosphorylation and GTP-Mediated Protein Translocation. *J. Proteome Res.* **2007**, *6* (8), 3256–3265.

(22) Liu, P.; Ying, Y.; Zhao, Y.; Mundy, D. I.; Zhu, M.; Anderson, R. G. W. Chinese Hamster Ovary K2 Cell Lipid Droplets Appear to Be Metabolic Organelles Involved in Membrane Traffic. *J. Biol. Chem.* **2004**, *279* (5), 3787–3792.

(23) Wang, W.; Wei, S.; Li, L.; Su, X.; Du, C.; Li, F.; Geng, B.; Liu, P.; Xu, G. Proteomic Analysis of Murine Testes Lipid Droplets. *Sci. Rep.* **2015**, *5*.

(24) Zehmer, J. K.; Huang, Y.; Peng, G.; Pu, J.; Anderson, R. G. W.; Liu, P. A Role for Lipid Droplets in Inter-Membrane Lipid Traffic. *Proteomics* **2009**, *9* (4), 914–921.

(25) Bozza, P. T.; Viola, J. P. B. Lipid Droplets in Inflammation and Cancer. *Prostaglandins Leukot. Essent. Fat. Acids PLEFA* **2010**, *82* (4–6), 243–250.

(26) Krahmer, N.; Farese, R. V.; Walther, T. C. Balancing the Fat: Lipid Droplets and Human Disease. *EMBO Mol. Med.* **2013**, *5* (7), 905–915.

(27) Herker, E.; Harris, C.; Hernandez, C.; Carpentier, A.; Kaehlcke, K.; Rosenberg, A. R.; Farese, R. V.; Ott, M. Efficient Hepatitis C Virus Particle Formation Requires Diacylglycerol Acyltransferase-1. *Nat. Med.* **2010**, *16* (11), 1295–1298.

(28) Tirinato, L.; Pagliari, F.; Limongi, T.; Marini, M.; Falqui, A.; Seco, J.; Candeloro, P.; Liberale, C.; Di Fabrizio, E. An Overview of Lipid Droplets in Cancer and Cancer Stem Cells. *Stem Cells Int.* **2017**, *2017*, 1656053.

(29) Abramczyk, H.; Surmacki, J.; Kopeć, M.; Olejnik, A. K.; Lubecka-Pietruszewska, K.; Fabianowska-Majewska, K. The Role of Lipid Droplets and Adipocytes in Cancer. Raman Imaging of Cell Cultures: MCF10A, MCF7, and MDA-MB-231 Compared to Adipocytes in Cancerous Human Breast Tissue. *The Analyst* **2015**, *140* (7), 2224–2235.

(30) Moscho, A.; Orwar, O.; Chiu, D. T.; Modi, B. P.; Zare, R. N. Rapid Preparation of Giant Unilamellar Vesicles. *Proc. Natl. Acad. Sci. U. S. A.* **1996**, *93* (21), 11443–11447.

(31) Reeves, J. P.; Dowben, R. M. Formation and Properties of Thin-Walled Phospholipid Vesicles. *J. Cell. Physiol.* **1969**, *73* (1), 49–60.

(32) Angelova, M. I.; Dimitrov, D. S. Liposome Electroformation. *Faraday Discuss. Chem. Soc.* **1986**, *81* (0), 303–311.

(33) Angelova, M. I.; Soléau, S.; Méléard, P.; Faucon, F.; Bothorel, P. Preparation of Giant Vesicles by External AC Electric Fields. Kinetics and Applications. In *Trends in Colloid and Interface Science VI*; Progress in Colloid & Polymer Science; Steinkopff, **1992**; pp 127–131.

(34) Baumgart, T.; Hunt, G.; Farkas, E. R.; Webb, W. W.; Feigenson, G. W. Fluorescence Probe Partitioning between Lo/Ld Phases in Lipid Membranes. *Biochim. Biophys. Acta BBA - Biomembr.* **2007**, *1768* (9), 2182–2194.

(35) Boldyrev, I. A.; Zhai, X.; Momsen, M. M.; Brockman, H. L.; Brown, R. E.; Molotkovsky, J. G. New BODIPY Lipid Probes for Fluorescence Studies of Membranes. *J. Lipid Res.* **2007**, *48* (7), 1518–1532.

(36) Mikhalyov, I.; Gretskaya, N.; Johansson, L. B.-Å. Fluorescent BODIPY-Labelled GM1 Gangliosides Designed for Exploring Lipid Membrane Properties and Specific Membrane-Target Interactions. *Chem. Phys. Lipids* **2009**, *159* (1), 38–44.

(37) Gaul, V.; Lopez, S. G.; Lentz, B. R.; Moran, N.; Forster, R. J.; Keyes, T. E. The Lateral Diffusion and Fibrinogen Induced Clustering of Platelet Integrin αIIbβ3 Reconstituted into Physiologically Mimetic GUVs. *Integr. Biol. Quant. Biosci. Nano Macro* **2015**, *7* (4), 402–411.

(38) Bagatolli, L. A. To See or Not to See: Lateral Organization of Biological Membranes and Fluorescence Microscopy. *Biochim. Biophys. Acta* **2006**, *1758* (10), 1541–1556.

(39) Rascol, E.; Devoisselle, J.-M.; Chopineau, J. The Relevance of Membrane Models to Understand Nanoparticles-Cell Membrane Interactions. *Nanoscale* **2016**, *8* (9), 4780–4798.

(40) Basit, H.; Gaul, V.; Maher, S.; Forster, R. J.; Keyes, T. E. Aqueous-Filled Polymer Microcavity Arrays: Versatile & Stable Lipid Bilayer Platforms Offering High Lateral Mobility to Incorporated Membrane Proteins. *The Analyst* **2015**, *140* (9), 3012–3018.

(41) Marquardt, D.; Geier, B.; Pabst, G. Asymmetric Lipid Membranes: Towards More Realistic Model Systems. *Membranes* **2015**, *5* (2), 180–196.

(42) Zimmerman, R.; Basabe-Desmonts, L.; Baan, F. van der; Reinhoudt, D. N.; Crego-Calama, M. A Combinatorial Approach to Surface-Confined Cation Sensors in Water. *J. Mater. Chem.* **2005**, *15* (27-28), 2772–2777.

(43) Kim, D. W.; Kim, K. K.; Lee, E. B.; Kim, J. S. Film Sensor for Zn2+ Ion via Self-Assembled Monolayer of Receptor on Quartz Plate Surfaces. *J. Photochem. Photobiol. Chem.* **2012**, *250*, 33–39.

(44) Séro, L.; Sanguinet, L.; Derbré, S.; Boury, F.; Brotons, G.; Dabos-Seignon, S.; Richomme, P.; Séraphin, D. Fluorescent Self-Assembled Monolayers of Umbelliferone: A Relationship between Contact Angle and Fluorescence. *Langmuir* **2013**, *29* (33), 10423–10431.

(45) Jadhav, S. A. Self-Assembled Monolayers (SAMs) of Carboxylic Acids: An Overview. *Cent. Eur. J. Chem.* **2011**, *9* (3), 369–378.

(46) Xu, Q.; Ma, H.; Yip, H.; Jen, A. K.-Y. Controlled Assembly of Large π-Conjugated Aromatic Thiols on Au(111). *Nanotechnology* **2008**, *19* (13), 135605.

(47) Vericat, C.; Vela, M. E.; Benitez, G.; Carro, P.; Salvarezza, R. C. Self-Assembled Monolayers of Thiols and Dithiols on Gold: New Challenges for a Well-Known System. *Chem. Soc. Rev.* **2010**, *39* (5), 1805–1834.

(48) Broekaert, J. A. C. *Analytical Atomic Spectrometry with Flames and Plasmas*; Wiley-VCH: Weinheim, 2002.

(49) Principles of Fluorescence Spectroscopy | Joseph R. Lakowicz | Springer http://www.springer.com/gp/book/9780387312781 (accessed Jul 27, 2017).

(50) Yogo, T.; Urano, Y.; Ishitsuka, Y.; Maniwa, F.; Nagano, T. Highly Efficient and Photostable Photosensitizer Based on BODIPY Chromophore. *J. Am. Chem. Soc.* **2005**, *127* (35), 12162–12163.

(51) Levi, V.; González Flecha, F. L. Labeling of Proteins with Fluorescent Probes: Photophysical Characterization of Dansylated Bovine Serum Albumin. *Biochem. Mol. Biol. Educ.* **2003**, *31* (5), 333–336.

(52) Crosby, G. A.; Demas, J. N. Measurement of Photoluminescence Quantum Yields. Review. *J. Phys. Chem.* **1971**, *75* (8), 991–1024.

(53) Würth, C.; Grabolle, M.; Pauli, J.; Spieles, M.; Resch-Genger, U. Relative and Absolute Determination of Fluorescence Quantum Yields of Transparent Samples. *Nat. Protoc.* **2013**, *8* (8), 1535–1550.

(54) Cooper, G. M. Structure of the Plasma Membrane. **2000**.

(55) Hilderbrand, S. A.; Weissleder, R. Near-Infrared Fluorescence: Application to in Vivo Molecular Imaging. *Curr. Opin. Chem. Biol.* **2010**, *14* (1), 71–79.

(56) Gao, X.; Cui, Y.; Levenson, R. M.; Chung, L. W. K.; Nie, S. In Vivo Cancer Targeting and Imaging with Semiconductor Quantum Dots. *Nat. Biotechnol.* **2004**, *22* (8), 969–976.

(57) Webb, R. Confocal Optical Microscopy. Reports Prog. Phys. 59, 427–471 (**1999**).

(58) O'Neil, M. P. Synchronously Pumped Visible Laser Dye with Twice the Efficiency of Rhodamine 6G. *Opt. Lett.* **1993**, *18* (1), 37–38.

(59) *Advanced Time-Correlated Single Photon Counting Techniques | Wolfgang Becker Springer*, ch. 9, 61-212.

(60) Ballew, R. M.; Demas, J. N. An Error Analysis of the Rapid Lifetime Determination Method for the Evaluation of Single Exponential Decays. *Anal. Chem.* **1989**, *61* (1), 30–33.

(61) Festy F, Ameer-Beg SM, Ngab T, Suhling K. Imaging Proteins in Vivo Using Fluorescence Lifetime Microscopy. Mol BioSyst. **2007**, *3*, 381-391.

(62) Martin, A.; Byrne, A.; Dolan, C.; J. Forster, R.; E. Keyes, T. Solvent Switchable Dual Emission from a Bichromophoric ruthenium–BODIPY Complex. *Chem. Commun.* **2015**, *51* (87), 15839–15841.

(63) Hell, S. W.; Wichmann, J. Breaking the Diffraction Resolution Limit by Stimulated Emission: Stimulated-Emission-Depletion Fluorescence Microscopy. *Opt. Lett.* **1994**, *19* (11), 780–782.

(64) Kasper, R.; Harke, B.; Forthmann, C.; Tinnefeld, P.; Hell, S. W.; Sauer, M. Single-Molecule STED Microscopy with Photostable Organic Fluorophores. *Small Weinh. Bergstr. Ger.* **2010**, *6* (13), 1379–1384.

(65) Wildanger, D.; Medda, R.; Kastrup, L.; Hell, S. W. A Compact STED Microscope Providing 3D Nanoscale Resolution. *J. Microsc.* **2009**, *236* (1), 35–43.

(66) Meyer, L.; Wildanger, D.; Medda, R.; Punge, A.; Rizzoli, S. O.; Donnert, G.; Hell, S. W. Dual-Color STED Microscopy at 30-Nm Focal-Plane Resolution. *Small Weinh. Bergstr. Ger.* **2008**, *4* (8), 1095–1100.

(67) Kolmakov, K.; Wurm, C. A.; Meineke, D. N. H.; Göttfert, F.; Boyarskiy, V. P.; Belov, V. N.; Hell, S. W. Polar Red-Emitting Rhodamine Dyes with Reactive Groups: Synthesis, Photophysical Properties, and Two-Color STED Nanoscopy Applications. *Chem. Weinh. Bergstr. Ger.* **2014**, *20* (1), 146–157.

(68) Klar, T. A.; Jakobs, S.; Dyba, M.; Egner, A.; Hell, S. W. Fluorescence Microscopy with Diffraction Resolution Barrier Broken by Stimulated Emission. *Proc. Natl. Acad. Sci. U. S. A.* **2000**, *97* (15), 8206–8210.

(69) Ulrich, G.; Ziessel, R.; Harriman, A. The Chemistry of Fluorescent Bodipy Dyes: Versatility Unsurpassed. *Angew. Chem. Int. Ed.* **2008**, *47* (7), 1184–1201.

(70) Karolin, J.; Johansson, L. B.-A.; Strandberg, L.; Ny, T. Fluorescence and Absorption Spectroscopic Properties of Dipyrrometheneboron Difluoride (BODIPY) Derivatives in Liquids, Lipid Membranes, and Proteins. *J. Am. Chem. Soc.* **1994**, *116* (17), 7801–7806.

(71) Kesavan, P. E.; Das, S.; Lone, M. Y.; Jha, P. C.; Mori, S.; Gupta, I. Bridged Bis-BODIPYs: Their Synthesis, Structures and Properties. *Dalton Trans.* **2015**, *44* (39), 17209–17221.

(72) Nepomnyashchii, A. B.; Cho, S.; Rossky, P. J.; Bard, A. J. Dependence of Electrochemical and Electrogenerated Chemiluminescence Properties on the Structure of BODIPY Dyes. Unusually Large Separation between Sequential Electron Transfers. *J. Am. Chem. Soc.* **2010**, *132* (49), 17550–17559.

(73) Loudet, A.; Burgess, K. BODIPY Dyes and Their Derivatives: Syntheses and Spectroscopic Properties. *Chem. Rev.* **2007**, *107* (11), 4891–4932.

(74) Bandichhor, R.; Thivierge, C.; Bhuvanesh, N. S. P.; Burgess, K. 4,4-Difluoro-1,3,5,7-Tetra-methyl-4-Bora-3a,4a-Diaza-S-Indacene. *Acta Crystallogr. Sect. E Struct. Rep. Online* **2006**, *62* (10), o4310–o4311. h

(75) Daly, H. C.; Sampedro, G.; Bon, C.; Wu, D.; Ismail, G.; Cahill, R. A.; O'Shea, D. F. BF2-Azadipyrromethene NIR-Emissive Fluorophores with Research and Clinical Potential. *Eur. J. Med. Chem.* **2017**, *135*, 392–400.

(76) Martin, A.; Long, C.; Forster, R. J.; Keyes, T. E. Near IR Emitting BODIPY Fluorophores with Mega-Stokes Shifts. *Chem. Commun.* **2012**, *48* (45), 5617.

(77) Wu, D.; O'Shea, D. F. Fluorogenic NIR-Probes Based on 1,2,4,5-Tetrazine Substituted BF2-Azadipyrromethenes. *Chem. Commun.* **2017**, *53* (78), 10804–10807.

(78) Jiao, L.; Yu, C.; Uppal, T.; Liu, M.; Li, Y.; Zhou, Y.; Hao, E.; Hu, X.; Vicente, M. G. H. Long Wavelength Red Fluorescent Dyes from 3,5-Diiodo-BODIPYs. *Org. Biomol. Chem.* **2010**, *8* (11), 2517.

(79) Kamkaew, A.; Burgess, K. Aza-BODIPY Dyes with Enhanced Hydrophilicity. *Chem. Commun.* **2015**, *51* (53), 10664–10667.

(80) Li, T.; Meyer, T.; Meerheim, R.; Höppner, M.; Körner, C.; Vandewal, K.; Zeika, O.; Leo, K. Aza-BODIPY Dyes with Heterocyclic Substituents and Their Derivatives Bearing a Cyanide Co-Ligand: NIR Donor Materials for Vacuum-Processed Solar Cells. *J. Mater. Chem. A* **2017**, *5* (21), 10696–10703.

(81) Wu, D.; Cheung, S.; Devocelle, M.; Zhang, L.-J.; Chen, Z.-L.; O'Shea, D. F. Synthesis and Assessment of a Maleimide Functionalized BF2 Azadipyrromethene near-Infrared Fluorochrome. *Chem. Commun.* **2015**, *51* (93), 16667–16670.

(82) Zheng, Q.; Xu, G.; Prasad, P. N. Conformationally Restricted Dipyrromethene Boron Difluoride (BODIPY) Dyes: Highly Fluorescent, Multicolored Probes for Cellular Imaging. *Chem. - Eur. J.* **2008**, *14* (19), 5812–5819.

(83) Zhao, C.; Zhang, Y.; Wang, X.; Cao, J. Development of BODIPY-Based Fluorescent DNA Intercalating Probes. *J. Photochem. Photobiol. Chem.* **2013**, *264*, 41–47.

(84) Li, L.; Nguyen, B.; Burgess, K. Functionalization of the 4,4-Difluoro-4-Bora-3a,4a-Diaza-S-Indacene (BODIPY) Core. *Bioorg. Med. Chem. Lett.* **2008**, *18* (10), 3112–3116.

(85) Truc Vu, T.; Méallet-Renault, R.; Clavier, G.; A. Trofimov, B.; K. Kuimova, M. Tuning BODIPY Molecular Rotors into the Red: Sensitivity to Viscosity vs. Temperature. *J. Mater. Chem. C* **2016**, *4* (14), 2828–2833.

(86) Wu, Y.; Štefl, M.; Olzyńska, A.; Hof, M.; Yahioglu, G.; Yip, P.; Casey, D. R.; Ces, O.; Humpolíčková, J.; Kuimova, M. K. Molecular Rheometry: Direct Determination of Viscosity in Lo and Ld Lipid Phases via Fluorescence Lifetime Imaging. *Phys. Chem. Chem. Phys.* **2013**, *15* (36), 14986–14993.

(87) Dent, M. R.; López-Duarte, I.; Dickson, C. J.; Geoghegan, N. D.; Cooper, J. M.; Gould, I. R.; Krams, R.; Bull, J. A.; Brooks, N. J.; Kuimova, M. K. Imaging Phase Separation in Model Lipid Membranes through the Use of BODIPY Based Molecular Rotors. *Phys Chem Chem Phys* **2015**, *17* (28), 18393–18402.

(88) Sobenina, L. N.; Vasil'tsov, A. M.; Petrova, O. V.; Petrushenko, K. B.; Ushakov, I. A.; Clavier, G.; Meallet-Renault, R.; Mikhaleva, A. I.; Trofimov, B. A. General Route

to Symmetric and Asymmetric *meso* -CF $_3$ -3(5)-Aryl(hetaryl)- and 3,5-Diaryl(dihetaryl)-BODIPY Dyes. *Org. Lett.* **2011**, *13* (10), 2524–2527.

(89) Zhu, S.; Bi, J.; Vegesna, G.; Zhang, J.; Luo, F.-T.; Valenzano, L.; Liu, H. Functionalization of BODIPY Dyes at 2,6-Positions through Formyl Groups. *RSC Adv.* **2013**, *3* (14), 4793.

(90) Niu, S. L.; Ulrich, G.; Ziessel, R.; Kiss, A.; Renard, P.-Y.; Romieu, A. Water-Soluble BODIPY Derivatives. *Org. Lett.* **2009**, *11* (10), 2049–2052.

(91) Jiao, L.; Yu, C.; Li, J.; Wang, Z.; Wu, M.; Hao, E. β-Formyl-BODIPYs from the Vilsmeier−Haack Reaction. *J. Org. Chem.* **2009**, *74* (19), 7525–7528.

(92) Ziessel, R.; Ulrich, G.; Harriman, A. The Chemistry of Bodipy: A New El Dorado for Fluorescence Tools. *New J. Chem.* **2007**, *31* (4), 496–501.

(93) Klfout, H.; Stewart, A.; Elkhalifa, M.; He, H. BODIPYs for Dye-Sensitized Solar Cells. *ACS Appl. Mater. Interfaces* **2017**, *9* (46), 39873–39889.

(94) Summers, G. H.; Lefebvre, J.-F.; Black, F. A.; Davies, E. S.; Gibson, E. A.; Pullerits, T.; Wood, C. J.; Zidek, K. Design and Characterisation of Bodipy Sensitizers for Dye-Sensitized NiO Solar Cells. *Phys. Chem. Chem. Phys.* **2015**, *18* (2), 1059–1070.

(95) Erbas, S.; Gorgulu, A.; Kocakusakogullari, M.; Akkaya, E. U. Non-Covalent Functionalized SWNTs as Delivery Agents for Novel Bodipy-Based Potential PDT Sensitizers. *Chem. Commun.* **2009**, No. 33, 4956.

(96) Gorbe, M.; Costero, A. M.; Sancenón, F.; Martínez-Máñez, R.; Ballesteros-Cillero, R.; Ochando, L. E.; Chulvi, K.; Gotor, R.; Gil, S. Halogen-Containing BODIPY Derivatives for Photodynamic Therapy. *Dyes Pigments* **2019**, *160*, 198–207.

(97) Zou, J.; Yin, Z.; Ding, K.; Tang, Q.; Li, J.; Si, W.; Shao, J.; Zhang, Q.; Huang, W.; Dong, X. BODIPY Derivatives for Photodynamic Therapy: Influence of Configuration versus Heavy Atom Effect. *ACS Appl. Mater. Interfaces* **2017**, *9* (38), 32475–32481.

(98) Waddell, P. G.; Liu, X.; Zhao, T.; Cole, J. M. Rationalizing the Photophysical Properties of BODIPY Laser Dyes via Aromaticity and Electron-Donor-Based Structural Perturbations. *Dyes Pigments* **2015**, *116*, 74–81.

(99) García, O.; Sastre, R.; del Agua, D.; Costela, A.; García-Moreno, I.; López Arbeloa, F.; Bañuelos Prieto, J.; López Arbeloa, I. Laser and Physical Properties of BODIPY Chromophores in New Fluorinated Polymeric Materials. *J. Phys. Chem. C* **2007**, *111* (3), 1508–1516.

(100) Baslak, C.; Nuri Kursunlu, A. A Naked-Eye Fluorescent Sensor for Copper(Ii) Ions Based on a Naphthalene Conjugate Bodipy Dye. *Photochem. Photobiol. Sci.* **2018**, *17* (8), 1091–1097.

(101) Dolan, C.; Byrne, A.; Long, C.; Czamara, K.; Kaczor, A.; Baranska, M.; Keyes, T. E. Polypyridyl Substituted BODIPY Derivatives; Water Switchable Imaging Probes That Exhibit Halogen Substituent Dependent Localisation in Live Cells. *RSC Adv.* **2017**, *7* (69), 43743–43754.

(102) Niu, L.-Y.; Li, H.; Feng, L.; Guan, Y.-S.; Chen, Y.-Z.; Duan, C.-F.; Wu, L.-Z.; Guan, Y.-F.; Tung, C.-H.; Yang, Q.-Z. BODIPY-Based Fluorometric Sensor Array for the Highly Sensitive Identification of Heavy-Metal Ions. *Anal. Chim. Acta* **2013**, *775*, 93–99.

(103) Manton, J. C.; Long, C.; Vos, J. G.; Pryce, M. T. A Photo- and Electrochemical Investigation of BODIPY–cobaloxime Complexes for Hydrogen Production, Coupled with Quantum Chemical Calculations. *Phys. Chem. Chem. Phys.* **2014**, *16* (11), 5229–5236.

(104) Courtis, A. M.; Santos, S. A.; Guan, Y.; Hendricks, J. A.; Ghosh, B.; Szantai-Kis, D. M.; Reis, S. A.; Shah, J. V.; Mazitschek, R. Monoalkoxy BODIPYs--a Fluorophore Class for Bioimaging. *Bioconjug. Chem.* **2014**, *25* (6), 1043–1051.

(105) Gao, T.; He, H.; Huang, R.; Zheng, M.; Wang, F.-F.; Hu, Y.-J.; Jiang, F.-L.; Liu, Y. BODIPY-Based Fluorescent Probes for Mitochondria-Targeted Cell Imaging with Superior Brightness, Low Cytotoxicity and High Photostability. *Dyes Pigments* **2017**, *141*, 530–535.

(106) Miller, L. W.; Cai, Y.; Sheetz, M. P.; Cornish, V. W. In Vivo Protein Labeling with Trimethoprim Conjugates: A Flexible Chemical Tag. *Nat. Methods* **2005**, *2* (4), 255–257.

(107) Liu, W.; Li, F.; Chen, X.; Hou, J.; Yi, L.; Wu, Y.-W. A Rapid and Fluorogenic TMP-AcBOPDIPY Probe for Covalent Labeling of Proteins in Live Cells. *J. Am. Chem. Soc.* **2014**, *136* (12), 4468–4471.

(108) Staudinger, C.; Breininger, J.; Klimant, I.; Borisov, S. M. Near-Infrared Fluorescent Aza-BODIPY Dyes for Sensing and Imaging of pH from the Neutral to Highly Alkaline Range. *The Analyst* **2019**, *144* (7), 2393–2402.

(109) Prasannan, D.; Arunkumar, C. A "turn-on-and-Off" pH Sensitive BODIPY Fluorescent Probe for Imaging E. Coli Cells. *New J. Chem.* **2018**, *42* (5), 3473–3482.

(110) Grossi, M.; Morgunova, M.; Cheung, S.; Scholz, D.; Conroy, E.; Terrile, M.; Panarella, A.; Simpson, J. C.; Gallagher, W. M.; O'Shea, D. F. Lysosome Triggered near-Infrared Fluorescence Imaging of Cellular Trafficking Processes in Real Time. *Commun.* **2016**, *7*, 10855.

(111) Marks, D. L.; Bittman, R.; Pagano, R. E. Use of Bodipy-Labeled Sphingolipid and Cholesterol Analogs to Examine Membrane Microdomains in Cells. *Histochem. Cell Biol.* **2008**, *130* (5), 819–832.

(112) de Wit, G.; Danial, J. S. H.; Kukura, P.; Wallace, M. I. Dynamic Label-Free Imaging of Lipid Nanodomains. *Proc. Natl. Acad. Sci. U. S. A.* **2015**, *112* (40), 12299–12303.

(113) Moss, F. R.; Boxer, S. G. Atomic Recombination in Dynamic Secondary Ion Mass Spectrometry Probes Distance in Lipid Assemblies: A Nanometer Chemical Ruler. *J. Am. Chem. Soc.* **2016**, *138* (51), 16737–16744.

(114) Nusshold, C.; Uellen, A.; Bernhart, E.; Hammer, A.; Damm, S.; Wintersperger, A.; Reicher, H.; Hermetter, A.; Malle, E.; Sattler, W. Endocytosis and Intracellular

Processing of BODIPY-Sphingomyelin by Murine CATH.a Neurons. *Biochim. Biophys. Acta* **2013**, *1831* (12), 1665–1678.

(115) Juhasz, J.; Davis, J. H.; Sharom, F. J. Fluorescent Probe Partitioning in Giant Unilamellar Vesicles of "lipid Raft" Mixtures. *Biochem. J.* **2010**, *430* (3), 415–423.

(116) Tyteca, D.; D'Auria, L.; Der Smissen, P. V.; Medts, T.; Carpentier, S.; Monbaliu, J. C.; de Diesbach, P.; Courtoy, P. J. Three Unrelated Sphingomyelin Analogs Spontaneously Cluster into Plasma Membrane Micrometric Domains. *Biochim. Biophys. Acta BBA - Biomembr.* **2010**, *1798* (5), 909–927.

(117) Song, K. C.; Livanec, P. W.; Klauda, J. B.; Kuczera, K.; Dunn, R. C.; Im, W. Orientation of Fluorescent Lipid Analogue BODIPY-PC to Probe Lipid Membrane Properties: Insights from Molecular Dynamics Simulations. *J. Phys. Chem. B* **2011**, *115* (19), 6157–6165.

(118) Sezgin, E.; Levental, I.; Grzybek, M.; Schwarzmann, G.; Mueller, V.; Honigmann, A.; Belov, V. N.; Eggeling, C.; Coskun, Ü.; Simons, K.; et al. Partitioning, Diffusion, and Ligand Binding of Raft Lipid Analogs in Model and Cellular Plasma Membranes. *Biochim. Biophys. Acta BBA - Biomembr.* **2012**, *1818* (7), 1777–1784.

(119) Klymchenko, A. S.; Kreder, R. Fluorescent Probes for Lipid Rafts: From Model Membranes to Living Cells. *Chem. Biol.* **2014**, *21* (1), 97–113.

(120) Samsonov, A. V.; Mihalyov, I.; Cohen, F. S. Characterization of Cholesterol-Sphingomyelin Domains and Their Dynamics in Bilayer Membranes. *Biophys. J.* **2001**, *81* (3), 1486–1500.

(121) Li, Z.; Mintzer, E.; Bittman, R. First Synthesis of Free Cholesterol−BODIPY Conjugates. *J. Org. Chem.* **2006**, *71* (4), 1718–1721.

(122) Figueira-Duarte, T. M.; Müllen, K. Pyrene-Based Materials for Organic Electronics. *Chem. Rev.* **2011**, *111* (11), 7260–7314.

(123) A. Laurent,. Ann. Chim. Phys **1837**, *66*, 136-213.

(124) Jia, W.-L.; McCormick, T.; Liu, Q.-D.; Fukutani, H.; Motala, M.; Wang, R.-Y.; Tao, Y.; Wang, S. Diarylamino Functionalized Pyrene Derivatives for Use in Blue OLEDs and Complex Formation. *J. Mater. Chem.* **2004**, *14* (22), 3344–3350.

(125) Bains, G.; Patel, A. B.; Narayanaswami, V. Pyrene: A Probe to Study Protein Conformation and Conformational Changes. *Molecules* **2011**, *16* (9), 7909–7935.

(126) Wu, J.; Zou, Y.; Li, C.; Sicking, W.; Piantanida, I.; Yi, T.; Schmuck, C. A Molecular Peptide Beacon for the Ratiometric Sensing of Nucleic Acids. *J. Am. Chem. Soc.* **2012**, *134* (4), 1958–1961.

(127) Niko, Y.; Didier, P.; Mely, Y.; Konishi, G.; Klymchenko, A. S. Bright and Photostable Push-Pull Pyrene Dye Visualizes Lipid Order Variation between Plasma and Intracellular Membranes. *Sci. Rep.* **2016**, *6*, 18870.

(128) Bondurant, B.; Last, J. A.; Waggoner, T. A.; Slade, A.; Sasaki, D. Y. Optical and Scanning Probe Analysis of Glycolipid Reorganization upon Concanavalin A Binding to Mannose-Coated Lipid Bilayers. *Langmuir* **2003**, *19* (5), 1829–1837.

(129) Duhamel, J. New Insights in the Study of Pyrene Excimer Fluorescence to Characterize Macromolecules and Their Supramolecular Assemblies in Solution. *Langmuir* **2012**, *28* (16), 6527–6538.
(130) Winnik, F. M. Photophysics of Pre-associated Pyrenes in Aqueous Polymer Solutions and in Other Organized Media. *Chem. Rev.* **1993**, *93* (2), 587–614.
(131) Shiraishi, Y.; Tokitoh, Y.; Hirai, T. pH- and H_2O-Driven Triple-Mode Pyrene Fluorescence. *Org. Lett.* **2006**, *8* (17), 3841–3844.
(132) Finkler, B.; Riemann, I.; Vester, M.; Grüter, A.; Stracke, F.; Jung, G. Monomolecular Pyrenol-Derivatives as Multi-Emissive Probes for Orthogonal Reactivities. *Photochem. Photobiol. Sci.* **2016**, *15* (12), 1544–1557.
(133) Okamoto, A.; Kanatani, K.; Saito, I. Pyrene-Labeled Base-Discriminating Fluorescent DNA Probes for Homogeneous SNP Typing. *J. Am. Chem. Soc.* **2004**, *126* (15), 4820–4827.
(134) Karpovich, D. S.; Blanchard, G. J. Relating the Polarity-Dependent Fluorescence Response of Pyrene to Vibronic Coupling. Achieving a Fundamental Understanding of the Py Polarity Scale. *J. Phys. Chem.* **1995**, *99* (12), 3951–3958.
(135) Kalyanasundaram, K.; Thomas, J. K. Environmental Effects on Vibronic Band Intensities in Pyrene Monomer Fluorescence and Their Application in Studies of Micellar Systems. *J. Am. Chem. Soc.* **1977**, *99* (7), 2039–2044.
(136) Kim, J. J.; Beardslee, R. A.; Phillips, D. T.; Offen, H. W. Fluorescence Lifetimes of Pyrene Monomer and Excimer at High Pressures. *J. Chem. Phys.* **1969**, *51* (6), 2761–2762.
(137) Brownrigg, J. T.; Kenny, J. E. Fluorescence Intensities and Lifetimes of Aromatic Hydrocarbons in Cyclohexane Solution: Evidence of Contact Charge-Transfer Interactions with Oxygen. *J. Phys. Chem. A* **2009**, *113* (6), 1049–1059.
(138) Tchebotareva, N.; Yin, X.; Watson, M. D.; Samorì, P.; Rabe, J. P.; Müllen, K. Ordered Architectures of a Soluble Hexa-Peri-hexabenzocoronene−Pyrene Dyad: Thermotropic Bulk Properties and Nanoscale Phase Segregation at Surfaces. *J. Am. Chem. Soc.* **2003**, *125* (32), 9734–9739.
(139) Wang, C.; Dong, H.; Hu, W.; Liu, Y.; Zhu, D. Semiconducting π-Conjugated Systems in Field-Effect Transistors: A Material Odyssey of Organic Electronics. *Chem. Rev.* **2012**, *112* (4), 2208–2267.
(140) Birks, J.B.; Dyson, D.; Munro, I. "Excimer" Fluorescence II. Lifetime Studies of Pyrene Solutions. *Proc. R. Soc. Lond. Ser. Math. Phys. Sci.* **1963**, *275* (1363), 575–588.
(141) Yeşilot, S.; Çoşut, B.; Alidağı, H. A.; Hacıvelioğlu, F.; Özpınar, G. A.; Kılıç, A. Intramolecular Excimer Formation in Hexakis(pyrenyloxy)cyclotriphosphazene: Photophysical Properties, Crystal Structure, and Theoretical Investigation. *Dalton Trans.* **2014**, *43* (9), 3428–3433.
(142) Safin, D. A.; Babashkina, M. G.; Mitoraj, M. P.; Kubisiak, P.; Robeyns, K.; Bolte, M.; Garcia, Y. An Intermolecular Pyrene Excimer in the Pyrene-Labeled N-

Thiophosphorylated Thiourea and Its nickel(II) Complex. *Inorg. Chem. Front.* **2016**, *3* (11), 1419–1431.

(143) Bains, G. K.; Kim, S. H.; Sorin, E. J.; Narayanaswami, V. The Extent of Pyrene Excimer Fluorescence Emission Is a Reflector of Distance and Flexibility: Analysis of the Segment Linking the LDL Receptor-Binding and Tetramerization Domains of Apolipoprotein E3. *Biochemistry (Mosc.)* **2012**, *51* (31), 6207–6219.

(144) Zhang, R.; Zhao, Y.; Zhang, T.; Xu, L.; Ni, Z. A Series of Short Axially Symmetrically 1,3,6,8-Tetrasubstituted Pyrene-Based Green and Blue Emitters with 4-Tert-Butylphenyl and Arylamine Attachments. *Dyes Pigments* **2016**, *130*, 106–115.

(145) Feng, X.; Hu, J.-Y.; Redshaw, C.; Yamato, T. Functionalization of Pyrene To Prepare Luminescent Materials-Typical Examples of Synthetic Methodology. *Chem. - Eur. J.* **2016**, *22* (34), 11898–11916.

(146) Zhan, Y.; Peng, J.; Ye, K.; Xue, P.; Lu, R. Pyrene Functionalized Triphenylamine-Based Dyes: Synthesis, Photophysical Properties and Applications in OLEDs. *Org. Biomol. Chem.* **2013**, *11* (39), 6814–6823.

(147) França, B. M. de; Bello Forero, J. S.; Garden, S. J.; Ribeiro, E. S.; Souza, R. da S.; Teixeira, R. S.; Corrêa, R. J. Green Fluorescence Pyrene-Based Dye as a New π-Extended System: Synthesis, Photophysical and Theoretical Studies. *Dyes Pigments* **2018**, *148*, 444–451.

(148) Feng, X.; Hu, J.-Y.; Iwanaga, F.; Seto, N.; Redshaw, C.; Elsegood, M. R. J.; Yamato, T. Blue-Emitting Butterfly-Shaped 1,3,5,9-Tetraarylpyrenes: Synthesis, Crystal Structures, and Photophysical Properties. *Org. Lett.* **2013**, *15* (6), 1318–1321.

(149) Niko, Y.; Sasaki, S.; Narushima, K.; Sharma, D. K.; Vacha, M.; Konishi, G. 1-, 3-, 6-, and 8-Tetrasubstituted Asymmetric Pyrene Derivatives with Electron Donors and Acceptors: High Photostability and Regioisomer-Specific Photophysical Properties. *J. Org. Chem.* **2015**, *80* (21), 10794–10805.

(150) Niko, Y.; Moritomo, H.; Sugihara, H.; Suzuki, Y.; Kawamata, J.; Konishi, G. A Novel Pyrene-Based Two-Photon Active Fluorescent Dye Efficiently Excited and Emitting in the "tissue Optical Window (650–1100 Nm)." *J. Mater. Chem. B* **2014**, *3* (2), 184–190.

(151) Zhang, H.; Wang, Y.; Shao, K.; Liu, Y.; Chen, S.; Qiu, W.; Sun, X.; Qi, T.; Ma, Y.; Yu, G.; et al. Novel Butterfly Pyrene-Based Organic Semiconductors for Field Effect Transistors. *Chem. Commun.* **2006**, *0* (7), 755–757.

(152) Tanhuanpää, K.; Virtanen, J.; Somerharju, P. Fluorescence Imaging of Pyrene-Labeled Lipids in Living Cells. *Biochim. Biophys. Acta* **2000**, *1497* (3), 308–320.

(153) Jana, A.; Saha, B.; Ikbal, M.; Kumar Ghosh, S.; Pradeep Singh, N. D. 1-(Hydroxyacetyl)pyrene a New Fluorescent Phototrigger for Cell Imaging and Caging of Alcohols, Phenol and Adenosine. *Photochem. Photobiol. Sci.* **2012**, *11* (10), 1558–1566.

(154) Zhang, D.; Liu, D.; Li, M.; Yang, Y.; Wang, Y.; Yin, H.; Liu, J.; Jia, B.; Wu, X. A Simple Pyrene-Based Fluorescent Probe for Highly Selective Detection of

Formaldehyde and Its Application in Live-Cell Imaging. *Anal. Chim. Acta* **2018**, *1033*, 180–184.

Chapter 2: Phase partitioning, solvent-switchable BODIPY probes for high contrast cellular imaging and FCS

Published in *New J. Chem*, 2018, **42**, 3671-3682.

Darragh O' Connor, Aisling Byrne, Ciarán Dolan and Tia E. Keyes.

Within this work I was the primary author and contributor to the experimental design, execution, analysis and preparation of this manuscript. I specifically contributed towards the following sections: synthesis and structural characterisation, photophysical characterisation, GUV preparation and partitioning studies and FCS studies. Dr. C. Dolan synthesised precursor **4**. Cell studies were carried out by Dr. A. Byrne. Supporting information associated with this chapter can be found in Appendix A.

2.1 Abstract

Lipophilic BODIPY fluorophores, in which the BODIPY core bears pendant dipyrido[3,2-*a*:2′,3′-*c*]phenazine (Dppz) or naphthyridyl and cholesterol substituents were designed and prepared as lipid probes for both liposomes and live cell imaging. The probes are non-emissive in water but permeate both GUV and live cell membranes and provide high contrast fluorescence and lifetime imaging of membranous structures and lipid droplets in cells and are suitable for FCS measurements on lipid membranes.

2.2 Introduction

Luminophores that can segregate into membrane domains are of interest both in the study of live cells and in biophysical studies of membrane models as a route to understanding the lateral order and fluidity of lipid domains.[1] Co-existing liquid phases can occur in liposomes comprising ternary or greater mixtures of phospholipids containing cholesterol and sphingomyelin. The two phases are liquid-disordered (Ld) phase and liquid-ordered (Lo) phase. The former lies between a liquid crystal or gel phase and the latter, which is enriched in cholesterol (Chol) and sphingolipids[2], is closer to a liquid-crystalline phase. Both phases exhibit a high degree of lateral fluidity. Phase separated liposomes are widely used as models for raft behaviour in cell membranes and it is desirable to develop fluorescent probes for lipid membrane labelling that can selectively differentiate between the liquid-ordered (Lo) and liquid disordered (Ld) phases to enable their study.[3–5] Most studies have shown that fluorescent probes that contain unsaturated chains have a preference to associate with the liquid-disordered (Ld) phase, while several polycylic aromatic hydrocarbons (PAHs) have exhibited preferential partitioning into to the liquid-ordered (Lo) phase.[6] In the context of cell imaging, lipophilic probes also have the capacity to associate intracellularly into lipid rich domains of the cell, including the cellular membrane and lipid droplets.

Lipid droplets (LDs) are hydrophobic cytoplasmic organelles that are responsible for the storage of neutral lipids. They consist of a triacylglycerol and cholesteryl ester core surrounded by a phospholipid–cholesterol monolayer.[7,8] and range in size from 1–100 μm.[9] LDs had once been regarded as fat deposits and transport vesicles. And, whilst indeed their main role is lipid storage, in the last decade it has become apparent that LDs are a much

more dynamic organelle, storing a diverse array of proteins on their surfaces and within their core.[10,11]

LDs have been shown to play a role in a number of physiological processes such as the immune response.[12] *In vivo* inflammation, stimulates production of LDs that accumulate within leukocytes and become activated in mast cells[13] effectors of immune reactions in diseases such as asthma and rheumatoid arthritis.[1–16] Some of the most important advances in understanding the real-time dynamics of LDs has come from imaging technologies such as confocal microscopy.[17,18] The fluorescent label Nile red has been mostly widely used as a selective stain to image LDs.[19] But a number of emerging commercial probes for imaging LDs are based on BODIPY derivatives.[20–24]

The 4,4-difluoro-4-bora-3*a*,4*a*-diaza-*s*-indacene (BODIPY) derivatives are attractive luminophores in biological and biophysical applications due to their outstanding photophysical characteristics; large quantum yields, sharp absorbance and emission features and their synthetic versatility.[25–32] In the context of LDs they offer superior photochemical stability to Nile red[33] and their optical properties can be tuned with relative ease *via* synthetic modification to the BODIPY core or *meso* positions. Such modification has led to diverse BODIPY dyes many of whom have been applied in biological labelling.[34–37] Several BODIPY lipid probes are available commercially for bio-imaging; for example, BODIPY PC and BODIPY FL C5-GM1 are used to label lipid membranes.[38,39] However, we are interested in developing lipid and phase selective probes that do not require arduous lipid conjugations to the fluorophore by developing probes that can spontaneously partition into membrane and lipid structures.

Herein, we describe two lipid membrane partitioning BODIPY derivatives. One containing a naphthyridyl pendant functionalised with cholesterol and the second bearing an aryl BODIPY derivative with pendant dipyrido[3,2-*a*:2′,3′-*c*]phenazine (Dppz). Both probes exhibit intense fluorescence (quantum yields >70 %) in chloroform which is extinguished in water. The former chosen because the naphthyridyl-BODIPY derivative shows exceptional quantum yield in non-aqueous solvent (>80 %) and the latter selected because the Dppz moiety has been shown previously to partition into lipid membranes.[40] We observe that both probes spontaneously assemble into GUV membranes to provide high contrast images of the

lipid membrane. Both also partition strongly to the Ld phases of phase separated membranes, where they were found to be suitable for fluorescence correlation spectroscopy. Both probes are also spontaneously internalised into live mammalian cells where they associate strongly with lipid droplets.

2.3 Materials and Methods

2.3.1 Materials

All reagents were purchased from Sigma Aldrich (Ireland) and used without further purification unless otherwise stated. 1,2-Dioleoyl-*sn-glycero*-3-phosphocholine (DOPC), brain sphingomyelin (BSM), and cholesterol (Chol) were obtained from Avanti Polar Lipids (Alabaster, AL, USA). DiD′ solid; DiIC18(5) solid (1,1′-dioctadecyl-3,3,3′,3′-tetramethylindodicarbocyanine, 4-chlorobenzenesulfonate salt) was purchased from Thermo Fisher Scientific (Waltham, Massachusetts, USA).

2.3.2 Instrumentation

^{1}H NMR spectra were recorded on either 400 MHz or 600 MHz Bruker spectrometer. All ^{13}C NMR spectra were obtained at 150 MHz. The spectra were processed using Bruker Topspin NMR software. High Resolution Mass Spectrometry (HR-MS) was carried out at the Mass Spectrometry facility, University College Dublin. MALDI-ToF mass spectrometry was performed on MALDI-Q-ToF Premier instrument at Trinity College Dublin. UV-Vis spectra were recorded on Varian Cary 50 spectrometer. Samples were analysed in Hellma quartz fluorescence cuvettes, with a path length of 1 cm, and spectral range of 200–800 nm unless otherwise stated. Background measurements were carried out at room temperature prior to each measurement. Emission Spectra were recorded on a Varian Cary Eclipse fluorescence spectrophotometer with excitation and emission slit widths of 2.5 nm. All analyses were carried out using quartz cuvettes and background correction was applied prior to measurement. Fluorescence lifetime measurements were carried out using a PicoQuant FluoTime 100 Compact FLS TCSPC system using a 450 nm pulsed laser source generated from a PicoQuant PDL800-B box. The instrument response function was determined using Ludox colloidal silica solution. Lifetime decay plots were analysed using PicoQuant

TimeHarp software. The goodness of each fit to exponential decay kinetics was assessed from chi-squared values (where $\chi^2 < 1.3$) and visual inspection of residuals.

2.3.3 Preparation of giant unilamellar vesicles (GUVs)

Lipid stock solutions were prepared in chloroform. For preparation of Ld/Lo phase separated GUVs, 1-2-dioleoyl-*sn-glycero*-3-phosphocoline (DOPC), brain sphingomyelin (BSM) and cholesterol (Chol) were mixed in a molar ratio 4:4:2 to a final concentration of 5 mM. For lipid diffusion (FCS) studies Dppz-Ar-BODIPY and naphthyridyl-BODIPY-2-cholesterol were included at a concentration of 0.001 mol% in the lipid content, while for partitioning (confocal fluorescence microscopy) studies Dppz-Ar-BODIPY or naphthyridyl-BODIPY-2-cholesterol, along with the lipophilic tracer dye, DiD was included at a concentration of 0.2 mol% in lipid content prior to electroformation. DiD is known to partition strongly to the Ld phase of GUVs, and was therefore used to identify this phase.[6] GUVs were formed by electroformation using the Vesicle Prep Pro (VPP) (Nanion Technologies, Munich, Germany). The lipids were added in 2 μL droplets onto a pair of conductive ITO slides and dried in a desiccator under vacuum for 45 minutes. The ITO slides were carefully placed in contact so as to avoid air bubbles. A voltage was then applied and increased over 10 minutes from 0 V to 3 V and then held for 125 minutes. The protocol was carried out at 37 °C. Once electroformation was completed, the GUVs were removed, diluted with 0.23 mM glucose solution and 0.5 % agarose solution and deposited on glass coverslides for imaging.[41] For uptake studies, GUVs were prepared as described above by electroformation using DOPC 100 mol%. GUVs in sucrose solution 230 mM were then diluted using an aqueous glucose solution 230 mM. The selected probe in chloroform was then added to this suspension to give a final dye concentration of 10 μM. GUVs in this mixed solution were then deposited onto a glass slide for microscopy. Uptake was monitored using confocal microscopy using fluorescence and white light imaging over a period of 1 h 45 minutes.

2.3.4 Confocal microscopy of giant unilamellar vesicles (GUVs)

Fluorescence imaging was carried out using a Leica TSP inverted (DMi8) confocal microscope. A 100× oil immersion objective was used for all measurements. A white light laser was used to excite the dyes. The excitation and emission wavelengths ($\lambda_{ex}/\lambda_{em}$) were as

follows: 498/511–570 nm for Dppz-Ar-BODIPY, 523/532–580 nm for naphthyridyl-BODIPY-2-cholesterol and 644/665–700 nm for DiD.

2.3.5 Fluorescence lifetime correlation spectroscopy (FLCS)

Diffusion coefficients for the BODIPY derivatives within labelled GUVs were obtained using fluorescence lifetime correlation spectroscopy, FLCS performed on a Microtime 200 system (Picoquant GmBH, Berlin, Germany) consisting of an inverted microscope model Olympus X1-71 with an Olympus UPlanSApo 60×/1.2 water immersion objective. The fluorophores were excited with a 440 nm PicoTA from Toptica (Picoquant). The laser was directed onto a 440/532 rpc dichroic mirror and focused on the aforementioned objective. The sample fluorescence was collected through the same objective and filtered by the dichroic mirror, and by a 460 nm interference filter. The sample fluorescence was passed through a 50 μM pinhole onto a single photon avalanche diode (SPAD) detector. The autocorrelation functions (ACFs) were fit using SymphoTime software (Picoquant GmBH, Berlin, Germany) to the following eqn (2.1):

$$G(\tau)=\frac{1}{N(1-T)}\left[1-T+Te^{\left(-\frac{\tau}{\tau_T}\right)}\right]\left[1+\left(\frac{\tau}{\tau_D}\right)^{\alpha}\right]^{-1}$$ Equation 2.1

where $G(\tau)$ is the autocorrelation function of fluorescence fluctuations; N is the average number of diffusing fluorophores in the effective volume; τ is the delay time; T is the fraction of molecules in the triplet state; α is the anomalous parameter; τ_D is the diffusion time of the molecules and τ_T is the decay time for the triplet state. Prior to performing FLCS measurements, confocal images of the GUVs were obtained in order to locate and identify suitable GUVs for measurement. The lipid bilayer of the liposome was located by z-scanning near the GUV membranes and locating the site of maximum intensity. Point FLCS measurements were then recorded for duration of 3 minutes. Measurements that exhibited any GUV drift were eliminated.

2.3.5 Fluorescent lifetime imaging microscopy (FLIM)

Fluorescence lifetime imaging was carried out using a PicoQuant 100 system attached to Leica TSP inverted (DMi8) confocal microscope using a 100× oil immersion objective. Each

sample was acquired for 120 s with a 512 × 512 resolution. A 498 nm white light laser was used to excite the GUV samples. Data was analysed using PicoQuant Symphotime software.

2.3.6 Cell culture

Two cell lines were studied; Chinese hamster ovarian (CHO-K1), an adherent mammalian cell line and HeLa cells, a cervical cancer cell line. The media used to culture the cells was Dulbecco's modified Eagle's medium (DMEM)/Hams F-12 for CHO and DMEM supplemented with 1 % L-glutamine for HeLa. Both were supplemented with 10% foetal bovine serum and 1 % penicillin–streptomycin and grown at 37 °C with 5% CO_2. Cells were harvested or split at 90 % confluency using 0.25 % trypsin for 5 minutes at 37 °C.

2.3.7 Confocal microscopy for cell imaging

HeLa and CHO cells were seeded at 1.5×10^5 cells in 2 mL culture media on poly-L-lysine coated, #1.5 coverslips in a 6-well plate and left for 24 h at 37 °C under 5 % CO_2. Dppz-Ar-BODIPY and naphthyridyl-BODIPY-2-cholesterol were added to the wells in cell media to give a final concentration of 5 μM (final DMSO concentration of 0.25 %) and were incubated for 24 h at 37 °C with 5 % CO_2. Prior to imaging, the compounds were removed, and the cells were washed once with PBS supplemented with 1.1 mM $MgCl_2$ and 0.9 mM $CaCl_2$. The cells were imaged live using a Leica TSP DMi8 confocal microscope with a 100× oil immersion objective lens. 498 nm selected from a white light laser was used to excite the compounds, and a 505–550 nm filter was used to collect the emission. For real-time imaging, both cell lines were seeded at 1.5×10^5 cells in 2 mL culture media on 35 mm high precision glass-bottom dishes (Ibidi, Germany) as described previously. Dppz-Ar-BODIPY and Naphthryidyl-BODIPY-2-cholesterol were added to Leibovitz media to give a final concentration of 5 μM and was added to live cells and imaged immediately using Time Series mode to capture images every 1 minute over a 25-minute period. To assess the mode of uptake, cells were prepared as mentioned above and incubated with the compounds at 4 °C for 24 h. Cells were washed with PBS (supplemented with 1.1 mM $MgCl_2$ and 0.9 mM $CaCl_2$) and imaged immediately.

2.3.8 Cytotoxicity studies

Cells were seeded in 96-well plates (Sarstedt flat-bottom cell + culture plate) at 1×10^4 for CHO and HeLa cells in 100 μL media for 24 h at 37 °C with 5 % CO_2. Dppz-Ar-BODIPY

and Naphthryidyl-BODIPY-2-cholesterol were added for 20 hours at 37 °C with 5 % CO_2. Final dye concentrations were 100, 50, 20, 10, 5 and 1 μM. The Alamar blue assay (Promocell GmbH) was used to measure cell viability by the addition of 10 μL resazurin reagent and cells were incubated for 7 h at 37 °C in the dark. Absorbance was measured using a Tecan 96-well plate reader at 570 nm and 600 nm (corrected for background).2.4 Results and discussion

2.4 Results and Discussion

2.4.1 Synthesis

The structures of the BODIPY derivatives and their route to synthesis are shown in Scheme 2.1. 11-Bromo-dipyrido[3,2-*a*,2′,3′-*c*]phenazine under Suzuki–Miyura coupling conditions afforded the intermediate aldehyde **2**. The aldehyde was then converted to Dppz-Ar-BODIPY *via* reaction with 2,4-dimethylpyrrole, boron trifluoride diethyletherate and triethylamine, in the presence of an oxidant *p*-chloranil in DCM purged with N_2. Purification was carried out by column chromatography on a silica gel column using $CHCl_3$/MeOH/H_2O/CH_3COOH (80:18:2:1 v/v) as the mobile phase giving BODIPY-Ar-Dppz as a dark red solid. Naphthyridyl-BODIPY-2-cholesterol was synthesised from the precursor naphthyridyl BODIPY derivative which was prepared as previously reported.[42] The less electropositive 2- position of the BODIPY core was formylated by treating BODIPY dye **4** with $POCl_3$ and DMF in dichloroethane as reported in literature.[43] Purification of the product by column chromatography on silica gel ($CHCl_3$/MeOH/H_2O/AcCOOH 80:18:2:1 v/v) gave a dark purple crystalline solid. The aldehyde was then converted to a carboxylic acid via Pinnick-type oxidation reaction.[44] This was achieved by treating the formylated BODIPY dye **5** with $NaClO_2$ and NH_2SO_3H in THF and water. The compound was isolated as an orange crystalline solid. ^{1}H NMR analysis confirmed the disappearance of the aldehyde peak at 9.99 ppm and thus the isolated BODIPY carboxylic acid intermediate **6** was subjected to the following steps without further purification. **6** was reacted with cholesterol in the presence of *N*,*N*′-dicyclohexylcarbodiimide and 4-dimethylaminopyridine to give the expected naphthyridyl-BODIPY-2-cholesterol conjugate after purification by column chromatography on silica gel

using (DCM/MeOH 9:1) as the mobile phase. Dppz-BODIPY and naphthyridyl-BODIPY-2-cholesterol were characterised by mass spectrometry and ^{1}H NMR spectroscopy and the data conformed to expected values.

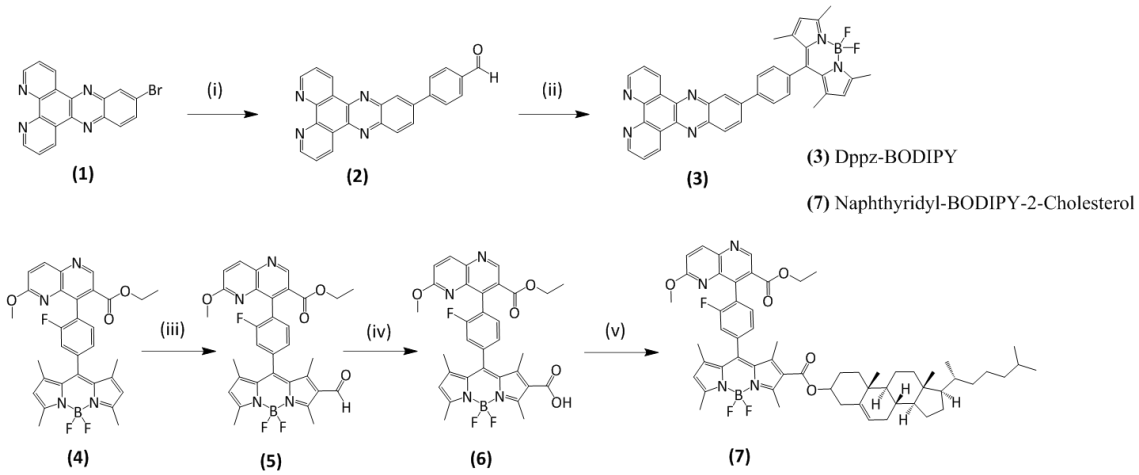

Scheme 2.1 Synthetic route to BODIPY derivatives (i) 4-formylphenylboronic acid, K_2CO_3, Pd(dppf)Cl_2.DCM Toulene/H_2O/EtOH (4:2:1), N_2, 12 h, 54 %; (ii) 2,4-diemthyl-1H-pyrrole, TFA, DCM 5 h; tetrachlorobenzoquinone, Et_3N, $BF_3{\cdot}OEt_2$, 12 h, 29 %; (iii) $POCl_3$, DMF, Dichloroethane, 50 °C, 2 h, 92 %; (iv) THF/H_2O (3:1), $NaClO_2$, NH_2SO_3H, 25 °C, 1 h, 79 %; (v) DMAP, DCC, DCM, 25 °C, 12 h, 96 %.

2.4.2 Photophysical Characterisation

Table 2.1 summaries the optical and photophysical properties of Dppz-Ar-BODIPY and naphthyridyl-BODIPY-2-cholesterol across a range of solvents. Both derivatives as expected, exhibit a $S_0 \rightarrow S_1$ (π–π^*) transition, centred at 500 ± 3 nm for Dppz-Ar-BODIPY and 515 ± 6 nm for the naphthyridyl-BODIPY-2-cholesterol in acetonitrile (Figure 2.1).[46] Emission was shifted for both derivatives to the red with decreasing solvent polarity, but the effect was most pronounced for Dppz-Ar-BODIPY. Conversely, emission is extinguished for both compounds in aqueous media. This is similar to behaviour reported for related BODIPY structures, where aqueous emission switch-off has been attributed to formation of nanoaggregates due to poor solubility in water or due to stabilisation of charge transfer states that are non-emissive.[47]

There are some distinctions in the solvent responses. Both compounds exhibit intense emission in non-protic solvent with quantum yields in chloroform of 0.71 and 0.88 respectively for Dppz-Ar-BODIPY and naphthyridyl-BODIPY-2-cholesterol respectively.

Table 2.1 Summary of photophysical data

Compound	Solvent	λ_{abs} (nm) (ε =x10^3 M^{-1} cm^{-1})	λ_{em} (nm)	τ_{lum} (ns) ± SD	ϕ_{lum}
Dppz-Ar-BODIPY	MeCN	497 (10.90)	511	3.50 ± 0.10	0.35
	H_2O	514 (2.85)	None	None	*
	DCM	501 (12.98)	518	3.88 ± 0.44	*
	$CHCl_3$	502 (15.51)	519	4.41 ± 0.18	0.71
	MeOH	499 (7.02)	511	3.17 ± 0.04 3.29 ± 0.1 [a]	0.17
Naphthyridyl-BODIPY-2-Cholesterol	MeCN	511 (10.93)	527	3.84 ± 0.14	0.44
	H_2O	521 (6.84)	None	None	*
	DCM	516 (11.36)	530	3.66 ± 0.09	*
	$CHCl_3$	517 (11.23)	531	3.50 ± 0.13	0.88
	MeOH	514(7.04)	530	4.41 ± 0.64 4.06 ± 0.5 [a]	0.55

All solutions were measured at concentrations of 10 μM. Slit widths for emission were set to 2.5 nm. Lifetime data was recorded in triplicate and curve fitting conformed to tail fit criteria of $\chi^2 < 1.3$. Quantum yields were measured using Fluorescein 0.1 M NaOH (ϕ= 0.90) as standard. *Not measured. [a] Measured at 37°C.

Dppz-Ar-BODIPY shows far greater sensitivity to protic media wherein it's quantum yield decreases to 0.17 in methanol and 0.35 in acetonitrile compared with 0.55 and 0.44 for naphthyridyl-BODIPY-2-cholesterol. This may be due to H-bridging to the N rich Dppz unit in protic solvent promoting non-radiative decay, such behaviour has been noted in Dppz containing luminescent metal complexes.[48,49] In this instance, the increased π-acceptor capability of the H-bridged Dppz may promote energy transfer from the BODIPY to the Dppz unit to extinguish the fluorescence. The lifetime data is consistent with this trend; Dppz-Ar-BODIPY exhibits a fluorescence lifetime of 4.41 ± 0.18 ns in chloroform that decreases with increasing solvent polarity. The lowest lifetime recorded was in methanol, where τ is 3.17 ± 0.04 ns. Conversely, naphthyridyl-BODIPY-2-cholesterol exhibits a fluorescence lifetime of 3.50 ± 0.13 in chloroform, with the longest-lived value 4.41 ± 0.64 ns occurring in methanol (4.41 ± 0.64 ns). As noted, the extinction of emission in aqueous media occurs for both compounds, and this behaviour was exploited here to enable collection of high contrast imaging of the probes in cells and GUVs in aqueous media. As live cell imaging studies are

conducted here at 37 °C we also examined the lifetime of the probes at this temperature in methanol and found, within experimental error that they were indistinguishable from room temperature values. Furthermore, over the concentration range 1 to 100 μM we found no evidence from fluorescence for aggregation of probe in organic media and dye absorbance followed Beer Lambert law as shown in Figure S2.14 (Appendix C). The concentrations used throughout subsequent studies are in the low micromolar range and nanomolar for FCS.

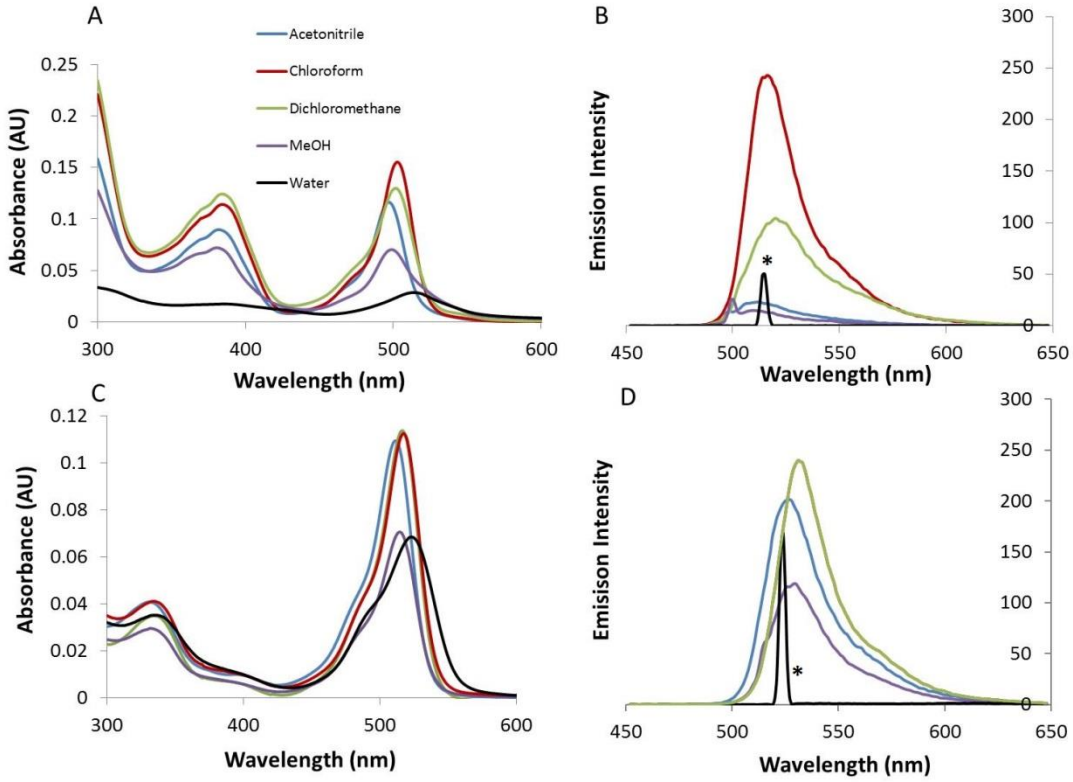

Figure 2.1 (a) Solvent dependence absorbance curves for 3 (10 μM). (b) Solvent dependence emission curves for 3 (10 μM, slit widths; 2.5 nm). (c) Solvent dependence absorbance curves for 7 (10 μM). (d) Solvent dependence emission curves for 7 (10 μM, slit widths; 2.5 nm). *excitation line, no emission observed in water.

2.4.3 GUV partitioning studies

Dppz and naphthyridine/cholesterol moieties were exploited here as pendants to the BODIPY fluorophores to promote membrane association. To explore the latter, the interaction of each

compound with giant unilamellar vesicles (GUVs) was investigated. Uptake of Dppz-Ar-BODIPY was monitored at 100 mol% DOPC GUVs by addition of the probe (in chloroform) to GUV containing aqueous solution, so that the final concentration was 10 μM, whilst imaging the GUVs using fluorescence microscopy. Dppz-Ar-BODIPY spontaneously partitions into GUVs with mission visible from the GUVs within 1 h and uptake was completed within 1 h 45 minutes (Figure S2.18). A low concentration of dye (10 μM) was used in order to ensure that any visible uptake was not due to overloading, as uptake is likely concentration dependent. When Dppz-Ar-BODIPY was added in a 1:1 mixture of chloroform and methanol it was found that uptake was completed in less than 1 h. This decrease in uptake time is expected due to the miscibility of methanol in water. It is important to note that the compounds did not emit from the background GUV solution and emission only appeared on partitioning of the probes into the vesicles. This property combined with the high quantum yields of these materials in the lipophilic environment meant that high quality high contrast images of the liposomes are produced even at very low concentrations of the probe.

In order to explore if the BODIPY derivatives showed any phase preference, GUVs composed of DOPC/BSM/Chol (4:4:2) were prepared. Betaneli *et al.* have shown that this composition produces phase separated GUVs and that an increase in the number of phase separated GUVs formed can be achieved by carrying out electroformation at higher temperatures, followed by cooling to room temperature.[50] This protocol was followed here.

The resulting phase separated GUVs are shown in Figure 2.2(B) labelled with Ld phase probe DiD.[6] The phase separated GUVs were prepared and labelled with Dppz-Ar-BODIPY and DiD or naphthyridyl-BODIPY-2-cholesterol and DiD, and the resulting structures were imaged using confocal fluorescence microscopy. Representative images are shown in Figure 2.2 that clearly demonstrate that both Dppz-Ar-BODIPY and naphthyridyl-BODIPY-2-cholesterol preferentially partition into the DOPC enriched Ld phase. The high quantum yields of these probes in non-aqueous environments and low aqueous emission mean concentrations in the low micromolar range are sufficient to yield high contrast images from the lipid phases, without background interference. This offers advantage over widely used reagents such as DiD which remains weakly fluorescent in water. Interestingly, whereas naphthyridyl-BODIPY-2-cholesterol appeared to be exclusively resident in the Ld phase,

Dppz-Ar-BODIPY whilst showing preference for Ld, also shows moderate fluorescence from the Lo phase. This is reflected in the fluorescence intensity plot shown in Figure 2.2(G) and is also evident in FLIM images as shown in Figure 2.2(H). The observed Ld partitioning preference is likely due to rotational conformation of the DPPZ ligand in relation to the BODIPY core about the phenyl linker. Similarly, the orthogonality of the cholesterol and BODIPY units may impede it's partitioning into the tightly packed Lo domains naphthyridyl-BODIPY-2-cholesterol. Even though the Ld phase is enriched with both cholesterol and SM, and cholesterol has shown a preference for raft domains in living cells.[51]

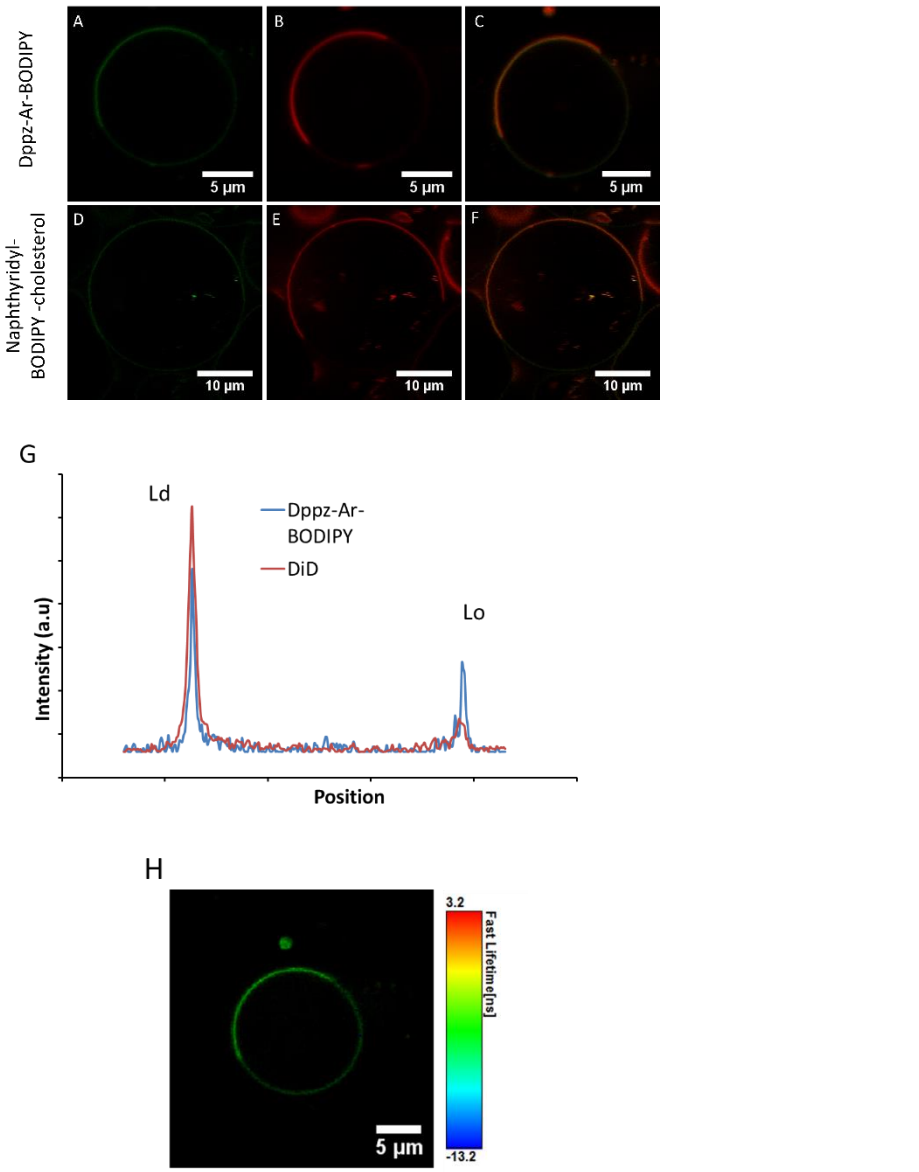

Figure 2.2 Confocal luminescent imaging of phase separated GUVs DOPC/ESM/Chol (4:4:2). GUV stained with compound Dppz-Ar-BODIPY (A), DiD (B) and overlay image (C). GUV stained with naphthyridyl-BODIPY-2-cholesterol (D), DiD (E) and overlay image (F). Fluorescent intensity plot of Dppz-Ar-BODIPY vs DiD, images A and B (G). Fluorescent lifetime image of Dppz-Ar-BODIPY in GUV DOPC/ESM/Chol (4:4:2) (H). Figures (A, B, C, D, E, F, G, H) are raw data images, without pre-processing.

2.4.5 FLIM and FLCS Studies in GUVs

It was recently reported for related BODIPY fluorophores that the fluorescent lifetime of the BODIPY probes is impacted by rotational diffusion of the substituent at the *meso* substituted phenyl unit from which an estimate of bilayer viscosity of GUVs could be obtained. From these viscosity measurements, using the Saffman Delbruk models convincing estimates of the diffusion values of the probes were obtained.[5]

To investigate the lifetimes of the present probes in GUVs we carried out fluorescence lifetime imaging. The benefit of lifetime imaging over intensity-based imaging is that it is independent of probe concentration. The false-colour image shown in Figure 2.2(H)shows the lifetime distributions of Dppz-Ar-BODIPY in GUV DOPC/ESM/Chol (4:4:2), the associated fitted lifetime data is shown in Table 2.2. The FLIM data from the GUVs fit best to a biexponential decay model. For the main component of the decay, the Dppz-Ar-BODIPY exhibits a lifetime of 3.46 ns, while naphthyridyl-BODIPY-2-cholesterol was 4.83 ns. The relatively short luminescent lifetimes of both probes mean they are oxygen independent. Therefore, any changes to the lifetime values can be attributed to the lipid environment and local viscosity.

Table 2.2 Fluorescent lifetimes and diffusion coefficients of Dppz-Ar-BODIPY and naphthyridyl-BODIPY-2-cholesterol in the GUVs, and in live CHO and HeLa cells

	Ex/Em	**GUV DOPC/SM/Chol 4/4/2 mol %**		**CHO**		**HeLa**		**GUV DOPC/SM/Chol 4/4/2 mol %**
	λ (nm)	**τ** (ns)	**τ_{Amp}** (%)	**τ** (ns)	**τ_{Amp}** (%)	**τ** (ns)	**τ_{Amp}** (%)	**Diffusion Coefficient D** ($\mu m^2\ s^{-1}$)
Dppz-Ar-BODIPY	498/511	τ_1 = 3.46 τ_2 = 0.62	60 40	τ_1 = 3.1 τ_2 = 4.5	84 16	τ_1 = 4.8 τ_2 = 2.6	81 19	4.18 ± 0.25
Naphthyridyl-BODIPY-2-Cholesterol	523/532	τ_1 = 4.83 τ_2 = 1.06	73 27	τ_1 = 5.5 τ_2 = 3.1 τ_3 = 1.1	60 31 9	τ_1 = 5.8 τ_2 = 3.0 τ_3 = 1.3	57 23 15	5.60 ± 0.43

Interestingly, the lifetime of the Dppz-Ar-BODIPY within the GUV was shorter than observed in either DCM or chloroform. Whereas on the basis of microviscosity, assuming the dielectric constant of the bilayer core is similar to chloroform, one would expect that the lifetime might increase within the bilayer, particularly given the Dppz-Ar-BODIPY does partition albeit less preferentially into the Lo phase. This may indicate that the Dppz unit is oriented into the bilayer with the BODIPY oriented closer to the bilayer aqueous interface where it is more exposed to the aqueous environment. Conversely, more in line with expectation, the fluorescent lifetime of naphthyridyl-BODIPY-2-cholesterol increased in GUVs compared to non-protic solvent from 3.66 ns and 4.20 ns in DCM and chloroform to 4.83 ns within the GUV. In both cases a short-lived component of the decay was observed at approximately 1 ns, the origin of this component is not clear but likely originates because the probes occupy more than one orientation at the bilayer. The shorter-lived component may arise from probe near the aqueous interface. Whereas one might expect a difference in lifetime of the probe between each phase this was not resolved for Dppz-Ar-BODIPY and so we can assume that the difference is small and by inference the quantum yield of the probe does not change substantially between the two phases. Thus we can exploit intensity measurements from Figure 2.2(G) to estimate the ratio of distribution of Dppz-Ar-BODIPY between the two phases as approximately 3:1. A key motivation in developing these probes was to evaluate their value as labels for FCS measurements. Ideally FCS probes should be capable of spontaneously partitioning into the bilayer and critically because of the very high susceptibility of this method to background interference, they should ideally either be highly localised to the region of interest, or, as in this case, only emit when at the region of interest.[52] This property, combined with their high quantum yields and photostability meant they were excellent FCS probes. This is reflected in the representative auto-correlation functions shown in Appendix A, which show high quality ACFs with little contribution from triplet formation and no evidence for photodecomposition.

Fitting the ACFs for each probe to equation (2.1) we obtained lateral diffusion coefficients within the phase forming DOPC/SM/Chol 4/4/2 mol% GUVs. The diffusion coefficient of Dppz-Ar-BODIPY was found to be 4.18 ± 0.25 $\mu m^2 s^{-1}$ while the diffusion coefficient of naphthyridyl-BODIPY-2-cholesterol was 5.60 ± 0.43 $\mu m^2 s^{-1}$. The distinction in diffusion coefficient for each probe is interesting as the composition of the GUV was identical in each

case. The value of 5.60 ± 1.0 $\mu m^2 s^{-1}$ for naphthyridyl-BODIPY-2-cholesterol is within the expected range for BODIPY probes in DOPC GUVs or in ternary GUVs at room temperature.[53–55] As described, for confocal imaging, Figure 2.2(D), naphthyridyl-BODIPY-2-cholesterol strongly localises to the DOPC rich region in phase separated GUVs. Conversely, Dppz-Ar-BODIPY was found to preferentially but not exclusively partition in the Ld region. Therefore, we attribute the lower diffusion coefficient observed for Dppz-Ar-BODIPY to contribution from the probe in the Lo phase. The diffusion value is indeed consistent with reports for BODIPY in this phase in ternary GUVs.[53,56]

2.4.6 Cell studies

Given the spontaneous uptake of the probes by GUVs and the high contrast images they produce from hydrophobic regions, we explored whether the probes are taken up by live cells and their distribution therein. Uptake studies of Dppz-Ar-BODIPY and naphthyridyl-BODIPY-2-cholesterol were assessed in both HeLa and CHO cells for a comparison of a cancer (HeLa) and non-cancer (CHO) cell lines. When added to live HeLa or CHO cells, both compounds are taken up instantaneously at the membrane and both Dppz-Ar-BODIPY and naphthyridyl-BODIPY-2-cholesterol cross the membrane of both cell lines within the first 5 minutes of exposure, (Figure S2.20–2.23). After 25 minutes, both probes had entered the cytoplasm and showed no affinity for any specific organelles. Figure 2.3 shows HeLa and CHO cells when incubated with 5 μM of Dppz-Ar-BODIPY and naphthyridyl-BODIPY-2-cholesterol for 24 h in the absence of light. The probes high quantum yields mean low μmol concentrations are enough for efficient staining leading to bright emission from within the cells without any background interference because of the probe water switch properties. To understand better the mechanism of uptake, the cells were incubated with the probes at 4 °C for 24 h. It was found that the probes were readily taken up by the cells under these conditions, indicating uptake is passive in nature, as expected given the lipophilicity of the probes (Figure S2.19).

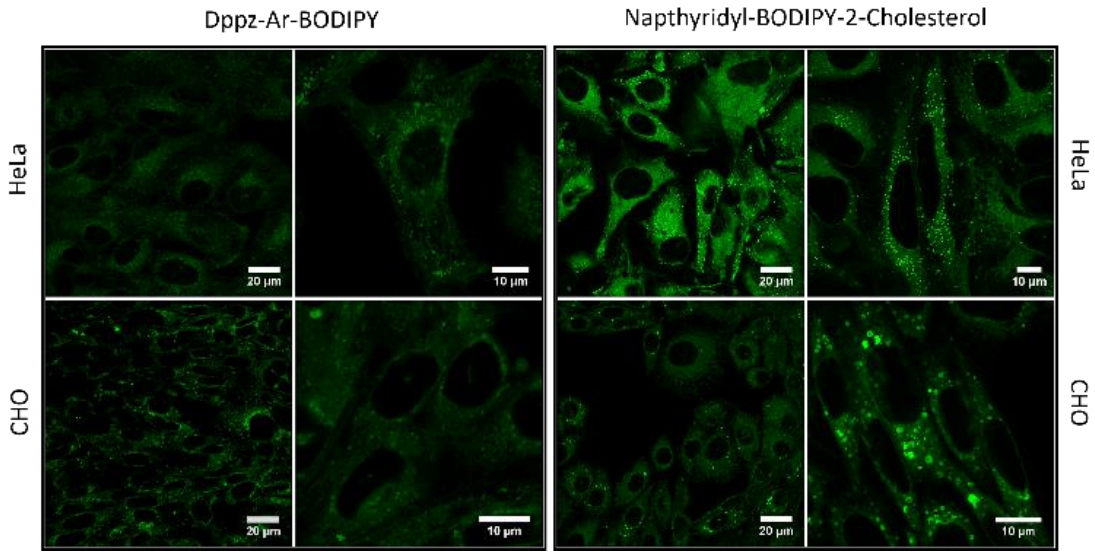

Figure 2.3 Confocal luminescent imaging of Dppz-Ar-BODIPY and naphthyridyl-BODIPY-2-cholesterol in HeLa and CHO cells. Cells were incubated with 5 μM for 24 h prior to imaging. In each case, a wide-field image and zoomed in image shows the distribution of the compounds in the cells throughout the sample.

Overall, Dppz-Ar-BODIPY did not emit as brightly as naphthyridyl-BODIPY-2-cholesterol from either cell line, which is expected based on their different quantum yields. Both Dppz-Ar-BODIPY and naphthyridyl-BODIPY-2-cholesterol are nuclear excluding, localising within the cell cytoplasm, but emitting only from hydrophobic structures. Dppz-Ar-BODIPY appears to bind non-selectively to cytoplasmic structures assumed to be membranous or proteinaceous in nature whilst naphthyridyl-BODIPY-2-cholesterol accumulates and emit intensely from spherical punctate regions of the cells characteristic of lipid droplets (LDs) in the cytoplasm with weaker background staining of membranous structures.[20,57,58] Naphthyridyl-BODIPY-2-cholesterol shows greater selectivity for LDs when compared to the lipophilic stain DiD which targets the general plasma membrane. LDs generally form as clusters in the cytoplasm that comprise of many smaller droplets, which corresponds to the localisation patterns observed here.[59] We recently observed this selective staining of lipid droplets in related water switchable BODIPY probes, and confirmed using Raman spectroscopy that the punctate features labelled were indeed LDs. Such selective labelling of LDs is useful as their overproduction in cells is linked to pathogenesis of inflammatory diseases, such as obesity, diabetes and atherosclerosis and also cancer cells proliferate such organelles.

Correspondingly, the pattern of LD staining by naphthyridyl-BODIPY-2-cholesterol between HeLa, a cancerous cell line, and CHO cells, a mammalian cell line, can be distinguished in Figure 2.3, which is representative of the general behaviour. On the basis of labelling the LDs are more numerous in the HeLa cells compared to CHO cells but the LDs form clusters in the latter. Cancer cells are known to show an increase in the biosynthesis of fatty acids in order to proliferate. For example, cholesterol metabolism pathways are modified in cancer cells where an increase in cholesterol levels are associated with tumour growth.[60] Excessive lipids and cholesterol levels in cancer cells are stored in LDs,[61] and recent findings suggest LDs may serve as an important energy source in cancer cells.[62] High numbers of LDs in tumours are now considered as hallmarks of cancer cells and how progressive they are.[10,63] For example, a higher number of LDs are seen in colon cancer cells and lung cancer cells (A549) compared to non-cancerous cells.[64] To further confirm localisation of naphthyridyl-BODIPY-2-cholesterol in the LDs, both HeLa and CHO cells were dual stained with Nile red. Nile red showed strong colocalisation with naphthyridyl-BODIPY-2-cholesterol in the LDs, shown in Figure 2.4. The corresponding x-y plot across a cluster of LDs in the cell shows the emission overlap of the two dyes in the LD regions.

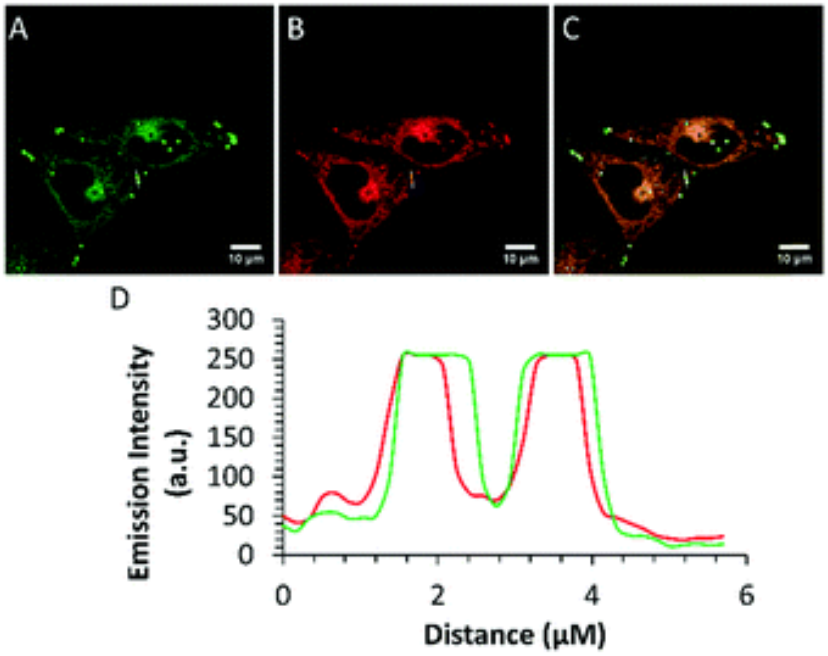

Figure 2.4 Confocal luminescent imaging of naphthyridyl-BODIPY-2-cholesterol in HeLa cells. Cells were treated with 5 μM for 24 h and 700 nM Nile red for 20 minutes naphthyridyl-BODIPY-2-cholesterol is shown in green (A), Nile red in red (B), and their colocalisation in yellow (C). The white cross-section and the corresponding distribution graph show their colocalisation over a cluster of lipid droplets (D).

The selectivity of naphthyridyl-BODIPY-2-cholesterol for LDs indicates that this luminophore is a useful probe for imaging the LD content of cells and perhaps in distinguishing such cells. The toxicity of Dppz-Ar-BODIPY and naphthyridyl-BODIPY-2-cholesterol were assessed using the resazurin assay over a 20 h exposure to a range of concentrations in the absence of light, shown in Figure 2.5, where the viability of the cells exposed to the compounds was compared the viability of control cells that were not exposed to the compounds but were treated in the same manner. It was found that both probes exhibited low toxicity toward HeLa cells but depending on concentration both were toxic toward CHO. Naphthyridyl-BODIPY-2-cholesterol showed a dose response cytotoxicity toward CHO becoming strongly cytotoxic above concentrations of 20 μmol. By contrast Dppz-Ar-BODIPY only became strongly cytotoxic above 50 μmol. The naphthyridyl-BODIPY-2-cholesterol showed low cytotoxicity at the concentration range, of 1 to 5 μM effective for imaging. The lack of toxicity of naphthyridyl-BODIPY-2-cholesterol particularly towards HeLa cells suggests that this compound is a suitable imaging probe of LDs in cancer cells. The

difference in toxicity between the CHO and HeLa cell lines may arise because the former is non-tumorigenic whilst the latter are tumorigenic. Tumor cells can show higher resistance to cytotoxic substances for a number of reasons but especially due to their upregulated expression of drug export proteins such as P-glycoprotein.[56] The low cytotoxicity of these materials toward cancer cell lines though should enable their use in long term monitoring of LD interactions in cancerous cells like HeLa, and permit study of their interactions with the other cell organelles such as the mitochondria, and the endoplasmic reticulum from where LDs are said to originate.[17,65]

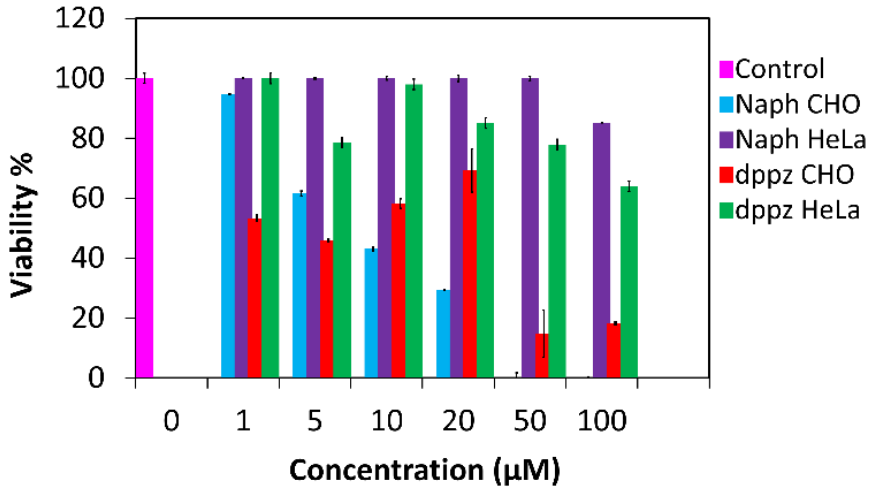

Figure 2.5 Cytotoxicity results of Dppz-Ar-BODIPY (dppz) and naphthyridyl-BODIPY-2-cholesterol (Naph) in HeLa and CHO cells over 20 h exposure to the compounds. Toxicity was measured using the Resazurin (Alamar Blue) assay (n = 3).

2.4.7 FLIM studies in cells

Fluorescence lifetime Imaging was carried out to evaluate the luminescent lifetimes of Dppz-Ar-BODIPY and naphthyridyl-BODIPY-2-cholesterol from within live cells. Figure 2.6 shows the false-colour FLIM images of both probes in HeLa and CHO cells. The average lifetimes observed outlined in Table 2.2, the FLIM obtained lifetimes conform to multiexponential decays and it is assumed that the contributing components reflects the different environments the probes occupy in the cell. Dppz-Ar-BODIPY exhibited two luminescent lifetimes from within the cells. Contrastingly, naphthyridyl-BODIPY-2-cholesterol fitted best to three lifetimes contributions. For the latter a short component; 1.3 ns in HeLa cells, and 1.1 ns in CHO cells is observed that is

not seen for Dppz-Ar-BODIPY in either cell type. As the probes were imaged under similar conditions, this contribution is unlikely to be attributed auto-fluorescence. Thus, we speculate it is due to probe occupying environments at hydrophilic/hydrophobic interfaces, as similarly short-lived components of the decay were observed for the probes in liposomes. The lifetimes and % amplitudes of each lifetime component are very similar for naphthyridyl-BODIPY-2-cholesterol in both CHO and HeLa. Whereas for Dppz-Ar-BODIPY, while the lifetimes of the two contributing components are very similar in each cell type; the longest component between 4.5 and 4.8 ns and the shorter at 2.6 to 3.1 ns. The percentage amplitude of each component is very different. The longer-lived component contributes approximately 80 % of decaying signal in HeLa compared with only 16 % in CHO.

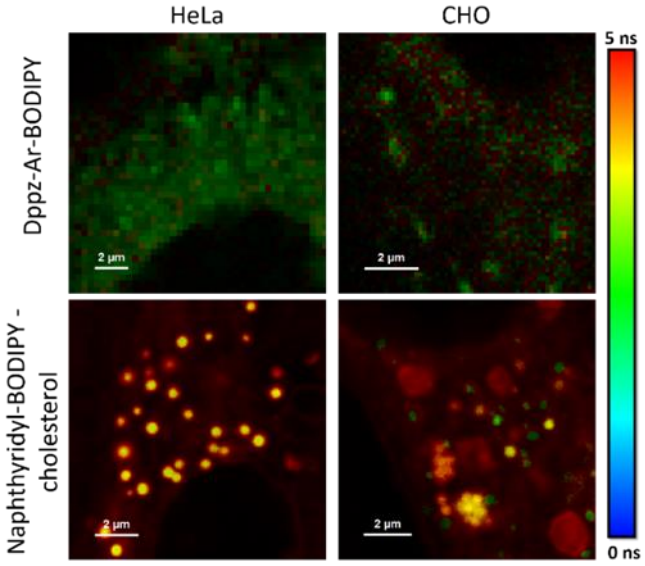

Figure 2.6 Fluorescence lifetime imaging microscopy (FLIM) of 3 and 7 in live HeLa and CHO cells. Cells were incubated with 5 µM for 24 h in the absence of light. FLIM image and lifetime were recorded with a 498 nm white light laser and the emission was collected using a band pass filter of 510–550 nm.

Consistent with steady state confocal imaging, live cell FLIM indicates that Dppz-Ar-BODIPY emits broadly from membranous structures throughout the cytoplasm, on the basis of FLIM it is difficult to discriminate LD and membrane contributions for this compound, Figure 2.6, top, although it is likely that the deviation in amplitude of the two contributions to the lifetime decay for this molecule may originate from the varying concentration of lipid droplets between cell type. In contrast, FLIM imaging for

naphthyridyl-BODIPY-2-cholesterol clearly demonstrates its localisation very specifically in LDs seen as orange spherical structures on a red background.

The cytoplasmic membranous structures are the origin of the longer lived 5.5 ns to 5.8 ns component of the decay while probe localised in LDs contribute most strongly to the shorter lifetime component of 3 ns. The longer lifetime from cytoplasmic membrane structures is consistent with the lifetime of the probe in the ternary GUVs The high lipid order as well as the cholesterol content in the cell membrane structures may also increase the lifetime of the probe.[66] The shorter lifetime of the probe within lipid droplets, which are expected to contain lipids such as triacylglycerols and phospholipids, may be due to the lower order of these regions compared to lipid membranes.[67]

2.5 Experimental

2.5.1 Synthesis of 11-bromo-dipyrido[3,2-a,2′,3′-c]phenazine (1)

Synthesised according to a reported method.[35] Yield: brown solid, 2.064 g (5.72 mmol, 77 %). ^{1}H NMR (600 MHz, $CDCl_3$) (ppm): 9.57 (t, *J* = 12 Hz, 2H); 9.30 (d, *J* = 6 Hz, 2H); 8.54 (s, 1H); 8.21 (d, *J* = 9 Hz, 1H); 8.00 (dd, *J* = 9, 2.2 Hz, 1H); 7.82–7.80 (m, 2H); ^{13}C NMR (DMSO-d_6) (ppm): 152.8, 152.7, 148.5, 148.3, 142.6, 141.5, 141.2, 141.0, 134.1, 133.7, 133.6, 131.6, 130.6, 127.2, 127.1, 124.8, 124.1.

2.5.2 Synthesis of Dppz-benzaldehyde (2)

11-Bromo-dipyrido[3,2-*a*,2′,3′-*c*]phenazine (**1**) (495 mg, 1.37 mmol), 4-formylphenylboronic acid (310 mg, 2.05 mmol) and dichloro[1,1′-bis(diphenylphosphino)ferrocene]palladium(II) complex with dichloromethane (59 mg, 0.068 mmol) was added to a mixture of toluene (20 mL) and ethanol (5 mL) and stirred, while being purged with nitrogen for 15 minutes. Following this K_2CO_3 (946 mg, 6.85 mmol) in water (10 mL) was added and the reaction mixture was heated at reflux for 24 h under nitrogen. The reaction mixture was then allowed to cool to room temperature and the crude product was concentrated to dryness via vacuum. The product was then dissolved in DCM and purified on neutral alumina by column chromatography using chloroform as the eluent. Yield: bright-yellow solid, 283 mg (0.732 mmol, 54 %). ^{1}H NMR (600 MHz, $CDCl_3$) (ppm): 10.07 (s, 1H); 9.56 (td, *J* = 4.2, 2.1 Hz, 2H); 9.21 (m, 2H); 8.53 (d, *J* = 1.8 Hz, 1H); 8.36

(d, *J* = 9 Hz, 1H); 8.14 (dd, *J* = 9, 2.4 Hz, 1H); 8.02 (d, *J* = 8 Hz, 2H); 7.96 (d, *J* = 8 Hz, 2H); 7.74–7.32 (m, 2H); ^{13}C NMR ($CDCl_3$) (ppm): 191.7, 152.9, 152.7, 148.5, 145.3, 142.7, 142.2, 141.7, 141.5, 136.0, 134.2, 133.8, 133.7, 131.6, 130.7, 130.5, 130.2, 130.0, 128.2, 127.6, 127.5, 127.4, 124.2. HR-MS (ESI-TOF) *m*/*z*: calculated for $C_{25}H_{15}N_4O$ $[M]^+$: 387.1233 found 387.1246.

2.5.3 Synthesis of Dppz-Ar-BODIPY (3)

Dichloromethane (60 mL) was purged with nitrogen for 30 minutes. To Dppz-Ar-Benzaldehyde **(2)** (307 mg, 0.794 mmol), 2,4-dimethylpyrrole (181 µL, 1.74 mmol) and TFA (cat) was added and stirred at room temperature for 5 h. Following this *p*-chloranil (236 mg, 0.96 mmol) in dichloromethane (20 mL) was added and the reaction mixture was stirred for 30 minutes followed by the addition of $BF_3{\cdot}OEt_2$ (2 mL) and Et_3N (2 mL). The reaction mixture was left to stir overnight. The crude mixture was washed with water (2 × 50 mL) and concentrated to dryness via vacuum. The crude product was purified on silica gel by column chromatography eluent: $CHCl_3$/MeOH/H_2O/CH_3COOH (80:18:2:1 v/v). Yield: dark-red solid, 140 mg (0.231 mmol, 29 %). ^{1}H NMR (600 MHz, $CDCl_3$) (ppm): 9.60 (t, *J* = 7.2 Hz, 2H); 9.22 (d, *J* = 1.8 Hz, 2H); 8.61 (d, *J* = 1.8 Hz, 1H); 8.42 (d, *J* = 3 Hz, 1H); 7.97 (d, *J* = 7.8 Hz, 2H); 7.77–7.75 (m, 2H); 7.45 (d, *J* = 7.8 Hz, 2H); 5.96 (s, 2H); 2.52 (s, 6H); 1.44 (s, 6H); ^{13}C NMR ($CDCl_3$) (ppm): 155.8, 152.7, 152.6, 143.2, 143.0, 142.6, 142.1, 141.7, 141.3, 140.9, 140.1, 135.3, 133.8, 131.3, 130.2, 130.1, 129.0, 128.2, 127.6, 127.5, 127.0, 124.2, 121.4, 118.9. HR-MS (ESI-TOF) *m*/*z*: calculated for $C_{37}H_{27}BF_2N_6$ $[M + H]^+$: 605.2329 found 605.2434

2.5.4 Synthesis of 1,3,5,7-tetramethyl-8-[(2-fluorophenyl)-6-methoxy-1,5-naphthyridine-3-ethylcarboxylate]-4,4′-difluoroboradiazaindacene (4)

Synthesised as previously reported.[42] Yield: brown solid, 300 mg (0.524 mmol, 54 %). ^{1}H NMR (400 MHz, $CDCl_3$) (ppm): 9.29 (s, 1H); 8.31 (d, *J* = 9.6 Hz, 1H); 7.48 (t, *J* = 7.4 Hz, 1H); 7.22 (s, 1H); 7.19 (d, *J* = 2 Hz, 1H); 7.16 (dd, *J* = 9.5, 1.5 Hz, 1H); 6.05 (s, 1H); 6.02 (s, 1H); 4.28 (m, 2H); 3.75 (s, 3H); 2.58 (s, 6H); 1.66 (s, 3H); 1.61 (s, 3H); 1.33 (t, *J* = 7.1 Hz, 3H).

2.5.6 Synthesis of naphthyridyl-BODIPY-2-formyl (5)

Phosphorous oxychloride (6 mL) was added dropwise to dimethylformamide (6 mL) in an ice batch for 5 minutes under nitrogen. The solution was allowed to warm to room temperature and stirred for 30 minutes. 1,3,5,7-Tetramethyl-8-[(2-fluorophenyl)-6-methoxy-1,5-naphthyridine-3-ethyl carboxylate]-4,4′-difluoroboradiazaindacene (**4**) (104 mg, 0.182 mmol) in dichloroethane

(30 mL) was added, the temperature raised to 50 °C and the reaction mixture was stirred for 2 h. Following this the reaction mixture was allowed to cool to room temperature and slowly poured over a saturated solution of K_2CO_3 (100 mL) in an ice-bath. The reaction mixture was once again allowed to warm to room temperature, stirred for 30 minutes and then washed with water (2 × 100 mL). The crude mixture was dried over $MgSO_4$ and dried under nitrogen. The crude product was purified on silica gel by column chromatography eluent: $CHCl_3$/MeOH/H_2O/CH_3COOH (80 : 18 : 2 : 1 v/v). Yield: dark-purple solid, 102 mg (0.169 mmol, 93 %). ^{1}H NMR (600 MHz, $CDCl_3$) (ppm): 9.98 (d, *J* =12 Hz, 1H); 9.32 (d, *J* = 4.8 Hz, 1H); 8.30 (dd, *J* = 12, 4 Hz, 1H); 7.52 (td, *J* = 11.4, 4.2 Hz, 1H); 7.20 (m, 3H); 6.21 (d, *J* = 12 Hz 1H); 4.29 (m, 2H); 3.76 (d, *J* = 13.8 Hz, 3H); 2.84 (d, *J* = 7.2 Hz, 3H); 2.64 (s, 3H); 1,91 (d, *J* = 21.6 Hz, 3H); 1.69 (d, *J* = 25.8 Hz, 3H) 1.35 (td, *J* = 10.8, 2.4 Hz, 3H); ^{13}C NMR ($CDCl_3$) (ppm): 155.8, 152.7, 152.6, 143.2, 143.0, 142.6, 142.1, 141.7, 141.3, 140.9, 140.1, 135.3, 133.8, 131.3, 130.2, 130.1, 129.0, 128.2, 127.6, 127.5, 127.0, 124.2, 121.4, 118.9. HR-MS (ESI-TOF) *m*/*z*: calculated for $C_{32}H_{29}BF_3N_4O_4$ $[M + H]^+$: 601.2259 found 601.2234.

2.5.7 Synthesis of naphthyridyl-BODIPY-2-carboxylic acid (6)

Naphthyridyl-BODIPY-2-formyl (**5**) (60.7 mg, 0.106 mmol) was added to a mixture of THF (6 mL) and water (2 mL) followed by the addition of $NaClO_2$ (95.8 mg, 1.06 mmol) and NH_2SO_3H (102.9 mg, 1.06 mmol). The reaction mixture was allowed to stir for 2 hours, following which it was diluted with ethyl acetate and washed using an aqueous solution of sodium thiosulfate (10 % w/v). The organic layer was collected and dried over $MgSO_4$. The product was concentrated to dryness. Yield: red-orange solid, 52.3 mg (0.084 mmol, 79 %). ^{1}H NMR (600 MHz, $CDCl_3$) (ppm): 9.34 (t, *J* = 4.3 Hz, 1H); 8.35–8.30 (m, 1H); 8.00–7.80 (2× dd, *J* = 8.4, 1.2, 9.6, 1.2 Hz, 1H); 7.44 (t, *J* = 7.8 Hz, 1H); 7.24–7.19 (m, 3H); 4.35–4.26 (m, 2H); 3.78 (d, *J* = 4.2 Hz, 2H); 3.73 (s, 1H); 2.88–2.65 (2× d, *J* = 1.2, 4.2 Hz, 3H); 1.96 (d, *J* = 24 Hz, 3H); 1.65 (d, *J* = 30 Hz, 3H); 1.39–1.34 (m, 3H); 1.25(s, 3H). ^{13}C NMR ($CDCl_3$) (ppm): 164.8, 162.6, 147.8, 139.6, 122.8, 118.6, 115.1, 61.7, 61.6, 53.7, 53.6, 29.6, 14.2, 13.8, 13.7, 13.5, 12.6, 12.3.

2.5.8 Synthesis of naphthyridyl-BODIPY-2-cholesterol (7)

To a stirred solution of 5 (50.3 mg, 0.0814 mmol,) and DMAP (1 mg, 0.00814 mmol) in DCM (4 mL), a solution of cholesterol (62.9 mg, 0.162 mmol) in DCM (2 mL) was added. The reaction mixture was stirred for 5 min at room temperature. A solution of DCC (18.4 mg, 0.089 mmol) in

DCM (2 mL) was added and the mixture was stirred at room temperature overnight. The crude mixture was concentrated to dryness via vacuum. The crude product was purified on silica gel by column chromatography eluent: DCM/MeOH (9 : 1). Yield: pink-red solid, 77.5 mg (0.078 mmol, 96 %). ^{1}H NMR (600 MHz, $CDCl_3$) (ppm): 9.31 (d, *J* = 3.6 Hz, 1H); 8.32–8.27 (m, 1H); 7.51 (q, *J* = 7.8 Hz, 1H); 7.41 (m, 1H); 7.23–7.16 (m, 3H); 4.32–4.26 (m, 3H); 3.78 (d, *J* = 4.2 Hz, 2H); 3.73 (s, 1H); 2.88 (d, *J* = 1.2 Hz, 2H); 2.66 (d, *J* = 4.2 Hz, 2H); 1.96 (d, *J* = 24 Hz, 3H); 1.65 (d, *J* = 30 Hz, 3H); 1.39–1.34 (m, 3H); 1.15–1.11 (m, 2H); ^{13}C NMR ($CDCl_3$) (ppm): 140.98, 121.94, 77.69, 72.03, 56.98, 56.37, 50.35, 49.41, 42.54, 42.52, 40.00, 39.73, 37.47, 36.72, 36.00, 34.16, 32.12, 31.89, 28.44, 28,23, 25.82, 25.12, 24.51, 23.03, 22.77, 21.30, 19.61, 18.93, 12.07. MALDI TOF MS LD+ calculated for $C_{59}H_{72}BF_3N_4O_5$: 984.6 found 980.6.

2.6 Conclusions

In summary, two novel lipophilic BODIPY fluorophores; Dppz-Ar-BODIPY and naphthyridyl-BODIPY-2-cholesterol that exhibit fluorescence only from non-aqueous environments were developed as probes of membranous and lipid structures in liposomes and cells. Both probes readily partition from aqueous solution into giant unilamellar vesicles (GUVs). Distribution of the probes in ternary domain forming GUVs showed that naphthyridyl-BODIPY-2-cholesterol partitions 100 % into Ld domains, whereas Dppz-Ar-BODIPY partitions preferentially into Ld domain at a ratio of Ld/Lo of approximately 3:1. The probes were demonstrated to be suitable for Fluorescence Correlation Spectroscopy where they exhibited diffusion coefficients in the domain forming GUVs of 4.18 ± 0.25 μm^2 s^{-1} and 5.60 ± 0.43 μm^2 s^{-1} reflecting the different distributions of the probes between Ld and mixed Lo/Ld respectively.

Both probes are readily cell permeable, taken up by passive diffusion into live HeLa and CHO cells where at low probe concentration they produce high contrast images selectively of the membranous regions of the cells. Naphthyridyl-BODIPY-2-cholesterol shows particularly high selectivity for lipid droplets within cells confirmed from both intensity and fluorescence lifetime imaging of the probes. Overall, these probes show excellent suitability as both lipid and membrane probes for biophysical and imaging applications. Although cytotoxic (towards non-cancer cells) at higher concentrations, under imaging conditions their cytotoxicity is low. The properties and selectivity of naphthyridyl-BODIPY-2-cholesterol suggests this probe is a useful marker for LDs

and in turn may find application in diagnosis and fundamental research into LD formation and fate which is still not fully understood.

2.7 Supporting Material

Supplementary data associated with this chapter can be found in Appendix A.

2.8 References

(1) Simons, K.; Ikonen, E. Functional Rafts in Cell Membranes. *Nature* **1997**, *387* (6633), 569.

(2) Pike, L. J. Lipid Rafts Bringing Order to Chaos. *J. Lipid Res.* **2003**, *44* (4), 655–667.

(3) Walde, P.; Cosentino, K.; Engel, H.; Stano, P. Giant Vesicles: Preparations and Applications. *ChemBioChem* **2010**, *11* (7), 848–865.

(4) Veatch, S. L.; Keller, S. L. Separation of Liquid Phases in Giant Vesicles of Ternary Mixtures of Phospholipids and Cholesterol. *Biophys. J.* **2003**, *85* (5), 3074–3083.

(5) Dent, M. R.; López-Duarte, I.; Dickson, C. J.; Geoghegan, N. D.; Cooper, J. M.; Gould, I. R.; Krams, R.; Bull, J. A.; Brooks, N. J.; Kuimova, M. K. Imaging Phase Separation in Model Lipid Membranes through the Use of BODIPY Based Molecular Rotors. *Phys Chem Chem Phys* **2015**, *17* (28), 18393–18402.

(6) Baumgart, T.; Hunt, G.; Farkas, E. R.; Webb, W. W.; Feigenson, G. W. Fluorescence Probe Partitioning between Lo/Ld Phases in Lipid Membranes. *Biochim. Biophys. Acta BBA - Biomembr.* **2007**, *1768* (9), 2182–2194.

(7) Cermelli, S.; Guo, Y.; Gross, S. P.; Welte, M. A. The Lipid-Droplet Proteome Reveals That Droplets Are a Protein-Storage Depot. *Curr. Biol.* **2006**, *16* (18), 1783–1795.

(8) Beller, M.; Thiel, K.; Thul, P. J.; Jäckle, H. Lipid Droplets: A Dynamic Organelle Moves into Focus. *FEBS Lett.* **2010**, *584* (11), 2176–2182.

(9) Farese, R. V.; Walther, T. C. Lipid Droplets Finally Get a Little R-E-S-P-E-C-T. *Cell* **2009**, *139* (5), 855–860.

(10) Accioly, M. T.; Pacheco, P.; Maya-Monteiro, C. M.; Carrossini, N.; Robbs, B. K.; Oliveira, S. S.; Kaufmann, C.; Morgado-Diaz, J. A.; Bozza, P. T.; Viola, J. P. Lipid Bodies Are Reservoirs of Cyclooxygenase-2 and Sites of Prostaglandin-E2 Synthesis in Colon Cancer Cells. *Cancer Res.* **2008**, *68* (6), 1732–1740.

(11) Bozza, P. T.; Bakker-Abreu, I.; Navarro-Xavier, R. A.; Bandeira-Melo, C. Lipid Body Function in Eicosanoid Synthesis: An Update. *Prostaglandins Leukot. Essent. Fat. Acids PLEFA* **2011**, *85* (5), 205–213.

(12) Mulay, S. V.; Yudhistira, T.; Choi, M.; Kim, Y.; Kim, J.; Jang, Y. J.; Jon, S.; Churchill, D. G. Substituent Effects in BODIPY in Live Cell Imaging. *Chem. - Asian J.* **2016**, *11* (24), 3598–3605.

(13) Dichlberger, A.; Schlager, S.; Kovanen, P. T.; Schneider, W. J. Lipid Droplets in Activated Mast Cells – a Significant Source of Triglyceride-Derived Arachidonic Acid for Eicosanoid Production. *Eur. J. Pharmacol.* **2016**, *785*, 59–69.

(14) Melo, R. C. N.; Weller, P. F. Lipid Droplets in Leukocytes: Organelles Linked to Inflammatory Responses. *Exp. Cell Res.* **2016**, *340* (2), 193–197.

(15) Greineisen, W. E.; Speck, M.; Shimoda, L. M. N.; Sung, C.; Phan, N.; Maaetoft-Udsen, K.; Stokes, A. J.; Turner, H. Lipid Body Accumulation Alters Calcium Signaling Dynamics in Immune Cells. *Cell Calcium* **2014**, *56* (3), 169–180.

(16) Dias, F. F.; Zarantonello, V. C.; Parreira, G. G.; Chiarini-Garcia, H.; Melo, R. C. N. The Intriguing Ultrastructure of Lipid Body Organelles Within Activated Macrophages. *Microsc. Microanal.* **2014**, *20* (03), 869–878.

(17) Digel, M.; Ehehalt, R.; Füllekrug, J. Lipid Droplets Lighting up: Insights from Live Microscopy. *FEBS Lett.* **2010**, *584* (11), 2168–2175.

(18) Somwar, R.; Roberts, C. T.; Varlamov, O. Live-Cell Imaging Demonstrates Rapid Cargo Exchange between Lipid Droplets in Adipocytes. *FEBS Lett.* **2011**, *585* (12), 1946–1950.

(19) Greenspan, P.; Mayer, E. P.; Fowler, S. D. Nile Red: A Selective Fluorescent Stain for Intracellular Lipid Droplets. *J. Cell Biol.* **1985**, *100* (3), 965–973.

(20) Spandl, J.; White, D. J.; Peychl, J.; Thiele, C. Live Cell Multicolor Imaging of Lipid Droplets with a New Dye, LD540. *Traffic* **2009**, *10* (11), 1579–1584.

(21) Kuerschner, L.; Moessinger, C.; Thiele, C. Imaging of Lipid Biosynthesis: How a Neutral Lipid Enters Lipid Droplets. *Traffic* **2008**, *9* (3), 338–352.

(22) Ranall, M.; Gabrielli, B.; Gonda, T. High-Content Imaging of Neutral Lipid Droplets with 1,6-Diphenylhexatriene. *BioTechniques* **2011**, *51* (1).

(23) Rumin, J.; Bonnefond, H.; Saint-Jean, B.; Rouxel, C.; Sciandra, A.; Bernard, O.; Cadoret, J.-P.; Bougaran, G. The Use of Fluorescent Nile Red and BODIPY for Lipid Measurement in Microalgae. *Biotechnol. Biofuels* **2015**, *8* (1), 42.

(24) Tirinato, L.; Liberale, C.; Di Franco, S.; Candeloro, P.; Benfante, A.; La Rocca, R.; Potze, L.; Marotta, R.; Ruffilli, R.; Rajamanickam, V. P.; et al. Lipid Droplets: A New Player in Colorectal Cancer Stem Cells Unveiled by Spectroscopic Imaging: Lipid Droplets: A New Player in Colorectal Cancer Stem Cells. *STEM CELLS* **2015**, *33* (1), 35–44.

(25) Ulrich, G.; Ziessel, R.; Harriman, A. The Chemistry of Fluorescent Bodipy

(26) Nastasi, F.; Puntoriero, F.; Campagna, S.; Olivier, J.-H.; Ziessel, R. Hybrid Complexes: Pt(II)-Terpyridine Linked to Various Acetylide-Bodipy Subunits. *Phys. Chem. Chem. Phys. PCCP* **2010**, *12* (27), 7392–7402.

(27) Loudet, A.; Burgess, K. BODIPY Dyes and Their Derivatives: Syntheses and Spectroscopic Properties. *Chem. Rev.* **2007**, *107* (11), 4891–4932.

(28) Ziessel, R.; Ulrich, G.; Harriman, A. The Chemistry of Bodipy: A New El Dorado for Fluorescence Tools. *New J. Chem.* **2007**, *31* (4), 496–501.

(29) Ziessel, R.; Bonardi, L.; Ulrich, G. Boron Dipyrromethene Dyes: A Rational Avenue for Sensing and Light Emitting Devices. *Dalton Trans.* **2006**, No. 23, 2913–2918.

(30) Strobl, M.; Rappitsch, T.; Borisov, S. M.; Mayr, T.; Klimant, I. NIR-Emitting Aza-BODIPY Dyes – New Building Blocks for Broad-Range Optical pH Sensors. *Analyst* **2015**, *140* (21), 7150–7153.

(31) Bessette, A.; Auvray, T.; Désilets, D.; Hanan, G. S. Non-Symmetric Benzo[b]-Fused BODIPYs as a Versatile Fluorophore Platform Reaching the NIR: A Systematic Study of the Underlying Structure–property Relationship. *Dalton Trans.* **2016**, *45* (18), 7589–7604.

(32) Müller, B. J.; Borisov, S. M.; Klimant, I. Red- to NIR-Emitting, BODIPY-Based, K+-Selective Fluoroionophores and Sensing Materials. *Adv. Funct. Mater.* **2016**, *26* (42), 7697–7707.

(33) Govender, T.; Ramanna, L.; Rawat, I.; Bux, F. BODIPY Staining, an Alternative to the Nile Red Fluorescence Method for the Evaluation of Intracellular Lipids in Microalgae. *Bioresour. Technol.* **2012**, *114*, 507–511.

(34) L, Y.; Y, L.; W, L.; C, M.; C, Z.; Y, L. Divinyl BODIPY Derivative: Synthesis, Photophysical Properties, Crystal Structure, Photostability and Bioimaging. *Bioorg. Med. Chem. Lett.* **2015**, *25* (24), 5716–5719.

(35) N. Deepika; C. Shobha Devi; Y. Praveen Kumar; K. Laxma Reddy; P. Venkat Reddy; D. Anil Kumar; Surya S. Singh; S. Satyanarayana. DNA-Binding, Cytotoxicity, Cellular Uptake, Apoptosis and Photocleavage Studies of Ru(II) Complexes. *J. Photochem. Photobiol. B* **2016**, *160*, 142–153.

(36) Jiang, X.-D.; Gao, R.; Yue, Y.; Sun, G.-T.; Zhao, W. A NIR BODIPY Dye Bearing 3,4,4a-Trihydroxanthene Moieties. *Org. Biomol. Chem.* **2012**, *10* (34), 6861.

(37) Papalia, T.; Lappano, R.; Barattucci, A.; Pisano, A.; Bruno, G.; Santolla, M. F.; Campagna, S.; Marco, P. D.; Puntoriero, F.; Francesco, E. M. D.; et al. A Bodipy as a Luminescent Probe for Detection of the G Protein Estrogen Receptor (GPER). *Org. Biomol. Chem.* **2015**, *13* (42), 10437–10441.

(38) Sarmento, M. J.; Pinto, S. N.; Coutinho, A.; Prieto, M.; Fernandes, F. Accurate Quantification of Inter-Domain Partition Coefficients in GUVs Exhibiting Lipid Phase Coexistence. *RSC Adv* **2016**, *6* (71), 66641–66649.

(39) Sezgin, E.; Levental, I.; Grzybek, M.; Schwarzmann, G.; Mueller, V.; Honigmann, A.; Belov, V. N.; Eggeling, C.; Coskun, Ü.; Simons, K.; et al. Partitioning, Diffusion, and Ligand Binding of Raft Lipid Analogs in Model and Cellular Plasma Membranes. *Biochim. Biophys. Acta BBA - Biomembr.* **2012**, *1818* (7), 1777–1784.

(40) Cosgrave, L.; Devocelle, M.; Forster, R. J.; Keyes, T. E. Multimodal Cell Imaging by Ruthenium Polypyridyl Labelled Cellpenetrating Peptides. *Chem Commun* **2010**, *46* (Journal Article), 103–105.

(41) Lira, R. B.; Steinkühler, J.; Knorr, R. L.; Dimova, R.; Riske, K. A. Posing for a Picture: Vesicle Immobilization in Agarose Gel. *Sci. Rep.* **2016**, *6*, 25254.

(42) Martin, A.; Long, C.; Forster, R. J.; Keyes, T. E. Near IR Emitting BODIPY F luorophores with Mega-Stokes Shifts. *Chem. Commun.* **2012**, *48* (45), 5617.

(43) Jiao, L.; Yu, C.; Li, J.; Wang, Z.; Wu, M.; Hao, E. β-Formyl-BODIPYs from the Vilsmeier−Haack Reaction. *J. Org. Chem.* **2009**, *74* (19), 7525–7528.

(44) Geng, H.; Hill, C. M.; Zhu, S.; Liu, H.; Huang, L.; Pan, S. Photoelectrochemical Properties and Interfacial Charge Transfer Kinetics of BODIPY-Sensitized TiO2 Electrodes. *RSC Adv.* **2013**, *3* (7), 2306–2312.

(45) Sawan, S. P.; James, T. L.; Gruenke, L. D.; Craig, J. C. Proton NMR Assignments for Cholesterol. Use of Deuterium NMR as an Assignment Aid. *J. Magn. Reson. 1969* **1979**, *35* (3), 409–413.

(46) Karolin, J.; Johansson, L. B.-A.; Strandberg, L.; Ny, T. Fluorescence and Absorption Spectroscopic Properties of Dipyrrometheneboron Difluoride (BODIPY) Derivatives in Liquids, Lipid Membranes, and Proteins. *J. Am. Chem. Soc.* **1994**, *116* (17), 7801–7806.

(47) Martin, A.; Byrne, A.; Dolan, C.; Forster, R. J.; Keyes, T. E. Solvent Switchable Dual Emission from a Bichromophoric ruthenium–BODIPY Complex. *Chem Commun* **2015**, *51* (87), 15839–15841.

(48) Friedman, A. E.; Chambron, J. C.; Sauvage, J. P.; Turro, N. J.; Barton, J. K. A Molecular Light Switch for DNA: $Ru(bpy)_2(dppz)^{2+}$. *J. Am. Chem. Soc.* **1990**, *112* (12), 4960–4962.

(49) Byrne, A.; Burke, C. S.; Keyes, T. E. Precision Targeted ruthenium(II) Luminophores; Highly Effective Probes for Cell Imaging by Stimulated Emission Depletion (STED) Microscopy. *Chem. Sci.* **2016**, *7* (10), 6551–6562.

(50) Betaneli, V.; Worch, R.; Schwille, P. Effect of Temperature on the Formation of Liquid Phase-Separating Giant Unilamellar Vesicles (GUV). *Chem. Phys. Lipids* **2012**, *165* (6), 630–637.

(51) Ahmed, S. N.; Brown, D. A.; London, E. On the Origin of Sphingolipid/cholesterol-Rich Detergent-Insoluble Cell Membranes: Physiological Concentrations of Cholesterol and Sphingolipid Induce Formation of a Detergent-Insoluble, Liquid-Ordered Lipid Phase in Model Membranes. *Biochemistry (Mosc.)* **1997**, *36* (36), 10944–10953.

(52) Basit, H.; Lopez, S. G.; Keyes, T. E. Fluorescence Correlation and Lifetime Correlation Spectroscopy Applied to the Study of Supported Lipid Bilayer Models of the Cell Membrane. *Methods* **2014**, *68* (2), 286–299.

(53) Ariola, F. S.; Li, Z.; Cornejo, C.; Bittman, R.; Heikal, A. A. Membrane Fluidity and Lipid Order in Ternary Giant Unilamellar Vesicles Using a New Bodipy-Cholesterol Derivative. *Biophys. J.* **2009**, *96* (7), 2696–2708.

(54) Macháň, R.; Hof, M. Lipid Diffusion in Planar Membranes Investigated by Fluorescence Correlation Spectroscopy. *Biochim. Biophys. Acta BBA - Biomembr.* **2010**, *1798* (7), 1377–1391.

(55) Przybylo, M.; Sýkora, J.; Humpolíckova, J.; Benda, A.; Zan, A.; Hof, M. Lipid Diffusion in Giant Unilamellar Vesicles Is More than 2 Times Faster than in Supported Phospholipid Bilayers under Identical Conditions. *Langmuir ACS J. Surf. Colloids* **2006**, *22* (22), 9096–9099.

(56) Kahya, N.; Scherfeld, D.; Bacia, K.; Schwille, P. Lipid Domain Formation and Dynamics in Giant Unilamellar Vesicles Explored by Fluorescence Correlation Spectroscopy. *J. Struct. Biol.* **2004**, *147* (1), 77–89.

(57) Lee, J. H.; So, J.-H.; Jeon, J. H.; Choi, E. B.; Lee, Y.-R.; Chang, Y.-T.; Kim, C.-H.; Bae, M. A.; Ahn, J. H. Synthesis of a New Fluorescent Small Molecule Probe and Its Use for in Vivo Lipid Imaging. *Chem. Commun.* **2011**, *47* (26), 7500.

(58) Yang, H.-J.; Hsu, C.-L.; Yang, J.-Y.; Yang, W. Y. Monodansylpentane as a Blue-Fluorescent Lipid-Droplet Marker for Multi-Color Live-Cell Imaging. *PLoS ONE* **2012**, *7* (3), e32693.

(59) Murphy, S.; Martin, S.; Parton, R. G. Lipid Droplet-Organelle Interactions; Sharing the Fats. *Biochim. Biophys. Acta BBA - Mol. Cell Biol. Lipids* **2009**, *1791* (6), 441–447..

(60) Lladó, V.; López, D. J.; Ibarguren, M.; Alonso, M.; Soriano, J. B.; Escribá, P. V.; Busquets, X. Regulation of the Cancer Cell Membrane Lipid Composition by NaCHOleate: Effects on Cell Signaling and Therapeutical Relevance in Glioma. *Membr. Struct. Funct. Relev. Cells Physiol. Pathol. Ther.* **2014**, *1838* (6), 1619–1627.

(61) Beloribi-Djefaflia, S.; Vasseur, S.; Guillaumond, F. Lipid Metabolic Reprogramming in Cancer Cells. *Oncogenesis* **2016**, *5* (1), e189.

(62) Roy, D.; Mondal, S.; Khurana, A.; Jung, D.-B.; Hoffmann, R.; He, X.; Kalogera, E.; Dierks, T.; Hammond, E.; Dredge, K.; et al. Loss of HSulf-1: The Missing Link between Autophagy and Lipid Droplets in Ovarian Cancer. *Sci. Rep.* **2017**, *7*, 41977.

(63) Yue, S.; Li, J.; Lee, S.-Y.; Lee, H. J.; Shao, T.; Song, B.; Cheng, L.; Masterson, T. A.; Liu, X.; Ratliff, T. L.; et al. Cholesteryl Ester Accumulation Induced by PTEN Loss and PI3K/AKT Activation Underlies Human Prostate Cancer Aggressiveness. *Cell Metab.* **2014**, *19* (3), 393–406.

(64) Koizume, S.; Miyagi, Y. Lipid Droplets: A Key Cellular Organelle Associated with Cancer Cell Survival under Normoxia and Hypoxia. *Int. J. Mol. Sci.* **2016**, *17* (9), 1430.

(65) Welte, M. A. Expanding Roles for Lipid Droplets. *Curr. Biol.* **2015**, *25* (11), R470–R481.

(66) Demchenko, A. P.; Mély, Y.; Duportail, G.; Klymchenko, A. S. Monitoring Biophysical Properties of Lipid Membranes by Environment-Sensitive Fluorescent Probes. *Biophys. J.* **2009**, *96* (9), 3461–3470.

(67) Song, Y. S.; Won, Y. J.; Kim, D. Y. Time-Lapse in Situ Fluorescence Lifetime Imaging of Lipid Droplets in Differentiating 3T3-L1 Preadipocytes with Nile Red. *Curr. Appl. Phys.* **2015**, *15* (12), 1634–1640.

Chapter 3: Linker Length in Fluorophore-Cholesterol Conjugates Directs Phase Selectivity and Cellular Localisation in GUVs and Live Cells

---

RSC Adv., 2019, **9**, 22805-22816

Darragh O' Connor, Aisling Byrne, and Tia E. Keyes.

Within this work I was the primary author and contributor to the experimental design, execution, analysis and preparation of this manuscript. I specifically contributed towards the following sections: synthesis and structural characterisation, photophysical characterisation and GUV preparation and partitioning studies. Cell studies were carried out by Dr. A. Byrne. Supporting information associated with this chapter can be seen in Appendix B.

3.1 Abstract

Lipid membrane fluorescent probes that are both domain-selective and compatible with demanding microscopy methods are crucial to elucidate the presence and function of rafts and domains in cells and biophysical models. Whereas targeting fluorescent probes to liquid-disordered (Ld) domains is relatively facile, it is far more difficult to direct probes with high selectivity to liquid-ordered (Lo) domains. Here, a simple, one-pot approach to probe-cholesterol conjugation is described using Steglich esterification to synthesise two identical BODIPY derivatives that differ only in the length of the aliphatic chain between the dye and cholesterol. In the first, BODIPY-Ar-Chol, the probe and cholesterol were directly ester linked and in the second BODIPY-Ahx-Chol, a hexyl linker separated probe from cholesterol. Uptake and distribution of each probe was compared in ternary, phase separated giant unilamellar vesicles (GUVs) using a commercial Ld marker as a reference. BODIPY-Ar-Chol targets almost exclusively the Ld domains with selectivity of >90 % whereas by contrast introducing the C_6 linker between the probe and cholesterol drove the probe to Lo with excellent selectivity (>80 %). The profound impact of the linker length extended also to uptake and distribution in live mammalian cells. BODIPY-Ahx-Chol associates strongly with the plasma membrane where it partitioned preferably into opposing micron dimensioned do-mains to a commercial Ld marker and its concentration at the membrane was reduced by cyclodextrin treatment of the cells. By contrast the BODIPY-Ar-Chol permeated the membrane and localised strongly to lipid droplets within the cell. The data demonstrates the profound influence of linker length in cholesterol bioconjugates in directing the probe.

3.2 Introduction

Lipid membranes of cells and their organelles are heterogenous and laterally organised into domains of different dimensions and composition. Amongst these, the existence and function of lipid rafts[1,2] in particular, remains controversial.[3–5] Rafts are believed to be tightly packed but mobile, cholesterol and sphingolipid-enriched, nano-platforms of liquid ordered lipid domain that diffuse laterally within the plasma membrane.[6] Lipid rafts are implicated in many important membrane-based functions, including protein trafficking and cell signaling.[3,7–10] They are often modelled in artificial membranes by using phase-separating lipid compositions containing sphingomyelin and cholesterol along with one or more low-melting phospholipid, to yield co-existing immiscible liquid phases. The two phases are liquid-disordered (Ld) phase and liquid-ordered (Lo) phase. The latter contains higher cholesterol (Chol) and sphingolipid content than Ld and is closer to a liquid-crystalline phase. The Ld phase exhibits a higher degree of lateral fluidity than the Lo phase which is more tightly packed and also less permeable than the Ld. Phase separated liposomes are widely used as models for raft behaviour in cell membranes, and the dimensions of the domains can be controlled by varying the identity and ratio of the lipid component.[11] However, although domains can be imaged fairly readily in model systems such as liposomes, rafts are far harder to reliably detect within cells using conventional fluorescence microscopy, due to their putative size and dynamic nature. In particular, imaging domains within cell membranes is challenging because probes that work well with liposomes, typically do not remain at the membrane but internalise unpredictably into the interior of live cells.

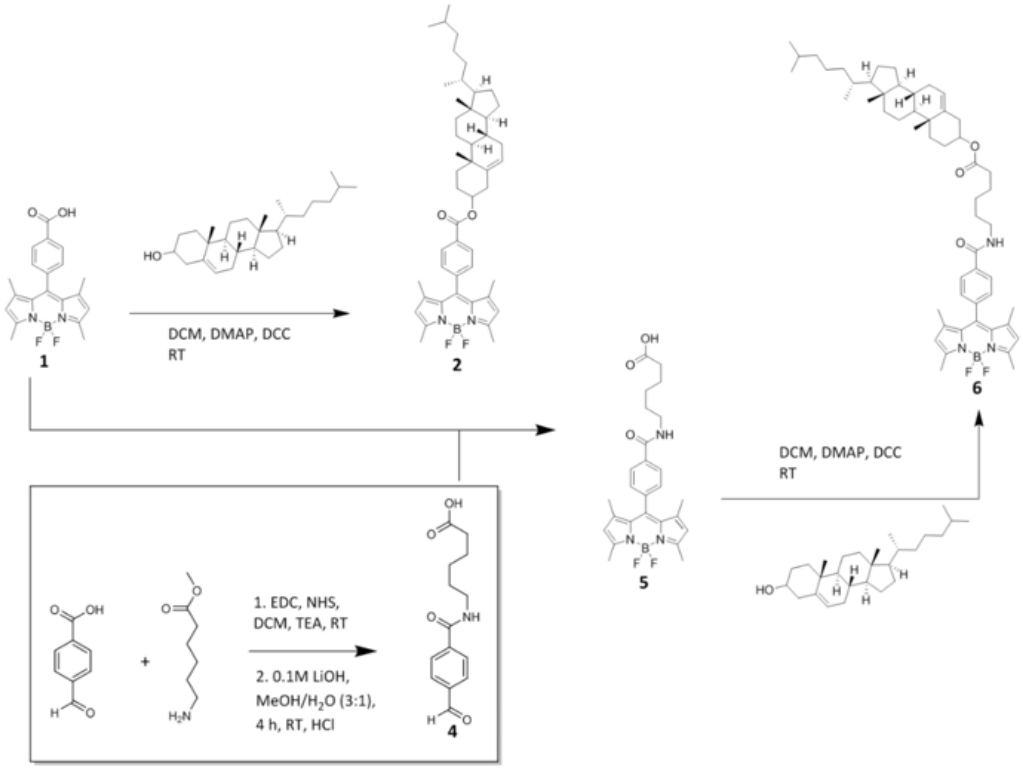

Scheme 3.1 Synthesis of BODIPY-Cholesterol Conjugates, BODIPY-Ar-Chol (**2**) and BODIPY-Ahx-Chol (**6**).

Although important advances have been made in detection of rafts through label free methods, including for example, through interferometric scattering microscopy imaging (iSCAT)[12], nano-secondary ion mass spectrometry nano(SIMS)[13] and AFM[14]. Fluorescence remains a key technique in many biophysical studies and probes that show phase partitioning can contribute to elucidation of domain structures. With recent advances in fluorescence microscopy, experiments that can directly monitor both temporally and dimensionally, rafts in cells, their organelles and associated models using fluorescence are within reach.[15] However, such experiments require luminescent probes that are compatible with the demands of the method and are both capable of preferential partitioning into L_o phases and in the case of live cells, of remaining localised at the membrane. There are relatively few probes that favour, with high specificity the Lo region. The majority of probes that show phase

preference, partition into the liquid disordered (Ld) phase. The most selective Lo partitioning probes reported, are based on polycyclic aromatic hydrocarbons.[16–18,19] whose planarity presumably permits intercalation into the tightly packed Lo lipid/sterol structure. Fluorescent cholesterol analogues have also been widely explored as fluorescent probes that favour the Lo phase. The fluorescent derivative cholestatrienol, for example, has been successfully used to probe membrane formation and structure[19], cholesterol trafficking[20] and sterol binding within human genes.[21] NBD-cholesterol and its derivatives have demonstrated lipid domain detection in both cells and models[22] and cholesterol distribution tracking in model membranes[23]. However, across PAHs and cholesterol analogues, the fluorophore excitation/emission is in the ultraviolet (UV)/blue spectral region[19], which typically is unsuitable for super-resolution imaging or correlation spectroscopy and there is limited opportunity for tuning their photochemical or photophysical properties without reducing their co-planarity. Non-PAH probes have been successfully driven to the Lo by appendage of a raft associating sterol or lipid, but discrimination typically, does not approach that achieved for Ld labelling.[21]

The 4,4-difluoro-4-bora-3a,4a-diaza-s-indacene (BODIPY) derivatives are excellent luminophores for bioimaging[22,23] with outstanding photophysical characteristics including sharp absorbance and emission features, high extinction coefficients, large quantum yields and photochemical robustness[24–27]. For these reasons, they have been widely applied to lipid membrane labelling in both artificial models and live cells[28–34]. Furthermore, due to the synthetic versatility of the BODIPY core and it's *meso*- positions it is amenable to bioconjugation. This has led to diverse families of BODIPY dyes that have found application in biological labelling.[35–39] Lipid tails or cholesterol have also been applied to the BODIPY to improve cell uptake[40–42] or to label lipid membranes.[21,43] The lipophilicity of the BODIPY core and its small size makes it attractive in this regard and indeed a number of BODIPY lipid conjugates are offered commercially for bio-imaging; for example, BODIPY FL C5-GM1, BODIPY PC and TopFLuor® BODIPY.

BODIPY modified with cholesterol and ganglioside GM1 have been applied as Lo membrane probes.[44] However, where they have shown tendency to sequester into both domains, they

have been domain sensitive rather than selective, where Lo discrimination is on basis of domain order or lifetime rather than selectivity.[18,45–47]

Such a complex was reported Kuimova et al[48], where appendage of a cholesterol to phenyl-BODIPY via a C_3 linker saw some partitioning into the Lo domain. As the parent phenyl-BODIPY partitions only to the Ld we were interested to see if incorporating additional carbons to the linker between the Chol and the probe might permit the Chol to localise at the Lo. If the distance was extended so that the hydrophobic BODIPY could orient at the partially hydrated boundary of bilayer core and hydrophilic interface. Comparing a directly linked cholesterol probe and analogue separated by a 6-carbon chain between cholesterol and phenyl BODIPY we observed that the former localises at the Ld while the latter shows strong preference for the Lo. The probes were prepared using a novel approach to cholesterol conjugation exploiting a one-step Steglich esterification which is very mild and less arduous than reported methods and should be widely applicable for cholesterol conjugation. Importantly, we found that the C_0 cholesterol probe was internalised into the cell, whereas the C_6 conjugate was retained at the living cell membrane where it appears to stain sterol-rich membranes distributing in a mutually exclusive way to Ld probe DiD.

3.3 Results and Discussion

3.3.1 Preparation of cholesterol conjugates

Scheme 3.1 illustrates the chemical structures and route to synthesis of the BODIPY-cholesterol conjugates. Cholesterol was appended to a BODIPY core via Steglich esterification either directly through the pendant carboxyl group or via a C_6 linker appended to the acid. Detailed synthetic protocols are described in the experimental section. In brief, precursor BODIPY-Ar-COOH (**1**),[49] was reacted with dimethylaminopyridine (1 equiv.), *N,N'*-dicyclohexylcarbodiimide (DCC) (1.1 equiv.) and cholesterol (2 equiv.) in DCM to yield BODIPY-Ar-Chol (**2**) at 38 % yield after chromatographic purification.

4-Formylphenyl-Ahx (**4**) was prepared by amide coupling of 4-formylbenzoic acid and 6-aminohexanoate, which was then hydrolysed to give **4**. Condensation of **4** with 2,4-dimethylpyrrole (2.2 equiv.) yielded BODIPY-Ahx (**5**). The cholesterol derivative BODIPY-

Ahx-Chol (**6**) was then simply prepared in 40.2 % yield using the same esterification method as **2**. Structural characterisation was carried out using high-resolution mass spectrometry, ^{1}H and ^{13}C NMR spectroscopy and can be found in Appendix B.

3.3.2 Conjugate Photophysical Characterisation

Figure S3.15 (Appendix B) shows the absorbance and emission profiles of BODIPY-Ar-Chol and BODIPY-Ahx-Chol in dichloromethane, chloroform, acetonitrile and methanol. Both derivatives exhibit the S_0-S_1 (π-π^*) transition centred at 500 ± 3 nm, and as expected, behaviour is nearly identical for both fluorophores across solvents.[50] Emission shifts to the red with decreasing dielectric constant, with the exception of BODIPY-Ahx-Cholesterol in acetonitrile which exhibited a slight red-shift compared to dichloromethane. BODIPY-Ar-Chol is insoluble in water whereas BODIPY-Ahx-Chol is weakly soluble but emission is extinguished in this medium.

Such behaviour, observed previously, in BODIPY derivatives, maybe due to aggregation induced quenching.51 Both compounds exhibit intense emission in organic media with quantum yields of ~40 % or greater with the exception of methanol where the quantum yield falls below 40 % for both compounds. Interestingly, BODIPY-Ahx-Chol shows consistently higher quantum yields across all solvents of the two compounds. And, correspondingly, BODIPY-Ar-Chol has a shorter fluorescence lifetime that decreases with increasing solvent polarity. The shortest lifetime for both compounds was in methanol, where τ is 2.25 ± 0.04 and 2.68 ± 0.002, whereas the longest lifetime was in chloroform, τ is 2.94 ± 0.002 and 3.27 ± 0.005 respectively. Photophysical data is summarised in Table 3.1.

Table 3.1 Summary of photophysical data

	Solvent	λ_{abs} (nm)	λ_{em} (nm)	ε (M^{-1} cm^{-1})	ϕ_{fl}	τ_{lum} (ns)	Dielectric Constatnt (ε_r)
BODIPY-Ar-Chol	Dichloromethane	501	513	63460	0.40	2.85 ± 0.008	8.93
	Chloroform	503	516	55484	0.45	2.94 ± 0.002	4.81
	Acetonitrile	498	511	49335	0.39	2.39 ± 0.009	36.6
	Methanol	498	513	44372	0.31	2.25 ± 0.04	32.6
BODIPY-Ahx-Chol	Dichloromethane	501	513	64345	0.50	3.10 ± 0.001	8.93
	Chloroform	503	518	102646	0.46	3.27 ± 0.005	4.81
	Acetonitrile	497	516	64332	0.43	2.98 ± 0.001	36.6
	Methanol	498	513	54070	0.39	2.68 ± 0.002	32.6

All solutions were measured at concentrations of 10 μM. Slit widths for emission were set to 2.5 nm. Lifetime data was recorded in triplicate. Quantum yields were measured using fluorescein 0.1_M NaOH (ϕ= 0.90)[40] a standard.

3.3.3 Partitioning and Photophysics in Giant Unilamellar Vesicles

Although widely distributed in the cell membrane, cholesterol is well-established as an essential component of detergent resistant membrane domains in cells and by extension in lipid rafts.[52] In model membranes cholesterol has been shown to promote formation of Lo domains and partitions with greater preference into these domains than the Ld.[53,54] The origin of cholesterol preference for Lo and its condensing effect on the membrane has been discussed widely in the literature.[55,56] The 'umbrella model' described by Huang and Feigenson[57] proposes cholesterol is shielded from unfavourable aqueous interaction by the headgroups of adjacent phospholipids which act as 'umbrellas'. Increasing cholesterol content causes reorientation of the phospholipids resulting in a more tightly packed and rigid bilayer. For sphingomyelin containing compositions, H-bonding interactions of cholesterol with SM are also thought to play a role in phase preference. In principle, this preference makes cholesterol an attractive appendage to drive labels to the Lo domains of phase separated membranes.

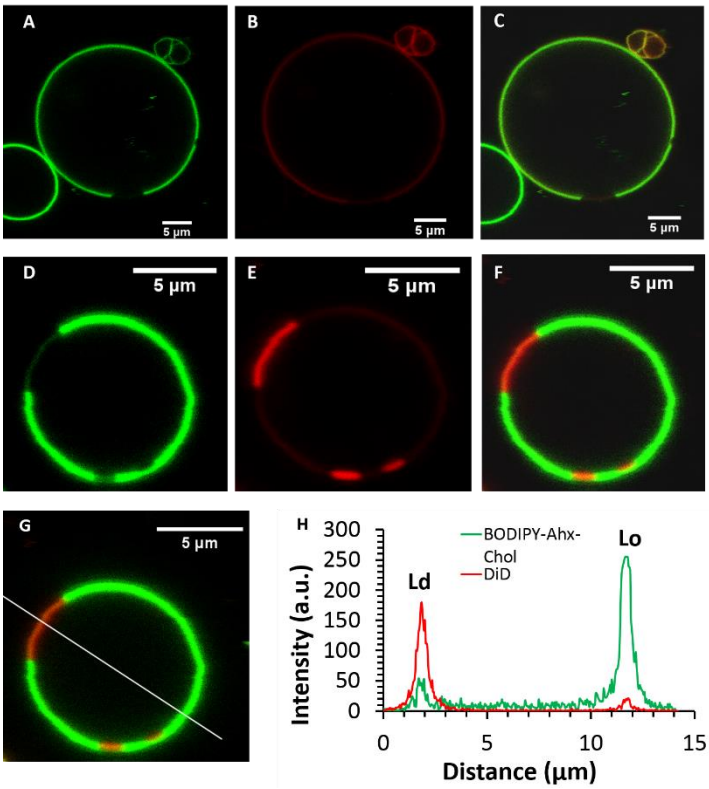

Figure 3.1 Confocal fluorescent imaging of phase separated GUVs DOPC/ BSM/Chol (4:4:2) mol %. GUV stained with compound BODIPY-Ar-Chol (A), DiD (B) and overlay image (C). GUV stained with BODIPY-Ahx-Chol (D), DiD (E) and overlay image (F). Figures (A–F) are raw data images, without pre-processing. Fluorescence intensity plot of BODIPY-Ahx-Chol (—) vs DiD (—) (G, H). Fluorescent lifetime image of BODIPY-Ahx-Chol(I) in a phase separated GUV of composition DOPC/BSM/Chol (4:4:2) with variation in lifetimes given by the colour bar. Fluorescent lifetime image of the difference in lifetime given by colour (Ld region = orange/yellow) and (Lo region = green). A 503 nm white light laser was used to excite the GUV samples and the emission collected between 511-570 nm.

But, conjugation of bulky fluorophore to cholesterol can prevent proper insertion and block e.g. H-bonding interactions or shielding between the cholesterol and adjacent phospho- and sphingolipids due to steric or electrostatic interference. In order to investigate whether such steric affects could be overcome by extending a lipophilic alkyl spacer between the Chol and probe we introduced C_6 linker between cholesterol and fluorophore (**6** in scheme 3.1) and compared the phase distribution of this probe with one in which the cholesterol was directly ester linked to the probe carboxyl (**2** in Scheme 3.1). It is worth noting that by conjugating a cholesterol onto a fluorophore via the lone hydroxyl group it is unlikely that the fluorescent cholesterol derivatives will have the same characteristics of cholesterol especially behaviour at the bilayer interface, where typically the hydroxyl group is most exposed at the interface.

To evaluate the phase distribution of each derivative, electroformed, phase-separated GUVs of composition DOPC/BSM/Chol (4:4:2 mol %), were incubated with BODIPY-Ar-Chol and DiD or BODIPY-Ahx-Chol and DiD. The resulting structures were imaged using confocal fluorescence microscopy (Figure. 3.1). Notably, each probe distributed preferentially into the opposing phase. To identify the Ld phase, DiD a commercial Ld probe was included at a concentration of 0.1 mol % of lipid content prior to electroformation.[19]

In separate studies (Figure S3.16) we confirmed that there is no cross-talk between DiD and the BODIPY probes. Figure 3.1A-C shows that BODIPY-Ar-Chol partitions almost exclusively into the Ld phase of the GUVs, where it colocalises with DiD. Remarkably, Figure 3.1D-F shows that BODIPY-Ahx-Chol associates preferentially to the Lo domains, where DiD is absent. The oppositional partitioning of the two probes is reflected also in the intensity profiles shown in Figure 3.1H. As discussed below, the probes show within experimental error, negligible difference in quantum yield when localised at Lo or Ld, we can assume that the fluorescence quantum yield is unaffected by phase. On this basis we can roughly approximate the Lo partitioning on the basis of intensity for BODIPY-Ahx-Chol as (% Lo ~80 %) (Figure S3.23) and the BODIPY-Ar-Chol partitioned to the Ld at ~90 %. The former may be an overestimate of BODIPY-Ahx-Chol Lo association, as although lifetimes are unchanged, xy scans of Lo and Ld associating probes in liposomes, prepared under the same probe concentrations suggest the probe at the Lo probe is slightly brighter than the Ld.

The GUVs were imaged by fluorescence lifetime imaging (FLIM) to evaluate the effect of domain on probe photophysics. As described, in solution, emission from both probes fit to mono-exponential decay kinetics. On partitioning into the lipid membrane of the GUVs, the BODIPY emission decayed according to a biexponential model irrespective of the phase into which the probe partitioned. The lifetime data is summarised in Table 3.2. The short component of the decay was within experimental error the same for both probes at 1.7 ns constituting 30 to 40 % of the amplitude of the decay. Its origin is unclear but similar effects have been noted previously in membrane bound probes and particularly molecular rotors attributed to a fraction of probe that is associated/oriented at the liposomes in such a way that it is strongly exposed to the less viscous membrane interface.[48] The dominant component of the decay (> 50 % of the amplitude for both probes) was longer lived. For BODIPY-Ar-Chol

fluorescence lifetime was determined as 4.74 ns from the Ld phase. By comparison for BODIPY-Ahx-Chol, localised at the Lo, the long component of the lifetime was recorded as 4.92 ns (Figure 3.2). The decay was confirmed from the Lo, by labelling with DID.

Recalling that in chloroform BODIPY-Ar-Chol and BODIPY-Ahx-Chol exhibit emission decays of 2.94 and 3.27 respectively. Both dyes show a significant increase in emission lifetime on association with GUV attributed to the membrane rigidity/increased micro-viscosity. Similar behaviour has been reported in other probes incorporated into liposomes.[18,46,58]

Because of the very high selectivity of each probe for their respective phases, we were unable to obtain reliable lifetime data from FLIM for the probes in the opposing phases. However, in previous reports, where probe associates with Lo as well as at Ld domains, it has been noted that the increased lipid order/rigidity of the Lo often reduces non-radiative decay to a greater extent than in Ld leading to notably longer emission lifetimes from this domain.[19] In a BODIPY cholesterol probe linked through a C_2 linker Heikal *et al* reported that the probe partitioned into both Lo and Ld phases and that the lifetime was longer from the Lo, with FLIM results also indicating a stronger preference for Lo domains .[46]

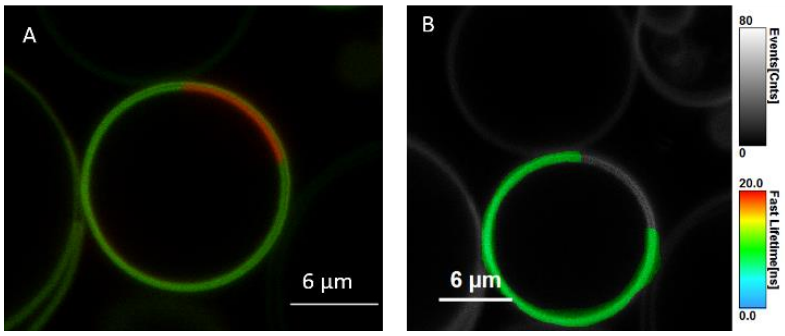

Figure 3.2 Confocal fluorescent image of a phase separated GUV of composition DOPC/BSM/Chol (4:4:2 mol %) co-stained with BODIPY-Ahx-Chol (green) and DiD (red) showing the different Ld (red) and Lo phases (green) (A). Fluorescent lifetime image (FLIM) of the same GUV showing BODIPY-Ahx-Chol in the Lo phase.

Thus, one might have expected a significant increase in lifetime of Lo associated BODIPY-Ahx-Chol given that its emission is already notably longer lifetime in chloroform than BODIPY-Ar-Chol. The negligible difference observed between BODIPY-Ar-Chol in the Ld and BODIPY-Ahx-Chol in the Lo thus seems initially counter-intuitive. However, we

speculate that the similarity in lifetimes between each probe in opposing phases arises because the BODIPY unit cannot intercalate deeply into Lo. It associates only when the linker is long enough between the cholesterol anchor and the fluorophore, to allow the cholesterol to partition while the probe orients at the interface of the bilayer with shallow penetration where photophysics are not strongly impacted by the rigidity of the Lo domain.

3.3.4 Cell Studies

Cell membranes contain cholesterol and sphingolipid enriched microdomains, that are resistant to non-ionic detergent solubilisation. These detergent-resistant membranes (DRMs) have many of the characteristics of the liquid-ordered (Lo) phase in model membranes. Given the strong selectivity of BODIPY-Ahx-Chol probes for Lo domains in GUVs, we investigated if this phase preference extended to its distribution in living cells and if we could distinguish membrane domain distributions in a cancer and non-cancer cell line.

Figure 3.3 shows confocal fluorescence images of live HeLa and CHO cells following their incubation with BODIPY-Ahx-Chol (5 μM) at 37 °C for 3 h. The imaging indicates that the probe localises at the plasma membranes. From z-scanning it is evident that BODIPY-Ahx-Chol also permeates the cell as emission can be seen from membranous regions therein, but it is excluded from the nucleus. To examine BODIPY-Ahx-Chol distribution in the membrane we focused on the lower cell membrane which is intensely but highly heterogeneously fluorescent.[59–61] In HeLa cells (Fig 3.3 A,B) discontinuous patches of sub-200 nm to 1 μm length as well as more ordered ringed structures are intensely fluorescently labelled. However, in addition dark, unlabelled regions of comparable dimensions (white arrows) are evident across the membrane.

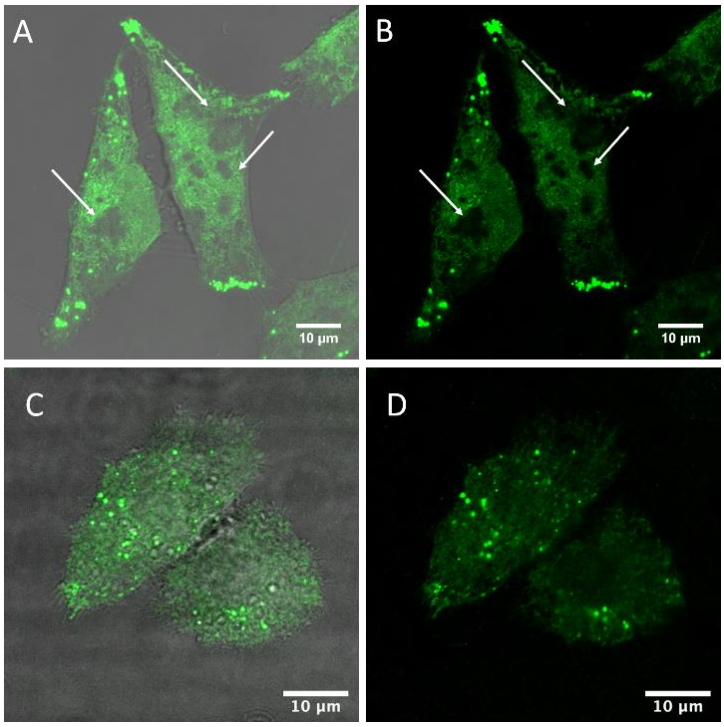

Figure 3.3 Live HeLa (A,B) and CHO cells (C,D) stained with BODIPY-Ahx-Chol (5 µM, 3 h 37 °C). White arrows highlighting the dark regions where BODIPY-Ahx-Chol does not localise. A,C overlay of BODIPY-Ahx-Chol and background channels. B,D BODIPY-Ahx-Chol channel.

On co-staining cells with DiD (800 nM) it was observed that, as at GUVs, BODIPY-Ahx-Chol and DiD distributed in a mutually exclusive way in the cell membrane. This is most obvious in HeLa cells where Figure 3.4A-C shows that DiD localises in the regions of the cell membrane from where BODIPY-Ahx-Chol is excluded.

The membranes of live cells are so complex that it is difficult to ascertain definitively what is labelled. Given the propensity for the probe to stain sterol-rich domains/regions and the fact that DiD is excluded from many of the regions that BODIPY-Ahx-Chol is localised suggests it is localising at sterol-rich domains. This may include Lo phases as well as caveolae at the cell membrane, protein aggregated domains and membrane bound protein. The staining is highly heterogenous and structured, over a range of sizes, that are difficult to resolve with confocal imaging.[60] Interestingly, when incubated with BODIPY-Ahx-Chol under identical conditions, CHO cells did not show the same distribution as shown in Figure 3.3C, D. The probe emission from the membrane is weaker but appears to distribute more homogenously across the membrane with less well defined bright and dark regions. Staining

of lipid droplets are evident as intense spherical features, in both CHO and HeLa images, this was confirmed from z-scanning which showed the features persisted outside the membrane.

The difference between probe distribution we attribute to different membrane compositions between the two cell lines as HeLa is a cancer line and CHO a mammalian non-cancer line. The cholesterol concentration within the cell membrane is highly regulated and has been shown to be significantly upregulated in many cancers leading to increased lipid order, and caveolae are often highly prevalent in cancer cell lines. In particular, detergent resistant/raft-like domains have been shown to be particularly prevalent in multidrug resistant cancer cell lines.[62–64] The distinctive membrane compositions lead to greater lipid order in the HeLa membrane compared to CHO. Of note, for BODIPY-Ar-Chol in the absence of the C_6 linker, the probe shows markedly different uptake and distribution. In both HeLa and CHO cells it permeates the membrane and localises with high selectively into lipid droplets (Figure S3.19). When co-stained with DiD, and focusing on the plasma membrane of the cell, no emission from BODIPY-Ar-Chol could be observed (Figure S3.20), confirming that without the linker, the complex does not localise in the plasma membrane in live cells.

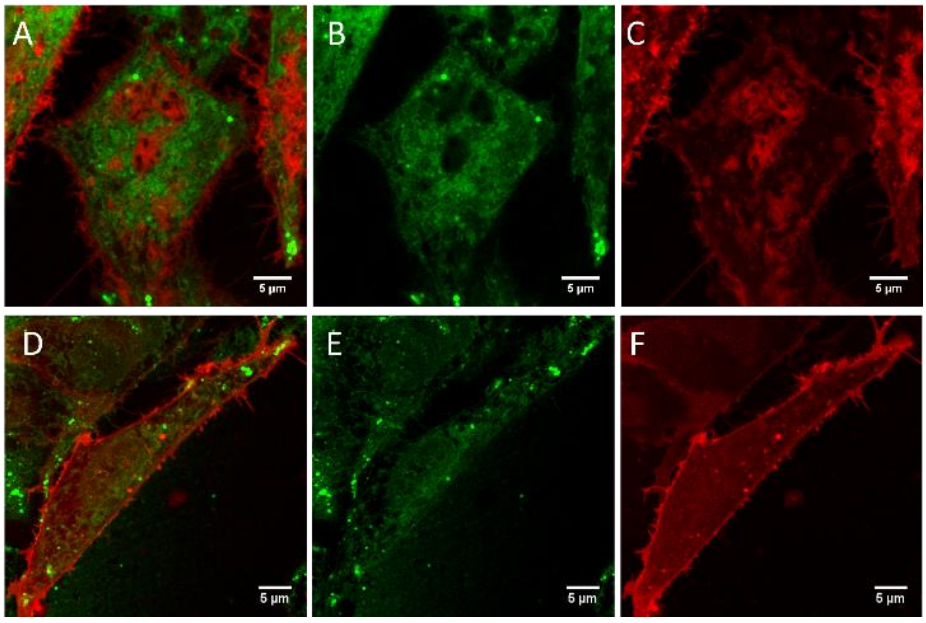

Figure 3.4 Live HeLa (A,B,C) and CHO cells (D,E,F) stained with BODIPY-Ahx-Chol and co-stained with DiD, (800 nM). Overlay of channels (A,D), the BODIPY-Ahx-Chol channel in green (B,E) and the DiD channel in red (C,F).

3.3.5 Probing Cholesterol in the Cell Membrane

In order to understand further if the BODIPY-Ahx-Chol localises in cholesterol-rich domains at HeLa and CHO cells, we examined if the presence of cholesterol in the membrane affected dye distribution. This was achieved by treating the cells with methyl-β-cyclodextrin (MβCD) which is widely used for cholesterol depletion from the plasma membrane, as it forms soluble host-guest inclusion complexes with cholesterol with high affinity.[46,65] It can also deplete lipids from the membrane but typically to a significantly lower extent than cholesterol.[66] Cells were initially exposed to MβCD (10 mM) for 1 hour in cell media, then removed and washed prior to adding the BODIPY-Ahx-Chol (5 μM) to the cells. Following probe exposure, the cells were washed and imaged without fixing. Figure 3.5A, B show HeLa cells after 2 h exposure to MβCD stained with BODIPY-Ahx-Chol. Focusing on the lower plasma membrane of the cell as before, after 2 hours, emission is still observed from the membrane and dark/unstained regions remain visible, similar to the non-cholesterol depleted cells (Figure 3.3A, B) however emission overall is less intense, and heterogeneity of the emission is much less defined.

Furthermore, emission for BODIPY-Ahx-Chol also appears to have migrated to the plasma membrane periphery, with bright spots located along the cell membrane. A similar pattern of behaviour has been reported for other ordered-domain sequestering probes upon cholesterol depletion with MβCD.[67] After 4 h of MβCD cholesterol depletion, the dark regions completely disappear, and the emission intensity of BODIPY-Ahx-Chol although more homogeneously distributed has decreased (4.6 a.u. to 3.3 a.u. intensity), shown in Figure 3.5 E,F.

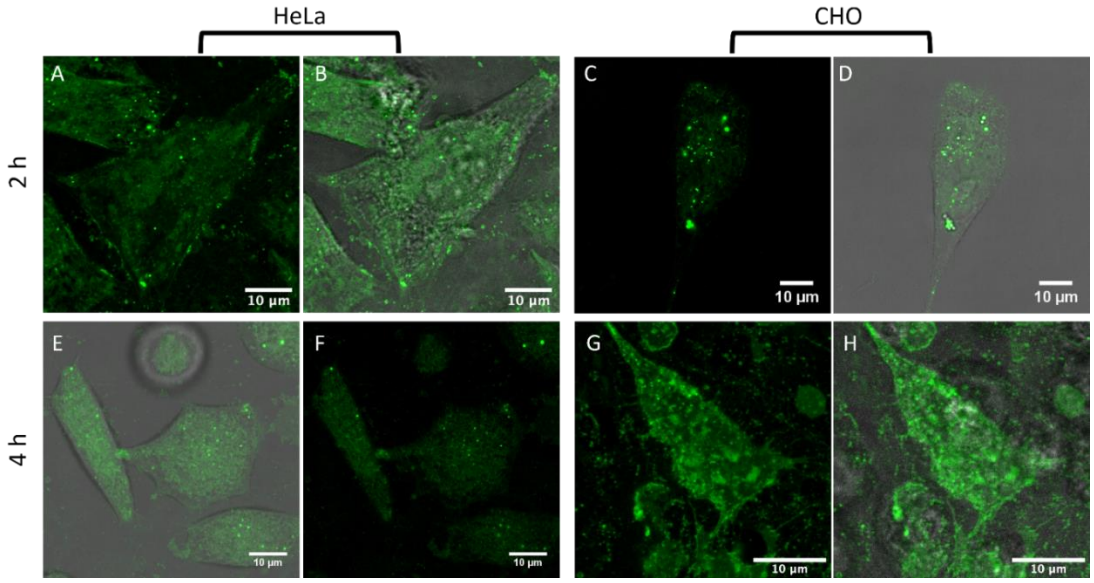

Figure 3.5 Live HeLa and CHO cells treated with MβCD. Cells were treated with 10 mM MβCD and after 2 h (A,B HeLa, C,D CHO) and 4 h, altering the cholesterol distribution in HeLa cells (E,F) and CHO cells (G,H). A,C,E,G showing the BODIPY-Ahx-Chol channel, and B,D,F,H showing the overlay of BODIPY-Ahx-Chol and background channels.

Overall, our data suggests that BODIPY-Ahx-Chol uptake to the cell membrane is greater at the cholesterol rich cell membrane of HeLa cells and that the probe associates in part, with cholesterol rich domains at the membrane of HeLa cells. The distribution observed here is also similar to that reported by Malim *et al*[68] and Yoshida *et al*[69] in HeLa cells. This is consistent with literature where between 50 and 80 % of cell membranes have been shown on the basis of detergent solubilisation resistance or fluorescence polarisation to be cholesterol rich raft-like domains.[8,70]

In the case of CHO cells, treatment with MβCD appears to have an opposite effect, where emission intensity Figure 3.5 G, H from the CHO membrane post treatment (3.9 a.u. to 6.9 a.u. intensity) increases. It is not clear why behaviour in the two cell lines on cholesterol depletion is so different, but our observations concur with data reported by Hao *et al*[67] who observed similar behaviour in CHO cells, that they speculated might be due coalescence of cholesterol bounded domains into microdomains on MβCD treatment.

Fluorescent lifetime imaging was carried out to evaluate the lifetime of BODIPY-Ahx-Chol from within live cells to gain further insight into the probe distribution in the membrane. Figure 3.6 show the false-color FLIM images of the lifetime distributions within the cell. The

fluorescent decay in cells fit to a bi-exponential decay, although in some cases a third component of the fit (lifetime <70 ps) was required to account for autofluorescence/background scatter (Table S3.1).

Table 3.2 Fluorescent lifetime of BODIPY-Ar-Chol and BODIPY-Ahx-Chol within phase separated GUVs containing both liquid-disordered and liquid-ordered domains, as well as live HeLa cells.

	Ex/Em	**GUV DOPC/SM/Chol 4/4/2 mol %**		**HeLa Cells**	
	λ (nm)	**τ** (ns)	**τ_{Amp}** (%)	**τ** (ns)	**τ_{Amp}** (%)
BODIPY-Ar-Chol (Ld phase)	503/511-570	$\tau_1 = 4.74 \pm 0.17$ $\tau_2 = 1.77 \pm 0.15$	57 43	- -	- -
BODIPY-Ahx-Chol (Lo phase)	503/511-570	$\tau_1 = 4.92 \pm 0.04$ $\tau_2 = 1.74 \pm 0.15$	54 46	$\tau_1 = 5.85 \pm 0.15$ $\tau_2 = 2.31 \pm 0.37$	67 33

The majority of the longer-lived components comes from the membrane structures, and notably, BODIPY-Ahx-Chol has a slightly longer lifetime of 5.85 ns in HeLa cells (Figure 3.6A) compared to 5.3 ns in CHO cells (Figure 3.6B). This is consistent with the higher content of cholesterol at the HeLa membrane which may contribute different phase distributions within the membrane. Comparing these lifetimes to those derived from GUVs, the longer lifetime of 4.9 ns is shorter than that observed in cells presumably reflecting the far greater complexity of the cell membrane, its diversity of lipids and roughly 50 % in dry weight, protein at the membrane interface. Interestingly, after exposure to MβCD, the longer-lived component of 5.85 ns in HeLa cells decreases to 5.35 ns while the shorter component of 2.31 ns is not affected.

However, in CHO cells, the lifetime of the major component increases post MβCD treatment (Table S3.1). This data reflects the confocal images where in CHO cells the lipid regions appear to cluster together upon cholesterol redistribution, this is not observed for HeLa cells. For HeLa cells, most of the long-lived component continues to arise from the membrane post MβCD treatment, and the shorter lifetime of 2.23 ns is attributed to lipid droplet structures from inside the cells, which was observed in both confocal and FLIM images (Fig 3.6C).

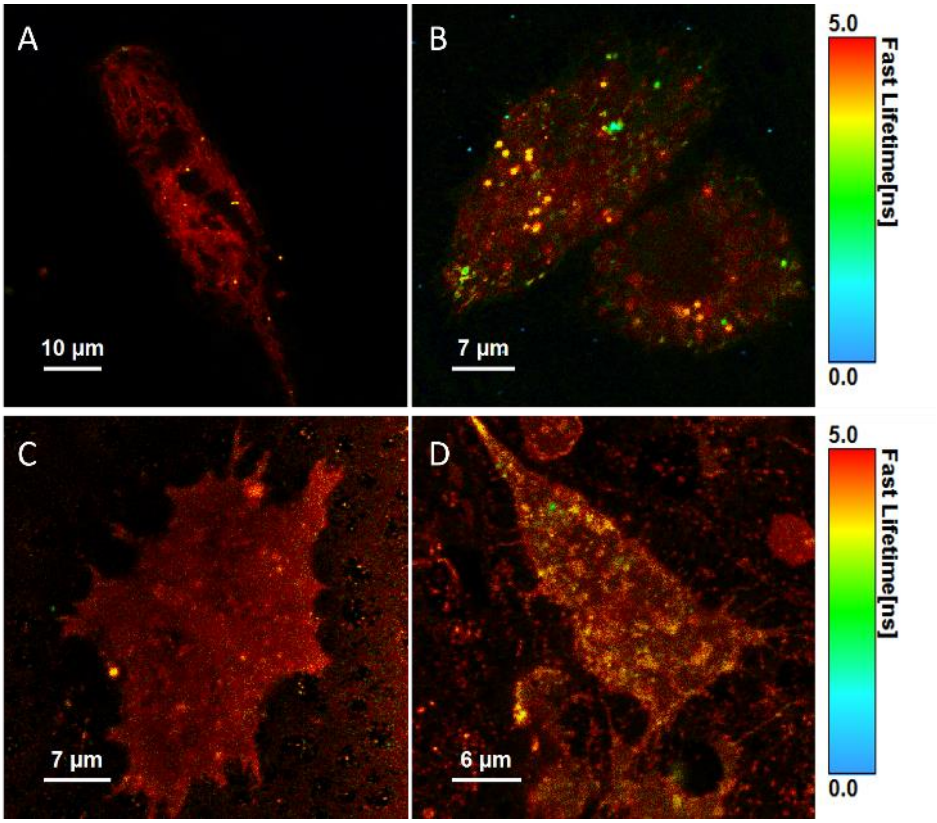

Figure 3.6. Fluorescent lifetime images (FLIM) of a live HeLa cell (A) and CHO cell (B) stained with BODIPY-Ahx-Chol (5 µM, 2h), and after treatment with MβCD (10 mM) in HeLa (C) and CHO (D) cells.

3.4 Conclusions

We demonstrate a simple approach by which phase preference of a simple BODIPY fluorophore can be switched between Lo or Ld at phase forming liposomes, by altering the number of carbons in the alkyl linker separating probe from cholesterol. The cholesterol conjugation is achieved via a simple and very mild Steglich esterification reaction via probe carboxyl and cholesterol hydroxyl. Phase preference in domain forming giant unilamellar vesicles (GUVs) confirmed, using a commercial Ld marker as reference, > 90 % Ld selectivity for BODIPY-Ar-Chol, where the probe is directly ester linked to cholesterol, which is reversed leading to approximately 80 % Lo partitioning when a hexyl linker is inserted between probe and cholesterol in the case of BODIPY-Ahx-Chol. The preference for cholesterol rich membrane persists in live cells where changing linker length has a profound impact on the localisation of the probe. Unlike liposomes, BODIPY-Ar-Chol does not stain the membrane of live cells but is directed through the membrane and localises in

lipid droplets in HeLa and CHO cell lines. Whereas BODIPY-Ahx-Chol is retained at the membrane in live cells where it partitions into regions from where the Ld probe DiD is excluded. The preference for cholesterol rich membrane is confirmed on treatment of HeLa cells with cyclodextrin. Raft like, detergent resistant domains are highly prevalent in cancer cells and BODIPY-Ahx-Chol membrane distribution varied significantly between HeLa and CHO which is a non-cancer cell. Robust fluorescent probes that can partition into and distinguish raft-like domains in live cells as well as in biophysical models are rare and can facilitate use of advanced microscopy applied to detailed studies into domains and rafts in cells. Ordered lipid domains are particularly prevalent in cancer and in multidrug resistant cells, probes that can be targeted to such domain should be useful in developing insights into such models. Ongoing work will explore whether the principle of extending a long linker to a lipophilic probe can be applied more universally to broader families of fluorescent probes.

3.5 Experimental Section

3.5.1 Preparation of Giant Unilamellar Vesicles (GUVs)

Lipid stock solutions were prepared in chloroform. For preparation of Ld/Lo phase separated GUVs, 1-2-dioleoyl-sn-glycero-3-phosphocoline (DOPC), brain sphingomyelin (BSM) and cholesterol (Chol) were mixed in a molar ratio 4:4:2 to a final concentration of 5 mM. For partitioning (confocal fluorescence microscopy) studies BODIPY-Ar-Chol or BODIPY-Ahx-Chol, along with the lipophilic tracer dye DiD, were all included respectively at a concentration of 0.1 mol % in lipid content prior to electroformation. DiD is a commercially available lipid stain that is known to associate strongly within the liquid-disordered phase of GUVs. It was therefore chosen in order to identify this phase during confocal fluorescence microscopy experiments. GUVs were formed by electroformation using the Vesicle Prep Pro (VPP) (Nanion Technologies, Munich, Germany). The lipids were added in 1.5 µL droplets onto a pair of conductive ITO slides and dried in a desiccator under vacuum for 45 minutes. The ITO slides were carefully placed in contact at an angle to avoid air bubbles. A voltage was then applied and increased over 10 minutes from 0 V to 3 V and then held for 125 minutes. The protocol was carried out at 37 °C. Once electroformation was completed, the GUVs were removed, diluted with 0.23 mM glucose solution and 0.5 % agarose solution and

deposited on glass coverslides for imaging. For uptake studies, GUVs were prepared as described above by electroformation using DOPC 100 mol %.

3.5.2 Confocal Microscopy of Giant Unilamellar Vesicles (GUVs)

Fluorescent confocal imaging was carried out using a Leica TSP inverted (DMi8) confocal microscope. A 100-oil immersion objective was used for all measurements. A white light laser was used to excite the dyes. The excitation and emission wavelengths (λex/λem) were as follows: 503/511–570 for BODIPY-Ar-Chol and BODIPY-Ahx-Chol, and 644/ 665–700 nm for DiD

3.5.3 Fluorescence Lifetime Imaging

Fluorescence lifetime imaging was carried out using a PicoQuant 100 system attached to Leica TSP inverted (DMi8) confocal microscope using a 100 x oil immersion objective. Each sample was acquired for 120 s with a 512 x 512 resolution. A 503 nm white light laser was used to excite the GUV samples. Data was analysed using PicoQuant Symphotime software.

3.5.4 Cell Culture and Imaging

HeLa cells were cultured using MEM media supplemented with 2% L-glutamine, 1% MEM non-essential amino acid solution, 10% foetal bovine serum and 1% penicillin-streptomycin and grown at 37°C with 5% CO_2. Cells were harvested or split at 90% confluency using 0.25% trypsin for 5 minutes at 37°C.

3.5.5 Confocal Microscopy for Cell Imaging

For imaging, cells were seeded at 7 x 10^4 cells in 2 mL culture media on 35 mm high precision glass-bottom dishes (Ibidi, Germany). BODIPY-Ar-Chol and BODIPY-Ahx-Chol were added to cell media to give a final concentration of 5 μM and left to incubate in the absence of light at 37°C with 5 % CO_2. Cells were washed twice with supplemented PBS (1.1 mM $MgCl_2$ and 0.9 mM $CaCl_2$) prior to imaging. The cells were imaged live using a Leica TSP DMi8 confocal microscope with a 100X oil immersion objective lens. Cells were excited at 497 nm and emission was collected between 518-610 nm. Co-staining with DiD was carried out by adding 800 nM DiD in PBS to the cells for 20 minutes at 37°C prior to imaging. DiD was excited at 640 nm and emission was collected between 660-760 nm.

3.5.6 FLIM of Live Cells

HeLa and CHO cells were prepared and stained as described for confocal imaging. Live FLIM images were acquired using SymphoTime 200, Picoquant, attached to a Leica TSP DMi8 confocal microscope using a 100X oil immersion objective. Each FLIM image was acquired for 2 minutes with 512 x 512 resolution, at 10 MHz and Resolution 16. A 497 nm laser was used to excite the sample, and emission collected between 520-620 nm. The data was analysed using PicoQuant Symphotime software. Lifetimes were fit to a tri-exponential decay, until a χ^2 value of 0.9-1.1 was achieved.

3.5.7 Synthesis of BODIPY-Ar-COOH (1):

Synthesis was carried out according to modified procedure.[45] DCM (60 mL) was purged with nitrogen for 30 min. To 4-formylbenzoic acid (500 mg, 3.3 mmol), 2,4-dimethylpyrrole (453 µL, 7.45 mmol) and TFA (cat.) was added and kept at room temperature while stirring for 5 hours. After the 5 hours tetrachlorobenzoquinone (p-chloranil) (973 mg, 3.95 mmol) in DCM (20 mL) was added and the reaction mixture was left to stir for 30 minutes followed by the addition of $BF_3.OEt_2$ (6.4 mL) and Et_3N (6.4 mL). The reaction mixture was left to stir overnight. The crude mixture was washed with water (2 x 50 mL), dried over $MgSO_4$ and concentrated to dryness via vacuum. The crude product was purified on a silica gel by column chromatography eluent: DCM/MeOH (30:1). Yield: purple solid, 158.3 mg (0.43 mmol, 13 %). ^{1}H NMR :(600 MHz, DMSO-d_6) δ(ppm): 9.60 (t, 2H); 9.22 (d, J=1.8 Hz, 2H); 8.61 (d, J=1.8 Hz, 1H); 8.42 (d, J=3 Hz, 1H); 7.97 (d, J=7.8 Hz, 2H); 7.77-7.75 (m, 2H); 7.45 (d, J=7.8 Hz, 2H); 5.96 (s, 2H); 2.52 (s, 6H); 1.44 (s, 6H). ^{13}C NMR :(150 MHz, DMSO-d_6) δ(ppm): 155.8, 152.7, 152.6, 143.2, 143.0, 142.6, 142.1, 141.7, 141.3, 140.9, 140.1, 135.3, 133.8, 131.3, 130.2, 130.1, 129.0, 128.2, 127.6, 127.5, 127.0, 124.2, 121.4, 118.9. HR-MS (ESI-TOF) m/z: calculated for $C_{20}H_{19}BF_2N_2O_2$ 369.1512 found 369.1586

3.5.8 Synthesis of BODIPY-Ar-Chol (2):

Bodipy-Ar-COOH (1) (100 mg, 0.272 mmol) and DMAP (32 mg, 0.0272 mmol) was dissolved in DCM (4 mL). Cholesterol (240 mg, 0.599 mmol) in DCM (2 mL) was added to the reaction mixture and stirred at room temperature for 5 min. Following this DCC (70 mg, 0.299 mmol) in DCM (2 mL) was added and the reaction mixture was left to stir overnight). The crude mixture was with brine solution, dried over $MgSO_4$ and concentrated to dryness. The crude product was purified on a silica gel by column chromatography eluent:

DCM/MeOH (30:1). Yield: orange solid, 78 mg (0.104 mmol, 38 %). ^{1}H NMR :(600 MHz, $CDCl_3$) δ(ppm): 8.17 (d, J=8.3 Hz, 2H); 7.39 (d, J=8.2 Hz, 2H); 5.98 (s, 1H); 2.50 (d, J=7.2, 2H); 2.05-1.97 (m, 3H); 1.98-1.92 (m, 1H); 1.87-1.74 (m, 2H); 1.61-1.56 (m, 2H); 1.540-1.46 (m, 4H); 1.36 (s, 6H); 1.35-1.32 (m, 2H); 1.28-0.98 (m, 16H); 0.92 (d, J=6.5 Hz, 3H); 0.86 (q, J=9.4, 2.7 Hz, 3H); 0.69 (s, 3H).). ^{13}C NMR :(150 MHz, $CDCl_3$) δ(ppm): 165.37, 139.53, 130.32, 128.29, 122.96, 121.46, 75.17, 56.71, 56.16, 50.07, 43.34, 39.52, 38.22, 37.64, 36.68, 36.19, 35.79, 31.95, 31.90, 28.22, 28.01, 27.89, 24.30, 23.83, 22.80, 22.55, 21.01, 19.37, 18.72, 14.55, 11.88. HR-MS (ESI-TOF) m/z: calculated for $C_{47}H_{63}BF_2N_2O_2$ 737.5055 found 737.5029

3.5.9 Synthesis of 4-formylphenyl-Ahx (4):

4-formybenzoic acid (1 g, 6.66 mmol), EDC (2.55 g, 13.32 mmol) and NHS (1.53 g, 13.32 mmol) was stirred in DCM (50 mL) at room temperature for 1 h. Following this 6-methyl-aminohexanoate (1.45 g, 9.99 mmol) in DCM (2 mL) was added with TEA (800 µL) and the reaction mixture was stirred overnight. The crude mixture was washed with 3 x 50 mL water, dried over $MgSO_4$ and concentrated to dryness. The reaction was monitored by TLC and NMR and was carried through to the next step without purification. To the reaction product was added MeOH (15 mL) and slowly the addition of 0.1 M LiOH in MeOH/H_2O (3:1). The reaction was stirred at room temperature for 4 h. The reaction mixture was concentrated to dryness and then rehydrated with water. The solution was acidified using conc. HCl until pH 2 was achieved. The product was obtained via filtration and purified on a silica gel by column chromatography eluent: DCM/MeOH (80:20). Overall yield for two steps: white solid, 164 mg (0.62 mmol, 9.4 %). ^{1}H NMR :(600 MHz, DMSO-d_6) δ(ppm): 12.02 (s, 1H); 10.08 (s, 1H); 8.67 (t, J=12 Hz, 1H); 7.99 (q, J=17.8, 8.7 Hz, 4H); 3.26 (q, J=14.8, 7.6, 2H); 2.21 (t, J=7.3, 2H); 1.54-1.52 (m, 4H); 1.339-1.335 (m, 2H). ^{13}C NMR :(150 MHz, DMSO-d_6) δ(ppm): 193.39, 174.94, 165.73, 140.18, 138.11, 129.85, 128.34, 34.08, 29.18, 26.48, 24.71. HR-MS (ESI-TOF) m/z: calculated for $C_{14}H_{17}NO_4$ 264.1241 found 264.1236

3.5.10 Synthesis of BODIPY-Ahx (5):

DCM (30 mL) was purged with nitrogen for 30 min. To 4-formylbenzoic acid (500 mg, 3.3 mmol), 2,4-dimethylpyrrole (144 µL, 1.4 mmol) and TFA (cat.) was added and kept at room temperature while stirring for 5 hours. After the 5 hours tetrachlorobenzoquinone (p-chloranil) (171 mg, 0.69 mmol) in DCM (20 mL) was added and the reaction mixture was

left to stir for 30 minutes followed by the addition of $BF_3.OEt_2$ (1.74 mL) and Et_3N (1.74 mL). The reaction mixture was left to stir overnight. The crude mixture was washed with water (2 x 50 mL), dried over $MgSO_4$ and concentrated to dryness via vacuum. The crude product was purified on a silica gel by column chromatography eluent: DCM/MeOH (30:1 followed by DCM/MeOH (90:10). Yield: orange solid, 37.6 mg (0.078 mmol, 13.4 %). ^1H NMR :(600 MHz,$CDCl_3$) δ(ppm): 7.91 (d, J= 8.2 Hz, 2H); 7.38 (d, J=8.16 Hz, 2H); 6.30 (t, J=5.58, 1H); 5.97 (s, 1H); 3.51-3.48 (m, 2H); 2.54 (s, 1H); 2.39 (t, J=7.9 Hz, 2H); 1.70-1.67 (m, 4H); 1.48-1.47 (m, 2H); 1.35 (s, 6H). ^{13}C NMR was not obtained due to poor solubility. HR-MS (ESI-TOF) m/z: calculated for $C_{26}H_{32}BF_2N_3O_3$ 482.2412 found 482.2427

3.5.11 Synthesis of BODIPY-Ahx-Chol (6):

To a stirred solution of 5 (32.6 mg, 0.067 mmol,) and DMAP (8.1 mg, 0.0067 mmol) in DCM (4 mL), a solution of cholesterol (51mg, 0.134 mmol) in DCM (2 mL) was added. The reaction mixture was stirred for 5 min at room temperature. A solution of DCC (15.2 mg, 0.073 mmol) in DCM (2 mL) was added and the mixture was stirred at room temperature overnight. The crude mixture was washed with brine solution, dried over $MgSO_4$ and concentrated to dryness via vacuum. The crude product was purified on silica gel by column chromatography eluent: DCM/MeOH (90:10). Yield: orange solid, 22.9 mg (0.026 mmol, 40.2 %). ^1H NMR :(600 MHz, $CDCl_3$) δ(ppm): 7.94 (d, J=8.2 Hz, 2H); 7.39 (d, J=8.2 Hz, 2H); 6.38 (t, J=5.46 Hz, 1H); 5.98 (s, 2H); 5.36 (d, J=4.8 Hz, 1H); 4.63-4.57 (m, 1H); 3.67-3.64 (m, 2H); 3.52 (q, J=14.2, 7 Hz, 2H); 2.55 (s, 6H); 2.34-2.30 (m 4H); 2.02-1.91 (m, 2H); 1.86-1.79 (m, 3H); 1.72-1.66 (m, 4H); 1.50-1.40 (m, 7H); 1.35 (s, 6H); 1.25 (s, 6H); 1.17-1.07 (m, 7H); 1.01 (s, 3H); 0.91 (d, J-6.7 Hz, 3H); 0.86 (dd, J=6.5, 2.9 Hz, 7H); 0.66 (s, 3H). ^{13}C NMR :(150 MHz, $CDCl_3$) δ(ppm): 173.23, 166.56, 155.93, 142.92, 140.35, 139.60, 138.26, 135.22, 131.07, 128.47, 127.77, 122.78, 121.46, 76.81, 74.06, 56.63, 56.13, 49.99, 42.30, 39.71, 39.52, 38.18, 37.00, 36.61, 36.18, 35.80, 34.30, 31.84, 29.71, 28.97, 28.24, 28.02, 27.82, 26.23, 24.26, 24.16, 23.83, 22.83, 22.57, 21.02, 19.32, 18.72, 14.64, 14.13, 11.85. HR-MS (ESI-TOF) m/z: calculated for $C_{53}H_{74}BF_2N_3O_3$ 850.5852 found 850.5870

3.6 Supporting Material

Supplementary data associated with this chapter can be found in Appendix B.

3.7 References

(1) Anchisi, L.; Dessi, S.; Pani, A.; Mandas, A. Cholesterol Homeostasis: A Key to Prevent or Slow down Neurodegeneration. *Front. Physiol.* **2013**, *3*, 486.

(2) Marsh, D. Cholesterol-Induced Fluid Membrane Domains: A Compendium of Lipid-Raft Ternary Phase Diagrams. *Biochim. Biophys. Acta BBA - Biomembr.* **2009**, *1788* (10), 2114–2123.

(3) Lingwood, D.; Simons, K. Lipid Rafts as a Membrane-Organizing Principle. *Science* **2010**, *327* (5961), 46–50.

(4) Sevcsik, E.; Brameshuber, M.; Fölser, M.; Weghuber, J.; Honigmann, A.; Schütz, G. J. GPI-Anchored Proteins Do Not Reside in Ordered Domains in the Live Cell Plasma Membrane. *Nat. Commun.* **2015**, *6*, 6969.

(5) Kraft, M. L. Plasma Membrane Organization and Function: Moving Past Lipid Rafts. *Mol. Biol. Cell* **2013**, *24* (18), 2765–2768.

(6) Simons, K.; Ehehalt, R. Cholesterol, Lipid Rafts, and Disease. *J. Clin. Invest.* **2002**, *110* (5), 597–603.

(7) Simons, K.; Van Meer, G. Lipid Sorting in Epithelial Cells. *Biochemistry (Mosc.)* **1988**, *27* (17), 6197–6202.

(8) Simons, K.; Ikonen, E. Functional Rafts in Cell Membranes. *Nature* **1997**, *387* (6633), 569–572.

(9) Korade, Z.; Kenworthy, A. K. Lipid Rafts, Cholesterol, and the Brain. *Neuropharmacology* **2008**, *55* (8), 1265–1273.

(10) Pike, L. J. The Challenge of Lipid Rafts. *J. Lipid Res.* **2009**, *50 Suppl*, S323–S328.

(11) Heberle, F. A.; Feigenson, G. W. Phase Separation in Lipid Membranes. *Cold Spring Harb. Perspect. Biol.* **2011**, *3* (4), a004630.

(12) de Wit, G.; Danial, J. S. H.; Kukura, P.; Wallace, M. I. Dynamic Label-Free Imaging of Lipid Nanodomains. *Proc. Natl. Acad. Sci. U. S. A.* **2015**, *112* (40), 12299–12303.

(13) Moss, F. R.; Boxer, S. G. Atomic Recombination in Dynamic Secondary Ion Mass Spectrometry Probes Distance in Lipid Assemblies: A Nanometer Chemical Ruler. *J. Am. Chem. Soc.* **2016**, *138* (51), 16737–16744.

(14) Shan, Y.; Wang, H. The Structure and Function of Cell Membranes Examined by Atomic Force Microscopy and Single-Molecule Force Spectroscopy. *Chem. Soc. Rev.* **2015**, *44* (11), 3617–3638.

(15) Honigmann, A.; Mueller, V.; Ta, H.; Schoenle, A.; Sezgin, E.; Hell, S. W.; Eggeling, C. Scanning STED-FCS Reveals Spatiotemporal Heterogeneity of Lipid Interaction in the Plasma Membrane of Living Cells. *Nat. Commun.* **2014**, *5*, 5412.

(16) Walde, P.; Cosentino, K.; Engel, H.; Stano, P. Giant Vesicles: Preparations and Applications. *ChemBioChem* **2010**, *11* (7), 848–865.

(17) Veatch, S. L.; Keller, S. L. Separation of Liquid Phases in Giant Vesicles of Ternary Mixtures of Phospholipids and Cholesterol. *Biophys. J.* **2003**, *85* (5), 3074–3083.

(18) Dent, M. R.; López-Duarte, I.; Dickson, C. J.; Geoghegan, N. D.; Cooper, J. M.; Gould, I. R.; Krams, R.; Bull, J. A.; Brooks, N. J.; Kuimova, M. K. Imaging Phase Separation in Model Lipid Membranes through the Use of BODIPY Based Molecular Rotors. *Phys Chem Chem Phys* **2015**, *17* (28), 18393–18402.
(19) Baumgart, T.; Hunt, G.; Farkas, E. R.; Webb, W. W.; Feigenson, G. W. Fluorescence Probe Partitioning between Lo/Ld Phases in Lipid Membranes. *Biochim. Biophys. Acta BBA - Biomembr.* **2007**, *1768* (9), 2182–2194.
(20) Crosby, G. A.; Demas, J. N. Measurement of Photoluminescence Quantum Yields. Review. *J. Phys. Chem.* **1971**, *75* (8), 991–1024.
(21) Sezgin, E.; Levental, I.; Grzybek, M.; Schwarzmann, G.; Mueller, V.; Honigmann, A.; Belov, V. N.; Eggeling, C.; Coskun, Ü.; Simons, K.; et al. Partitioning, Diffusion, and Ligand Binding of Raft Lipid Analogs in Model and Cellular Plasma Membranes. *Biochim. Biophys. Acta BBA - Biomembr.* **2012**, *1818* (7), 1777–1784.
(22) Daly, H. C.; Sampedro, G.; Bon, C.; Wu, D.; Ismail, G.; Cahill, R. A.; O'Shea, D. F. BF2-Azadipyrromethene NIR-Emissive Fluorophores with Research and Clinical Potential. *Eur. J. Med. Chem.* **2017**, *135*, 392–400.
(23) Grossi, M.; Morgunova, M.; Cheung, S.; Scholz, D.; Conroy, E.; Terrile, M.; Panarella, A.; Simpson, J. C.; Gallagher, W. M.; O'Shea, D. F. Lysosome Triggered near-Infrared Fluorescence Imaging of Cellular Trafficking Processes in Real Time. *Nat. Commun.* **2016**, *7*, 10855.
(24) Dura, L.; Wächtler, M.; Kupfer, S.; Kübel, J.; Ahrens, J.; Höfler, S.; Bröring, M.; Dietzek, B.; Beweries, T. Photophysics of BODIPY Dyes as Readily-Designable Photosensitisers in Light-Driven Proton Reduction. *Inorganics* **2017**, *5* (2), 21.
(25) Tang, Q.; Si, W.; Huang, C.; Ding, K.; Huang, W.; Chen, P.; Zhang, Q.; Dong, X. An Aza-BODIPY Photosensitizer for Photoacoustic and Photothermal Imaging Guided Dual Modal Cancer Phototherapy. *J. Mater. Chem. B* **2017**, *5* (8), 1566–1573.
(26) Strobl, M.; Walcher, A.; Mayr, T.; Klimant, I.; Borisov, S. M. Trace Ammonia Sensors Based on Fluorescent Near-Infrared-Emitting Aza-BODIPY Dyes. *Anal. Chem.* **2017**, *89* (5), 2859–2865.
(27) Fu, Y.; Finney, N. S. Small-Molecule Fluorescent Probes and Their Design. *RSC Adv.* **2018**, *8* (51), 29051–29061.
(28) Ulrich, G.; Ziessel, R.; Harriman, A. The Chemistry of Fluorescent Bodipy Dyes: Versatility Unsurpassed. *Angew. Chem. Int. Ed.* **2008**, *47* (7), 1184–1201.
(29) Nastasi, F.; Puntoriero, F.; Campagna, S.; Olivier, J.-H.; Ziessel, R. Hybrid Complexes: Pt(II)-Terpyridine Linked to Various Acetylide-Bodipy Subunits. *Phys. Chem. Chem. Phys. PCCP* **2010**, *12* (27), 7392–7402.
(30) Loudet, A.; Burgess, K. BODIPY Dyes and Their Derivatives: Syntheses and Spectroscopic Properties. *Chem. Rev.* **2007**, *107* (11), 4891–4932.
(31) Ziessel, R.; Ulrich, G.; Harriman, A. The Chemistry of Bodipy: A New El Dorado for Fluorescence Tools. *New J. Chem.* **2007**, *31* (4), 496–501.

(32) Ziessel, R.; Bonardi, L.; Ulrich, G. Boron Dipyrromethene Dyes: A Rational Avenue for Sensing and Light Emitting Devices. *Dalton Trans.* **2006**, No. 23, 2913–2918.
(33) Kowada, T.; Maeda, H.; Kikuchi, K. BODIPY-Based Probes for the Fluorescence Imaging of Biomolecules in Living Cells. *Chem Soc Rev* **2015**, *44* (14), 4953–4972.
(34) Ni, Y.; Wu, J. Far-Red and near Infrared BODIPY Dyes: Synthesis and Applications for Fluorescent pH Probes and Bio-Imaging. *Org. Biomol. Chem.* **2014**, *12* (23), 3774.
(35) L. Yang, Y. Liu, W. Liu, C. Ma, C. Zhang and Y. Li, Divinyl BODIPY Derivative: Synthesis, Photophysical Properties, Crystal Structure, Photostability and Bioimaging, Bioorg. Med. Chem. Lett., **2015**, 25 (24), 5716–5719.
(36) Deepika, N.; Devi, C. S.; Kumar, Y. P.; Reddy, K. L.; Reddy, P. V.; Kumar, D. A.; Singh, S. S.; Satyanarayana, S. DNA-Binding, Cytotoxicity, Cellular Uptake, Apoptosis and Photocleavage Studies of Ru(II) Complexes. *J. Photochem. Photobiol. B* **2016**, *160*, 142–153.
(37) Jiang, X.-D.; Gao, R.; Yue, Y.; Sun, G.-T.; Zhao, W. A NIR BODIPY Dye Bearing
(38) Papalia, T.; Lappano, R.; Barattucci, A.; Pisano, A.; Bruno, G.; Santolla, M. F.; Campagna, S.; Marco, P. D.; Puntoriero, F.; Francesco, E. M. D.; et al. A Bodipy as a Luminescent Probe for Detection of the G Protein Estrogen Receptor (GPER). *Org. Biomol. Chem.* **2015**, *13* (42), 10437–10441.
(39) Staudinger, C.; Breininger, J.; Klimant, I.; Borisov, S. M. Near-Infrared Fluorescent Aza-BODIPY Dyes for Sensing and Imaging of pH from the Neutral to Highly Alkaline Range. *The Analyst* **2019**, *144* (7), 2393–2402.
(40) Liu, Z.; Thacker, S. G.; Fernandez-Castillejo, S.; Neufeld, E. B.; Remaley, A. T.; Bittman, R. Synthesis of Cholesterol Analogues Bearing BODIPY Fluorophores by Suzuki or Liebeskind-Srogl Cross-Coupling and Evaluation of Their Potential for Visualization of Cholesterol Pools. *Chembiochem Eur. J. Chem. Biol.* **2014**, *15* (14), 2087–2096.
(41) Hölttä-Vuori, M.; Uronen, R.-L.; Repakova, J.; Salonen, E.; Vattulainen, I.; Panula, P.; Li, Z.; Bittman, R.; Ikonen, E. BODIPY-Cholesterol: A New Tool to Visualize Sterol Trafficking in Living Cells and Organisms. *Traffic* **2008**, *9* (11), 1839–1849.
(42) Li, Z.; Mintzer, E.; Bittman, R. First Synthesis of Free Cholesterol−BODIPY Conjugates. *J. Org. Chem.* **2006**, *71* (4), 1718–1721.
(43) Sarmento, M. J.; Pinto, S. N.; Coutinho, A.; Prieto, M.; Fernandes, F. Accurate Quantification of Inter-Domain Partition Coefficients in GUVs Exhibiting Lipid Phase Coexistence. *RSC Adv* **2016**, *6* (71), 66641–66649.
(44) Klymchenko, A. S.; Kreder, R. Fluorescent Probes for Lipid Rafts: From Model Membranes to Living Cells. *Chem. Biol.* **2014**, *21* (1), 97–113.
(45) Niko, Y.; Didier, P.; Mely, Y.; Konishi, G.; Klymchenko, A. S. Bright and Photostable Push-Pull Pyrene Dye Visualizes Lipid Order Variation between Plasma and Intracellular Membranes. *Sci. Rep.* **2016**, *6*, 18870.

(46) Ariola, F. S.; Li, Z.; Cornejo, C.; Bittman, R.; Heikal, A. A. Membrane Fluidity and Lipid Order in Ternary Giant Unilamellar Vesicles Using a New Bodipy-Cholesterol Derivative. *Biophys. J.* **2009**, *96* (7), 2696–2708.
(47) Kwiatek, J. M.; Owen, D. M.; Abu-Siniyeh, A.; Yan, P.; Loew, L. M.; Gaus, K. Characterization of a New Series of Fluorescent Probes for Imaging Membrane Order. *PLoS ONE* **2013**, *8* (2), e52960.
(48) Wu, Y.; Štefl, M.; Olzyńska, A.; Hof, M.; Yahioglu, G.; Yip, P.; Casey, D. R.; Ces, O.; Humpolíčková, J.; Kuimova, M. K. Molecular Rheometry: Direct Determination of Viscosity in Lo and Ld Lipid Phases via Fluorescence Lifetime Imaging. *Phys. Chem. Chem. Phys.* **2013**, *15* (36), 14986–14993.
(49) Wei, C.; Wang, R.; Wei, L.; Cheng, L.; Li, Z.; Xi, Z.; Yi, L. O-Fluorination of Aromatic Azides Yields Improved Azido-Based Fluorescent Probes for Hydrogen Sulfide: Synthesis, Spectra, and Bioimaging. *Chem. – Asian J.* **2014**, *9* (12), 3586–3592.
(50) Karolin, J.; Johansson, L. B.-A.; Strandberg, L.; Ny, T. Fluorescence and Absorption Spectroscopic Properties of Dipyrrometheneboron Difluoride (BODIPY) Derivatives in Liquids, Lipid Membranes, and Proteins. *J. Am. Chem. Soc.* **1994**, *116* (17), 7801–7806.
(51) Martin, A.; Byrne, A.; Dolan, C.; J. Forster, R.; E. Keyes, T. Solvent Switchable Dual Emission from a Bichromophoric ruthenium–BODIPY Complex. *Chem. Commun.* **2015**, *51* (87), 15839–15841.
(52) Aureli, M.; Grassi, S.; Sonnino, S.; Prinetti, A. Isolation and Analysis of Detergent-Resistant Membrane Fractions. *Methods Mol. Biol. Clifton NJ* **2016**, *1376*, 107–131.
(53) Crane, J. M.; Tamm, L. K. Role of Cholesterol in the Formation and Nature of Lipid Rafts in Planar and Spherical Model Membranes. *Biophys. J.* **2004**, *86* (5), 2965–2979.
(54) Silvius, J. R. Role of Cholesterol in Lipid Raft Formation: Lessons from Lipid Model Systems. *Biochim. Biophys. Acta BBA - Biomembr.* **2003**, *1610* (2), 174–183.
(55) McConnell, H. M.; Vrljic, M. Liquid-Liquid Immiscibility in Membranes. *Annu. Rev. Biophys. Biomol. Struct.* **2003**, *32*, 469–492.
(56) McMullen, T. P. W.; Lewis, R. N. A. H.; McElhaney, R. N. Cholesterol–phospholipid Interactions, the Liquid-Ordered Phase and Lipid Rafts in Model and Biological Membranes. *Curr. Opin. Colloid Interface Sci.* **2004**, *8* (6), 459–468.
(57) Huang, J.; Feigenson, G. W. A Microscopic Interaction Model of Maximum Solubility of Cholesterol in Lipid Bilayers. *Biophys. J.* **1999**, *76* (4), 2142–2157.
(58) O'Connor, D.; Byrne, A.; Dolan, C.; Keyes, T. E. Phase Partitioning, Solvent-Switchable BODIPY Probes for High Contrast Cellular Imaging and FCS. *New J. Chem.* **2018**, *42* (5), 3671–3682.
(59) Mundy, D. I. Dual Control of Caveolar Membrane Traffic by Microtubules and the Actin Cytoskeleton. *J. Cell Sci.* **2002**, *115* (22), 4327–4339.
(60) Mundy, D. I.; Li, W. P.; Luby-Phelps, K.; Anderson, R. G. Caveolin Targeting to Late Endosome/lysosomal Membranes Is Induced by Perturbations of Lysosomal pH and Cholesterol Content. *Mol. Biol. Cell* **2012**, *23* (5), 864–880.

(61) Hansen, C. G.; Howard, G.; Nichols, B. J. Pacsin 2 Is Recruited to Caveolae and Functions in Caveolar Biogenesis. *J. Cell Sci.* **2011**, *124* (16), 2777–2785.
(62) Lladó, V.; López, D. J.; Ibarguren, M.; Alonso, M.; Soriano, J. B.; Escribá, P. V.; Busquets, X. Regulation of the Cancer Cell Membrane Lipid Composition by NaCHOleate: Effects on Cell Signaling and Therapeutical Relevance in Glioma. *Biochim. Biophys. Acta* **2014**, *1838* (6), 1619–1627.
(63) Bernardes, N.; M. Fialho, A. Perturbing the Dynamics and Organization of Cell Membrane Components: A New Paradigm for Cancer-Targeted Therapies. *Int. J. Mol. Sci.* **2018**, *19* (12), 3871.
(64) Zalba, S.; Ten Hagen, T. L. M. Cell Membrane Modulation as Adjuvant in Cancer Therapy. *Cancer Treat. Rev.* **2017**, *52*, 48–57.
(65) Neufeld, E. B.; Cooney, A. M.; Pitha, J.; Dawidowicz, E. A.; Dwyer, N. K.; Pentchev, P. G.; Blanchette-Mackie, E. J. Intracellular Trafficking of Cholesterol Monitored with a Cyclodextrin. *J. Biol. Chem.* **1996**, *271* (35), 21604–21613.
(66) Fukasawa, M.; Nishijima, M.; Itabe, H.; Takano, T.; Hanada, K. Reduction of Sphingomyelin Level without Accumulation of Ceramide in Chinese Hamster Ovary Cells Affects Detergent-Resistant Membrane Domains and Enhances Cellular Cholesterol Efflux to Methyl-Beta -Cyclodextrin. *J. Biol. Chem.* **2000**, *275* (44), 34028–34034.
(67) Hao, M.; Mukherjee, S.; Sun, Y.; Maxfield, F. R. Effects of Cholesterol Depletion and Increased Lipid Unsaturation on the Properties of Endocytic Membranes. *J. Biol. Chem.* **2004**, *279* (14), 14171–14178.
(68) Gallois-Montbrun, S.; Holmes, R. K.; Swanson, C. M.; Fernandez-Ocana, M.; Byers, H. L.; Ward, M. A.; Malim, M. H. Comparison of Cellular Ribonucleoprotein Complexes Associated with the APOBEC3F and APOBEC3G Antiviral Proteins. *J. Virol.* **2008**, *82* (11), 5636–5642.
(69) Nishimura, S.; Ishii, K.; Iwamoto, K.; Arita, Y.; Matsunaga, S.; Ohno-Iwashita, Y.; Sato, S. B.; Kakeya, H.; Kobayashi, T.; Yoshida, M. Visualization of Sterol-Rich Membrane Domains with Fluorescently-Labeled Theonellamides. *PLoS ONE* **2013**, *8* (12), e83716.
(70) Maxfield, F. R. Plasma Membrane Microdomains. *Curr. Opin. Cell Biol.* **2002**, *14* (4), 483–487.

Chapter 4: Mega-Stokes Pyrene Ceramide Conjugates for STED Imaging of Lipid Droplets in Live Cells

---

Published in *Analyst*, **2019**,**144**, 1608-1621

Darragh O' Connor, Aisling Byrne, Guilherme Berselli, Conor Long and Tia E. Keyes.

Within this work, my colleague, Dr. A. Byrne, and I contributed towards experimental design, execution and manuscript preparation. I have written complete sections with significant contribution to the overall manuscript preparation specifically towards the following sections: design of dyes, synthesis and structural characterisation, photophysical characterisation, FLIM studies on supported lipid bilayers. I assisted G. Berselli in the section lateral mobility studies. Cell studies and STED imaging was carried out by Dr. A. Byrne. Prof. C. Long carried out computational studies and the SFI/HEA Irish Centre for High-End Computing (ICHEC) is gratefully acknowledged for the provision of computational facilities and support. Supporting information associated with this chapter can be found in Appendix C.

4.1 Abstract

Lipid droplets are dynamic subcellular organelles that participate in a range of physiological processes including metabolism, regulation and lipid storage. Their role in disease, such as cancer, where they are involved in metabolism and in chemoresistance, has emerged over recent years. Thus, the value of lipid droplets as diagnostic markers is increasingly apparent where number and size of droplets can be a useful prognostic. Although diverse in size, LDs are typically too small to be easily enumerated by conventional microscopy. The advent of super-resolution microscopy methods offers the prospect of detailed insights but there are currently no commercial STED probes suited to this task and STED, where this method has been used to study LDs it has relied on fixed samples. Here, we report a pyrene-based ceramide conjugate PyLa-C_{17}Cer, that stains lipid droplets with exceptionally high precision in living cells and shows excellent performance in stimulated emission depletion microscopy. The parent compound PyLa comprises a pyrene carboxyl core appended with 3,4-dimethylaminophenyl. The resulting luminophore exhibits high fluorescent quantum yield, mega-Stokes shift and low cytotoxicity. From DFT calculations the Stokes shifted fluorescent state arises from a dimethylaniline to pyrene charge-transfer transition. While the parent compound is cell permeable, it is relatively promiscuous, emitting from both protein and membranous structures within the living mammalian cell. However, on conjugation of C_{17} ceramide to the free carboxylic acid, the resulting PyLa-C_{17}Cer, remains passively permeable to the cell membrane but targets lipid droplets within the cell through a temperature dependent mechanism, with high selectivity. Targeting was confirmed through colocalisation with the commercial lipid probe Nile Red. PyLa-C_{17}Cer offers outstanding contrast of LDs both in fluorescence intensity and lifetime imaging due to its large Stokes shift and very weak emission from aqueous media. Moreover, because the compound is exceptionally photochemically stable with no detectable triplet emission under low temperature conditions, it can be used as an effective probe for fluorescence correlation spectroscopy (FCS). These versatile fluorophores are powerful multimodal probes for combined STED/FCS/lifetime studies of lipid droplets and domains in live cells.

4.2 Introduction

Lipid droplets (LDs), are ubiquitous intracellular organelles rich in neutral lipids. In recent years, it has emerged that LDs have much more diverse and far-reaching activity in the cell than merely fat storage.[1–3] Evidence of their broader importance originated with discovery of the protein, perilipin on the surface of LDs within adipocytes. This focused investigation onto their role in metabolic activity and sites of protein-protein interactions.[2,4,5] The functions of LDs are still emerging but it is now known that they play a pivotal role in protein interactions, signalling, lipid metabolism and are important in immunity, infection and inflammation, cardiovascular disease, cancer, fatty liver disease and diabetes.[6–16] In 1963, Aboumrad *et al*. observed a high quantity of lipid vesicles in the cytoplasm of a type of mammary carcinoma[17], one of the first to link high cellular lipid content and cancer. The correlation between accumulations of a high number of LDs in the cytoplasm of cancer cells compared to normal cells has been observed in cell lines including in breast and prostate cancers.[18] Lipid droplets play an important role in facilitating the abnormal metabolic pathways of cancer cells and are implicated in chemoresistance. Therefore, both from the perspective of interrogative tools for understanding lipid droplets and as diagnostic/prognostic markers, fluorescent probes capable of selectively targeting lipid droplets are important.

Since both quantity and size of LDs are diagnostic parameters, probes that resolve LDs with high contrast from background are required. Because LDs vary widely in size from nano-dimensioned to micron dimensioned size (notwithstanding the very large mono-droplets observed in adipocytes) super-resolution methods are essential for detailed quantitative insights.[19,20] Furthermore, as LDs are motile and change dynamically in living cells probes amenable to *live cell* super-resolution are necessary and this can be a significant challenge.

Conventional confocal fluorescence microscopy is restricted by the Abbe or diffraction limit, meaning that only features separated by approximately $\lambda/2NA$ can be resolved, where λ is the exciting wavelength and NA the numerical aperture of the microscope objective. Optical super-resolution microscopy methods permit sub-diffraction resolution of nano-scale structure and a number of these methods have been commercialised. One of the first reports of super resolution imaging of LDs applied structured Illumination Microscopy (SIM) and

demonstrated the value of using super-resolution imaging to interrogate these organelles.[21] However, SIM has a physically imposed resolution limit of about half that achievable by diffraction limited microscopy although specialised fluorescent probes are not necessary for this method.[22]

In terms of versatility, STimulated Emission Depletion (STED) microscopy is an attractive method as it has achieved resolutions as low as 29 nm[23] with 50 nm resolution readily achievable on commercial instruments which are well suited to LD evaluation. And, importantly for LDs, unlike other higher resolution localisation microscopy methods such as STORM and PALM, STED is amenable to live cell and dynamic investigations.

In STED, the depletion laser must match the emission wavelength of the luminophore in order to stimulate its emission and the resolution of the image scales with the inverse square root of the STED depletion laser intensity. Consequently, a STED probe must be capable of withstanding the high intensity depletion irradiation (>MW/cm^2).[24] Such powers typically cause accelerated photobleaching of commercial organic probes. Photobleaching/photochemistry is particularly prevalent in probes with small Stokes shifts, where if the STED laser excites too close to probe absorbance this can lead to population of undesirable excited states. In practice, this is avoided to an extent in STED by stimulating emission at a wavelength far into the red tail of the emission dye spectrum. However, this limits resolution as the probability of stimulated emission is reduced with reduced resonance of the depletion dye and the emission maxima of the probe.

We recently reported that ruthenium(II) polypyridyl luminophores are well suited as STED probes due to their photostability and their large Stokes shift which permitted closer resonance between the emission maxima of the dye and depletion wavelength without excitation into destructive dark states. The limitation of such complexes however is their relatively low emission quantum yields. In this work we report on the use of new pyrene-based charge transfer fluorophores that provide high emission quantum yields but retain the large Stokes shift ideally needed for STED microscopy. Furthermore, contrast can be improved through either highly selective targeting of the probe or through environmental sensitivity where the probe only emits from the target site. The probes presented in this work have both properties, they are selective for and emit strongly from the LD environment.[25–30]

STED is also amenable to multi-modal methods including combination with fluorescence correlation spectroscopy (FCS) to permit diffusional studies on probe within sub-diffraction limited volumes. We, therefore, also evaluated the probes in the context of FCS which makes similar demands of the probe. This technique has been used extensively to study protein binding[31–34], toxin interactions[35,36] and lipid membrane structure.[37–40] Fluorophores compatible with FCS must have high absorption coefficients and high quantum yields to facilitate the low nanomolar concentrations of probe used in such studies. As per STED, probes must be photostable and lack low-lying dark, particularly triplet-excited states, both of which negatively impact the accurate fitting of the autocorrelation functions collected during measurements. In addition, aggregation of the probe should be avoided, previously a significant problem for pyrene-based probes.

For lipid droplet imaging BODIPY derivatives and particularly Nile Red[41,42] are probably the most widely used probes. Whereas BODIPY 493/503 has a small Stokes shift[43] Nile Red is attractive because it emits only weakly from aqueous media and emits in the red region. However, both dyes have low selectivity, localising in general lipid regions resulting in strong background signal. Both are also prone to aggregate-induced quenching at high concentrations. This is a drawback when probes are highly targeted as local concentrations may be high.

Pyrene is a widely studied fluorophore because of its stability, high quantum yield and noted propensity for excimer-led photophysical changes. It has not been widely applied to bioimaging as it is excited and emits in the ultraviolet region. However, by exploiting the capacity to functionalise the pyrene core, synthetic strategies have been developed to design pyrene donor-acceptor complexes that have displayed good photophysical characteristics with large absorption coefficients, high fluorescence quantum yields and large Stokes shifts.[44–49] Pyrene has been exploited both as an acceptor in such complexes and as a mediator supporting donor and acceptor substituents.[50,51] The design and synthesis of the push-pull pyrene dye PA by Niko *et al* demonstrated the potential for pyrene derivatives to be used as successful lipid probes, outperforming the commercially available Laurdan with excellent photophysical properties.[52] However due to their tendency to form excimers[53,54], pyrene derivatives have not been successfully used for FCS.

Herein, we present a charge-transfer pyrene compound with a mega Stokes-shifted emission and its C_{17} ceramide derivative, that fulfil the demands of both STED and FCS. They are highly emissive and remarkably photostable. Both are cell permeable. The parent is non-selective and emits from lipid and proteinaceous regions whereas the ceramide derivative very specifically targets lipid droplets in live mammalian cells providing outstanding resolution and high contrast STED images of LDs in live cells. PyLa-C_{17}Cer also shows excellent FCS performance. This is to our knowledge the first pyrene-lipid conjugate, to be applied to single molecule counting FCS or STED microscopy. This work demonstrates the value of exploiting charge transfer luminophores in STED imaging and in exploiting lipid conjugates for targeting lipid droplets.

4.3 Results and Discussion

4.3.1 Synthesis

The structures of PyLa **(4)** and Pyla-C_{17}Cer **(5)** and their route to synthesis are shown in Scheme 1. Oxidation of pyrene-1-carboxaldehyde (**1**) with potassium permanganate in pyridine and water gave pyrene-1-carboxylic acid (**2**) in yields similar to reported literature.[55] The compound was prepared as a free carboxylic acid unit to enable subsequent conjugation. Bromination of the 3, 6 and 8-positions of pyrene-1-carboxylic **(2)** was carried using four equivalents of bromine in nitrobenzene.[46] Substitution of bromine dramatically reduced the solubility of the compound preventing characterisation. The resulting yellow powder presumed to be 3, 6, 8-tris-bromo-pyrene-1-carboxylic acid was submitted to Suzuki-Miyaura coupling with 4-(dimethylamino)phenyl boronic acid and tetrakis(triphenylphosphine) palladium (0) ($Pd(PPh_3)_4$) as the catalyst to afford PyLa (**4**) as a yellow powder in good yield (57 %). Lipid conjugation at the free carboxylic acid at the 1-position was carried out via Steglich esterification following a procedure previously reported.[56,57] Wherein, Pyla (**4**) was treated with *N,N'*-dicyclohexylcarbodiimide and 4-dimethylaminopyridine in the presence of C_{17} ceramide using DCM as the solvent.

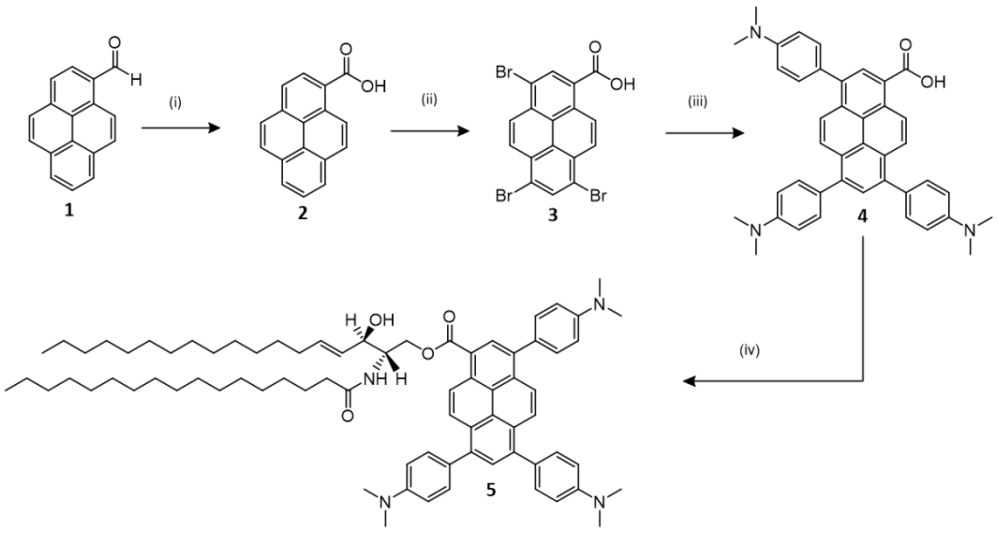

Scheme 4.1 Synthesis of novel PyLa (**4**) and its ceramide conjugate PyLa-C_{17}Cer (**5**). (i) $KMnO_4$, H_2O, piperidine, 100 °C, 12 h, 57 %; (ii) Br_2, nitrobenzene, 140 °C, 5 h, 84 %; (iii) 4-dimethylaminophenylboronic acid, K_2CO_3, $Pd(PPh_3)_4$, toluene/EtOH (2/1), 110 °C, 24 h, N_2, 57 %; (iv) DMAP, DCC, DCM, 25 °C, 24 h, 8.6 %.

Purification of the product by column chromatography on silica gel using eluent (DCM/MeOH 90:10) resulted in the isolation of PyLa-C_{17}Cer **(5)** as a yellow powder with a yield of 8.6 %.

PyLa **(4)** was characterised by ^{1}H and ^{13}C NMR, high-resolution mass spectrometry and high-performance liquid chromatography. ^{1}H NMR analysis confirmed the 18 protons contributed to six methyl groups on the dimethylamino phenyl groups, evident by three large singlets at 3 ppm. The carboxylic acid proton can also be seen at 13 ppm. High-resolution mass spectrometry returned the expected mass of 604.2964. ^{1}H NMR analysis confirmed the expected aliphatic peaks attributed to the C_{17} ceramide tail of PyLa-C_{17}Cer **(5)** at 1.2 ppm, while Maldi-TOF mass spectrometry returned the expected mass as 1136.8058 ([M+)]. High-performance liquid chromatography was carried out to determine purity, wherein a single peak eluted at 3.1 min with no evidence of the parent dye present. Full synthetic protocols and detailed characterisation spectra are provided in Appendix C.

4.3.3 Photophysical Characterisation

Figure 4.1 (a) and (b) show the absorption and emission spectra of PyLa and PyLa-C_{17}Cer in acetonitrile and dichloromethane and data across a range of solvents is shown in Table S4.1 in supplementary information. Consistent with a charge transfer transition, in both cases broad unstructured absorption features with intense mega-Stokes shifted emission (Stokes-shift exceeding 100 nm) in all solvents is observed. Both compounds show negative solvatochromism, the effect is weak in PyLa-C_{17}Cer but pronounced in PyLa. Where the λ_{max} absorbance centred at 396 nm in methanol and 399 nm in acetonitrile shifts to 431 nm in dichloromethane. This is unexpected for a charge transfer transition[58], but the effect is attributed to changes to the pKa of the carboxyl unit in PyLa with solvent. The carboxylate is expected to be stabilised in high dielectric and protic solvents with the neutral carboxyl prevalent in low dielectric, non-protic solvent. This conclusion is supported by DFT computation, shown below, that reflects comparable shifts to higher energy for the carboxylate compared to the acid. Correspondingly, the apparent solvatochromism is much weaker in PyLa-C_{17}Cer as it lacks the carboxyl moiety, although the trend, but for acetonitrile is similar.

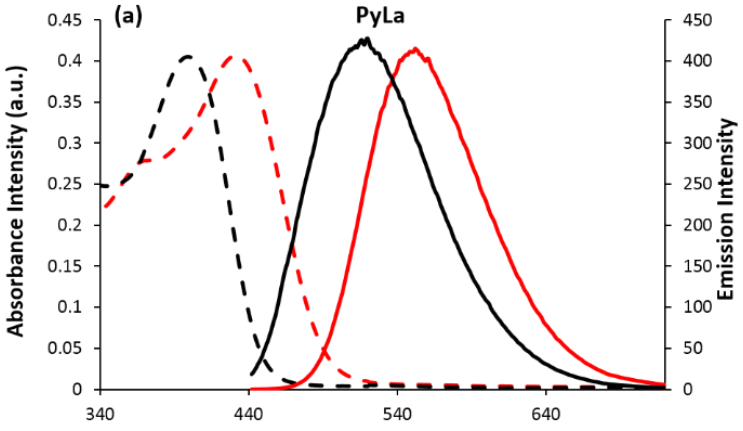

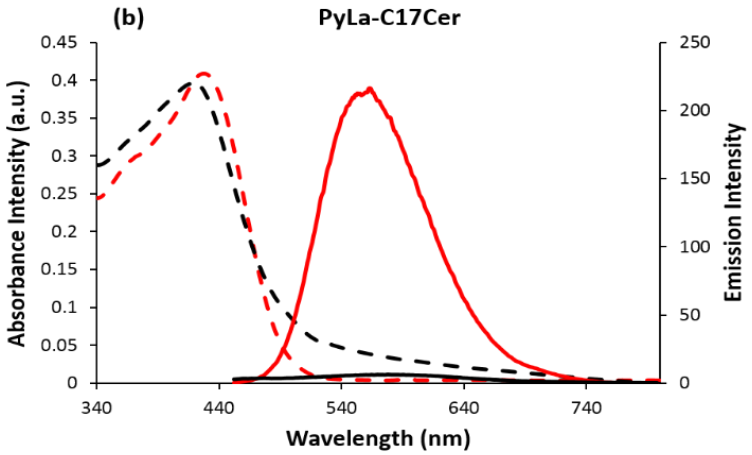

Figure 4.1 Absorption (dashed line) and fluorescence emission (solid line) spectra of (a) 4 and (b) 5 in DCM red (-) and CH_3CN black (-). Both dyes were absorbance matched at 0.4 absorbance intensity (a.u).

In methanol, emission is centred at 525 nm and 510 nm for PyLa and PyLa-C_{17}Cer respectively. The emission maxima shift to 552 nm and 562 nm in DCM for each compound and markedly red shifts in acetone to 580 nm and 592 nm respectively. In acetonitrile the behaviour diverges, with PyLa centred at 520 nm and PyLa-C_{17}Cer at 582 nm. Notably, as shown in Table S4.1, the emission quantum yield and lifetime had also significantly diminished for PyLa-C_{17}Cer in this solvent.

Both probes show oxygen independent fluorescence lifetimes that show modest solvent dependence, particularly for PyLa-C_{17}Cer, (Table S4.1). The fluorescence lifetimes of PyLa and PyLa-C_{17}Cer at 4.42 ns and 4.34 ns are comparable in DCM, but the lifetimes of PyLa-C_{17}Cer are shorter by approximately 1 ns compared with PyLa in more polar solvents. PyLa-C_{17}Cer has notably lower quantum yield than PyLa. In DCM, the quantum yield of PyLa is 0.4 compared with 0.1 for PyLa-C_{17}Cer and in acetonitrile PyLa exhibits a quantum yield of 0.49, compared to 0.08 for PyLa-C_{17}Cer.

77 K emission spectra were obtained for both compounds (Figure S4.16–17) in butyronitrile. Importantly from the perspective of fluorescence correlation spectroscopy, there was no evidence of a phosphorescent state, as previously discussed, population of triplet states can contribute interference in the autocorrelation function in FCS.[59]

The molar extinction coefficient of PyLa was determined as > 20,000 M^{-1} cm^{-1} in dichloromethane, acetonitrile and methanol. This value is close to the literature value for other donor acceptor pyrene-based compounds.[46] Ceramide substitution reduces the extinction coefficient across all solvents. Notably, both PyLa and PyLa-C_{17}Cer are almost non-fluorescent in aqueous media. Representative spectra on water titration into methanol solutions are shown in supplemental materials (Figure S4.13-4.14). Since Density Functional Theory (DFT) calculations, vide infra, on PyLa showed very little difference in the lowest energy levels in both dichloromethane and water, an electronic explanation for the impact of water on emission is not clear. (full details of calculations in Appendix C). Aggregation induced quenching due to hydrophobic-hydrophobic interactions in water, may be the origin of the emission extinction. However, in organic solvent, plots of absorbance and emission intensity versus concentration of PyLa and PyLa-C_{17}Cer in dichloromethane over the range 0.5-50 μM yields a straight line (Figure S4.19) suggesting aggregation does not occur in non-polar media at least. Pyrene tends towards π-π stacking and excimer formation[53,59] and absence of this behaviour here, in organic solvent at least, is attributed to the orthogonal orientation of the dimethylaminophenyl groups attached to PyLa.

4.3.4 Computational Studies

To gain more insight into the optical behaviour of the compounds, DFT calculations were performed on the parent pyrene, PyLa, both in the acid or carboxylate form and as a model methyl ester derivative to mimic the ceramide compound. The main purpose of these calculations was to model the lowest energy singlet excited state and to understand if the solvent medium causes a significant change to the optically accessible excited state that might account for the very low emission intensity in water and the negative solvatochromism observed for PyLa. A number of basis sets were used ranging from the large 6-311++G(d,p)[60,61] to the more tractable double zeta quality 6-31G(d)[62–64] or LanL2DZ[65] sets. TDDFT methods were used to characterise transition to singlet excited states and these transition energies were used to simulate the UV/visible spectrum.[66,67] The hybrid density function method (B3LYP) or the Coulomb attenuated model (camB3LYP) were used or these calculations. Calculations were conducted using two solvent media water and dichloromethane (DCM). All model chemistries (method/basis set combinations) explored underestimated the transition energy to the lowest energy singlet state by approximately 3000

cm^{-1} and consequently the smaller 6-31G(d) or LanL2DZ basis sets were considered adequate to simulate the UV/visible spectra (see supporting information for the excitation energies obtained using various basis sets, Appendix C). The large 6-311++G(d,p) basis set was used to model the electron density difference maps of the excited states of the acid and the carboxylate of PyLa.

Notably, the simulated UV/visible spectra of the acid in either water or DCM are similar. The spectrum in water suffers a minor bathochromic shift of some 200 cm^{-1} (Figure 4.2). The nature of the lowest energy singlet state is identical in both solvents and consists mainly of a dimethylaminophenyl-to-pyrene charge-transfer state.

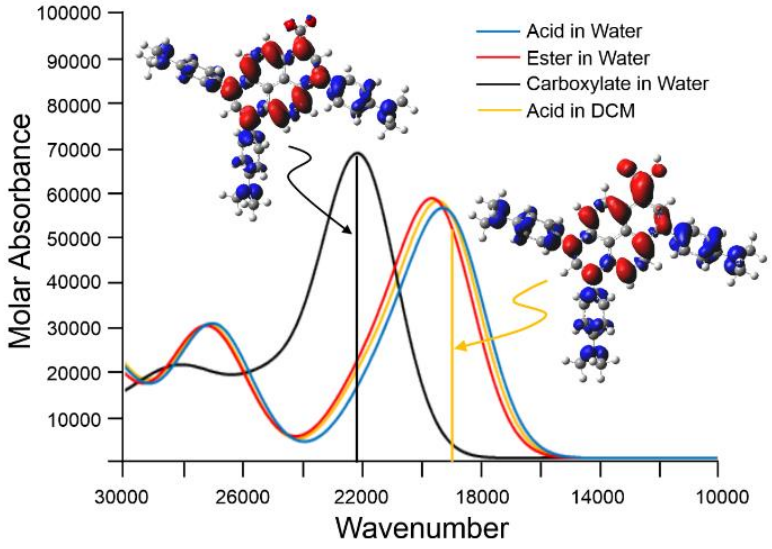

Figure 4.2 The simulated UV/visible spectra (TDDFT/B3LYP/6-31G(d)) of PyLa in water (blue) and DCM (orange) showing the electron density difference map for the first singlet excited state where the regions of reduced electron density compared to the ground state are indicated in blue and the regions of increased electron density in red; the vertical energy to the first excited state is indicated by an orange vertical line, the simulated spectrum of the carboxylate species in water is presented as in black including the electron density difference map for its first singlet excited state indicated by the black vertical line; the spectrum of the methyl ester is red.

Consistent with experiment, a substantial hypsochromic shift of some 2300 cm^{-1} measured in methanol and acetonitrile reflects the formation of the carboxylate species in these solvents. The simulated spectrum of the carboxylate ion exhibits a similar (2700 cm^{-1}) shift

compared to the acid spectrum. Construction of an electron density difference map for its first singlet excited state confirmed that this state is also a dimethylaminophenyl-to-pyrene charge-transfer state.

Media that can facilitate the ionisation of the parent acid will result in the observed hypsochromic shift of both the absorption and emission bands. Obviously, this effect is not observed in the ester compound which lacks an acid functionality, which also explains the much weaker solvent shifts for the ceramide derivatives. To explain the large Stoke's shifts observed for these systems, we examined the changes to the structure in moving from the ground-state (GS) to the lowest singlet state (S_1) in the parent acid compound in water. These calculations were conducted at the B3LYP/LanL2DZ level. The principal structural change in moving from the GS to S_1 involves a change to the relative planes of the pyrene centre and the dimethylaminophenyl units. In the ground state, the average angle between these planes is 48.7 ° while in S_1 the angle drops to 44.7 °. Using the optimised structure for S_1, the TDDFT method was applied to provide the energy difference between the GS at the S_1 geometry and the S_1 at the S_1 optimised geometry. The Stoke's shift predicted by calculation is 1800 cm^{-1}, compared to an experimental shift of approximately 4000 cm^{-1}. It should be stressed that the experimental shift reflects shifts in the band maxima which are subject to distortion because of vibronic coupling.

Thus, as described, computational data indicate that the reduced emission in water is not due to a change in the origin of the optical transition. However, given that the anionic form of the parent pyrene persists in water it is unlikely that aggregation of the pyrene moieties will occur in aqueous environments. Although there is some evidence in baseline drift that might suggest that aggregation is occurring in water the Stokes shift of the emission would preclude self-quenching in aggregates, indeed the material remains emissive in the solid state. A similar light-switch behaviour has been observed for cationic ruthenium systems, where triplet emission is quenched in water but returns when the complex is in a hydrophobic environment. The ability of water to quench emission has been explained by the interaction of the luminescent excited state with water molecules which are hydrogen bonded to uncoordinated peripheral nitrogen atoms on complex. It is possible that a similar process is responsible for quenching the luminescence for the pyrene compounds. Irrespective of the

origin of the reduced emission in water the phenomenon is useful in the context of STED imaging.

4.3.5 Cell Studies

To determine uptake and distribution of the Pyrene series in live cells, HeLa cells were incubated with 2 μM of PyLa or PyLa-C_{17}Cer for 1-6 h to determine uptake. As the Pyrene dyes emit extremely weakly from aqueous solution, live uptake was initially difficult to follow, however emission from the cytoplasmic structures can been seen after 1 h incubation (Figure S4.22) at 37 °C in the absence of light. Figure 4.3A shows PyLa in live HeLa cells after 2 h incubation where it appears to emit brightly from the endoplasmic reticulum. On ceramide substitution, PyLa-C_{17}Cer distributes inside the cell in a similar pattern to PyLa, but in addition localises to brightly stained spherical punctate spots (Figure 4.3B). Both dyes are nuclear excluding and emit brightly within the cell giving high quality images at a low concentration of 2 μM. The Pearson's Coefficient, which quantifies the degree of colocalisation of two fluorophores, was determined to be 0.88 for PyLa and 0.63, for PyLa-C_{17}Cer with ER Tracker Red, signifying a higher degree of colocalisation for PyLa in the ER. In addition, PyLa-C_{17}Cer also localises at lipid droplets present in some of the cells, attributed to the bright punctate spots. This was confirmed by colocalisation studies with Nile Red (Figure 4.3E), a well-known commercial lipid droplet stain. To understand the mechanism of uptake, HeLa cells were incubated with PyLa and PyLa-C_{17}Cer at 4 °C for 4 h. Interestingly, although both dyes remained permeable to the cell membrane at this temperature, there was negligible change in uptake rate or localisation in PyLa at 4 ^{o}C (Figure S4.23) whereas uptake of PyLa-C_{17}Cer was reduced at this temperature and distribution changed, with appearance of PyLa-C_{17}Cer only in the ER without localisation to LDs. This result suggests that in both PyLa and PyLa-C_{17}Cer cell permeation is by passive diffusion whereas uptake by LDs is temperature dependent. This may be due to an active mechanism at the LDs or due to the reduced fluidity of the droplet membranes at lower temperature.

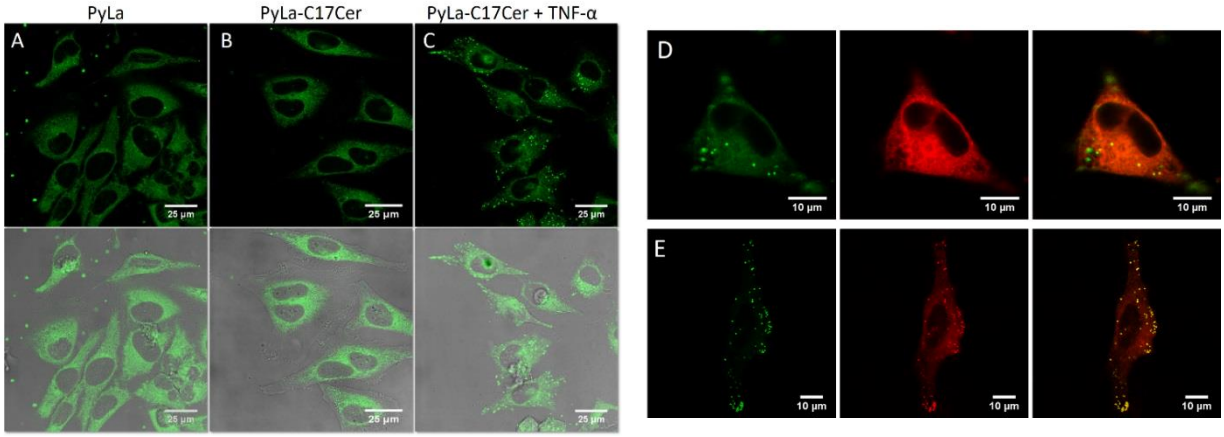

Figure 4.3 Confocal imaging of live HeLa cells stained with 2 µM PyLa (A) and PyLa-C_{17}Cer (B) for 2 h. For LD stimulation HeLa cells were incubated with TNF-α (10 ng/mL) for 16 h in media, and then incubated with PyLa-C_{17}Cer for 2 h (C). All samples were excited at 405 nm and the emission was collected between 520 -620 nm. Pyrene series emission channel and overlays with background fluorescence are shown. Colocalisation of PyLa-C_{17}Cer with ER Tracker RED (D), with PyLa-C_{17}Cer in green, ER Tracker Red in red, and their colocalisation in yellow. Colocalisation of PyLa-C_{17}Cer and Nile red in HeLa cells treated with TNF-α (E), with PyLa-C_{17}Cer in green, Nile Red in red, and their colocalisation in the lipid droplets in yellow

The cytotoxicity of PyLa and PyLa-C_{17}Cer was assessed using the Alamar Blue assay. After 24 h exposure to the Pyrene series, PyLa has an IC_{50} value of 88.1 µM, while interestingly, PyLa-C_{17}Cer exhibits a higher IC_{50} value of 47.9 µM in the absence of light. This may be due to the lipophilicity of the ceramide derivative. Nonetheless it was found that 80 % of the cells remained viable after 24 hours exposure to 5 µM of PyLa-C_{17}Cer, which is more than twice the concentration of 2 µM required for imaging (Figure 4.4). Cell viability was compromised at concentrations exceeding 25 µM for PyLa-C_{17}Cer where it decreases to 60 % but this level of cytotoxicity was not observed until 100 µM of PyLa. The low toxicity under imaging concentrations over long exposure times will allow for imaging over long-time frames. To date there have been relatively few reports of pyrene derivatives in cells, and those reported have shown to induce moderate toxicity on the cells.[68,69]

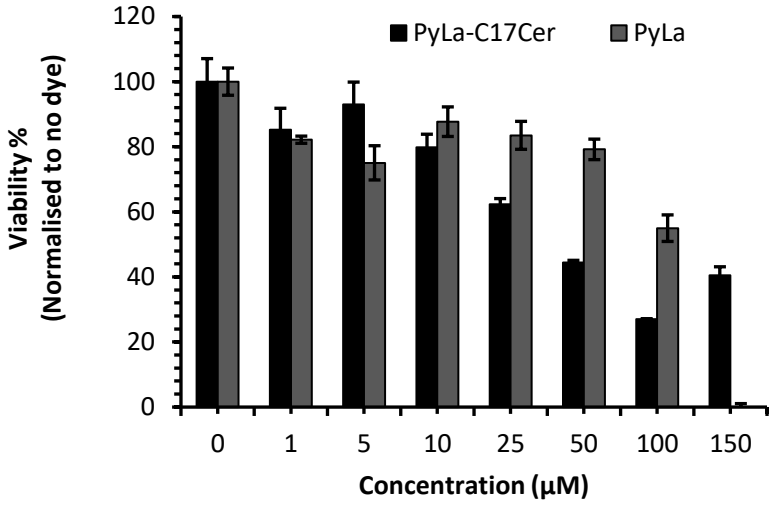

Figure 4.4 Cytotoxicity of PyLa and PyLa-C_{17}Cer in live Hela cells over 24 h in the absence of light. Viability was determined using the Alamar Blue resazurin assay. (n=3).

It is important to note that PyLa-C_{17}Cer does not induce phototoxicity in HeLa cells (Figure S4.24-4.25). To confirm this, live HeLa cells stained with PyLa-C_{17}Cer were irradiated (Ex 405 nm, 0.06 mW/cm^2 compared to 0.03 mW/cm^2) at 5-minute intervals, then imaged to assess cell integrity using DRAQ 7, a commercial viability probe that only enters the nuclei of dead cells. Cells remained viable after 30 minutes continuous irradiation, and cell morphology remained.

To further confirm that the punctate spots observed in cells stained with PyLa-C_{17}Cer were attributable to LDs, we stimulated inflammation in the cells to increase the number of LDs present using TNF-α (Bio-techne Ltd.). TNF-α is a cell signalling protein that has been shown to increase production of LDs. [15] HeLa cells were incubated with TNF-α (10 ng/mL) for 16 h, and PyLa-C_{17}Cer (2 μM) was added to the cells after stimulation. Figure 4.3C shows live HeLa cells, post this process, revealing a dramatic increase in the number of brightly emitting spherical features stained with PyLa-C_{17}Cer**.** Co-staining with Nile Red further confirmed that PyLa-C_{17}Cer and Nile Red colocalise (Figure 4.3E), with a Pearson's Coefficient of 0.73. Interestingly, this process was repeated using the parent compound PyLa, but it was found not to enter the LDs, instead remaining in the ER after TNF-α stimulation (Figure S4.26). LDs are formed at the ER membrane, where neutral-lipid-

synthesising enzymes are located.[70] LD biogenesis occurs when neutral lipids accumulate between the two leaflets of the ER membrane, which are then thought to bud from the ER to form the cytosolic structures.[71,72] The presence of the ceramide tail, a neutral lipid chain, likely promote PyLa-C_{17}Cer's entry to the LD on TNF-α stimulated biogenesis facilitated by its localisation on the ER. As demonstrated, without the ceramide, the probe is unable to enter the LDs.

To evaluate if the probes environment can be distinguished on the basis of fluorescence lifetime in the ER and LDs, fluorescence lifetime imaging of PyLa and PyLa-C_{17}Cer was carried out in live cells. Figure 4.5 shows the confocal fluorescence image and the corresponding false-colour FLIM image of the dyes in live HeLa cells. The fluorescent lifetime of PyLa was measured to be 4 ns in the ER (Figure 4.5 A(iii)). On the other hand, PyLa-C_{17}Cer exhibits bi-exponential fluorescent decay in the LDs of 3.18 ns and 5.9 ns, where 3.18 ns is the prevalent component of the emission decay (81 %), shown in Figure 4.5 B(iii). As the lifetimes of the Pyrene series are not sensitive to oxygen, the changes in lifetimes can be attributed to the lipid environment of the cell. Figure 4.5 D shows the 3D FLIM of a group of lipid droplets stained with PyLa-C_{17}Cer in a live HeLa cell. Here the distribution of the two lifetimes can be seen within the image, where the longer-lived component is localised at the surface and attributed to the tighter packed lipids at the interface of the lipid droplet (red), while the shorter component, which is more abundant is tentative, is attributed to the free lipids in the core of the LD (green).[73–75] LDs can be found to form in clusters, and appear to fuse, a process called LD fusion, where the surface of the initial droplets become continuous and the contents merge.[76] This process gives an elongated spherical profile to the LDs in the X-Z, which is seen in the 3D FLIM image that some LDs are spherical while others are non-elongated and spherical i.e. not in the fusion process (ESI Video 1). But in both types of LDs, the lifetime distribution remains the same.

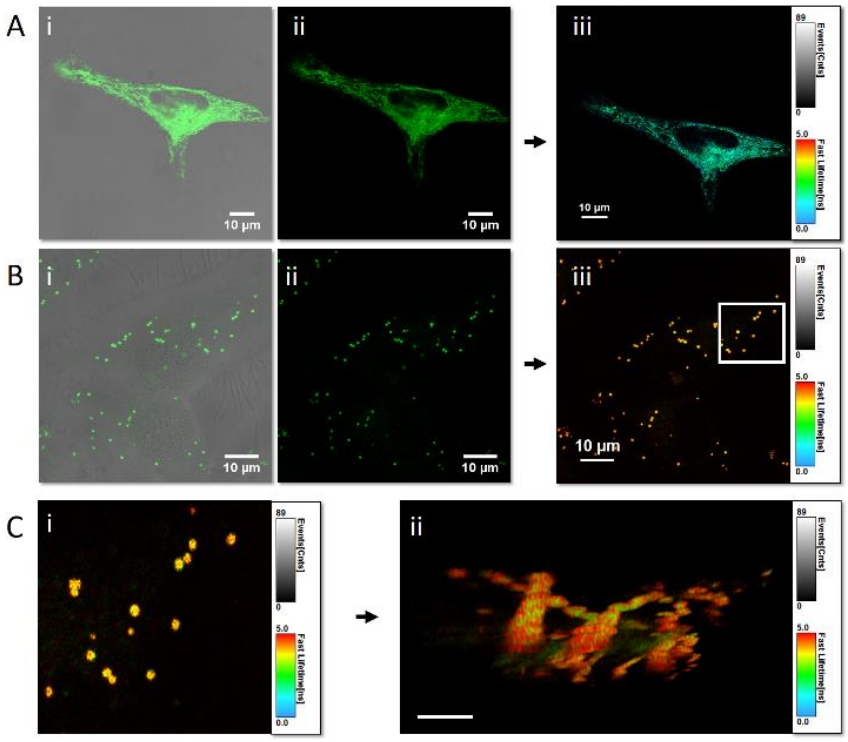

Figure 4.5 FLIM imaging of PyLa and PyLa-C_{17}Cer in live HeLa cells. The corresponding confocal images showing the Pyrene emission channels and overlay with backlight (A (i) and B (i)), the Pyrene emission channel only (A (ii) and B (ii)), and the false-colour fluorescent lifetime images (A (iii) and B (iii)). A close up of a group of lipid droplets (C (i)) highlighted in the white box in B (iii) and 3D FLIM Z-stack through a group of lipid droplets demonstrates the two distinct lifetimes (C (ii)) Scale bar 5 µm.

4.3.6 STED Super-Resolution Imaging of Lipid Droplets in Live HeLa Cells

Given the localisation of PyLa-C_{17}Cer to LDs, which are sub-diffraction limit dimensioned, we examined the performance of PyLa-C_{17}Cer as a STED nanoscopy probe. In this regard, it is essential that the probe be suitable for *live* cell STED and so all of the subsequent experiment and discussion is based on live cells. Figure S4.17 shows the excitation and emission profile of PyLa-C_{17}Cer in DCM and shows that the 660 nm STED depletion laser lies well with the red end of PyLa-C_{17}Cer's emission (—) profile. Live Hela cells were incubated with TNF-α (10 ng/mL) for 16 h, to insure a high number of LDs for imaging, and the cells were stained with PyLa-C_{17}Cer (2 µM, 2 h). Images were obtained using a Leica TSP8 microscope with a 660 nm STED depletion laser, the cells were maintained at 37 ^{o}C during the entire process. Figure 4.6 shows the confocal and corresponding STED images of the resulting live HeLa cells. Both confocal and STED images demonstrate high quality

images at low concentrations and negligible background are obtained (A and B). Figure 4.6 (D,F) focuses on a small region of interest containing LDs. In the confocal image (D) there appears to be a single, large LD with a diameter of 0.864 µm (blue arrow), however by applying STED imaging (F), it is evident that this feature is resolved into 3 distinct LDs with diameters of 0.339 µm, 0.385 µm, and 0.319 µm. Similarly, Figure 4.6 (H) shows a single LD unresolved under confocal, with a diameter of 0.801 µm that is resolved into two well-distinguished LDs of similar size under STED (J), with diameters of 0.341 µm and 0.449 µm. The corresponding plot profile (K) clearly demonstrates the single LD from the confocal image (─) to be resolved to two LDs after applying STED (─). Figure 4.6 not only demonstrates a clear increase in the uniformity of LDs compared to confocal but also a significant increase in resolution is achieved by using PyLa-C_{17}Cer and STED microscopy. This result is important as LDs are known to form in clusters and, the number of LDs has been demonstrated to be a prognostic marker for cancer aggression.[76]

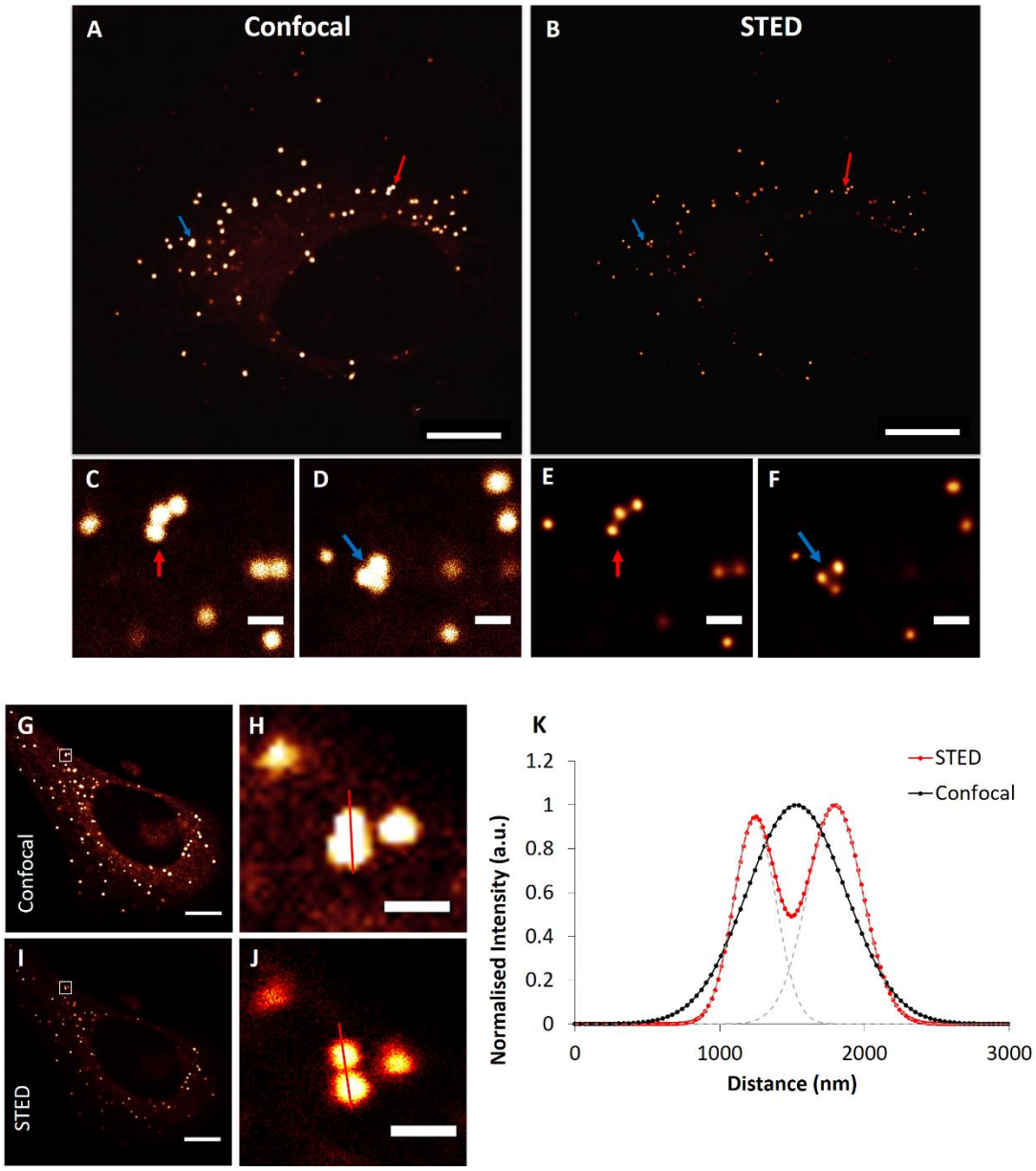

Figure 4.6 Confocal versus STED images of PyLa-C_{17}Cer in live HeLa cells. The blue and red arrows highlight regions of interest in the whole cell (A and B), and their corresponding images focusing on LDs (C and D) showing the improved resolution of LDs after applying STED (E and F). Scale bars = 10 µm and 1 µm. The comparison of confocal versus STED on a second HeLa cell (G and I) zooming in on what appears to be a single lipid droplet in the confocal image (H), is resolved to reveal two separate lipid droplets after applying STED (J). Scale bars = 10 µm and 1 µm. The corresponding plot profile (K) demonstrates the single LD in the confocal image (--) two resolved lipid droplets in the STED image (--) from a single lipid droplet in the confocal. HeLa cells were stimulated with TNF-α (10 ng/mL) for 16 h prior to adding PyLa-C_{17}Cer (2 µM, 2h), and was excited using a 405 nm laser, and depleted using a 660 nm STED laser.

To determine the average size of LDs, images were collected of many HeLa cells. The apparent diameter of LDs was measured (Image J) to obtain the full width half maximum (FWHM) for confocal and STED (Figure S4.31-4.32). We found that LD size ranged 0.41-0.96 μm in confocal, with the average FWHM to be 0.537 ± 0.154 μm. However, STED greatly improved the resolution, where the range of size changed significantly to 0.294 - 0.52 μm, and an average size of 0.384 ± 0.06 μm was recorded. Therefore, enabled by the pyrene ceramide probe resolution was improved in cells by over 100 nm, with significant narrowing of the standard deviation of droplet radii.

STED performance of PyLa-C_{17}Cer indicates it has excellent photostability. Photo resistance is critical in a good STED probe as irreversible photoreaction inhibits stimulated emission and photostability is important for dynamic studies to enable repeated imaging/scanning over time. To confirm photo resistance, we compared the photostability of PyLa-C_{17}Cer to that of Nile Red in live HeLa cells. The cells were imaged under STED conditions continuously for 20 minutes with a pixel dwell time of 2.43 μs and 0.03 W/cm^2 incident laser power to assess for photobleaching. Figure 4.7 shows the normalised log plot decays of the emission intensities at each frame for PyLa-C_{17}Cer and Nile Red (Figure S4.34). As expected, the emission intensity for each, decreases with every acquired STED image. We determined the rate constants for photobleaching as 3 x 10^{-4} s^{-1} for PyLa-C_{17}Cer and 1 x 10^{-3} s^{-1} for Nile Red. The photostability of PyLa-C_{17}Cer is shown to be as good as the commercial probe Nile Red under the same STED imaging conditions, with PyLa-C_{17}Cer bleaching at a slower rate, with greater than 70 % of fluorescence intensity retained after 20 minutes of continuous irradiation, compared with less than 40 % for Nile Red. It is important to note that throughout STED irradiation, the HeLa cells were not compromised, with no evidence of phototoxic effects (Figure S4.34). This result is significant as it indicates the probe is suitable for dynamic STED imaging of live cells over extended periods.

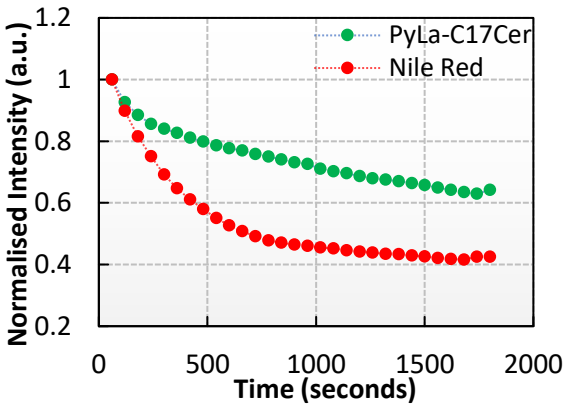

Figure 4.7 Photostability of PyLa-C_{17}Cer (●) and Nile Red (●) over 20 minutes of continuous STED imaging of live HeLa cells. The rate of decay was estimated by fitting the data to a first order decay model and rates of fluorescence intensity loss were determined as 1 x 10^{-3} s^{-1} for Nile Red compared with 3 x 10^{-4} s^{-1} for PyLa-C_{17}Cer. Nile Red was excited at 560 nm and emission collected between 580-670 nm. PyLa-C_{17}Cer was excited at 405 nm, and emission collected between 520-620 nm.

4.3.7 FLIM Studies at Lipid Bilayers

As both PyLa and PyLa-C_{17}Cer selectively stain lipid-rich regions in live mammalian cells, their ability to partition into artificial lipid membranes was also evaluated. Fluorescence lifetime imaging was carried out to ascertain the luminescent lifetimes of PyLa and PyLa-C_{17}Cer when incorporated into lipid bilayers; both at DOPC bilayers and phase-separated lipid composition of DOPC/SM/Chol 4:4:2 mol %.[77] Figure 4.8 shows the false-colour FLIM images of both probes in phase separated lipid bilayers. The average lifetimes are reported in Table 4.2. The measured lifetimes of both PyLa and PyLa-C_{17}Cer conform to bi-exponential decays and it is assumed that the contributing components, as with the LDs reflect the surrounding lipid environment and media. The short components of the decay ranging from 0.89-1.20 ns were observed for both dyes in both DOPC 100 mol % and DOPC/SM/Chol 4:4:2 mol % bilayers. This component is tentatively attributed to probes oriented at the lipid aqueous interface. The long component of the fluorescence decays and their % amplitudes are very similar for PyLa and PyLa-C_{17}Cer across both lipid bilayer compositions. In DOPC (100 mol %) PyLa exhibits a lifetime of 3.62 ns while PyLa-C_{17}Cer is 3.93 ns. Interestingly both dyes are longer-lived when partitioned into the phase separated composition at 4.03 ns for PyLa and 4.06 ns for PyLa-C_{17}Cer. This increase in lifetime is attributed to the increased

rigidity of the lipid bilayer due to the presence of liquid-ordered domains not present in DOPC 100 mol % bilayer.[78]

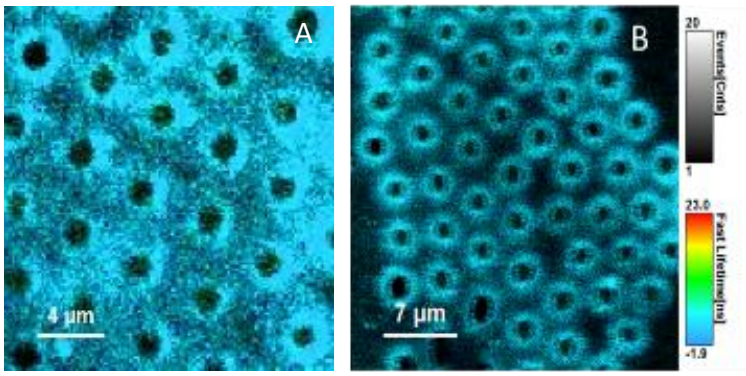

Figure 4.8 Fluorescence lifetime imaging microscopy (FLIM) of PyLa on lipid bilayer of composition DOPC/SM/Chol 4:4:2 mol % (A) and PyLa-C_{17}Cer on lipid bilayer of composition DOPC/SM/Chol 4:4:2 mol % (B). Both dyes were used at a concentration of 10 µM. FLIM image and lifetime were recorded with a 405 nm pulsed laser and the emission was collected using a band pass filter of 550 – 700 nm.

Table 4.1 Fluorescent lifetimes of PyLa and PyLa-C_{17}Cer in lipid bilayers DOPC 100 mol % and DOPC/SM/Chol 4:4:2 mol %

	Ex/Em	**Bilayer DOPC 100 mol %**		**Bilayer DOPC/SM/Chol 4/4/2 mol %**	
	λ (nm)	τ (ns)	τ_{Amp} (%)	τ (ns)	τ_{Amp} (%)
PyLa	405/550	τ_1 = 3.62	62	τ_1 = 4.03	57
		τ_2 = 0.89	38	τ_2 = 1.20	43
PyLa-C_{17}Cer	523/550	τ_1 = 3.93	44	τ_1 = 4.06	48
		τ_2 = 0.95	56	τ_2 = 0.95	52

4.3.8 Later Mobility of PyLa-C_{17}Cer in Suspended Lipid Bilayers

We then evaluated PyLa-C_{17}Cer as a probe in fluorescence correlation spectroscopy whereby it was included in a microcavity supported lipid bilayer.[33] Diffusion studies were carried out on DOPC 100 mol % bilayers and on DOPC/SM/Chol 4:4:2 mol % compositions suspended across the microcavities. We have shown previously that MSLBs exhibit the fluidity of liposomes but with much improved stability and addressability. The bilayers were labelled with PyLa-C_{17}Cer at a concentration of 10 nM which constitutes approximately a ratio of

1:50,000 dye:lipid. To accurately identify and distinguish the bilayer at the top planar regions of the array and bilayer suspended over the cavities for the FLCS experiment, both reflectance and fluorescence images were recorded (Figure 4.7 A, B and C). Autocorrelation functions (ACFs) were then recorded for bilayer at each (planar and cavity) surface region. The ACFs obtained were fit to the 2-dimensional model described in equation 4.1 to obtain the lateral diffusion coefficient of PyLa-C_{17}Cer in the bilayer.

$$G(\tau) = \frac{1}{N(1-T)}\left[1 - T + Te^{\left(-\frac{\tau}{\tau_T}\right)}\right]\left[1 + \left(\frac{\tau}{\tau_D}\right)^{\alpha}\right]^{-1} \quad \text{Equation 4.1}$$

Where G(τ) is the autocorrelation function of fluorescence fluctuations; N is the average number of diffusing fluorophores in the effective volume; τ is the delay time; T is the fraction of molecules in the triplet state; α is the anomalous parameter; τ_D is the diffusion time of the molecules and τ_T is the decay time for the triplet state. The lateral diffusion of Py-C_{17}Cer was obtained from transient 2-D time by the following relation $D = \omega^2/\tau_D$. In order to determine the confocal volume using excitation 450 nm, a reference dye Atto-425 in water at 25 °C 438 $\mu m^2.s^{-1}$ was used to calibrate the system.[79] Figure 4.9 (g) shows the autocorrelation functions obtained for PyLa-C_{17}Cer in MSLBs comprised of DOPC and the ternary lipid mixture. The ACFs are of high quality with no evidence for artefactual effects, e.g. from triplet state. Fitting these functions (solid lines) to equation 4.1, the lateral diffusion of PyLa-C_{17}Cer in a DOPC suspended lipid bilayer above filled microcavities was found to be 10.18 ± 1.8 $\mu m^2.s^{-1}$. The α coefficient was 0.99 ± 0.02, suggesting that the diffusion is normal Brownian. This value is consistent with previous reports for phospholipid membranes at microcavity arrays, e.g. for a DOPC lipid bilayers, Basit *et al* found comparable diffusion coefficient for DOPE-Atto655 from FLCS.[33] GUVs have also shown comparable diffusion values for membranes composed of DOPC.[80]

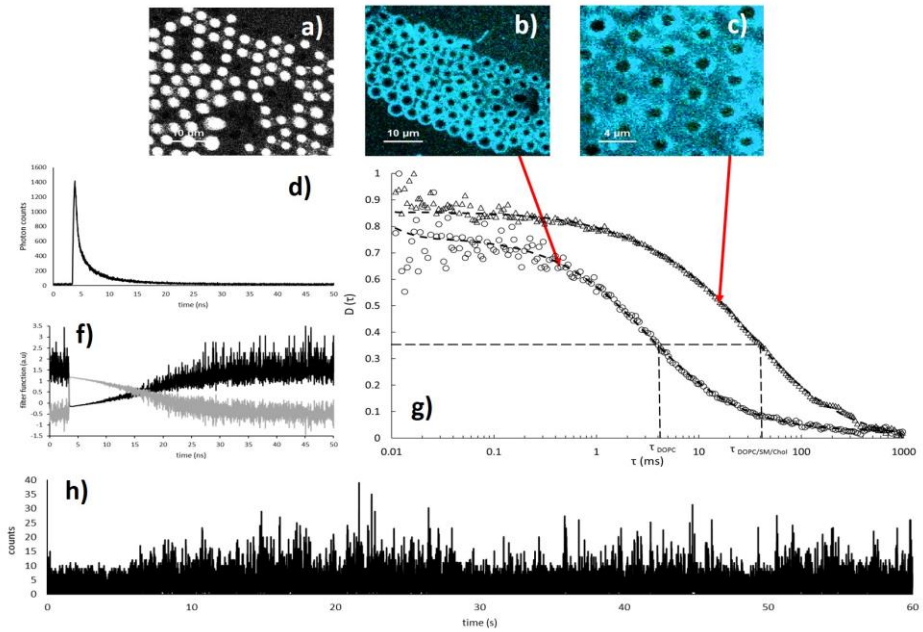

Figure 4.9 Confocal images of spanned lipid bilayers on microcavities array. (a) shows reflectance images collected using OD3 filter to position the laser on cavities; (b) and (c) shows the fluorescence of PyLa-C_{17}Cer on lipid bilayers at 10 nM in (a) DOPC and (b) DOPC/SM/Chol. (d) and (f) shows the removal of background acquired by Fluorescence Lifetime Correlation Spectroscopy (FLCS): (d) photon histogram from time correlated single photon counting (TCSPC) and (f) FLCS filters from signal (black) and background (grey); (g) Normalised autocorrelation functions (ACFs) for PyLa-C_{17}Cer above buffer filled microcavities for DOPC (circles) and DOPC/SM/Chol (2:2:1) (triangles). Fitted ACF curves (dash line). h) Fluctuating photon-count time trace from a single point measurement (60 s) in the lipid membrane plan for DOPC lipid bilayer.

By comparison at the ternary microcavity supported bilayer; DOPC/SM/Cholesterol (4:4:2), the diffusion coefficient of PyLa-C_{17}Cer found was determined as 0.59 ± 0.09 $\mu m^2.s^{-1}$, with α coefficient of 0.87 ± 0.12. The low diffusion and α values indicate that PyLa-C_{17}Cer partitions to liquid-ordered domains, as similar mobility was found for such ordered phases in GUVs and α coefficient < 1, indicates that ceramide is in a lipid enclosed environment formed by obstacles to its diffusion.[39] This is, to the best of our knowledge the first example of a pyrene-lipid conjugate applied to fluorescence correlation spectroscopy. The suitability of this probe to FCS is consistent with its performance in STED where many of the same characteristics are required. Our data suggests that this probe is well suited to advanced microscopy techniques such as STED/FCS (Table 4.2).

Table 4.2 Fluorescence correlation spectroscopy data for PyLa-C_{17}Cer in supported lipid bilayers of composition DOPC 100 mol % and DOPC/SM/Chol 4:4:2 mol %.

	Lipid Bilayer Composition	Diffusion Coefficient [μm²/s]	α	N
PyLa-C_{17}Cer	**DOPC 100 mol %**	10.18 ± 1.8	0.99 ± 0.02	6.17 ± 2.38
	DOPC/SM/Chol 4:4:2 mol %	0.59 ± 0.09	0.87 ± 0.12	3.64 ± 1.08

*Concentration of dye used was 10 nM. Mean and standard deviations obtained from at least 20 different measurements across two samples.

4.4 Conclusion

Pyrene-based Donor-Acceptor derivatives that exhibit intense emission in non-aqueous media with weak emission from water were prepared as bio-probes for lipid droplets and membranous structures. When conjugated to a ceramide tail the pyrene probe specifically targets with high selectivity, lipid droplets in live cells. The outstanding photostability of these compounds their mega-Stokes shifted emission and low background from aqueous regions enabled multi-modal imaging of LDs in live HeLa cells. To obtain super resolution imaging by stimulated emission depletion microscopy requires high photostability and it was shown that PyLa-C_{17}Cer performs to a high standard when compared to Nile Red. The pyrene probe provided resolution of droplets separated by less than 80 nm and the average droplet diameter could be accurately measured wherein it had been assessed as 894 nm from confocal imaging, it was determined as 294 nm by STED. The impact of TNF-α treatment of live HeLa cells in terms of droplet number and density could be readily followed using this probe by STED microscopy. The high intensity emission of the probe meant it was suitable for imaging at concentrations much lower than its IC_{50}. Using fluorescence lifetime imaging two different lipid environments could distinguished. Given the similar demands of STED and fluorescence correlation spectroscopy we then evaluated the ceramide probe for study of lipid diffusion using FCS using microcavity supported lipid bilayers labelled with the ceramide probe. The negligible triplet yield from the pyrene probes, their photostability and high quantum yielded excellent auto-correlation functions from which diffusion coefficients

for 100 % DOPC bilayers were obtained as 10.18 ± 1.8 compared with 0.59 ± 0.09 for a phase forming lipid composition of DOPC/SM/Chol 4:4:2 mol %. The data indicates significant partitioning of the ceramide probe into the liquid ordered phase of the MSLBs.

This, to our knowledge, is the first example of a pyrene derivative used in super-resolution STED microscopy and one of the first examples of LD imaging in live cells by STED. The work highlights the value of using charge transfer luminophores in STED and demonstrates the use of ceramide to drive targeting of LDs. We hope that the multimodal probes demonstrated here will facilitate dynamic studies into lipid droplet biogenesis and quantitation in live cells advancing understanding of these important organelles.

4.5 Supporting Material

Supplementary data associated with this chapter can be found in Appendix C.

4.6 References

(1) Walther, T. C.; Farese, R. V. Lipid Droplets and Cellular Lipid Metabolism. *Annu. Rev. Biochem.* **2012**, *81* (1), 687–714.

(2) Brasaemle, D. L. Thematic Review Series: Adipocyte Biology. The Perilipin Family of Structural Lipid Droplet Proteins: Stabilization of Lipid Droplets and Control of Lipolysis. *J. Lipid Res.* **2007**, *48* (12), 2547–2559.

(3) Bickel, P. E.; Tansey, J. T.; Welte, M. A. PAT Proteins, an Ancient Family of Lipid Droplet Proteins That Regulate Cellular Lipid Stores. *Biochim. Biophys. Acta* **2009**, *1791* (6), 419–440.

(4) Kimmel, A. R.; Brasaemle, D. L.; McAndrews-Hill, M.; Sztalryd, C.; Londos, C. Adoption of PERILIPIN as a Unifying Nomenclature for the Mammalian PAT-Family of Intracellular Lipid Storage Droplet Proteins. *J. Lipid Res.* **2010**, *51* (3), 468–471.

(5) The Perilipins: Major Cytosolic Lipid Droplet–Associated Proteins and Their Roles in Cellular Lipid Storage, Mobilization, and Systemic Homeostasis | Annual Review of Nutrition https://www.annualreviews.org/doi/10.1146/annurev-nutr-071813-105410 (accessed Apr 20, 2018).

(6) Wang, J.-B.; Fang, X.-Q.; Pan, X.; Dai, S.-Y.; Song, Q.-H. New 2, 6-Modified Bodipy Sensitizers for Dye-Sensitized Solar Cells. *Chem. - Asian J.* **2012**, *7* (4), 696–700.

(7) Zehmer, J. K.; Huang, Y.; Peng, G.; Pu, J.; Anderson, R. G. W.; Liu, P. A Role for Lipid Droplets in Inter-Membrane Lipid Traffic. *Proteomics* **2009**, *9* (4), 914–921.

(8) Bozza, P. T.; Viola, J. P. B. Lipid Droplets in Inflammation and Cancer. *Prostaglandins Leukot. Essent. Fat. Acids PLEFA* **2010**, *82* (4–6), 243–250.

(9) Herker, E.; Harris, C.; Hernandez, C.; Carpentier, A.; Kaehlcke, K.; Rosenberg, A. R.; Farese, R. V.; Ott, M. Efficient Hepatitis C Virus Particle Formation Requires Diacylglycerol Acyltransferase-1. *Nat. Med.* **2010**, *16* (11), 1295–1298.
(10) Tirinato, L.; Pagliari, F.; Limongi, T.; Marini, M.; Falqui, A.; Seco, J.; Candeloro, P.; Liberale, C.; Di Fabrizio, E. An Overview of Lipid Droplets in Cancer and Cancer Stem Cells. *Stem Cells Int.* **2017**, *2017*, 1656053.
(11) Abramczyk, H.; Surmacki, J.; Kopeć, M.; Olejnik, A. K.; Lubecka-Pietruszewska, K.; Fabianowska-Majewska, K. The Role of Lipid Droplets and Adipocytes in Cancer. Raman Imaging of Cell Cultures: MCF10A, MCF7, and MDA-MB-231 Compared to Adipocytes in Cancerous Human Breast Tissue. *The Analyst* **2015**, *140* (7), 2224–2235.
(12) Camus, G.; Vogt, D. A.; Kondratowicz, A. S.; Ott, M. Lipid Droplets and Viral Infections. In *Methods in Cell Biology*; Elsevier, 2013; Vol. 116, pp 167–190.
(13) Onal, G.; Kutlu, O.; Gozuacik, D.; Dokmeci Emre, S. Lipid Droplets in Health and Disease. *Lipids Health Dis.* **2017**, *16* (128), 1-15.
(14) Dinish, U. S.; Wong, C. L.; Sriram, S.; Ong, W. K.; Balasundaram, G.; Sugii, S.; Olivo, M. Diffuse Optical Spectroscopy and Imaging to Detect and Quantify Adipose Tissue Browning. *Sci. Rep.* **2017**, 7(41357), 1–11.
(15) Czamara, K.; Majzner, K.; Selmi, A.; Baranska, M.; Ozaki, Y.; Kaczor, A. Unsaturated Lipid Bodies as a Hallmark of Inflammation Studied by Raman 2D and 3D Microscopy. *Sci. Rep.* **2017**, *7*, 40889.
(16) Kochan, K.; Maslak, E.; Krafft, C.; Kostogrys, R.; Chlopicki, S.; Baranska, M. Raman Spectroscopy Analysis of Lipid Droplets Content, Distribution and Saturation Level in Non-Alcoholic Fatty Liver Disease in Mice. *J. Biophotonics* **2015**, *8* (7), 597–609.
(17) Aboumrad, M. H.; Horn, R. C.; Fine, G. Lipid-Secreting Mammary Carcinoma. Report of a Case Associated with Paget's Disease of the Nipple. *Cancer* **1963**, *16*, 521–525.
(18) Scalfi-Happ, C.; Udart, M.; Hauser, C.; Rück, A. Investigation of Lipid Bodies in a Colon Carcinoma Cell Line by Confocal Raman Microscopy. *Med. Laser Appl.* **2011**, *26* (4), 152–157.
(19) Thiam, A. R.; Farese Jr, R. V.; Walther, T. C. The Biophysics and Cell Biology of Lipid Droplets. *Nat. Rev. Mol. Cell Biol.* **2013**, *14* (12), 775–786.
(20) Suzuki, M.; Shinohara, Y.; Ohsaki, Y.; Fujimoto, T. Lipid Droplets: Size Matters. *J. Electron Microsc. (Tokyo)* **2011**, *60* (suppl_1), S101–S116.
(21) Zheng, X.; Zhu, W.; Ni, F.; Ai, H.; Yang, C. A Specific Bioprobe for Super-Resolution Fluorescence Imaging of Lipid Droplets. *Sens. Actuators B Chem.* **2018**, *255*, 3148–3154.
(22) Wegel, E.; Göhler, A.; Lagerholm, B. C.; Wainman, A.; Uphoff, S.; Kaufmann, R.; Dobbie, I. M. Imaging Cellular Structures in Super-Resolution with SIM, STED and Localisation Microscopy: A Practical Comparison. *Sci. Rep.* **2016**, *6* (1).
(23) Lukinavičius, G.; Mitronova, G. Y.; Schnorrenberg, S.; Butkevich, A. N.; Barthel, H.; Belov, V. N.; Hell, S. W. Fluorescent Dyes and Probes for Super-Resolution

Microscopy of Microtubules and Tracheoles in Living Cells and Tissues. *Chem. Sci.* **2018**, *9* (13), 3324–3334.

(24) Bordenave, M. D.; Balzarotti, F.; Stefani, F. D.; Hell, S. W. STED Nanoscopy with Wavelengths at the Emission Maximum. *J. Phys. Appl. Phys.* **2016**, *49* (36), 365102.

(25) Lavis, L. D.; Raines, R. T. Bright Building Blocks for Chemical Biology. *ACS Chem. Biol.* **2014**, *9* (4), 855–866.

(26) Grimm, J. B.; English, B. P.; Chen, J.; Slaughter, J. P.; Zhang, Z.; Revyakin, A.; Patel, R.; Macklin, J. J.; Normanno, D.; Singer, R. H.; et al. A General Method to Improve Fluorophores for Live-Cell and Single-Molecule Microscopy. *Nat. Methods* **2015**, *12* (3), 244–250.

(27) Inglese, J.; Johnson, R. L.; Simeonov, A.; Xia, M.; Zheng, W.; Austin, C. P.; Auld, D. S. High-Throughput Screening Assays for the Identification of Chemical Probes. *Nat. Chem. Biol.* **2007**, *3* (8), 466–479.

(28) Hilderbrand, S. A.; Weissleder, R. Near-Infrared Fluorescence: Application to in Vivo Molecular Imaging. *Curr. Opin. Chem. Biol.* **2010**, *14* (1), 71–79.

(29) Lukinavičius, G.; Umezawa, K.; Olivier, N.; Honigmann, A.; Yang, G.; Plass, T.; Mueller, V.; Reymond, L.; Corrêa, I. R.; Luo, Z.-G.; et al. A near-Infrared Fluorophore for Live-Cell Super-Resolution Microscopy of Cellular Proteins. *Nat. Chem.* **2013**, *5* (2), 132–139.

(30) Byrne, A.; Burke, C. S.; Keyes, T. E. Precision Targeted ruthenium(II) Luminophores; Highly Effective Probes for Cell Imaging by Stimulated Emission Depletion (STED) Microscopy. *Chem. Sci.* **2016**, *7* (10), 6551–6562.

(31) Melo, A. M.; Prieto, M.; Coutinho, A. Quantifying Lipid-Protein Interaction by Fluorescence Correlation Spectroscopy (FCS). In *Fluorescence Spectroscopy and Microscopy*; Methods in Molecular Biology; Humana Press, Totowa, NJ, 2014; pp 575–595.

(32) Langowski, J. Protein-Protein Interactions Determined by Fluorescence Correlation Spectroscopy. *Methods Cell Biol.* **2008**, *85*, 471–484.

(33) Basit, H.; Gaul, V.; Maher, S.; Forster, R. J.; Keyes, T. E. Aqueous-Filled Polymer Microcavity Arrays: Versatile & Stable Lipid Bilayer Platforms Offering High Lateral Mobility to Incorporated Membrane Proteins. *The Analyst* **2015**, *140* (9), 3012–3018.

(34) García-Sáez, A. J.; Schwille, P. Single Molecule Techniques for the Study of Membrane Proteins. *Appl. Microbiol. Biotechnol.* **2007**, *76* (2), 257–266.

(35) Posokhov, Y. O.; Rodnin, M. V.; Das, S. K.; Pucci, B.; Ladokhin, A. S. FCS Study of the Thermodynamics of Membrane Protein Insertion into the Lipid Bilayer Chaperoned by Fluorinated Surfactants. *Biophys. J.* **2008**, *95* (8), L54–L56.

(36) Chiantia, S.; Ries, J.; Schwille, P. Fluorescence Correlation Spectroscopy in Membrane Structure Elucidation. *Biochim. Biophys. Acta BBA - Biomembr.* **2009**, *1788* (1), 225–233.

(37) Sezgin, E.; Levental, I.; Grzybek, M.; Schwarzmann, G.; Mueller, V.; Honigmann, A.; Belov, V. N.; Eggeling, C.; Coskun, Ü.; Simons, K.; et al. Partitioning, Diffusion, and Ligand Binding of Raft Lipid Analogs in Model and Cellular Plasma Membranes. *Biochim. Biophys. Acta BBA - Biomembr.* **2012**, *1818* (7), 1777–1784.

(38) Kahya, N.; Scherfeld, D.; Bacia, K.; Poolman, B.; Schwille, P. Probing Lipid Mobility of Raft-Exhibiting Model Membranes by Fluorescence Correlation Spectroscopy. *J. Biol. Chem.* **2003**, *278* (30), 28109–28115.

(39) Kahya, N.; Scherfeld, D.; Bacia, K.; Schwille, P. Lipid Domain Formation and Dynamics in Giant Unilamellar Vesicles Explored by Fluorescence Correlation Spectroscopy. *J. Struct. Biol.* **2004**, *147* (1), 77–89.

(40) Gaul, V.; Lopez, S. G.; Lentz, B. R.; Moran, N.; Forster, R. J.; Keyes, T. E. The Lateral Diffusion and Fibrinogen Induced Clustering of Platelet Integrin αIIbβ3 Reconstituted into Physiologically Mimetic GUVs. *Integr. Biol. Quant. Biosci. Nano Macro* **2015**, *7* (4), 402–411.

(41) Greenspan, P.; Mayer, E. P.; Fowler, S. D. Nile Red: A Selective Fluorescent Stain for Intracellular Lipid Droplets. *J. Cell Biol.* **1985**, *100* (3), 965–973.

(42) *Life Technologies Https://www.thermofisher.com/*.

(43) Loudet, A.; Burgess, K. BODIPY Dyes and Their Derivatives: Syntheses and Spectroscopic Properties. *Chem. Rev.* **2007**, *107* (11), 4891–4932.

(44) França, B. M. de; Bello Forero, J. S.; Garden, S. J.; Ribeiro, E. S.; Souza, R. da S.; Teixeira, R. S.; Corrêa, R. J. Green Fluorescence Pyrene-Based Dye as a New π-Extended System: Synthesis, Photophysical and Theoretical Studies. *Dyes Pigments* **2018**, *148*, 444–451.

(45) Feng, X.; Hu, J.-Y.; Iwanaga, F.; Seto, N.; Redshaw, C.; Elsegood, M. R. J.; Yamato, T. Blue-Emitting Butterfly-Shaped 1,3,5,9-Tetraarylpyrenes: Synthesis, Crystal Structures, and Photophysical Properties. *Org. Lett.* **2013**, *15* (6), 1318–1321.

(46) Niko, Y.; Sasaki, S.; Narushima, K.; Sharma, D. K.; Vacha, M.; Konishi, G. 1-, 3-, 6-, and 8-Tetrasubstituted Asymmetric Pyrene Derivatives with Electron Donors and Acceptors: High Photostability and Regioisomer-Specific Photophysical Properties. *J. Org. Chem.* **2015**, *80* (21), 10794–10805.

(47) Zhan, Y.; Peng, J.; Ye, K.; Xue, P.; Lu, R. Pyrene Functionalized Triphenylamine-Based Dyes : Synthesis, Photophysical Properties and Applications in OLEDs. *Org. Biomol. Chem.* **2013**, *11* (39), 6814–6823.

(48) Crawford, A. G.; Dwyer, A. D.; Liu, Z.; Steffen, A.; Beeby, A.; Pålsson, L.-O.; Tozer, D. J.; Marder, T. B. Experimental and Theoretical Studies of the Photophysical Properties of 2- and 2,7-Functionalized Pyrene Derivatives. *J. Am. Chem. Soc.* **2011**, *133* (34), 13349–13362.

(49) Ji, L.; Krummenacher, I.; Friedrich, A.; Lorbach, A.; Haehnel, M.; Edkins, K.; Braunschweig, H.; Marder, T. B. Synthesis, Photophysical, and Electrochemical Properties of Pyrenes Substituted with Donors or Acceptors at the 4- or 4,9-Positions. *J. Org. Chem.* **2018**, *83* (7), 3599–3606.

(50) Merz, J.; Fink, J.; Friedrich, A.; Krummenacher, I.; Al Mamari, H. H.; Lorenzen, S.; Haehnel, M.; Eichhorn, A.; Moos, M.; Holzapfel, M.; et al. Pyrene Molecular Orbital Shuffle—Controlling Excited State and Redox Properties by Changing the Nature of the Frontier Orbitals. *Chem. – Eur. J.* **2017**, *23* (53), 13164–13180.

(51) Li, S.-S.; Jiang, K.-J.; Yu, C.-C.; Huang, J.-H.; Yang, L.-M.; Song, Y.-L. A 2,7-Pyrene-Based Dye for Solar Cell Application. *New J. Chem.* **2014**, *38*, 4404.

(52) Niko, Y.; Didier, P.; Mely, Y.; Konishi, G.; Klymchenko, A. S. Bright and Photostable Push-Pull Pyrene Dye Visualizes Lipid Order Variation between Plasma and Intracellular Membranes. *Sci. Rep.* **2016**, *6*, 18870.

(53) Haedler, A. T.; Misslitz, H.; Buehlmeyer, C.; Albuquerque, R. Q.; Köhler, A.; Schmidt, H.-W. Controlling the π-Stacking Behavior of Pyrene Derivatives: Influence of H-Bonding and Steric Effects in Different States of Aggregation. *ChemPhysChem* **2013**, *14* (9), 1818–1829.

(54) Sankararaman, S.; Venkataramana, G.; Varghese, B. Conformational Isomers from Rotation of Diacetylenic Bond in an Ethynylpyrene-Substituted Molecular Hinge. *J. Org. Chem.* **2008**, *73* (6), 2404–2407.

(55) Rajakumar, P.; Visalakshi, K.; Ganesan, S.; Maruthamuthu, P.; Suthanthiraraj, S. A. Synthesis of Pyrene-Based Ester Dendrimers for Applications in Dye-Sensitized Solar Cells. *Bull. Chem. Soc. Jpn.* **2012**, *85* (8), 902–911.

(56) Neises, B.; Steglich, W. Simple Method for the Esterification of Carboxylic Acids. *Angew. Chem. Int. Ed. Engl.* **1978**, *17* (7), 522–524.

(57) O'Connor, D.; Byrne, A.; Dolan, C.; Keyes, T. E. Phase Partitioning, Solvent-Switchable BODIPY Probes for High Contrast Cellular Imaging and FCS. *New J. Chem.* **2018**, *42* (5), 3671–3682.

(58) Fu, Y.; Finney, N. S. Small-Molecule Fluorescent Probes and Their Design. *RSC Adv.* **2018**, *8* (51), 29051–29061.

(59) Ito, F.; Kakiuchi, T.; Sakano, T.; Nagamura, T. Fluorescence Properties of Pyrene Derivative Aggregates Formed in Polymer Matrix Depending on Concentration. *Phys. Chem. Chem. Phys.* **2010**, *12* (36), 10923–10927.

(60) Petersson, G. A.; Al-Laham, M. A. A Complete Basis Set Model Chemistry. II. Open-shell Systems and the Total Energies of the First-row Atoms. *J. Chem. Phys.* **1991**, *94* (9), 6081–6090.

(61) Petersson, G. A.; Bennett, A.; Tensfeldt, T. G.; Al-Laham, M. A.; Shirley, W. A.; Mantzaris, J. A Complete Basis Set Model Chemistry. I. The Total Energies of Closed-shell Atoms and Hydrides of the First-row Elements. *J. Chem. Phys.* **1988**, *89* (4), 2193–2218.

(62) Ditchfield, R.; Hehre, W. J.; Pople, J. A. Self-Consistent Molecular-Orbital Methods. IX. An Extended Gaussian-Type Basis for Molecular-Orbital Studies of Organic Molecules. *J. Chem. Phys.* **1971**, *54* (2), 724–728.

(63) Hehre, W. J.; Ditchfield, R.; Pople, J. A. Self—Consistent Molecular Orbital Methods. XII. Further Extensions of Gaussian—Type Basis Sets for Use in Molecular Orbital Studies of Organic Molecules. *J. Chem. Phys.* **1972**, *56* (5), 2257–2261.

(64) Hariharan, P. C.; Pople, J. A. The Influence of Polarization Functions on Molecular Orbital Hydrogenation Energies. *Theor. Chim. Acta* **1973**, *28* (3), 213–222.

(65) *Dunning Jr, T. H.; Hay, P. J., Modern Theoretical Chemistry. In Modern Theoretical Chemistry, Schaefer III, H. F., Ed. Plenum Press: New York, 1977; Vol. 3.*

(66) Stratmann, R. E.; Scuseria, G. E.; Frisch, M. J. An Efficient Implementation of Time-Dependent Density-Functional Theory for the Calculation of Excitation Energies of Large Molecules. *J. Chem. Phys.* **1998**, *109* (19), 8218–8224.

(67) Bauernschmitt, R.; Ahlrichs, R. Treatment of Electronic Excitations within the Adiabatic Approximation of Time Dependent Density Functional Theory. *Chem. Phys. Lett.* **1996**, *256* (4), 454–464.

(68) Lewkowski, J.; Rodriguez Moya, M.; Wrona-Piotrowicz, A.; Zakrzewski, J.; Kontek, R.; Gajek, G. Synthesis, Fluorescence Properties and the Promising Cytotoxicity of Pyrene–derived Aminophosphonates. *Beilstein J. Org. Chem.* **2016**, *12*, 1229–1235.

(69) Chao, J.; Wang, H.; Zhang, Y.; Yin, C.; Huo, F.; Sun, J.; Zhao, M. A Novel Pyrene-Based Dual Multifunctional Fluorescent Probe for Differential Sensing of pH and HSO_3^- and Their Bioimaging in Live Cells. *New J. Chem.* **2018**, *42* (5), 3322–3333.

(70) Mishra, S.; Khaddaj, R.; Cottier, S.; Stradalova, V.; Jacob, C.; Schneiter, R. Mature Lipid Droplets Are Accessible to ER Luminal Proteins. *J. Cell Sci.* **2016**, *129* (20), 3803–3815.

(71) Szymanski, K. M.; Binns, D.; Bartz, R.; Grishin, N. V.; Li, W.-P.; Agarwal, A. K.; Garg, A.; Anderson, R. G.; Goodman, J. M. The Lipodystrophy Protein Seipin Is Found at Endoplasmic Reticulum Lipid Droplet Junctions and Is Important for Droplet Morphology. *Proc. Natl. Acad. Sci.* **2007**, *104* (52), 20890–20895.

(72) Salo, V. T.; Belevich, I.; Li, S.; Karhinen, L.; Vihinen, H.; Vigouroux, C.; Magré, J.; Thiele, C.; Hölttä-Vuori, M.; Jokitalo, E.; et al. Seipin Regulates ER–lipid Droplet Contacts and Cargo Delivery. *EMBO J.* **2016**, *35* (24), 2699–2716.

(73) Byrne, A.; Dolan, C.; Moriarty, R. D.; Martin, A.; Neugebauer, U.; Forster, R. J.; Davies, A.; Volkov, Y.; Keyes, T. E. Osmium(II) Polypyridyl Polyarginine Conjugate as a Probe for Live Cell Imaging; a Comparison of Uptake, Localization and Cytotoxicity with Its ruthenium(II) Analogue. *Dalton Trans* **2015**, *44* (Journal Article), 14323–14332.

(74) Stöckl, M. T.; Herrmann, A. Detection of Lipid Domains in Model and Cell Membranes by Fluorescence Lifetime Imaging Microscopy. *Microsc. Imaging Membr. Domains* **2010**, *1798* (7), 1444–1456.

(75) Suhling, K.; French, P. M. W.; Phillips, D. Time-Resolved fluorescence Microscopy. *Photochem Photobiol Sci* **2005**, *4* (Journal Article), 13–22.

(76) Murphy, S.; Martin, S.; Parton, R. G. Quantitative Analysis of Lipid Droplet Fusion: Inefficient Steady State Fusion but Rapid Stimulation by Chemical Fusogens. *PLoS ONE* **2010**, *5* (12), e15030.
(77) Bezlyepkina, N.; Gracià, R. S.; Shchelokovskyy, P.; Lipowsky, R.; Dimova, R. Phase Diagram and Tie-Line Determination for the Ternary Mixture DOPC/eSM/cholesterol. *Biophys. J.* **2013**, *104* (7), 1456–1464.
(78) Demchenko, A. P. *Advanced Fluorescence Reporters in Chemistry and Biology I: Fundamentals and Molecular Design*; Springer Science & Business Media, 2010.
(79) Štefl, M.; Benda, A.; Gregor, I.; Hof, M. The Fast Polarization Modulation Based Dual-Focus Fluorescence Correlation Spectroscopy. *Opt. Express* **2014**, *22* (1), 885.
(80) Heinemann, F.; Betaneli, V.; Thomas, F. A.; Schwille, P. Quantifying Lipid Diffusion by Fluorescence Correlation Spectroscopy: A Critical Treatise. *Langmuir ACS J. Surf. Colloids* **2012**, *28* (37), 13395–13404.

Chapter 5: pH Dependence of Dimethylaniline Functionalised Pyrene Fluorophores; Dual Colour Switching in Solution and SAMs

---

Submitted to *PCCP,* September **2019**

Darragh O' Connor, Carolin Müeller, Nirod Sarangi, Aisling Byrne and Tia E. Keyes

Within this work I was the primary author and contributor to the experimental design, execution, analysis and preparation of this manuscript. I have written complete sections with significant contribution to the overall manuscript preparation specifically towards the following sections: synthesis and structural characterisation, photophysical characterisation and pH-dependent studies in solution and on substrates. C. Müeller assisted with preliminary photophysics and carried out computational studies. Electrochemical studies were carried out by Dr. N. Sarangi. Dr. A. Byrne assisted with fluorescence detection of PyLaOT on gold substrate. Supporting information associated with this chapter can be seen in Appendix D.

5.1 Abstract

A pyrene charge transfer fluorophore with three ionizable *N*,*N*-dimethylaniline moieties was explored as an interfacial pH switch. The parent carboxylate compound and the thiolated derivative were shown by spectroscopy combined with DFT calculation to be successively and reversibly protonated. Protonation leads to progressive decrease of intensity of the 550 nm centred *N*,*N*-dimethylaniline to pyrene charge transfer emission which on protonation of the third site, leads to extinction of this transition and evolution of an intense blue (450 nm) pyrene-centred emission. Concomitant loss of the charge transfer absorbance was observed, and the changes are reversed on neutralisation of pH. A self-assembled monolayer of the thiolated derivative was prepared on gold and found from voltammetry of Ferricyanide/ Ferrocyanide probe to form close packed monolayers. The probe voltammetry, label-free electrochemical impedance spectroscopy of the film was monitored as a function of pH and progressive, but reversible protonation steps were reflected in decreasing film resistance. The Stokes shift of the probe prevents self-quenching so a broad, charge transfer fluorescence centred around 540 nm was recorded for the self-assembled monolayer whereas per solution, progressive and reversible reduction in intensity was observed. The facile assembly, impedance and optical switching make these materials potentially interesting as *on–off* or two colour *on-off-on* fluorescence switches with potential applications in logic gates or in responsive surface applications.

5.2 Introduction

Molecular switches are the functional units of molecular logic gates exemplified in the ground-breaking work of de Silva *et al*.[1] In organic-based molecular logic gates, switches that modulate fluorescence signal in response to external stimuli such as pH, ions, potential or light are widely explored.[2–7] The most common format is a single colour process, where the fluorescence signal is modulated between on and off states in response to stimuli.[8–11] An attractive alternative, as it is less prone to artefact, e.g. from background in the dark state, is to use multicolour luminophores that can switch between at least two well resolved emissive states.[12]

In the context of pH there are very many examples of pH induced *on-off* fluorescence switches,[13–16] but fewer that exhibit multiple emissive states. [17,17–19]

The immobilisation of fluorescent switches at conducting surfaces is a facile means to interface the molecular with the macroscopic leading to read (external stimuli) write (response) signal that have application across diverse domains from molecular opto-electronics to biosensing.[14,20]

Pyrene is an attractive and widely used fluorophore because of its well understood photophysics, its intense, long lived and solvent sensitive emission and tendency to form fluorescent excimers.[21] Pyrene has featured in a number of charge transfer derivatives functionalised with donor groups that reduce the energy gap between the frontier orbitals leading to compounds that exhibit large Stokes shifts and high quantum yields.[19,22–25]

We previously demonstrated that functionalising pyrene with three dimethylaniline moieties generated a charge transfer compound with desirable photophysical properties, including mega-Stokes shifted fluorescence, high quantum yield and excellent photostability that rendered them suitable for diverse imaging applications including fluorescent confocal microscopy, stimulated emission depletion spectroscopy (STED) and fluorescence correlation spectroscopy (FCS).[26]

Dimethylamino (DMA) groups are ionisable and where they participate in charge transfer transitions this can have a profound effect on the absorbance and photophysics of the donor-acceptor compound.[27] We were therefore interested to understand if sequential ionisation of

the of the pyrene could enable it to serve as a switch. We report herein on the pH dependent photophysics, in solution and on immobilisation at an interface, of two pyrene derivatives, the previously reported 3,6,8-tris(4-(dimethylamino)phenyl)-pyrene-1-carboxylic acid (PyLa)[26] and its newly synthesised thiol derivative 3,6,8-tris(4-(dimethylamino)phenyl)-pyrene-octanethiol (PyLaOT). Both fluorophores bear three electron dononating *N*,*N*-dimethylaniline groups that have been covalently linked via Suzuki-Miyaura coupling to the pyrene chromophore acting as an extended-bridge to the carboxylic acid or octanethiol group at the 1-position.

The absorption and emission properties of PyLa and PyLaOT as a function of solvent and pH are described. In addition, the pH-dependent fluorescent and electrochemical impedance properties of SAMs of PyLaOT on a gold surface is reported. Detailed photophysical and electrochemical interrogation are supported by theoretical insights from time dependent density functional theory (TD-DFT) calculations. Our data indicates sequential protonation of the compound leads to switchable and reversible fluorescent and optical changes that are also active in interfacial films PyLaOT.

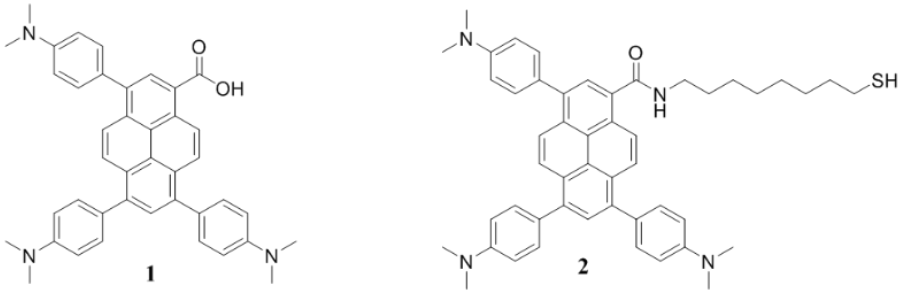

Figure 5.1 Structure of pyrene dyes PyLa (**1**) and PyLaOT (**2**).

5. 3 Results and Discussion

5.3.1 Synthesis

PyLa **(1)** was synthesised as previously reported and thiolated using an amide coupling reaction with PyLa and 8-amino-octhanethiol using PyBOP coupling. PyLaOT was prepared

by via an amide coupling reaction with PyLa and 8-amino-octhanethiol using PyBOP in *N*,*N*-dimethylformamide at room temperature over 24 h. PyLaOT **(2)** was characterised by ^{1}H and ^{13}C NMR and Maldi-TOF mass spectrometry. Detailed synthesis and characterisation spectra are provided in the Electronic Supplementary Information (Appendix D).

5.3.2 Computation and pH dependent Absorbance

To gain insight into the pH dependent ground state absorption properties of PyLa, TD-DFT calculations on the fully optimised ground state equilibrium geometries of PyLa and its mono- (PyLa13, PyLa16 and PyLa18), di-protonated (PyLa236, PyLa238 and PyLa268) and tris-protonated forms (PyLa31) were performed (see Figure 5.2, Figure S5.7 and Tables S5.1-6). The nomenclature is as follows: the first number indicates the total positive charge (number of attached protons), whereas the following number(s) indicate(s) the position(s) of the attached protons(s). The vertical excitation energies and oscillator strengths of PyLa were obtained from TD-DFT calculations (20 lowest excited states) using a triple-ζ-valence-polarisation (TZVP) basis set based on the integral equation formalism of the polarizable continuum model (IEFPCM) of acetonitrile. The calculations were performed by means of four functional with different amounts of Hartree-Fock exchange: B3LYP (20%), PBE0 (25%), M06-2X (54**%**)[31] and CAM-B3LYP (19-65%). As the experimental absorption spectrum of PyLa in acetonitrile is very well described using the CAM-B3LYP hybrid functional (*cf.* Figure S5.6), the TD-DFT simulations of the mono-, di- and tris-protonated forms were performed on this level of theory. To describe the influence of different mesomeric forms; PyLa13, PyLa16 and PyLa18 or PyLa236, PyLa238 and PyLa268 on the ground state absorption properties, their oscillator strengths were statistically weighted using the Boltzmann distribution as defined in equation **(1)**, where p_i is the probability of state *i*, E_i the energy of state *i* (*cf.* Table S5.2), k_B the Boltzmann constant, T the temperature and *n* the number of investigated derivatives belonging in each case to one total charge.

$$p_i = \exp\left(-\frac{E_i}{k_B \cdot T}\right) \cdot \left[\sum_i^n \exp\left(-\frac{E_i}{k_B \cdot T}\right)\right]^{-1}$$ Equation 5.1

TD-DFT simulations on PyLa indicate, that lowest energy absorbance originates from the S_1 state attributed to a charge-transfer (CT) state originating from the DMA substituents in the 3-, 6- and 8-position (HOMO) to the pyrene moiety (LUMO). This agrees with previous assignment of a mono DMA substituted pyrene reported by Techert *et al*[25]. The shoulder at around 370 nm is assigned to a CT state from the DMA substituent in the 6-position to the LUMO of the pyrene (see Figures S5.5–7 and Table S5.1)). The width of the lowest energy absorption band can be related to superimposition of different electronically coupled states due to the free rotation between the DMA and the pyrene moiety (inhomogeneous spectral line broadening). An angle of 65° leads to the largest electronic coupling between the donor and acceptor moiety.[25] In Figure 2 the simulated absorption spectra of PyLa (A) and its tris-protonated species (D) as well as the Boltzmann statistically weighted simulated absorption spectra of the mono- (B) or di-protonated species (C) are plotted and compared to experimental data, which was obtained from PyLa (50 µM) in acetonitrile titrated against known concentrations of perchloric acid.[‡] Due to overlapping protonation equilibria isolation of pure protonations states experimentally was not possible, but the spectra correspond to points along the pH titration where spectral change had plateaued (Appendix D). The experimental spectra show the PyLa at pH 5.5, can be attributed predominantly to the mono-protonated species, at pH 4.4 to the di-protonated and pH 1.5 to the tri-protonated species. By adding at least one equivalent of acid, *i.e.* on protonation of the carboxylate to form uncharged PyLa species, the absorption bands with maxima at 262 nm (4.73 eV) and 400 nm (3.10 eV) are bathochromically shifted by 0.05 and 0.21 eV, respectively. TD-DFT simulate a similar bathochromic shift by 0.21 eV when going from the PyLa-anion to PyLa. At pH 5.5 the absorption maximum red-shifts to 408 nm. A similar shift of 0.04 eV is observed in the simulated vertical excitation energies when transforming the neutral PyLa into the mono-protonated derivatives PyLa13, PyLa16 and PyLa18 (Figure 5.B). Of note, DFT calculations predict similar ground state energies for those cations (ΔE_{max} = 3 meV). At pH 4.4 the absorption feature at around 408 nm forms a bathochromically shifted shoulder on the main absorption band centred around 380 nm. This absorption feature is shifted

hypsochromically as the pH is decreased to 1.5. According to TD-DFT results the absorption feature at around 408 nm can be assigned to contributions of both, the S_1 states of PyLa13, PyLa16 and PyLa18 as well as PyLa236, PyLa238 and PyLa268 (Figure 5.2B and 5.2C) and the maximum at 380 nm can be attributed to the tri-protonated species PyLa3368 which dominates at pH 1.5 (Figure 5.2D). Overall, TD-DFT calculations predict a progressive hypsochromic shift of 0.34 eV when going from PyLa to PyLa3368, which is in good agreement with the experimentally observed shifts.

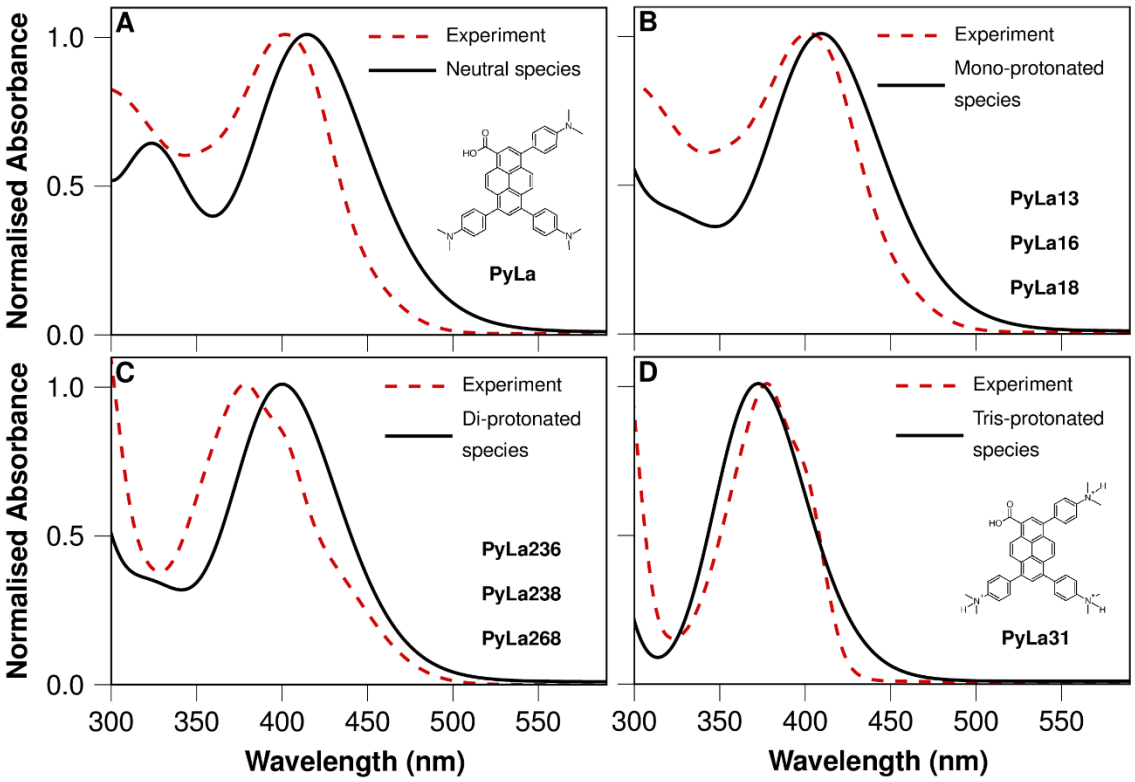

Figure 5.2 (A) TD-DFT simulated UV-Vis spectra of PyLa with experimental (-) spectrum in acetonitrile (c = 50 μM). (B) Simulated UV-Vis spectra (B3LYP/TZVP//CAM-B3LYP/TZVP in the IEFPCM of acetonitrile) of the monoprotonated species PyLa13, PyLa16 and PyLa18 in comparison to the experimental UV-Vis spectrum of PyLa in acetonitrile at apparent pH 5.5 (c = 50 μM). (C) Simulated UV-Vis spectra (B3LYP/TZVP//CAM-B3LYP/TZVP in the IEFPCM of acetonitrile) of the di-protonated species PyLa236, PyLa238 and PyLa268 in comparison to the experimental UV-Vis spectrum of PyLa in acetonitrile at apparent pH 4.4 (c = 50 μM). (D) Simulated UV-vis spectra (B3LYP/TZVP//CAM-B3LYP/TZVP in the IEFPCM of acetonitrile) of the tris-protonated species PyLa31 in comparison to the experimental UV-Vis spectrum of PyLa in acetonitrile at apparent pH 1.5 (c = 50 μM). Chemical structures for B and C can be found in Appendix D Figure S5.7.

As expected, PyLaOT shows similar pH dependent absorbance spectra to PyLa. Although the spectra are cleaner and exhibit a pseudo-isosbestic point (because of super-imposed

equilibria a true isosbestic point is not observed) around 400 nm. This is because without the carboxylate, there is one less ionisation step. The neutral species exhibits an absorption maximum at 418 nm. This value remains the same at pH 5.5. However, a decrease in intensity is observed. By pH 4.8 the maximum is bathochromically shifted by 50 meV to 424 nm with a further decrease in intensity. At pH 4 the absorption feature at 418 nm is replaced by an intense, structured band with a maximum at 384 nm. This maximum is blue-shifted by 50 meV to 378 nm at pH 1.5 (Figure 5.3B).

In phosphate buffered saline (PBS) solution both, PyLa and PyLaOT show similar behaviour, although the evolution of the spectral features appears more complicated, because of aqueous solvation. The absorption maximum of PyLa in PBS at approximately 417 nm can be seen to undergo a decrease in intensity and red-shift with decreasing pH (Figure S5.13). Loss of the absorption feature at 417 nm occurs below pH 3.0, at which point the solution becomes colourless (Figure S5.19).

A blue-shifted absorption shoulder with a maximum at 380 nm appears and increases in intensity with increasing pH. Behaviour again is similar for PyLaOT (Figure S5.15). Extraction of ground state and excited state pKa values from the data is difficult because of superimposition of multiple equilibria. Instead, comparison of calculated and experimental data was used to identify pH at which each ionisation state was predominant. Obviously at neutral and acidic pH the neutral and fully protonated species could be isolated. In subsequent studies we use pH 7.4, pH 5.5, pH 4.4 and pH 1.5, those at which the individual neutral, 1^+, 2^+ and 3^+ states of the compounds are dominant. Notably, the pH induced changes are reversible. The absorption spectrum of the neutral species was recovered on addition of excess of base (Figure S5.15-16).

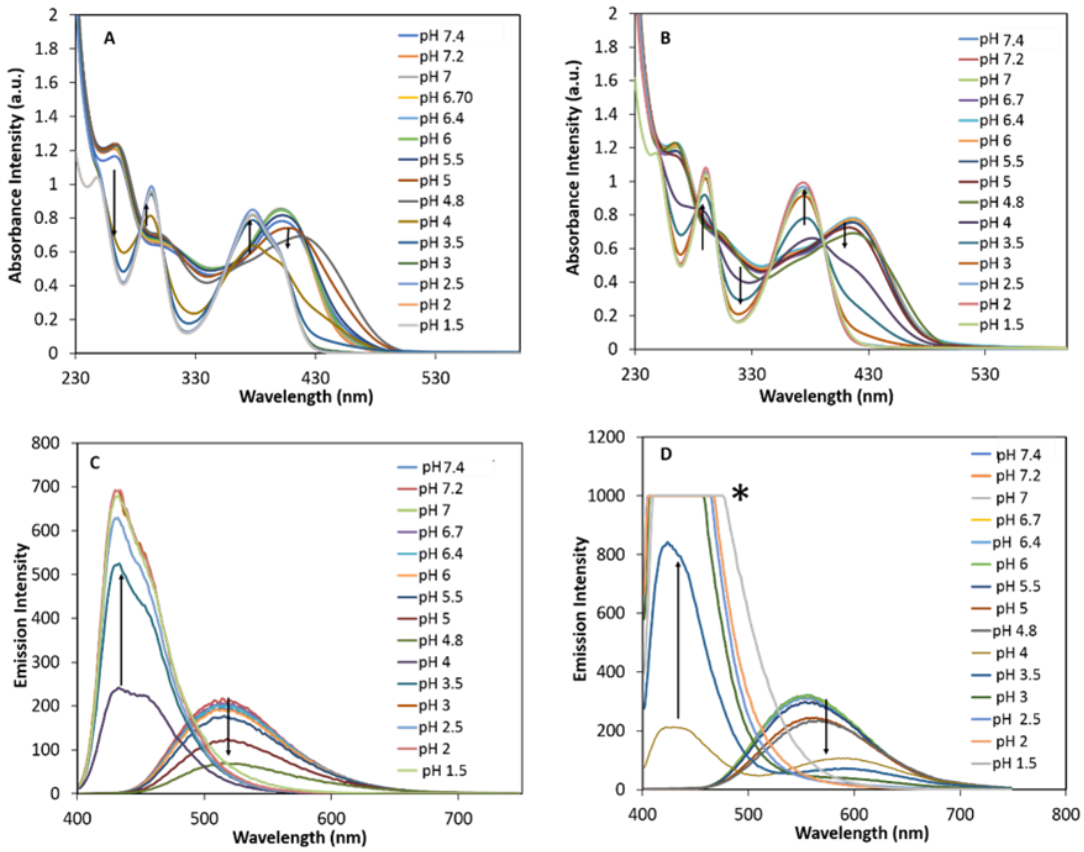

Figure 5.3 Absorption and emission spectra of PyLa (**1**) (A,C) and PyLaOT (**2**) (B,D) in acetonitrile using titrations of perchloric acid. Both absorption spectra (A,B) show decrease in absorbance max and slight red-shift with decreasing pH. Disappearance of this absorbance shoulder is observed below pH 4 with the formation of a pyrene like absorbance max at approximately 378 nm which then increases in intensity with decreasing pH. The emission maxima of both PyLa (C) and PyLaOT (D) decreases with decreasing pH. At pH 4 the charge-transfer emission band at 520-552 nm is replaced by a band in the UV region at approximately 426-430 nm, which resembles the emission of a pyrene core. This emission band the increases with decreasing pH. Excitation and emission slit widths were set to 2.5 nm and 5 nm PyLa (C) and PyLaOT were excited at 384 nm and 392 nm respectively to coincide as close as possible to isosbestic point. All samples were (c = 50 μM). * Signal difference is so great that the pyrene signal saturates the detector. Figure S5.20 shows pyrene emission at lower slit width.

5.3.3 Photophysical Characterisation

The photophysical properties of PyLa and PyLaOT are summarised in Table S6 (Appendix D). As reported for PyLa, both compounds exhibit broad, unstructured and intense mega-Stokes shifted emission that persists across a range of solvents. The absorbance spectra of PyLa, noted previously, exhibits an unexpected negative solvatochromism[32], where for example, λ_{max} of PyLa centred at 396 nm in methanol and ethanol shifts to 431 nm in

dichloromethane. For PyLaOT in the same solvents, the effect is far less pronounced, λ_{max} shifts from 398 and 404 nm to 410 nm respectively for these solvents indicating as before that the unusual solvatochromism and can be attributed to changes of the pKa of the carboxyl group of PyLa with solvent. DFT calculations shown above indicate that the carboxylate is stabilised in high dielectric and protic solvents with the neutral carboxyl prevalent in low dielectric, non-protic solvent.

Both dyes exhibit single exponential, oxygen independent fluorescence decays within the range 2-4.5 ns (Table S5.7). The lifetimes of PyLa and PyLaOT are comparable in more polar solvents such as 1-butanol and 2-propanol, where the lifetimes of PyLa are 2.7 ns and 2.4 respectively compared to 2.7 ns and 2.1 ns for PyLaOT. The lifetimes of PyLaOT tend to be approximately 1 ns shorter than PyLa across a range of solvents. The most noticeable difference is in dichloromethane where PyLa exhibits a lifetime of 4.4 ns which is nearly double that of PyLaOT (at 2.6 ns). As expected, the quantum yields for the charge transfer emissions (in neutral solution) follow similar trends. For example, PyLa exhibits a quantum yield of 0.4 in DCM compared to quantum yield of 0.73 for PyLaOT. 77 K emission spectra obtained for both probes (Fig. S5.9-10) show that across a range of solvents, the expected hypsochromatic shift is obtained with no evidence of phosphorescence.[33]

5.3.4 pH-Dependent Fluorescence in Solution

The effect of pH on the fluorescence of the probes was investigated under analogous conditions to the absorbance studies. Figure 3 shows that the fluorescence intensity of PyLa and PyLaOT decreases with decreasing pH in acetonitrile, until the charge-transfer emission band at approximately 520 nm for PyLa and 552 nm for PyLaOT is eventually extinguished below pH 4. At this pH, an intense emission feature centred at approximately 430 nm grows in with decreasing pH and maximises at pH 1.5. According to the experimental and computational results on the pH dependent absorption properties, this emission feature is assigned to the tris-protonated species. The emission changes are reversible and charge transfer emission is restored when the solution is neutralised. (Figure S5.13-16). Notably, the emission for the fully protonated form is very intense and its maxima and computation indicate that it is a pyrene π-π^* centred transition. Exciting at 384 nm, the pyrene centred

emission, shows vibrational progression (433 nm and 458 nm), with no evidence of excimer emission. This is not surprising, given the 3^+ charge on the complex and orthogonal orientation of the substituents which both would be expected to impede the self-association characteristic of pyrene.

Thus, between the extremes of pH 7.4 and pH 1.5 the compounds exhibit two colour pH switching. The behaviour, albeit weaker for the CT transition, is observed in both aqueous and organic solvents. We previously reported PyLa displays negligible emission in deionised water.[33] In PBS solution pH dependent changes in PyLa can be observed using maximum slit widths, however emission intensity is very weak compared to acetonitrile . It is evident from the data that with each sequential protonation of the dimethylaniline group the emission intensity is reduced, which, as the emission wavelength of the CT transition does not change significantly, may be related to the reduction in oscillator strength of the CT transition as the contributing dimethylaniline groups are sequentially protonated.[34,35]

5.3.5 Formation of the PyLaOT SAM sensing layer on gold

In the interest of creating an interfacial switch, we explored if the pH dependent photophysics persist in a self-assembled monolayer (SAM) of PyLaOT. PyLaOT SAMs were prepared by overnight adsorption of a micromolar concentration solution of the compound in contact with gold electrode. As shown in Figure 5.4a, the modified electrodes were investigated at pH=7.4, 5.5, 4.4 and 1.5, corresponding approximately to the neutral, mono- di and tris-protonated forms of PyLaOT, by cyclic voltammetry in contact with a 1:1 mixture of 1 mM $[Fe(CN)_6]^{3-/4-}$ as redox probe. The Ferricyanide/ Ferrocyanide probe was used to interrogate monolayer formation as the voltammetry of the compound is outside of the potential window of gold.[26] The bare gold electrodes show the expected, reversible redox cycle for the probe (black) with a peak separation (ΔEp) of 65 mV. The formation of well-packed monolayer is confirmed from inhibition of the Faradaic process for the redox probe, evident as decreased current and increased peak-peak separation of $[Fe(CN)_6]^{3-/4-}$ voltammogram. The impact is pH dependent. At pH 7.4. the cathodic and anodic current is decreased to about 30% of that of the unmodified electrode, and the peak-peak separation increases from 65 to 666 mV. For pH 5.5 (green), 4.4 (blue) and 1.5 (cyan), ΔEp was measured as 654, 595 and 137 mV respectively. Notably, the ΔEp at pH 1.5, for tris-protonated PyLaOT is significantly

decreased to 137 mV compared to the neutral species (666 mV), although it remains quasi-reversible. Concomitantly, the peak current has recovered to roughly 70% of the bare electrode. This may be due to the combined effects of looser packing of the monolayer due to electrostatic repulsion between the charged compounds at acidic pH and electrostatic interaction of the $[Fe(CN)_6]^{3-/4-}$ with the positively charged SAM.

Crucially, on returning the SAM modified electrode to electrolyte at neutral pH (to evaluate the stability of the SAM under acidic conditions), we observed that the peak to peak separation is restored (consistent with inhibition of $[Fe(CN)_6]^{3-/4-}$ electrochemistry at the SAM coated electrode) to almost identical values (ΔEp= 593 mV, magenta) as observed at neutral pH. This confirms the pH induced changes at the electrode are reversible and the SAM remains stable.

We then evaluated the pH dependent impedance (EIS) of the SAMs. Figure 5.4b shows the Nyquist plot for bare gold and SAM modified electrode in the presence of redox probe. The bare gold electrode (black open symbol) which can be described as a semicircle near the origin of real axis (Z′) at high frequencies followed by a linear plot at low frequencies with a slope of unity. Nyquist plots for the gold electrode after SAM modification shows a clear change in impedance data as the surface of gold electrode blocks almost all faradaic current. This can be attributed to the insulating nature of PyLaOT SAM, again this is consistent with formation of a well-packed monolayer. The diameter of the semicircle for the PyLaOT modified gold electrode (Figure 5.4b and c, red open symbol) is a measure of the charge transfer resistance, R_{CT} which is considerably increased compared to bare gold electrode. However, the low frequency region, is no longer linear and cannot be fit (dotted line) adequately by a simple Randles circuit as shown in dashed box in inset Figure 5.4c.

Table 5.1: Effect of pH on the resistance and capacitance of PyLaOT faradaic processes

Parameters	Bare gold	pH 7.4	pH 5.5	pH 4.4	pH 1.5	After wash
Rs/Ω	159 ± 20	70.8 ± 1.2	75.3 ± 1.8	75.4 ± 1.3	72.5 ± 1.2	76.6 ± 1.4
R_{CT}/kΩ	0.12 ± 0.01	1.44 ± 0.02	1.25 ± 0.03	1.20 ± 0.02	0.23 ± 0.06	1.08 ± 0.05
C/μF	5.59 ± 0.03	0.46 ± 0.002	0.45 ± 0.014	0.42 ± 0.02	0.45 ± 0.01	0.45 ± 0.002
R_T/MΩ		0.26 ± 0.05	0.23 ± 0.03	0.25 ± 0.02		0.30 ± 0.01

*Values derived from the modified Randles circuit except for the bare gold electrode and SAM modified electrode at pH 1.5 for which the data were fit to the unmodified Randles circuit.

Similar observations were made for the SAM modified electrode at both pH of 5.5 and 4.4. Conversely, for the case of pH 1.5, the shape of the impedance data is the same as that of the unmodified electrode albeit with considerably higher R_{CT} than that of bare gold electrode. Both bare gold and PyLaOT modified SAM at pH 1.5 (cyan) could be fit adequately using standard Randles circuit. However, the impedance measurement of the SAM modified electrode in the absence of redox probe (non-Faradaic) resulted in nonlinear behaviour which is not expected for a simple insulator (Figure 5.4d).

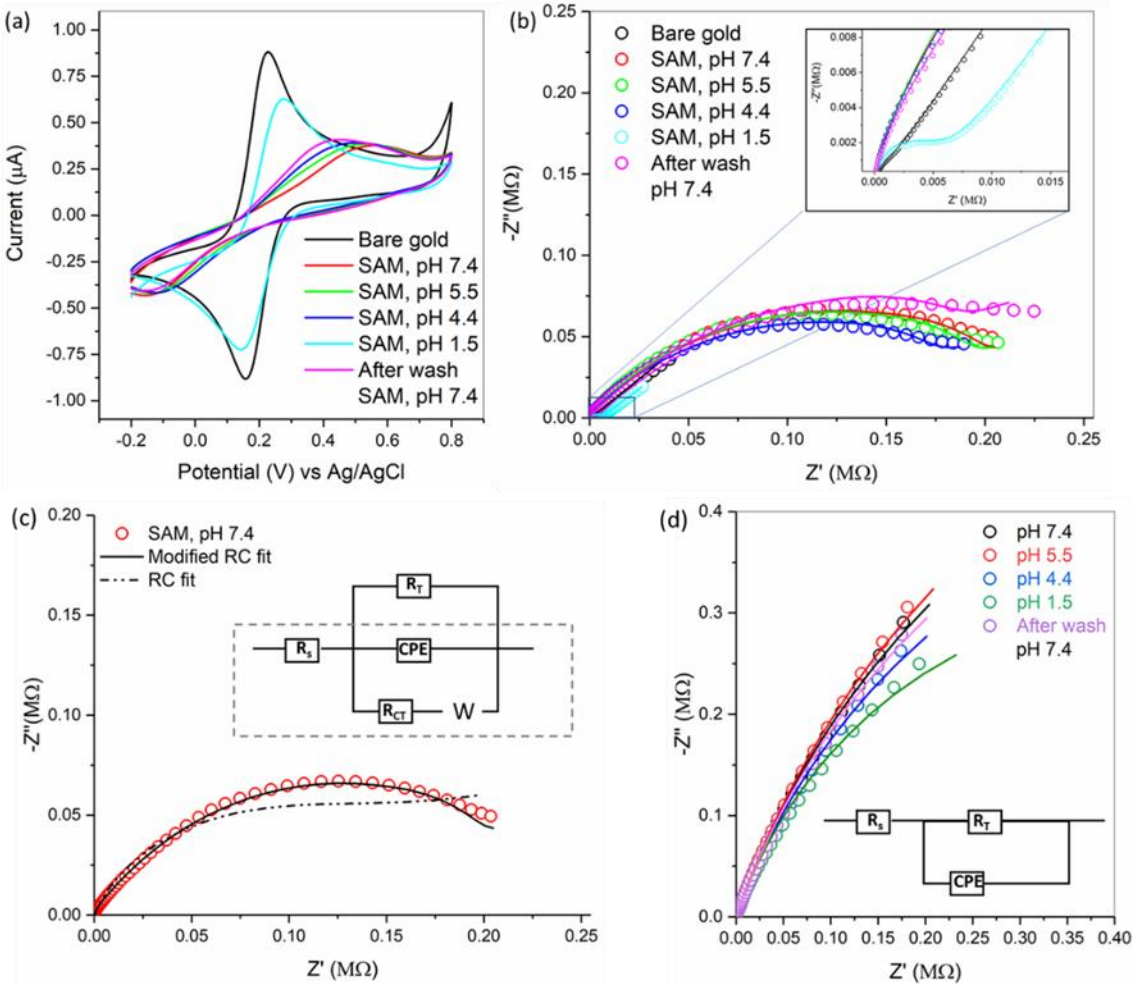

Figure 5.4 (a) The CVs of bare gold electrode and gold electrode after SAM modification at different pH's in 1mM $[Fe(CN)_6]^{3-/4-}$ (1:1) and 0.1M KCl. Scan rate was 50 mV s^{-1}. Nyquist plot represent the impedance spectra (imaginary *versus* real impedance) of bare gold and PyLaOT SAM with 1mM $[Fe(CN)_6]^{3-/4-}$ (1:1) mixture as redox probe in 0.1M KCl solution at varied pH (7.4, 5.5, 4.4 and 1.5). Frequency measured from 0.01 Hz to 10^4 Hz, with amplitude of 10 mV, applied potential 0.26 V versus Ag/AgCl. Inset shows the expanded region of(b). In all the cases experimental measured data points are shown as open symbol and solid line represents the fit to the modified Randles circuit. (c) Illustrates the experimental EIS data of PyLaOT SAM at pH 7.4 (open symbol), and the solid and dotted lines are the fit to the modified Randle circuit (inset) and standard Randles circuit (circuit within the dashed box, inset) respectively. R_s, solution resistance; R_T resistance through the PyLaOT; R_{CT}, charge transfer resistance; CPE, constant phase element; W, Warburg impedance. (d) Nyquist plot in the absence of redox probe for PyLaOT SAM at different pH in 0.1 M KCl. In each case, the experimental data (open symbol) were fit to the equivalent circuit shown.

Nevertheless, the EIS data could be fit with a simple circuit (inset, Fig. 4d) comprising of a capacitor with a resistance in parallel. These results suggest that the presence of an additional internal resistance, R_T, that can be added in parallel to the Randles circuit as shown in inset

of Figure 5.4c. The EIS data at pH 7.4, 5.5 and 4.4 then gives an excellent fit (solid line in Figure 5.4c and 5.4b) to the experimental data using the modified Randles circuit. For quantitative insight, we extracted the resistance as well as the capacitance values of the PyLaOT SAM by fitting the EIS data to the circuit shown in Figure 5.4c (inset) and the fit parameters are tabulated in Table 1. Note that a constant phase element (CPE) was used instead of pure capacitor to improve the quality of data fitting. The complex impedance of a CPE can be defined as $1/(j\omega Q)^m$, where Q is analogous to a capacitance, ω is the angular frequency and m is a real number which varies between 0.5 to 1 (m=1 correspond to pure capacitor and m=0.5 correspond to Warburg element). In our case for Faradaic process, m was found to be 0.86. The capacitance did not change significantly with decreasing pH. Given the inverse relationship between the thickness of the film to the capacitance, it confirms, as expected that the thickness of the PyLaOT did not change, i.e. that the film is stable. Consistent with probe voltammetry EIS reverts to the neutral pH after washing SAM modified electrodes at pH 1.5 resulted in recover of very similar R_{CT} values to that of the initial EIS data at pH 7.4.

From the above electrochemical data, it is clear the SAM can be sequentially and reversibly protonated without significantly affecting the integrity of the monolayer. In the intermediate pHs e.g., for the case of predominantly mono (pH, 5.5) and di-protonated (pH, 4.4) PyLaOT the R_{CT} decreases slightly compared to the neutral SAM suggesting the packing arrangement of pyrene is modestly perturbed and that the charge on the layer impacts the lateral packing within the monolayer, which is expected given the charge on the film. The effect of pH is significantly greater for probe electrochemistry than EIS, suggesting as indicated above that redox probe-SAM electrostatic interactions are important in the observed behaviour.

5.3.6 pH-Dependent Fluorescence on Solid Substrates

Given the SAMs are pH responsive and stable, we then investigated if the reversible photophysical pH response of PyLaOT in solution, persists in the self-assembled monolayers. As the SAMs are on a reflective surface, a microscope was used to collect the fluorescence spectra. Under 458.7 nm, the self-assembled monolayers show an intense and broad fluorescence centred around 530 nm in contact with water. Notably, the films strong

emissivity indicates that the probes are likely oriented upright on the surface, thus avoiding quenching by the gold surface

The effect of pH on the emission spectra of PyLaOT bound to a planar gold electrode was studied also using fluorescence microscopy under 458.7 nm excitation using an Ar ion laser. The modified gold electrode was placed in contact with PBS buffer and the pH varied using concentrated HCl. Representative fluorescence spectra are shown in Figure 5.5.

Interestingly, consistent with solution behaviour, between 7.4 and 1.5 there is a continuous decrease in the emission intensity. attributed to progressive protonation of the DMA groups in the 3-, 6- and 8-position of the pyrene. Interestingly, we do not see complete extinction of emission but beyond pH 3 the fluorescence intensity remains relatively constant with over 85 % intensity compared with neutral pH. As the pyrene emission appears at around 433 nm and cannot be excited at 458.7 nm (requiring UV excitation), we were unable to confirm its switch-on in this experiment. The absence of complete extinction of emission may suggest that the due to either differences in local pH and dielectric (as the monolayer is not likely to behave as bulk) and/or inaccessibility of the final DMA unit there may be differences in interfacial and solution photophysical behaviour. Nonetheless, upon neutralisation the charge transfer emission is recovered in terms of peak maxima and band shape. However, approximately 15 % of emission is lost, which may be attributed to some degradation of the SAM under laser irradiation, as comparable loss was not observed from impedance studies.

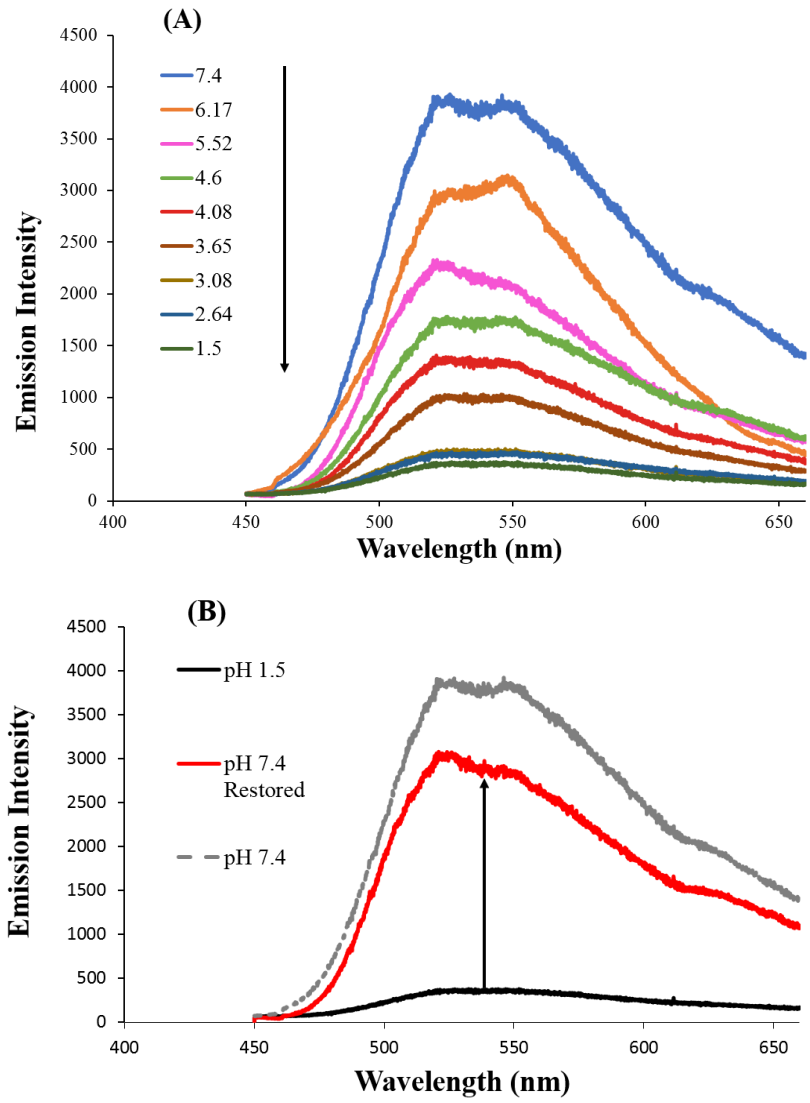

Figure 5.6 Fluorescence emission spectra of PyLaOT SAM (absorbed from 1 mM ethanolic solution) onto flat gold and submerged in PBS as function of pH by using microlitre titrations of HCl (A). Fluorescence emission spectra of PyLaOT on gold submerged in PBS showing restoration of the fluorescence intensity by increasing the pH (B).

5.4 Conclusions

In summary, we present two-colour pH modulated fluorescent switches based on a previously reported pyrene core functionalised with carboxylate or a surface-active alkane thiol and three ionisable dimethylaniline moieties. Detailed pH dependent photophysical data, supported by computational studies demonstrate that the parent compound undergoes sequential protonation steps that increasingly confines dimethylamino to pyrene charge

transfer transition to the deionised dimethylaniline donor units. Upon complete protonation of the dimethylamino substituents the emission switches from a Stokes shifted charge transfer fluorescent approximately 540 nm to an intense pyrene emission centred at 424 nm.

The thiolated charge-transfer compound forms a stable self-assembled bilayer on gold, confirmed by ferrocyanide probe voltammetry and label-free impedances spectroscopy which both confirmed presence of a close packed monolayer. Both methods demonstrate that the film undergoes sequential and reversible protonation steps, that on formation of fully ionised, 3^+ compound, renders the film both dramatically more conducting reflected in a large decrease in charge transfer resistance and in large decrease of peak to peak separation of the ferrocyanide voltammogram. The resistance of the film is recovered on neutralisation of the film. The self-assembled monolayers remain strongly luminescent and switching the pH between neutral and acidic progressively and reversibly switches the charge transfer transition off. Thus, these interfacial films look promising as an approach dual-modal and multicolour pH switches.

5.5 Supporting Material

Supplementary data associated with this chapter can be found in Appendix D.

5.6 Notes and References

‡ We refer here to pH as an approximation; pH -log[$HClO_4$] as perchloric acid was used in acetonitrile as the dissociation constant is known to be sufficiently high in this solvent that concentration of added acid gives an approximate (apparent pH).

(1) Prasanna de Silva, A.; McClenaghan, N. D. Proof-of-Principle of Molecular-Scale Arithmetic. *J. Am. Chem. Soc.* **2000**, *122* (16), 3965–3966.

(2) Tang, Q.; Zhang, J.; Sun, T.; Wang, C.-H.; Huang, Y.; Zhou, Q.; Wei, G. A Turn-on Supramolecular Fluorescent Probe for Sensing Benzimidazole Fungicides and Its Application in Living Cell Imaging. *Spectrochim. Acta. A. Mol. Biomol. Spectrosc.* **2018**, *191*, 372–376.

(3) Shanmugaraju, S.; Jadhav, H.; Karthik, R.; Mukherjee, P. S. Electron Rich Supramolecular Polymers as Fluorescent Sensors for Nitroaromatics. *RSC Adv.* **2013**, *3* (15), 4940–4950.

(4) Gao, M.; Tang, B. Z. Fluorescent Sensors Based on Aggregation-Induced Emission: Recent Advances and Perspectives. *ACS Sens.* **2017**, *2* (10), 1382–1399.

(5) Liu, C.; Wang, P.; Liu, X.; Yi, X.; Zhou, Z.; Liu, D. Supramolecular Fluorescent Sensor Array for Simultaneous Qualitative and Quantitative Analysis of Quaternary Ammonium Herbicides. *New J. Chem.* **2018**.

(6) Lin, T.; Su, X.; Wang, K.; Li, M.; Guo, H.; Liu, L.; Zou, B.; Zhang, Y.-M.; Liu, Y.; Zhang, S. X.-A. An AIE Fluorescent Switch with Multi-Stimuli Responsive Properties and Applications for Quantitatively Detecting pH Value, Sulfite Anion and Hydrostatic Pressure. *Mater. Chem. Front.* **2019**, *3* (6), 1052–1061.

(7) Ling, J.; Naren, G.; Kelly, J.; Moody, T. S.; de Silva, A. P. Building pH Sensors into Paper-Based Small-Molecular Logic Systems for Very Simple Detection of Edges of Objects. *J. Am. Chem. Soc.* **2015**, *137* (11), 3763–3766.

(8) Molina-Muriel, R.; Aragay, G.; Escudero-Adán, E. C.; Ballester, P. Switching from Negative-Cooperativity to No-Cooperativity in the Binding of Ion-Pair Dimers by a Bis(Calix[4]Pyrrole) Macrocycle. *J. Org. Chem.* **2018**, *83* (21), 13507–13514.

(9) Schneider, H.-J. Strain Effects Determine the Performance of Artificial Allosteric Systems: Calixarenes as Models. *Chem. Commun.* **2019**, *55* (24), 3433–3444.

(10) de Silva, A. P.; Gunaratne, H. Q. N.; Gunnlaugsson, T.; Huxley, A. J. M.; McCoy, C. P.; Rademacher, J. T.; Rice, T. E. Signaling Recognition Events with Fluorescent Sensors and Switches. *Chem. Rev.* **1997**, *97* (5), 1515–1566.

(11) McConnell, A. J.; Beer, P. D. Heteroditopic Receptors for Ion-Pair Recognition. *Angew. Chem. Int. Ed Engl.* **2012**, *51* (21), 5052–5061.

(12) Tian, Z.; Wu, W.; Wan, W.; Li, A. D. Q. Single-Chromophore-Based Photoswitchable Nanoparticles Enable Dual-Alternating-Color Fluorescence for Unambiguous Live Cell Imaging. *J. Am. Chem. Soc.* **2009**, *131* (12), 4245–4252.

(13) Lin, Q.; Zhu, X.; Fu, Y.-P.; Zhang, Y.-M.; Wei, T.-B. Highly Reversible "on–off–on" Fluorescence Switch and Logic Gate Accurately Controlled by pH Based on Nitrophenylfuran–Acylhydrazone. *Dyes Pigments* **2015**, *112*, 280–282.

(14) Shiraishi, Y.; Tokitoh, Y.; Nishimura, G.; Hirai, T. Solvent-Driven Multiply Configurable On/Off Fluorescent Indicator of the pH Window: A Diethylenetriamine Bearing Two End Pyrene Fragments. *J. Phys. Chem. B* **2007**, *111* (19), 5090–5100.

(15) Grossi, M.; Morgunova, M.; Cheung, S.; Scholz, D.; Conroy, E.; Terrile, M.; Panarella, A.; Simpson, J. C.; Gallagher, W. M.; O'Shea, D. F. Lysosome Triggered Near-Infrared Fluorescence Imaging of Cellular Trafficking Processes in Real Time. *Nat. Commun.* **2016**, *7*, 10855.

(16) Saito G.; Velluto D.; Resmini M. Synthesis of 1,8-Naphthalimide-Based Probes with Fluorescent Switch Triggered by Flufenamic Acid. *R. Soc. Open Sci. 5* (6), 172137.

(17) McDonnell, S. O.; O'Shea, D. F. Near-Infrared Sensing Properties of Dimethlyamino-Substituted BF2−Azadipyrromethenes. *Org. Lett.* **2006**, *8* (16), 3493–3496.

(18) Maus, M.; Rurack, K. Monitoring pH and Solvent Proticity with Donor–Acceptor-Substituted Biphenyls: A New Approach towards Highly Sensitive and Powerful Fluorescent Probes by Tuning the Molecular Structure. *New J. Chem.* **2000**, *24* (9), 677–686.

(19) Zöphel, L.; Enkelmann, V.; Müllen, K. Tuning the HOMO–LUMO Gap of Pyrene Effectively via Donor–Acceptor Substitution: Positions 4,5 Versus 9,10. *Org. Lett.* **2013**, *15* (4), 804–807.

(20) Fabbrizzi, L.; Foti, F.; Licchelli, M.; Maccarini, P. M.; Sacchi, D.; Zema, M. Light-Emitting Molecular Machines: pH-Induced Intramolecular Motions in a Fluorescent Nickel(II) Scorpionate Complex. *Chem. Weinh. Bergstr. Ger.* **2002**, *8* (21), 4965–4972.

(21) Bünau, G. v. J. B. Birks: Photophysics of Aromatic Molecules. Wiley-Interscience, London 1970. 704 Seiten. Preis: 210s. *Berichte Bunsenges. Für Phys. Chem.* **1970**, *74* (12), 1294–1295.

(22) Niko, Y.; Sasaki, S.; Narushima, K.; Sharma, D. K.; Vacha, M.; Konishi, G. 1-, 3-, 6-, and 8-Tetrasubstituted Asymmetric Pyrene Derivatives with Electron Donors and Acceptors: High Photostability and Regioisomer-Specific Photophysical Properties. *J. Org. Chem.* **2015**, *80* (21), 10794–10805.

(23) Ji, L.; Krummenacher, I.; Friedrich, A.; Lorbach, A.; Haehnel, M.; Edkins, K.; Braunschweig, H.; Marder, T. B. Synthesis, Photophysical, and Electrochemical Properties of Pyrenes Substituted with Donors or Acceptors at the 4- or 4,9-Positions. *J. Org. Chem.* **2018**, *83* (7), 3599–3606.

(24) Kurata, R.; Ito, A.; Gon, M.; Tanaka, K.; Chujo, Y. Diarylamino- and Diarylboryl-Substituted Donor–Acceptor Pyrene Derivatives: Influence of Substitution Pattern on Their Photophysical Properties. *J. Org. Chem.* **2017**, *82* (10), 5111–5121.

(25) Techert, S.; Schmatz, S.; Wiessner, A.; Staerk, H. Photophysical Characteristics of Directly Linked Pyrene−Dimethylaniline Derivatives. J. Phys. Chem. A 2000, 104 (24), 5700–5710.

(26) Connor, D. O.; Byrne, A.; Berselli, G. B.; Long, C.; Keyes, T. E. Mega-Stokes Pyrene Ceramide Conjugates for STED Imaging of Lipid Droplets in Live Cells. *Analyst* **2019**, *144* (5), 1608–1621.

(27) Ojadi, E. C. A.; Linschitz, H.; Gouterman, M.; Walter, R. I.; Lindsey, J. S.; Wagner, R. W.; Droupadi, P. R.; Wang, W. Sequential Protonation of Meso-[p-(Dimethylamino)Phenyl]Porphyrins: Charge-Transfer Excited States Producing Hyperporphyrins. *J. Phys. Chem. 97* (50), 13192–13197.

(28) Perdew, J. P.; Burke, K.; Ernzerhof, M. Generalized Gradient Approximation Made Simple. *Phys. Rev. Lett.* **1996**, *77* (18), 3865–3868.

(29) Perdew, J. P.; Burke, K.; Ernzerhof, M. Generalized Gradient Approximation Made Simple [Phys. Rev. Lett. 77, 3865 (1996)]. *Phys. Rev. Lett.* **1997**, *78* (7), 1396–1396.

(30) Adamo, C.; Barone, V. Toward Reliable Density Functional Methods without Adjustable Parameters: The PBE0 Model. *J. Chem. Phys.* **1999**, *110* (13), 6158–6170.

(31) Zhao, Y.; Truhlar, D. G. The M06 Suite of Density Functionals for Main Group Thermochemistry, Thermochemical Kinetics, Noncovalent Interactions, Excited States, and Transition Elements: Two New Functionals and Systematic Testing of Four M06-Class Functionals and 12 Other Functionals. *Theor. Chem. Acc.* **2008**, *120* (1), 215–241.

(32) Fu, Y.; Finney, N. S. Small-Molecule Fluorescent Probes and Their Design. *RSC Adv.* **2018**, *8* (51), 29051–29061.

(33) Connor, D. O.; Byrne, A.; Berselli, G. B.; Long, C.; Keyes, T. E. Mega-Stokes Pyrene Ceramide Conjugates for STED Imaging of Lipid Droplets in Live Cells. *Analyst* **2019**.

(34) Hou, J.-T.; Ren, W. X.; Li, K.; Seo, J.; Sharma, A.; Yu, X.-Q.; Kim, J. S. Fluorescent Bioimaging of PH: From Design to Applications. *Chem. Soc. Rev.* **2017**, *46* (8), 2076–2090.

(35) Han, J.; Burgess, K. Fluorescent Indicators for Intracellular PH. *Chem. Rev.* **2010**, *110* (5), 2709–2728.

Chapter 6: Conclusions and Future Perspectives

This thesis focused on the design and synthesis of novel fluorescent dyes based on two series of fluorophores, BODIPY and pyrene for application in imaging lipid environments in cells and sensing lipid domain formation in artificial model membranes. Both BODIPY and pyrene were selected due to their many desirable photophysical and structural traits. Both fluorophores and their derivatives exhibit high molecular brightness, quantum yields, photostability and molar extinction coefficients. Structurally they are lipophilic in nature and highly tuneable. Many BODIPY and pyrene derivatives reported in literature, exhibit low cytotoxicity at imaging concentrations, emit in the red to NIR region and can be used at low micromolar concentrations, all desirable traits for biological imaging. By incorporating lipophilic moieties including Dppz, naphthyridine, octanethiol as well as cholesterol and ceramide, a range of fluorophores were synthesised and used to study lipid-domains and lipid regions within artificial lipid models and live cells, using a wide range of techniques including confocal fluorescent microscopy, FLIM, FCS and in chapter 4, STED microscopy. The reported fluorophores and their respective lipid/sterol conjugates displayed high selectively to lipid regions in both model membranes and live cells, with focus on Ld domains, Lo domains and lipid droplets.

In chapter 2, Dppz-BODIPY was prepared using to investigate whether the Dppz ligand could be successfully used as a cholesterol mimic to aid lipid partitioning when bonded to a fluorophore, as its ability to intercalate in DNA has been widely reported. The fluorophore was synthesised using Suzuki-Miyuara coupling and knoevanegal type condensation. Dppz is a polycyclic aromatic hydrocarbon similar in size to cholesterol with similar planarity. It was thought that the Dppz ligand would not only contribute to the overall lipophilicity and thus targeting of lipid regions, but that it may also intercalate within lipid domains. Due to the excellent photophysical properties of a similar naphthyridine-BODIPY derivative within the group, a naphthyridyl-cholesterol conjugate was also explored. Interestingly both dyes displayed emission only from non-aqueous environments which resulted in high quality, low background images of both live cells and GUVs. Dppz-BODIPY and naphthyridyl-BODIPY-

2-Cholesterol displayed cytotoxic affects to non-cancer cell lines at high concentrations, however were relatively non-cytotoxic to HeLa cells under imaging concentrations (low micromolar). The successful incorporation of both dyes into GUVs resulted in phase separated images and FLIM data. The high photostability combined with high quantum yields and low propensity to access triplet excited states meant the probes are well suited for FCS. Diffusion coefficients were measured for both Dppz-BODIPY and naphthyridyl-BODIPY-2-cholesterol in phase separated GUVs. Interestingly naphthyridyl-BODIPY-2-cholesterol displayed a high selectivity for lipid droplets within live cells HeLa cells. The selective targeting of lipid droplets was further explored in chapter 4. These probes displayed good suitability for use as both lipid and membrane probes in cells and artificial lipid models, however they both showed preference for liquid-disordered domains.

Chapter 3 further explored lipid partitioning probes with focus on selectively targeting liquid-ordered domains in artificial lipid models. Very few liquid-ordered partitioning probes are reported in literature, with many partitioning into both Ld and Lo domains, but exhibit different excitation, emission or lifetime, depending on the domain environment. Many successful Lo probes exploit conjugation with known Lo associating lipids/sterols, mainly cholesterol. Hence, a simple BODIPY-phenyl-cholesterol conjugate was investigated with respect to the distance between the BODIPY fluorophore and the cholesterol moiety. By using Steglich esterification the lone hydroxyl group of cholesterol was exploiting, resulting in a facile synthesis for cholesterol conjugation. Using this synthetic route, two derivatives BODIPY-Ar-Chol and BODIPY-Ahx-Chol, differing in the distance between fluorophore and cholesterol were prepared. The addition of a C_6 amino-hexanoate linker between the BODIPY core and the cholesterol unit resulted in the difference between Lo and Ld partitioning. Confocal fluorescent images were successfully obtained of both BODIPY-Ar-Chol and BODIPY-Ahx-Chol illuminating Ld and Lo domains respectively. FLIM data was acquired to relate the difference in luminescent lifetime to the structural environments of the individual lipid regions. Both dyes were successfully used to stain membranous regions in cells with focus on the partitioning BODIPY-Ahx-Chol into what we believe are sterol-rich domains. Both HeLa and CHO cell lines were treated with cyclodextrin to investigate what effect this had on the partitioning behaviour of the dyes and cellular structure. FLIM was used to compare the structural significance on the photophysics of the dyes. BODIPY-Ahx-

Chol is a simple yet effective fluorophore that offers insight on the structural requirements of Lo partitioning. Further investigations will be carried out in order to determine if this strategy for Lo targeting is viable using a number of different fluorophores.

Chapter 4 describes the synthesis of a novel pyrene derivative PyLa and its C_{17} ceramide conjugate PyLa-C_{17}Cer. By exploiting the relative ease of brominating the 3,6 and 8-positions of the pyrene core, palladium catalysed Suzuki-Miyaura coupling was used to incorporate dimethylaniline substituents, resulting in a bathochromic-shift in the emission and the formation of a charge-transfer fluorophore. By functionalising the pyrene core with a carboxylic acid at the 1-position, Steglich esterification was applied to conjugate on a ceramide, which is a known to associate within lipid droplets. The photophysical properties of PyLa including mega-Stokes shift, high quantum yields, excellent photostability and good extinction coefficients combined with the targeting of the ceramide resulted in a fluorescent ceramide conjugate that was demonstrated to selectively target lipid droplets and could be used for STED super resolution microscopy. Due to the excellent photostability and lack of triplet excited states PyLa-C1Cer was also successfully used to obtain FCS diffusion data on supported lipid bilayers of varying lipid compositions. This, to the best of our knowledge, is the first example of a pyrene derivative used in super-resolution STED microscopy and FCS.

Chapter 5 explored in further detail the photophysical properties of PyLa with focus on the pH sensitivity of the 4-dimethylaminophenyl substituents. The coupling of octanethiol to PyLa resulted in the derivative PyLaOT, which is capable of binding to gold surfaces and displays the same pH sensitivity as PyLa. The dimethylaniline groups were shown to exhibit three ionisation states. As a result of protonation, the charge transfer transition from the dimethyaniline substituents to the pyrene core is gradually inhibited and these changes can be detected in the emission profiles of both fluorophores. This process was monitored by the disappearance of the initial charge-transfer band and the appearance of a newly hypsochromatically shifted band in the absorption and a switch-off emission. Computational studies carried out by C. Müller on the parent fluorophore PyLa predicting the photophysical properties of the protonated species which was then compared to experimental results. Electrochemistry was carried out on the thiol derivative PyLaOT investigating the effect of pH when a self-assembled monolayer if formed on a gold electrode, in efforts to build a two-

colour interfacial pH switch. Results showed that the same changes seen in the photophysical data with respect to changes in pH can be seen in the impedance data, resulting in a decrease in resistivity with decreasing pH that can be restored when brought back to a neutral environment. Future work to emerge from this chapter will focus on incorporating the thiol derivative PyLaOT onto our gold microcavity arrays. This work will involve forming a PyLaOT self-assembled monolayer onto the gold substrate of the microcavity array. A supported lipid bilayer of varying lipid composition consisting of phospholipids, sphingomyelin, cholesterol and the protein bacteriorhodopsin will be suspended on top the cavities and filled with PBS buffer. Bacteriorhodopsin is a protein that acts a proton pump that can capture and use light to move protons across membranes resulting in a proton gradient. The change in pH caused by the bacteriorhodopsin will be detected by the PyLaOT monolayer in the microcavities, using fluorescence techniques, thus resulting in a molecular machine type artificial membrane model.

For the BODIPY and pyrene lipid/sterol conjugates further work is ongoing concerning the synthesis of mega-Stokes shifted alkyne derivatives that can be used to create fluorescent sulfatide conjugates via click chemistry reactions. Sulfatides are a class of sulfolipids that are found not only in the myelin sheath but also the extracellular leaflet of the plasma membrane. Sulfatides are of great biological interest as they are known to bind to many bacteria such as *E. coli* and viruses including HIV-1, influenza A and hepatitis C. The focus of future work will centre on synthesising fluorescent sulfatide conjugates with desirable photophysical properties that are compatible with FCS and STED. These fluorophores will be incorporated into lipid domains within our supported lipid bilayer microcavity arrays, and using a combination of confocal fluorescent microscopy, FCS, FLIM and STED, protein-lipid interactions will be investigated by studying the viral protein hemagglutinin (HA) on supported lipid bilayer microcavity arrays.

Appendices A-D

Appendix A

Supporting information associated with Chapter 2.

S2.1. Multinuclear NMR and Additional Characterisation

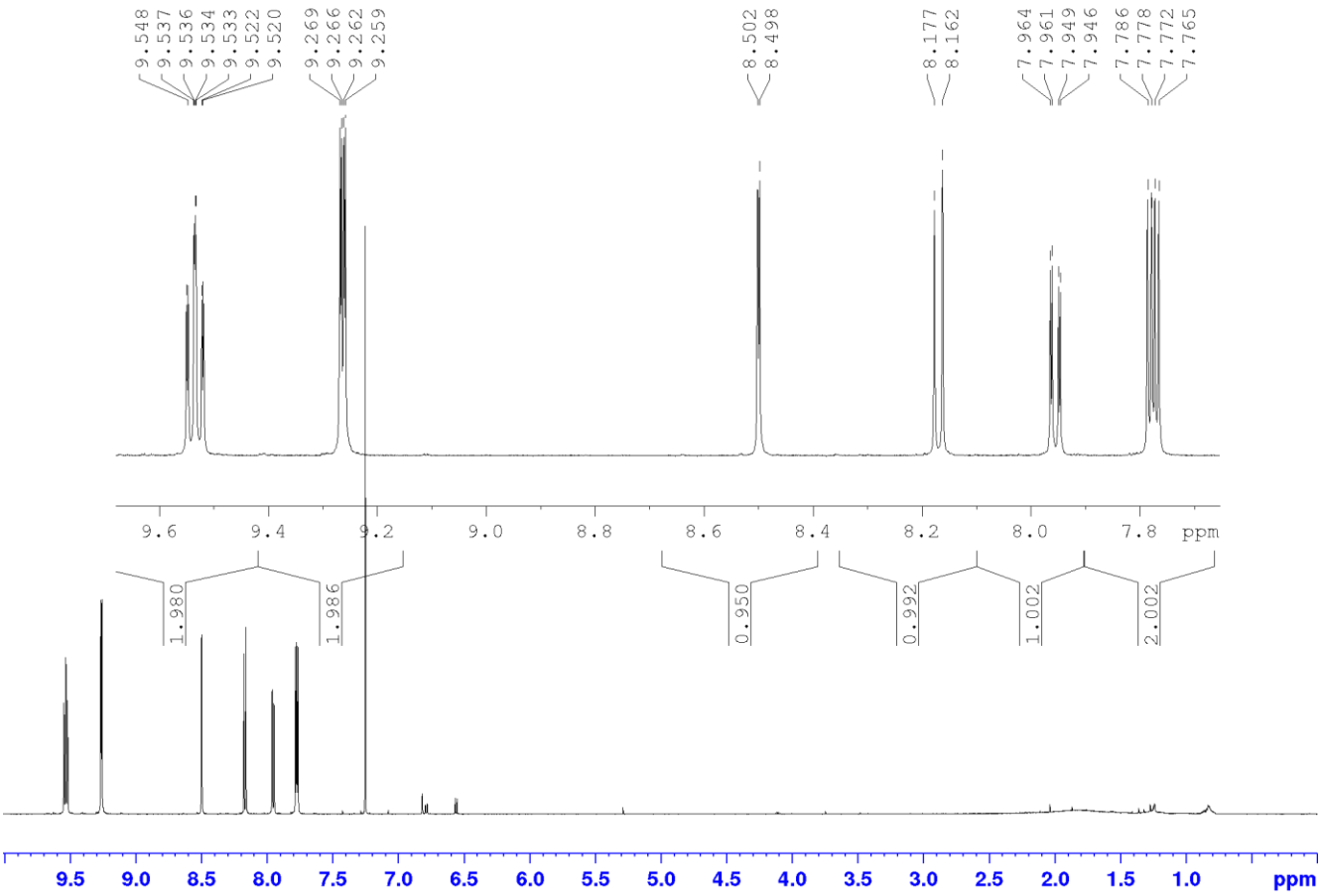

Figure S2.1 1H NMR (600 MHz) of **(1)** in $CDCl_3$

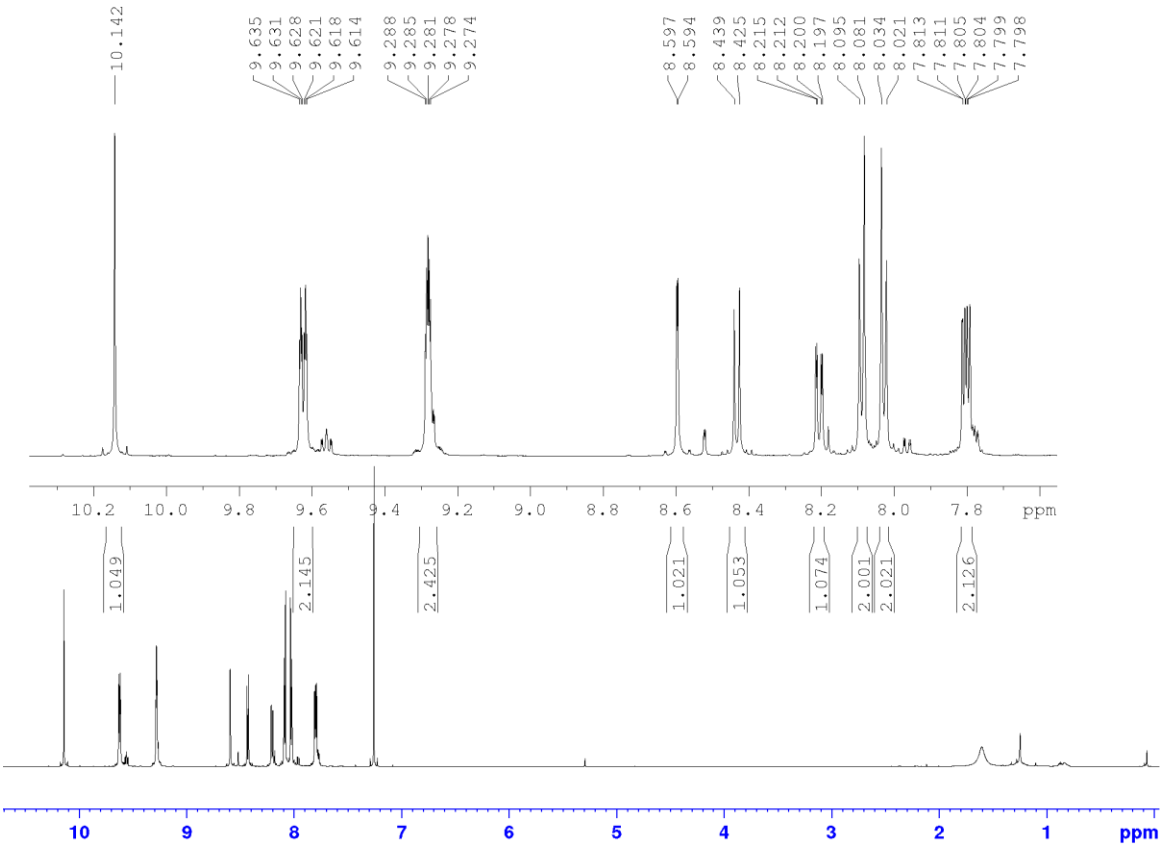

Figure S2.2 ^{1}H NMR (600 MHz) of **(2)** in $CDCl_3$

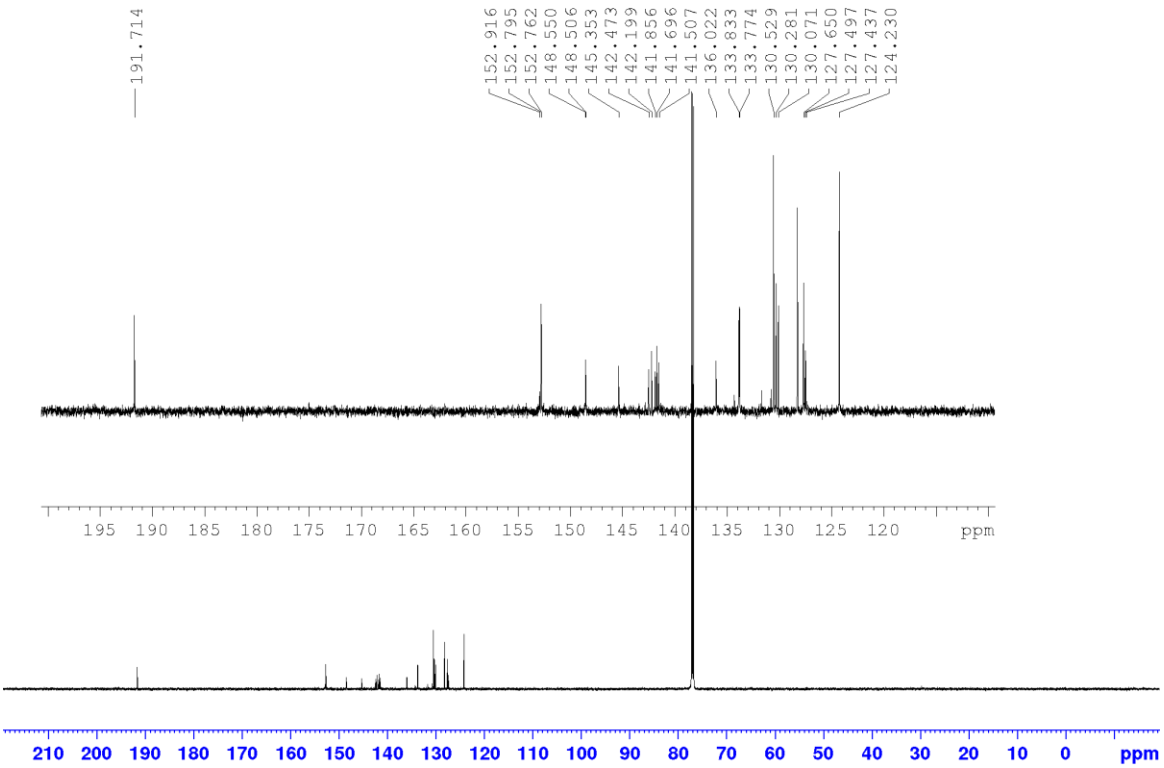

Figure S2.3 ^{13}C NMR (150 MHz) of **(2)** in $CDCl_3$

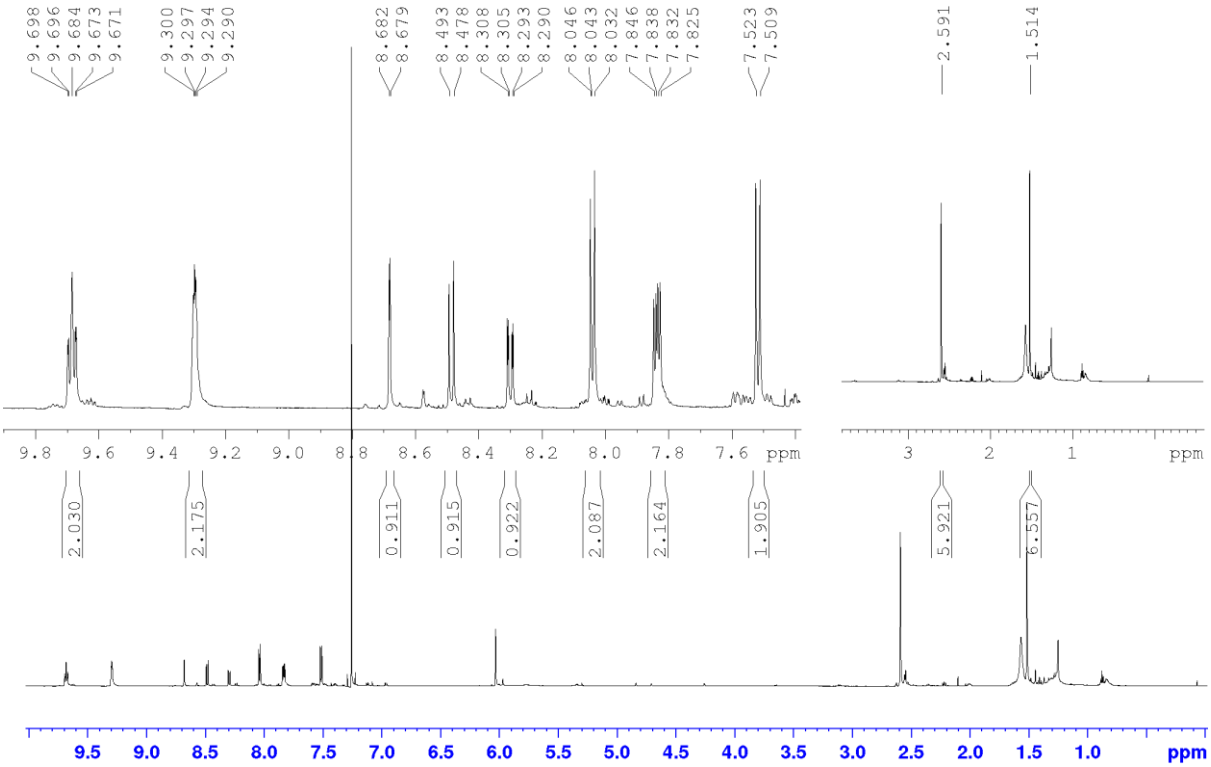

Figure S2.4 ^{1}H NMR (600 MHz) of **(3)** in $CDCl_3$

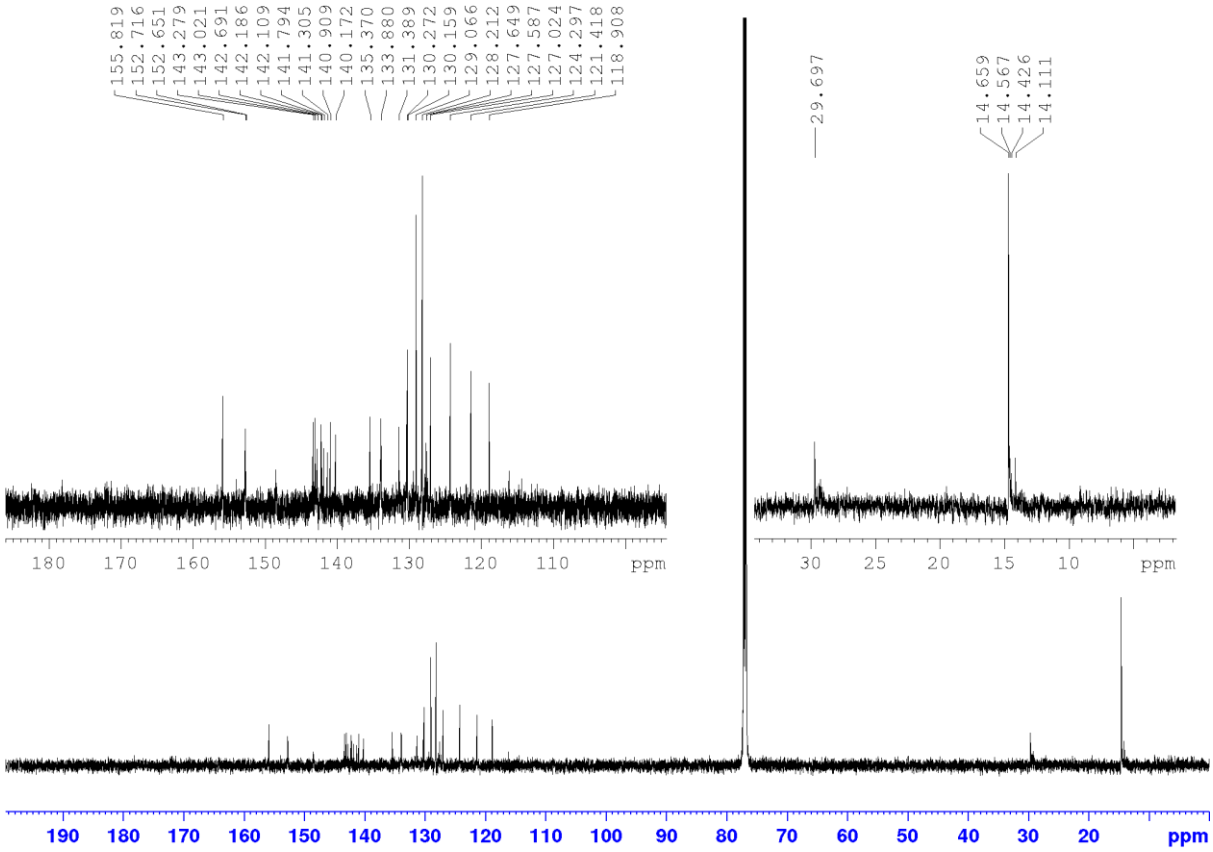

Figure S2.5 ^{13}C NMR (150 MHz) of **(3)** in $CDCl_3$

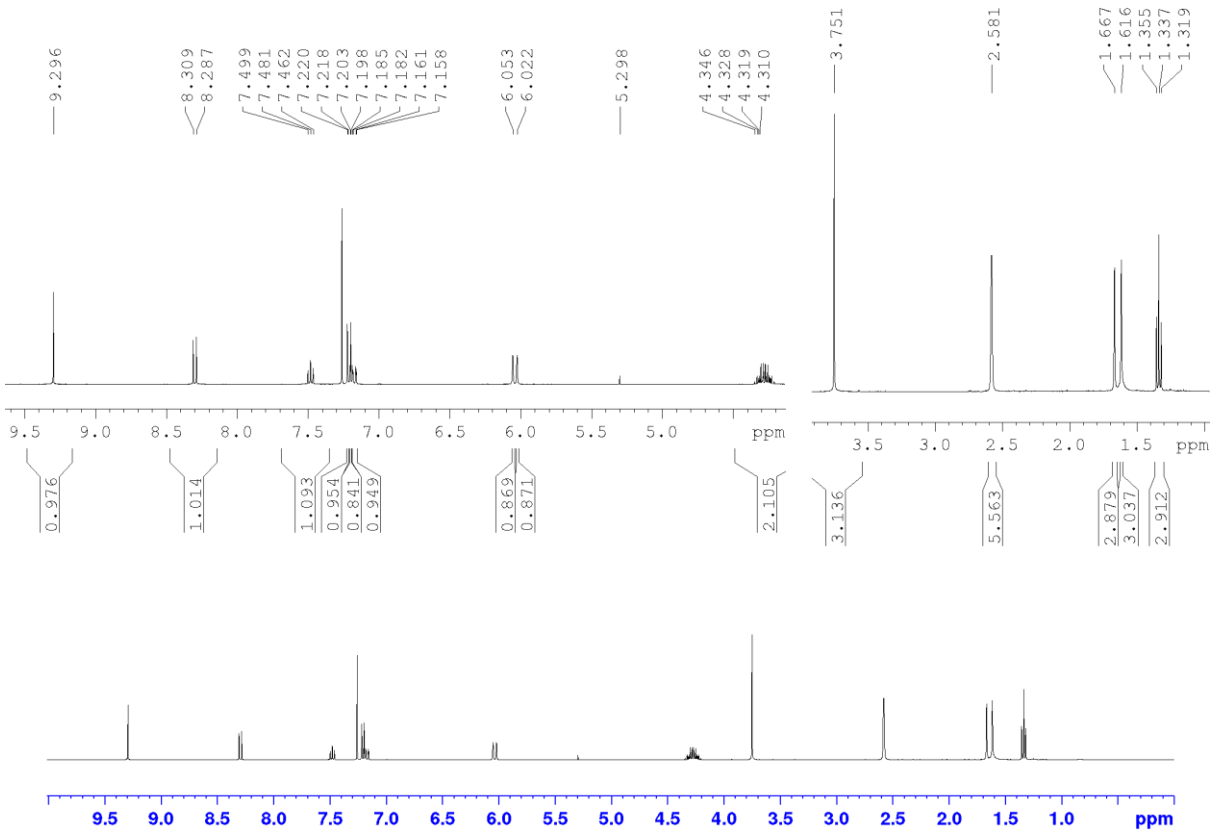

Figure S2.6 ^{1}H NMR (600 MHz) of **(4)** in $CDCl_3$

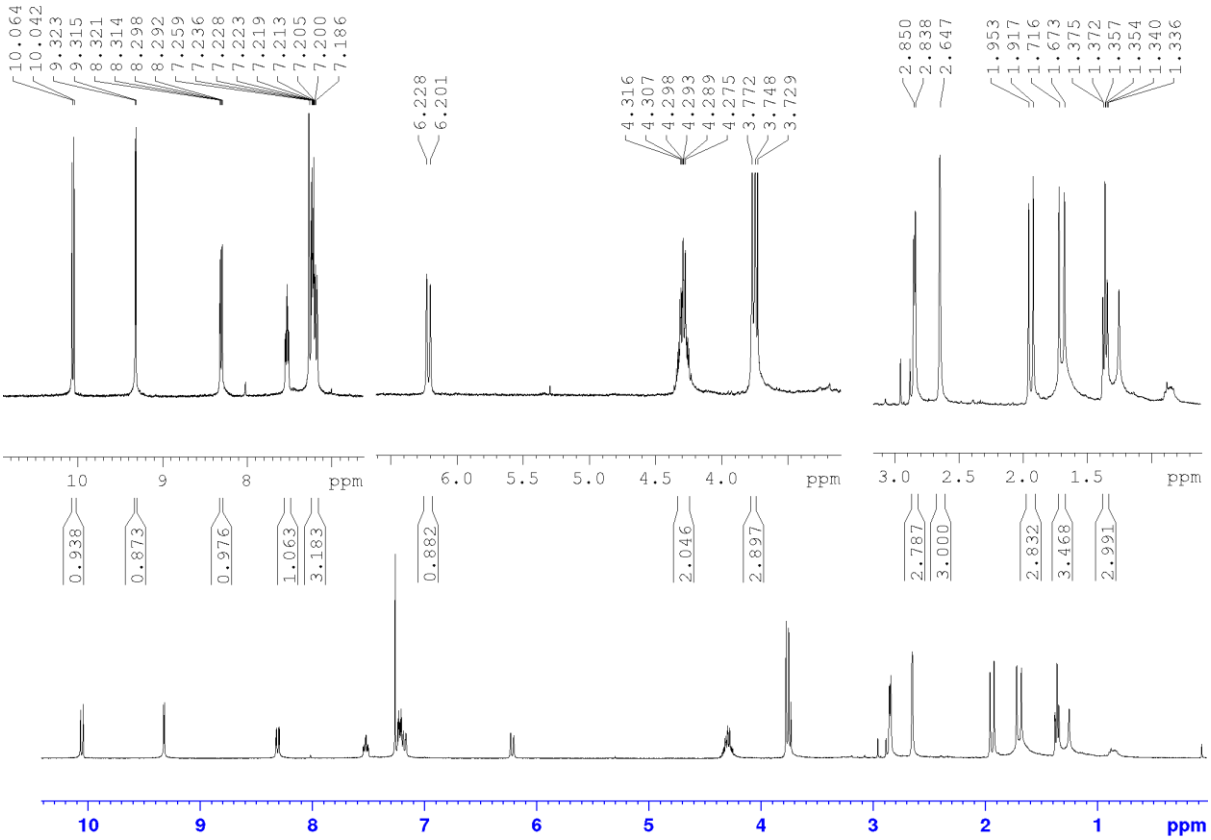

Figure S2.7 ^{1}H NMR (600 MHz) of (**5**) in $CDCl_3$

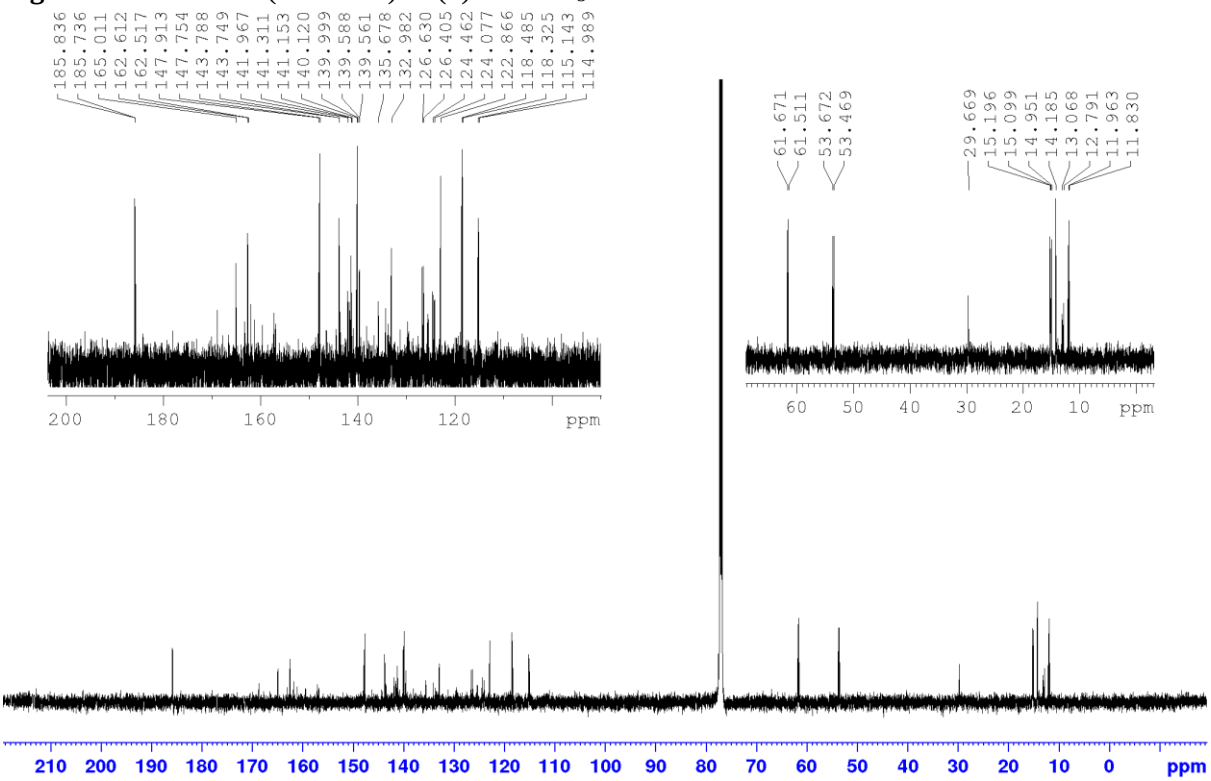

Figure S2.8 ^{13}C NMR (150 MHz) of (**5**) in $CDCl_3$

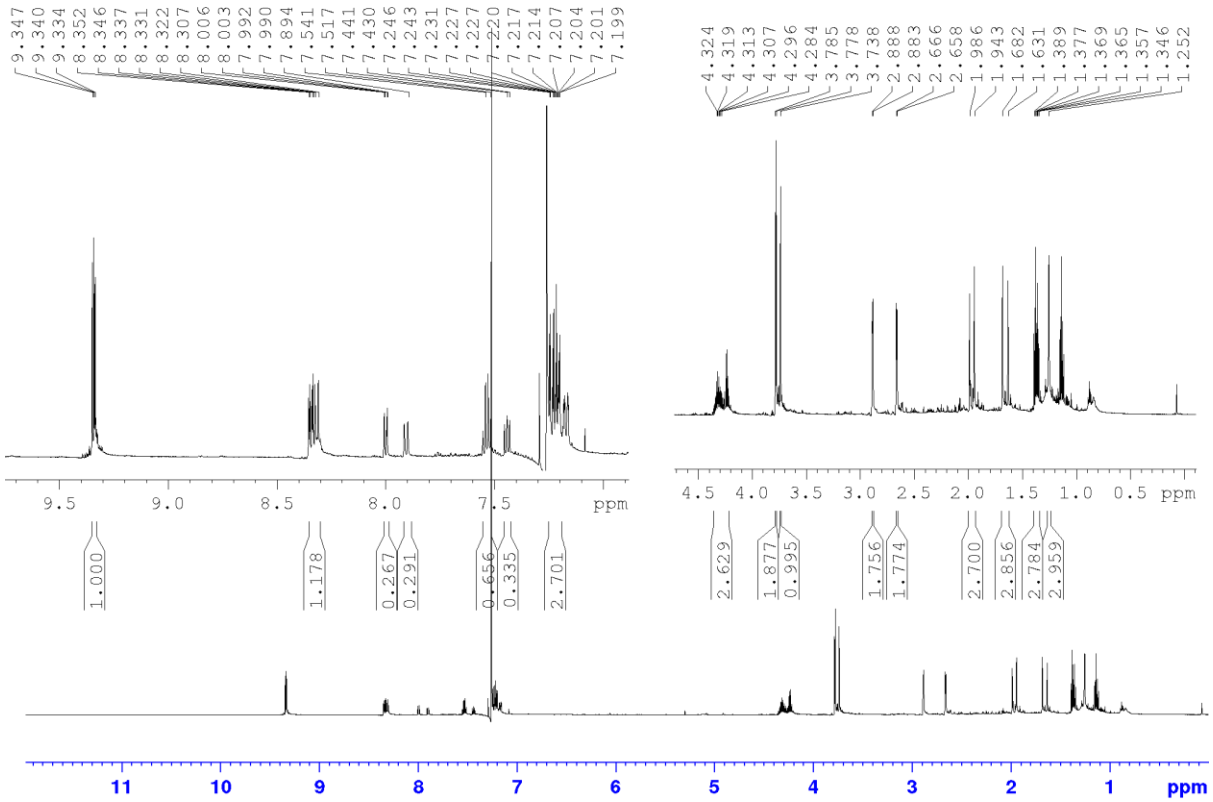

Figure S2.9 ^{1}H NMR (600 MHz) of **(6)** in $CDCl_3$

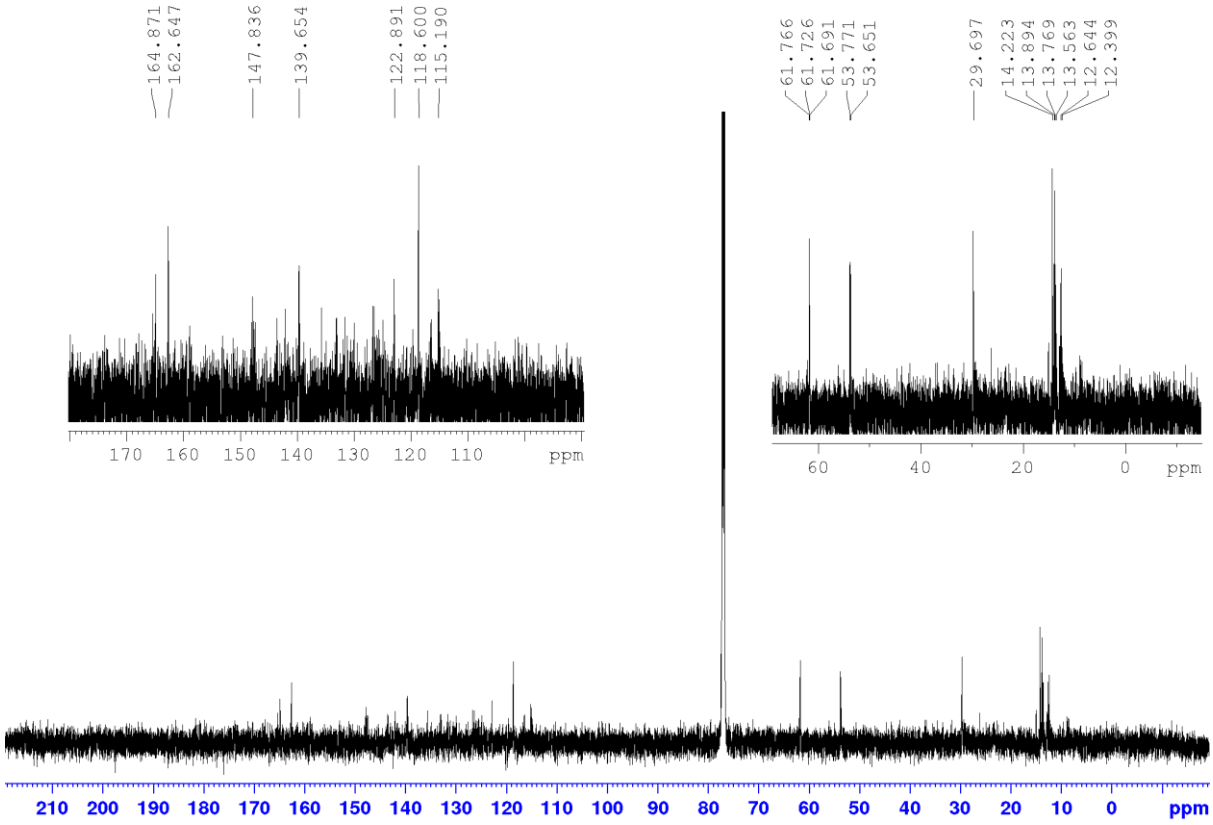

Figure S2.10 ^{13}C NMR (150 MHz) of **(6)** in $CDCl_3$

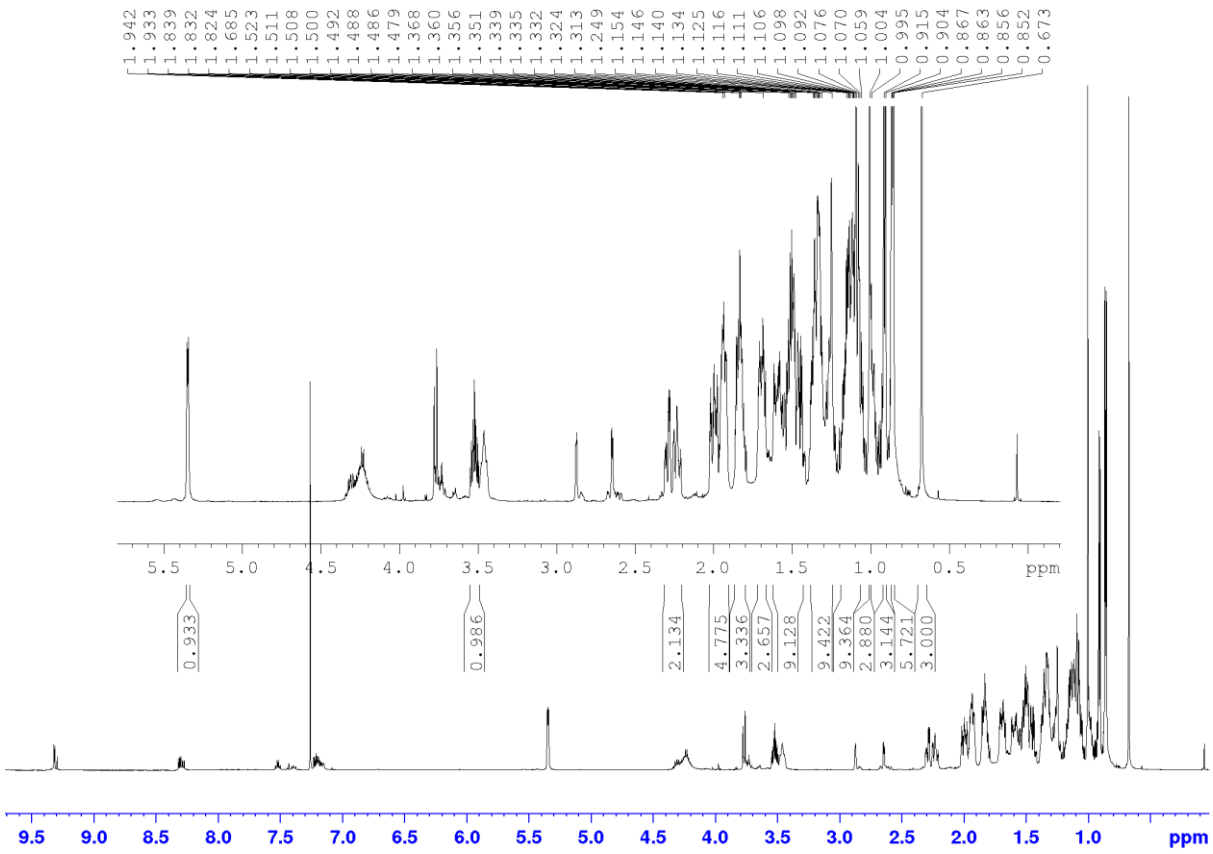

Figure S2.11 ^{1}H NMR (600 MHz) of **(7)** in $CDCl_3$. Inset Cholesterol peaks accounting for 57H

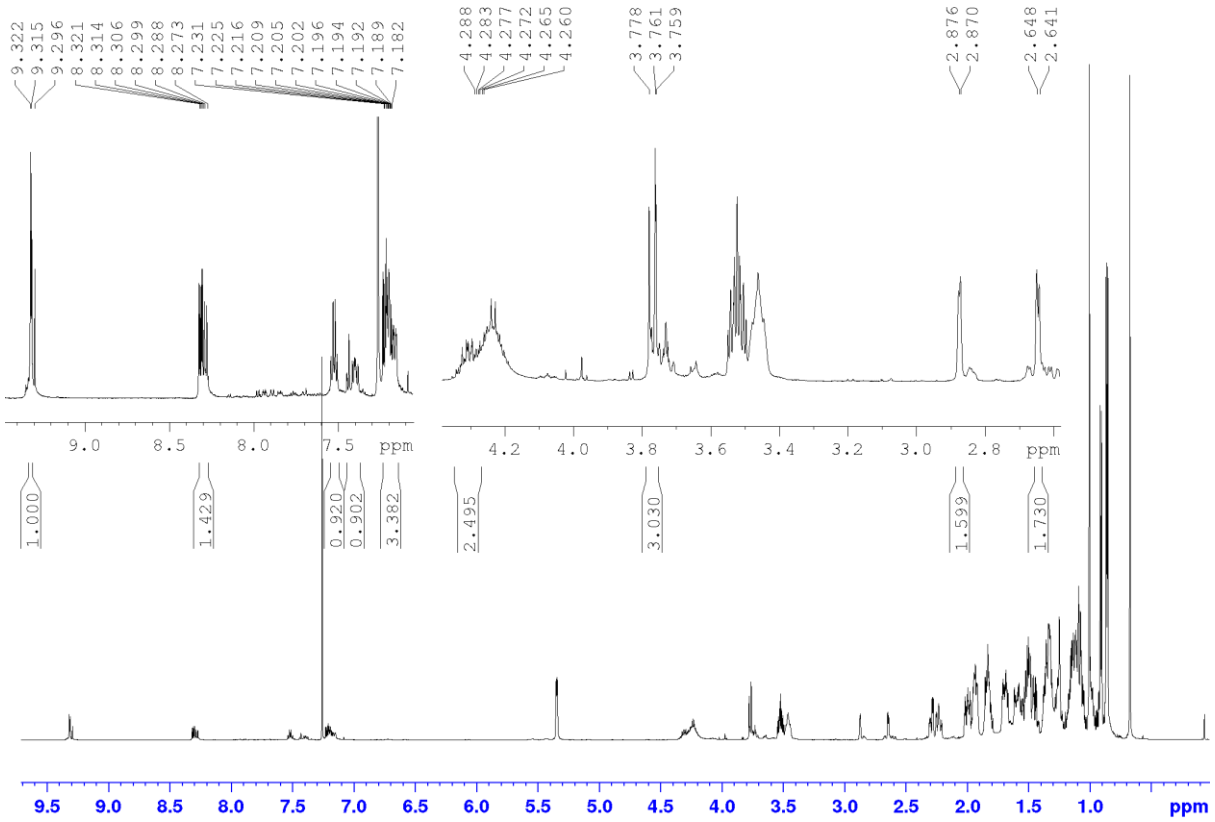

Figure S2.12 ^{1}H NMR (600 MHz) of **(7)** in $CDCl_3$. Inset naphthyridyl peaks accounting for 15H

S2.2 Additional Photophysics

For Dppz-Ar-BODIPY an investigation into the effect of water on the luminescent emission was carried out. A 10 µM solution of Dppz-Ar-BODIPY in acetonitrile was prepared. 3 mL of this solution was taken and the luminescent emission of Dppz-Ar-BODIPY was obtained in acetonitrile. Water was titrated into the sample, agitated and left to stand. Following this the emission spectrum was obtained. This was repeated in 30 µL titrations until 10 % of the sample volume had been added. The results showed that a 50 % decrease in emission intensity was observed upon adding 300 µL of water.

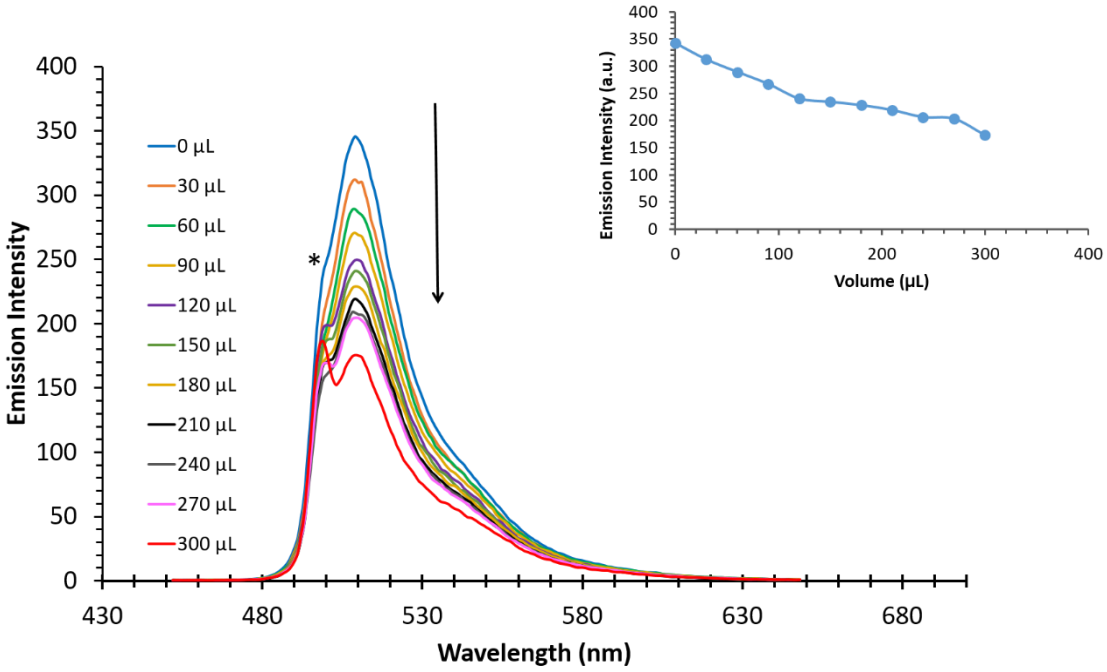

Figure S2.13 Emission spectra of Dppz-Ar-BODIPY **(3)** acetonitrile 5 mL (λex 501 nm, 10 µM, slit widths 2.5 nm). A total volume of 300 µL of water was titrated, resulting in a volume change of 6 %, shown in the graph inset. * indicates contribution from the excitation source.

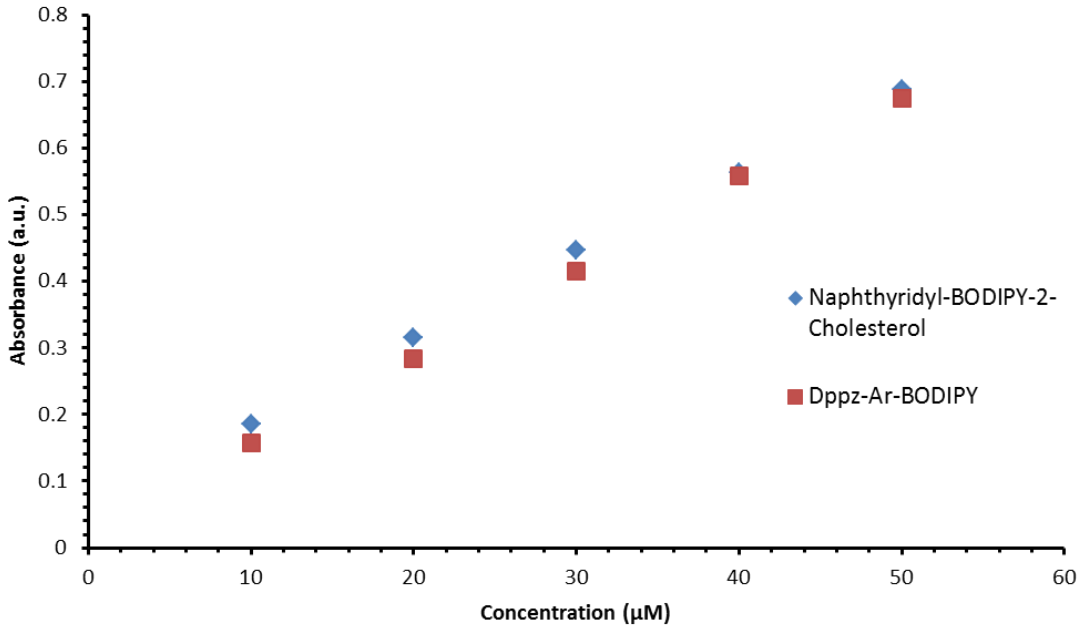

Figure S2.14 Concentration dependence study of Dppz-Ar-BODIPY **(3)** and naphthyridyl-BODIPY-2-cholesterol **(7)** in acetonitrile.

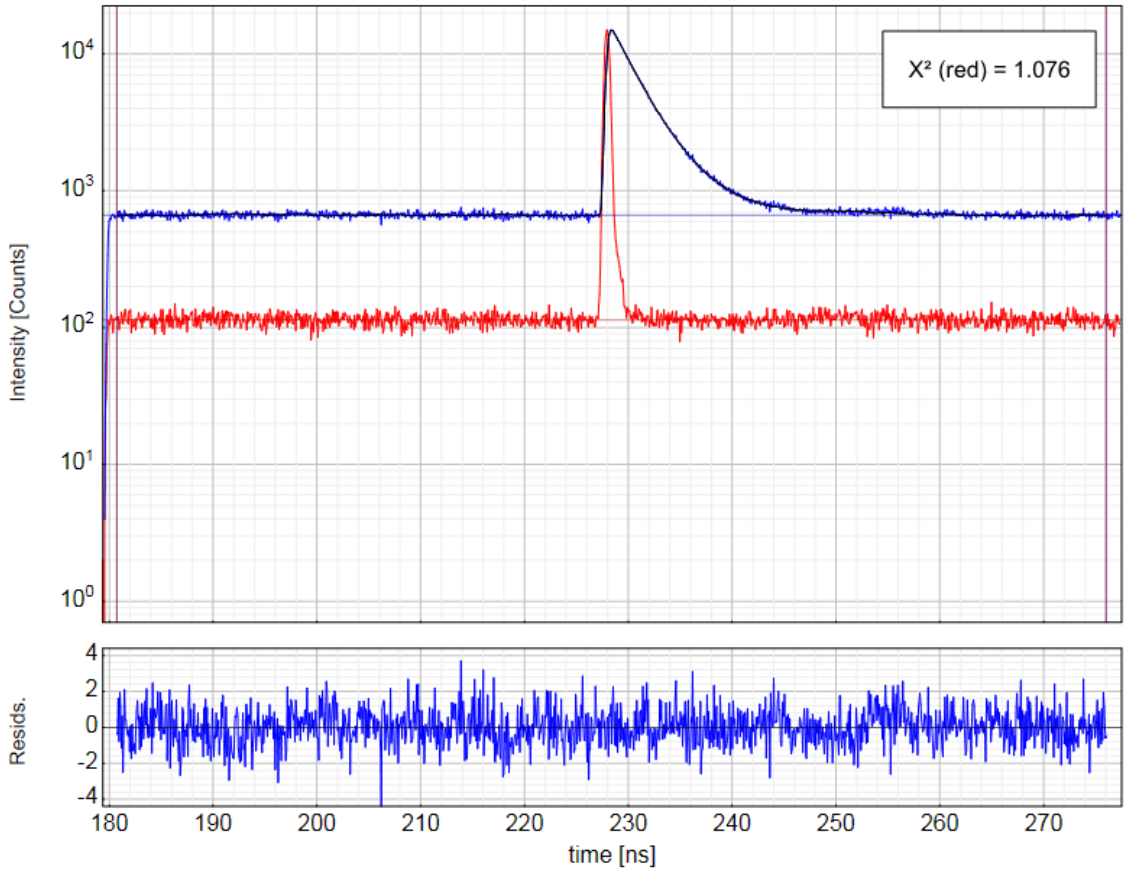

Figure S2.15 Time correlated Single Photon counting trace for Dppz-Ar-BODIPY **(3)** in Chloroform (10 µM) with IRF (red) at room temperature.

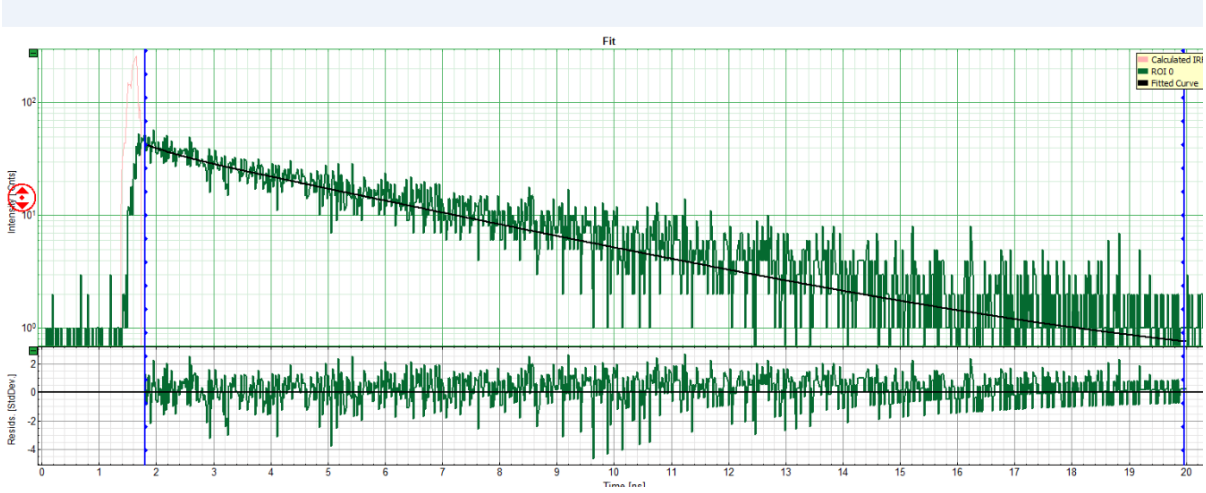

Figure S2.16 Fluorescent lifetime imaging decay for naphthyridyl-BODIPY-2-cholesterol **(7)** in GUVs DOPC/BSM/Chol 4:4:2 mol % (10 µM).

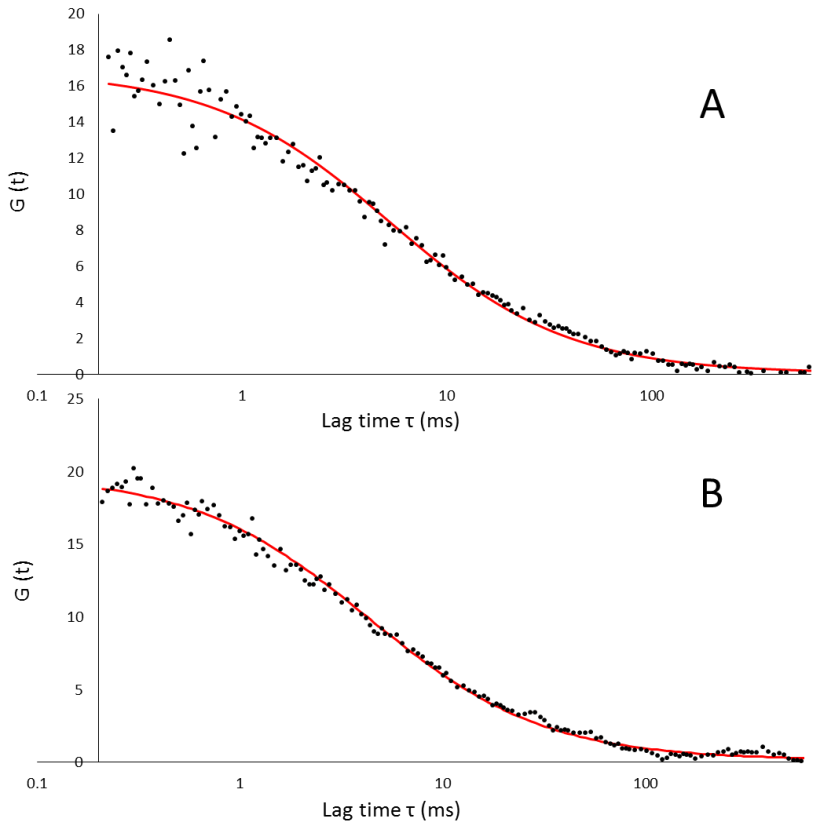

Figure S2.17 (A) Fluorescent correlation spectroscopy autocorrelation function for Dppz-Ar-BODIPY in GUVs DOPC/BSM/Chol 4:4:2 mol % at concentration 0.001 mol % at room temperature. (B) Naphthyridyl-BODIPY-2-cholesterol **(7)** in GUVs DOPC/BSM/Chol 4:4:2 mol % at concentration 0.001 mol % at room temperature.

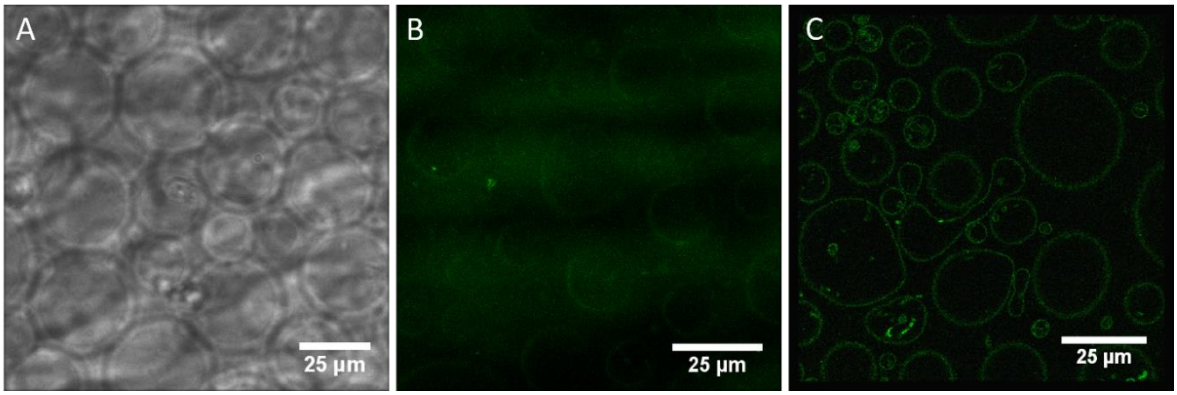

Figure S2.18 Uptake of Dppz-Ar-BODIPY in GUVs of composition DOPC 100 %. Dppz-Ar-BODIPY in CHCl3 was added to a solution of GUVs in glucose 230 mM to give a final concentration of 10 µM. Uptake was monitored over a 105-minute period using confocal microscope and images after A) 60, B) 75, and C) 105 minutes.

S2.3 Cell Studies

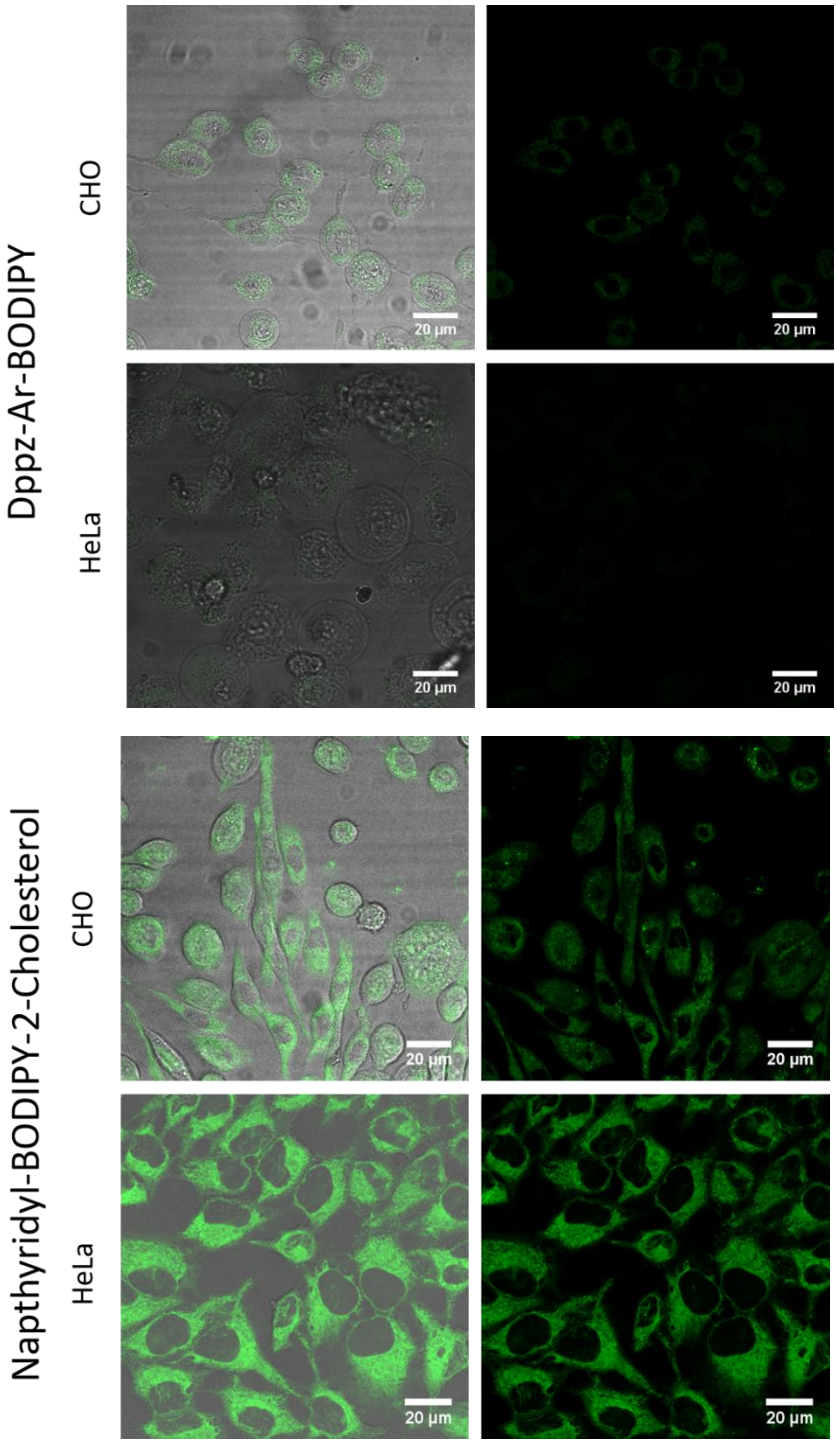

Figure S2.19 Confocal imaging of CHO and HeLa cells incubated with 5 µM Dppz-Ar-BODIPY and naphthyridyl-BODIPY-2-Cholesterol compound at 4°C for 24 h, showing the overlay of the BODIPY and background channels (column 1) and the BODIPY channel only (column 2).

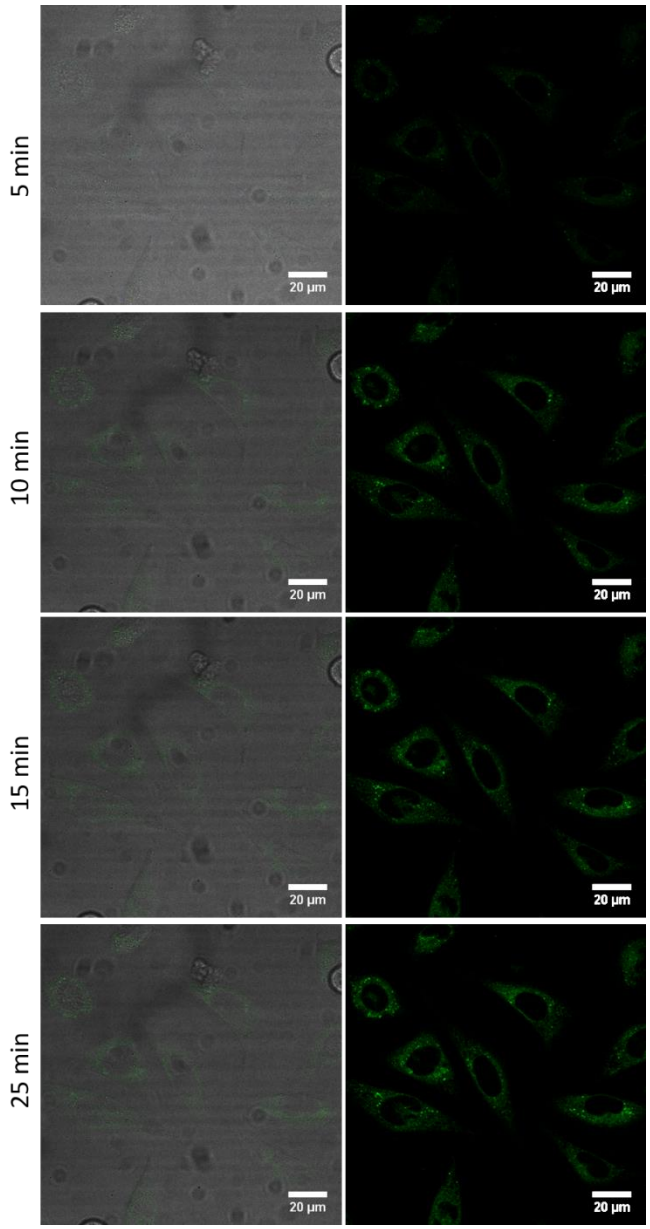

Figure S2.20 Live uptake of Dppz-Ar-BODIPY in live CHO cells. 5 µM of Dppz-Ar-BODIPY in cell media was added to CHO cells, and the uptake was monitored over 25 minutes using confocal microscopy, showing the overlay channels (column 1) and the emission of the BODIPY channel only (column 2).

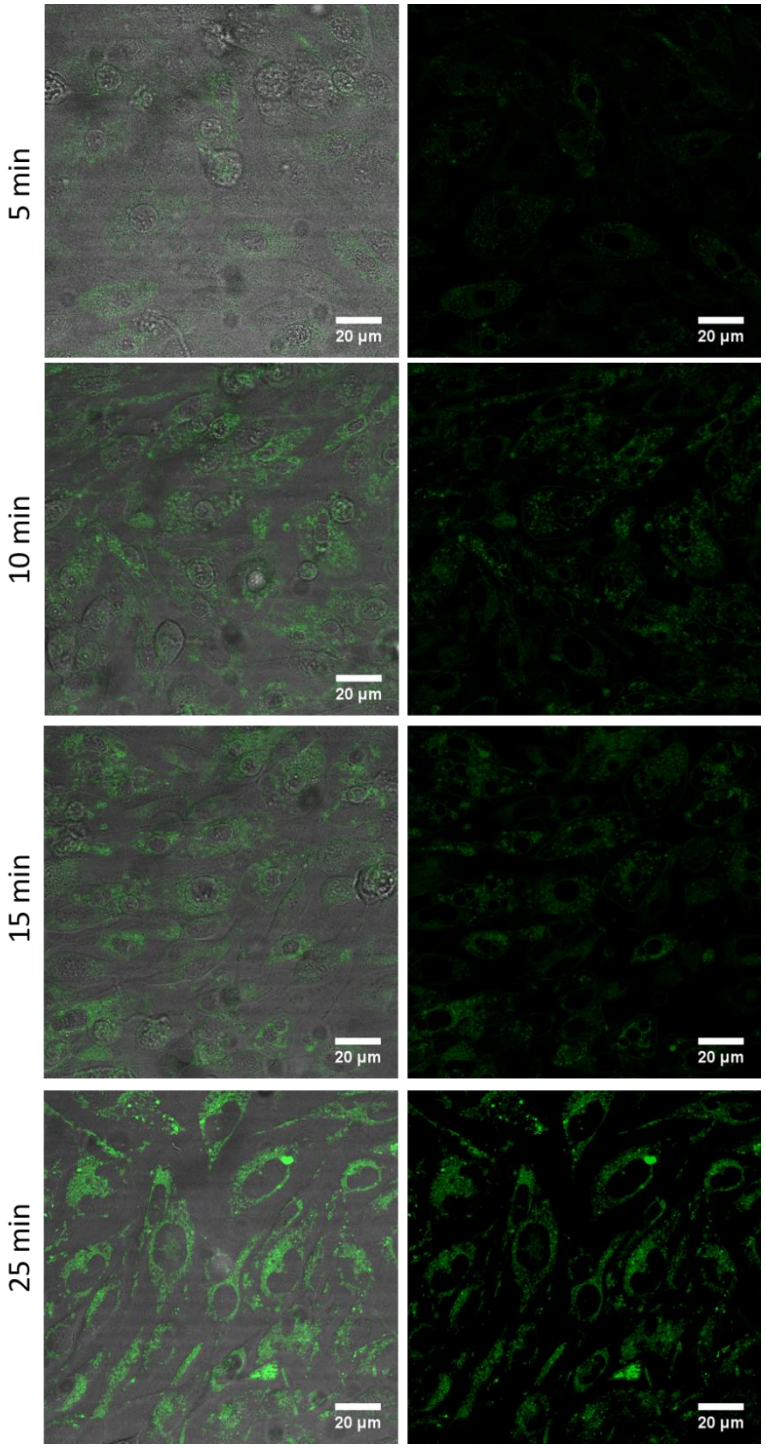

Figure S2.21 Live uptake of Dppz-Ar-BODIPY in HeLa cells. 5 µM of Dppz-Ar-BODIPY in cell media was added to HeLa cells, and the uptake was monitored over 25 minutes using confocal microscopy, showing the overlay channels (column 1) and the emission of the BODIPY channel only (column 2).

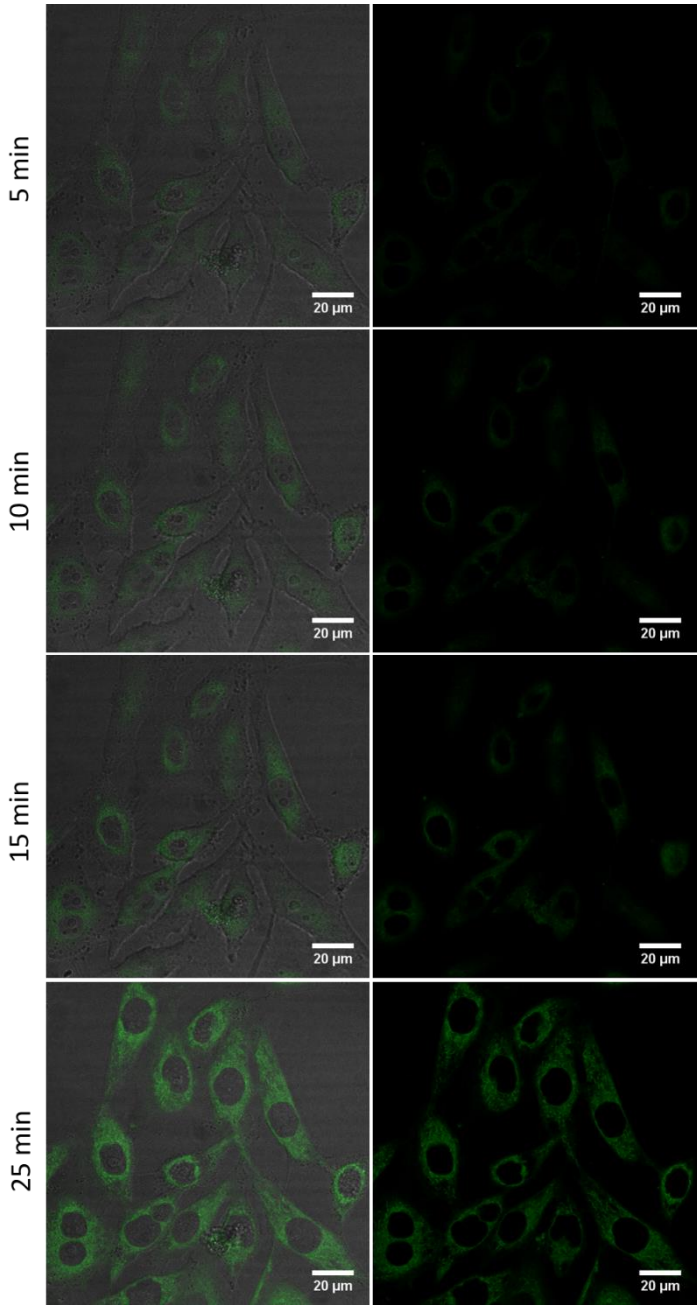

Figure S2.22 Live uptake of naphthyridyl-BODIPY-2-Cholesterol in HeLa cells. 5 µM of naphthyridyl-BODIPY-2-Cholesterol in cell media was added to HeLa cells, and the uptake was monitored over 25 minutes using confocal microscopy, showing the overlay channels (column 1) and the emission of the BODIPY channel only (column 2).

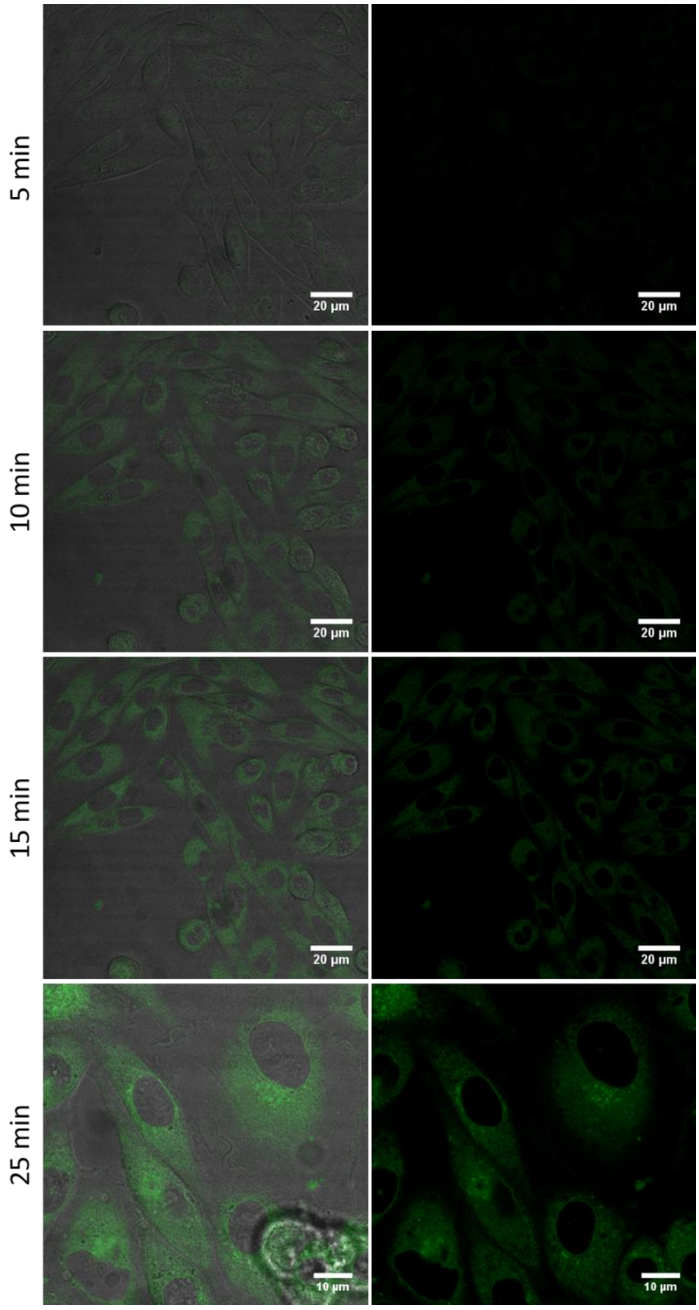

Figure S2.23 Live uptake of naphthyridyl-BODIPY-2-Cholesterol in CHO cells. 5 µM of naphthyridyl-BODIPY-2-Cholesterol in cell media was added to CHO cells, and the uptake was monitored over 25 minutes using confocal microscopy, showing the overlay channels (column 1) and the emission of the BODIPY channel only (column 2).

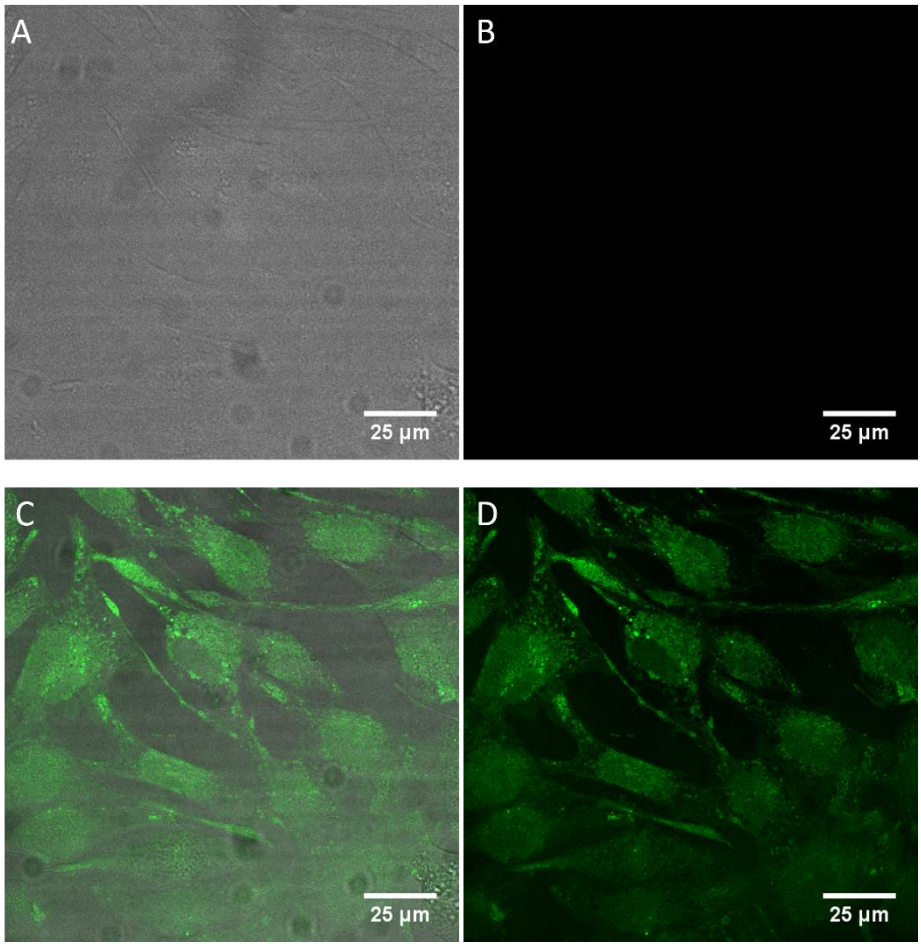

Figure S2.24 Control of Nile Red imaging settings without Nile Red present. To ensure there was no cross talk between naphthyridyl-BODIPY-2-Cholesterol and Nile Red for the colocalisation studies, HeLa cells stained with naphthyridyl-BODIPY-2-Cholesterol (5 µM) were imaged using the Nile Red imaging settings, without any Nile Red present in the sample. The cells (A) showed no emission from the Nile Red channel (B). C and D represent the naphthyridyl-BODIPY-2-Cholesterol imaging settings to show that naphthyridyl-BODIPY-2-Cholesterol was present in the sample.

Appendix B

Supporting information associated with Chapter 3.

S3.1 Experimental Details

S3.1.1 Materials

All reagents were purchased from Sigma Aldrich (Ireland) and used without further purification unless otherwise stated. 1,2- Dioleoyl-sn-glycero-3-phosphocholine (DOPC), brain sphingomyelin (BSM), and cholesterol (Chol) were obtained from Avanti Polar Lipids (Alabaster, AL, USA). DiD solid; DiIC18(5) solid (1,10 -dioctadecyl-3,3,30 ,30 -tetramethylindodicarbocyanine, 4-chlorobenzenesulfonate salt) was purchased from Thermo Fisher Scientific (Waltham, Massachusetts, USA). High purity fluorescein was purchased from Fluorochem Ltd.

S3.1.2 Instrumentation

^{1}H NMR spectra were recorded on either 400 MHz or 600 MHz Bruker spectrometer. All ^{13}C NMR spectra were obtained at 150 MHz. The spectra were processed using Bruker Topspin NMR software. High Resolution Mass Spectrometry (HR-MS) was carried out at the Mass Spectrometry facility, University College Dublin. Absorbance spectra were carried out using a Varian Cary 50 spectrometer. Samples were analysed in Hellma quartz fluorescence cuvettes, with a path length of 1 cm, and spectral range of 280–800 nm unless otherwise stated. Background measurements were carried out at room temperature prior to each measurement. Fluorescence emission spectra were obtained using a Varian Cary Eclipse fluorescence spectrophotometer with excitation and emission slit widths of 2.5 nm. All analyses were carried out using quartz cuvettes and background correction was applied prior to measurement. The lifetime of the excited state was measured using a PicoQuant FluoTime 100 Compact FLS TCSPC system using a 450 nm pulsed laser source generated from a PicoQuant PDL800-B box. Lifetime decay plots were analysed using PicoQuant TimeHarp software. The goodness of each fit to exponential decay kinetics was assessed from chi-squared values (where $\chi^2 < 1.3$) and visual inspection of residuals. Giant unilamellar vesicles were prepared using the Vesicle Prep Pro (VPP) (Nanion Technologies, Munich, Germany).

Fluorescent confocal imaging was carried out using a Leica TSP inverted (DMi8) confocal microscope. A 100-oil immersion objective was used for all measurements. A white light laser was used to excite the dyes. The excitation and emission wavelengths (λex/λem) were as follows: 503/511–570 nm for BODIPY-Ar-Chol and BODIPY-Ahx-Chol 644/ 665–700 nm for DiD and.

S3.2 Structural Characterisation

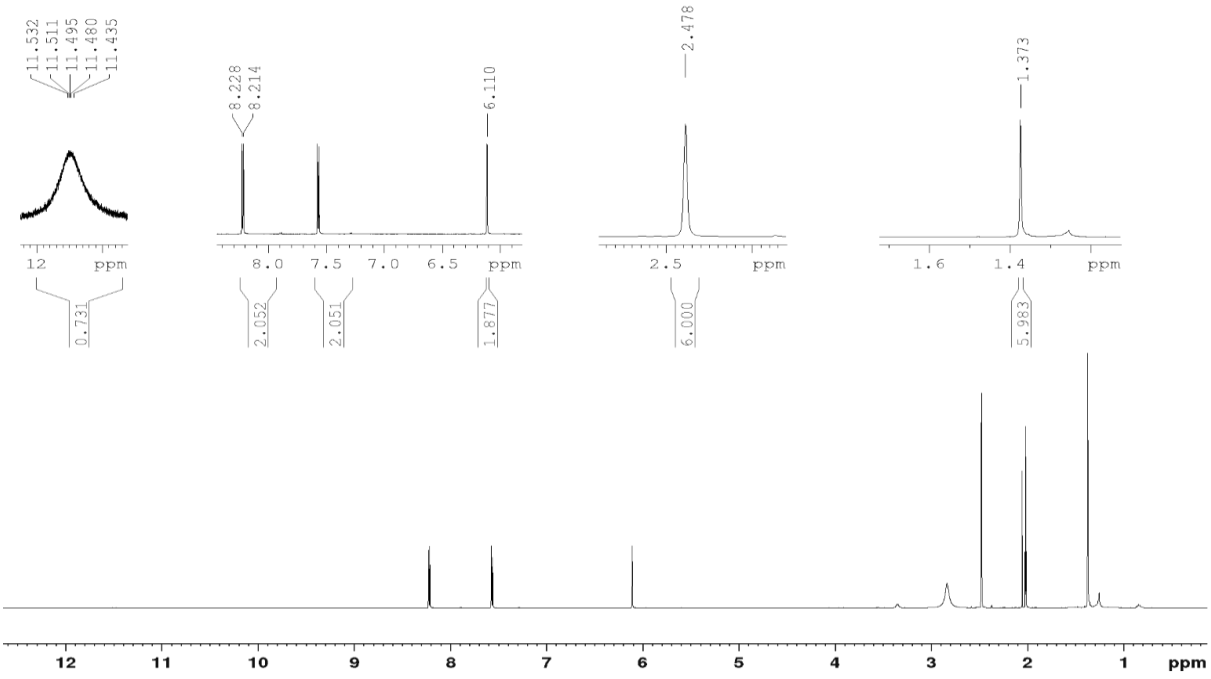

Figure S3.1 ^{1}H NMR (600 MHz) of **1** in DMSO-d_6.

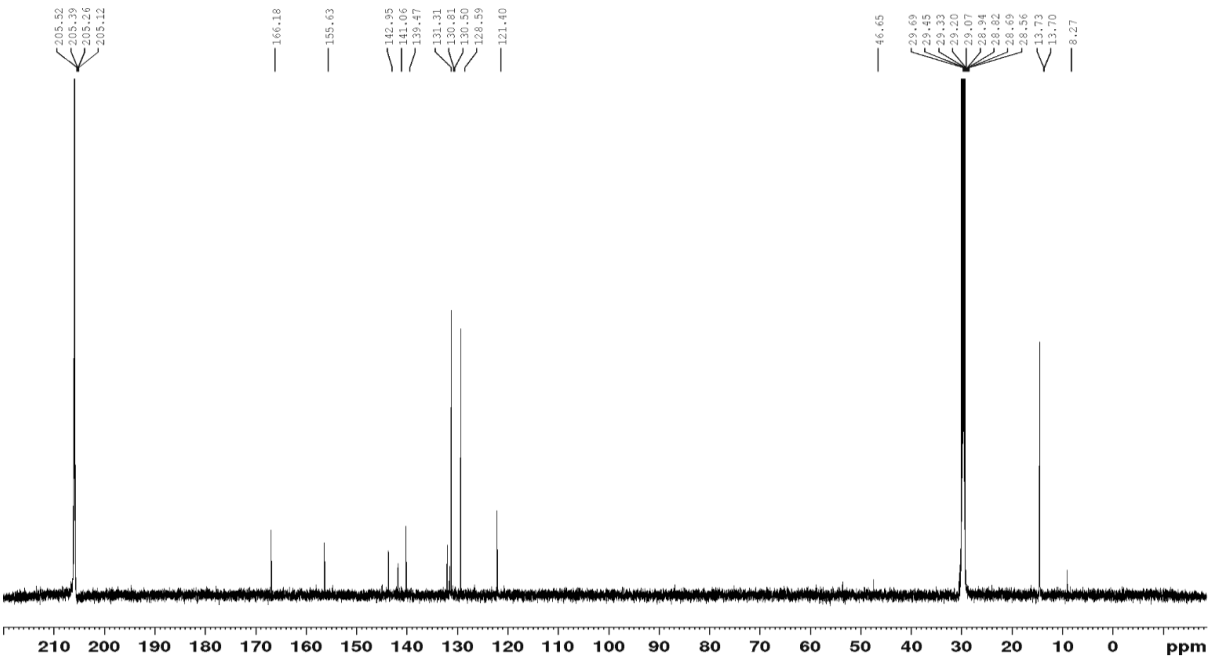

Figure S3.2 ^{13}C NMR (150 MHz) of **1** in DMSO-d_6.

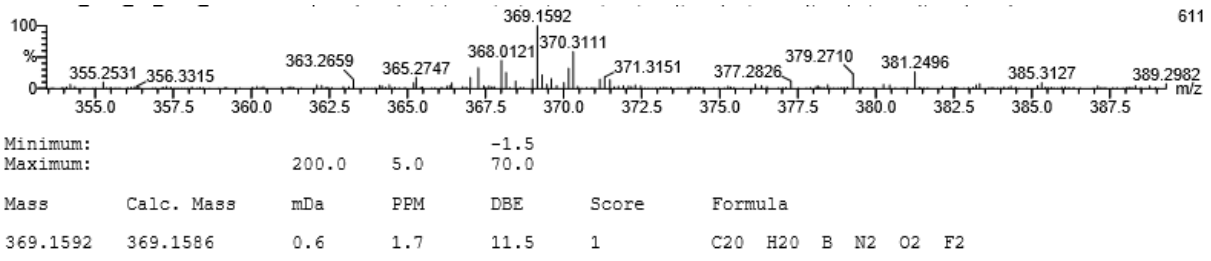

Minimum:				-1.5		
Maximum:		200.0	5.0	70.0		
Mass	Calc. Mass	mDa	PPM	DBE	Score	Formula
369.1592	369.1586	0.6	1.7	11.5	1	C20 H20 B N2 O2 F2

Figure S3.3 HR-MS (ESI-QTOF): Single Mass Analysis of **(1)** indicating $[M + H]^+$.

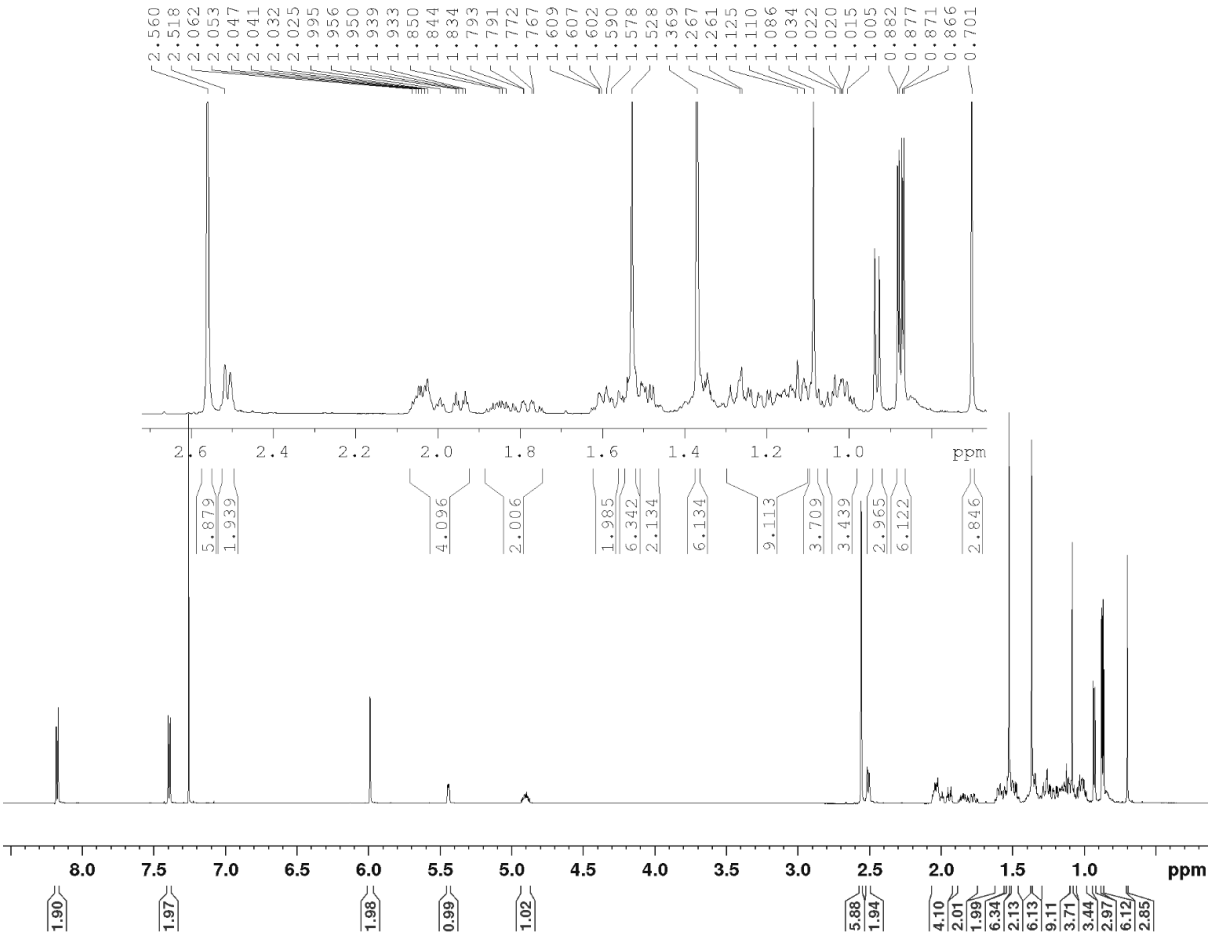

Figure S3.4 ^{1}H NMR (600 MHz) of **2** in $CDCl_3$.

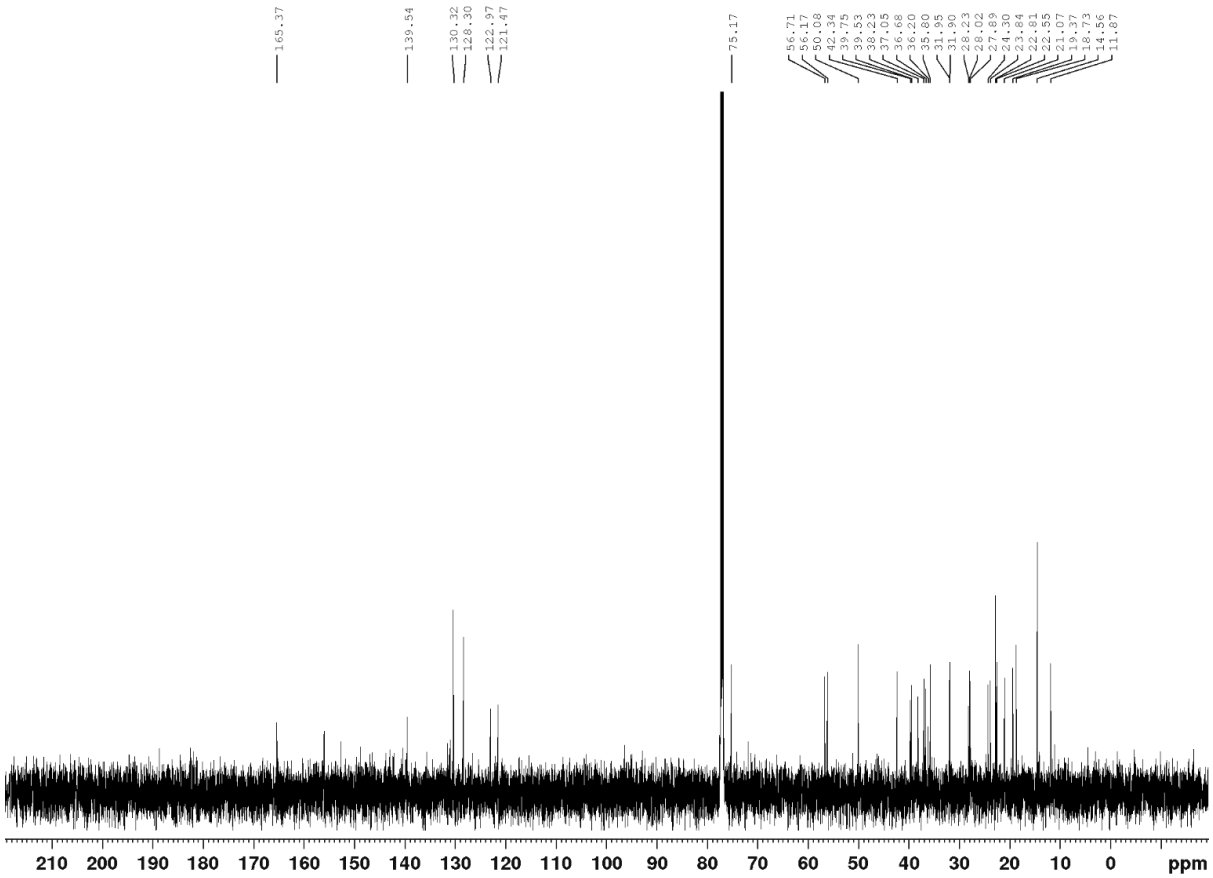

Figure S3.5 ^{13}C NMR (150 MHz) of **2** in $CDCl_3$.

Elemental Composition Report **Page 1**

Single Mass Analysis
Tolerance = 5.0 PPM / DBE: min = -1.5, max = 70.0
Isotope cluster parameters: Separation = 1.0 Abundance = 1.0%

Monoisotopic Mass, Odd and Even Electron Ions
39 formula(e) evaluated with 1 results within limits (all results (up to 1000) for each mass)

DCU - Tia KEyes
DCU_TK_DOC_BODIPY-8-Ar-Chol_20171003_run3 18 (0.369) AM (Cen,5, 80.00, Ar,1.0,556.28,0.70,LS 1); Sm (SG, 4x4.00); Sb (16,20.00); Cm (14:21)

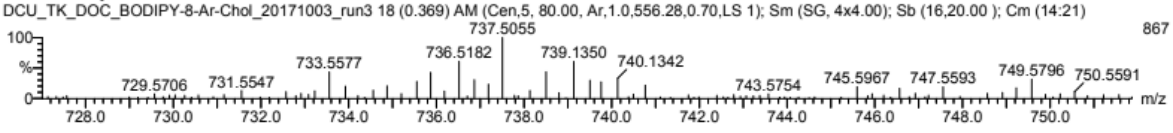

Minimum:				-1.5		
Maximum:		200.0	5.0	70.0		
Mass	Calc. Mass	mDa	PPM	DBE	Score	Formula
737.5055	737.5029	2.6	3.5	16.5	1	C47 H64 B N2 O2 F2

Figure S3.6 HR-MS (ESI-QTOF): Single Mass Analysis of **2** indicating $[M + H]^+$.

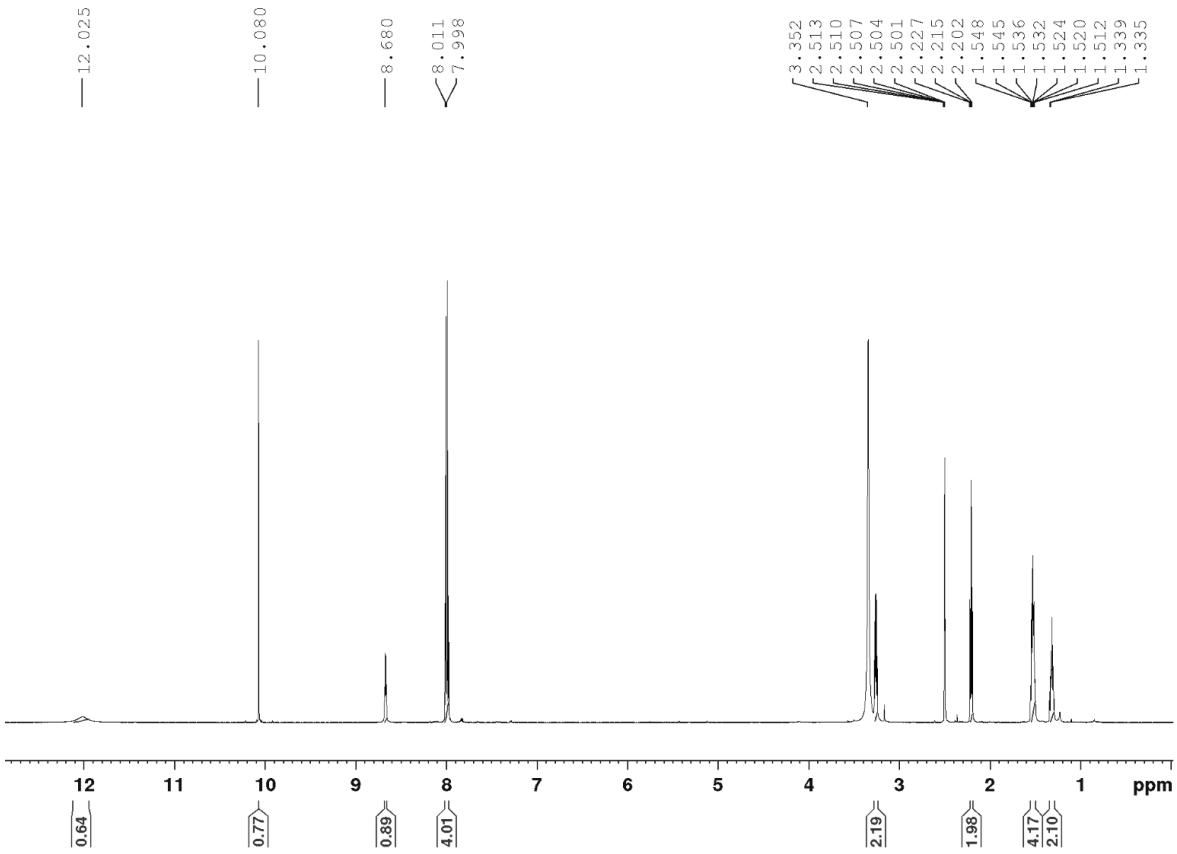

Figure S3.7 ^{1}H NMR (600 MHz) of **4** in DMSO-d_6.

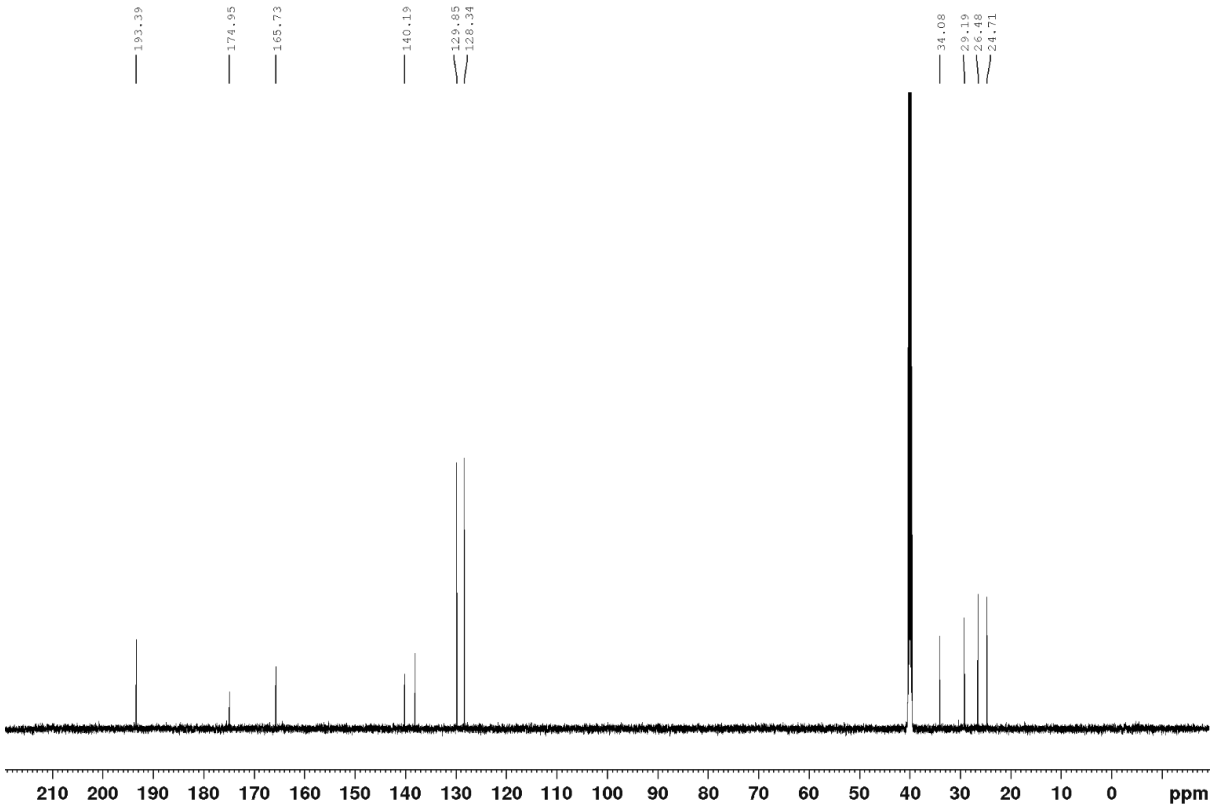

Figure S3.8 ^{13}C NMR (150 MHz) of **4** in DMSO-d_6.

Single Mass Analysis
Tolerance = 5.0 PPM / DBE: min = -1.5, max = 70.0
Isotope cluster parameters: Separation = 1.0 Abundance = 1.0%

Monoisotopic Mass, Odd and Even Electron Ions
8 formula(e) evaluated with 1 results within limits (all results (up to 1000) for each mass)

External Client
DCU_TK_DOC_3-4-formylphenyl-6-Ahx-OH 10 (0.333) AM (Cen,5, 80.00, Ar,1.0,556.28,0.70,LS 1); Sm (Mn, 4x4.00); Sb (16,20.00); Sb (16,20.00); Cm (9:10)

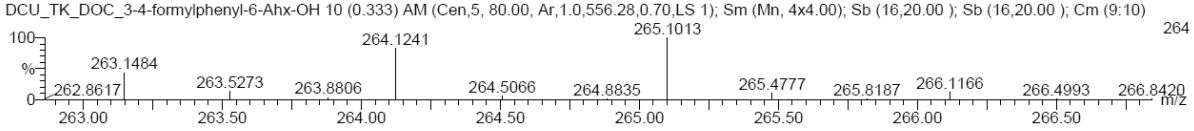

Minimum:				-1.5		
Maximum:		200.0	5.0	70.0		
Mass	Calc. Mass	mDa	PPM	DBE	Score	Formula
264.1241	264.1236	0.5	2.0	6.5	1	C14 H18 N O4

Figure S3.9 HR-MS (ESI-QTOF): Single Mass Analysis of **4** indicating $[M + H]^+$.

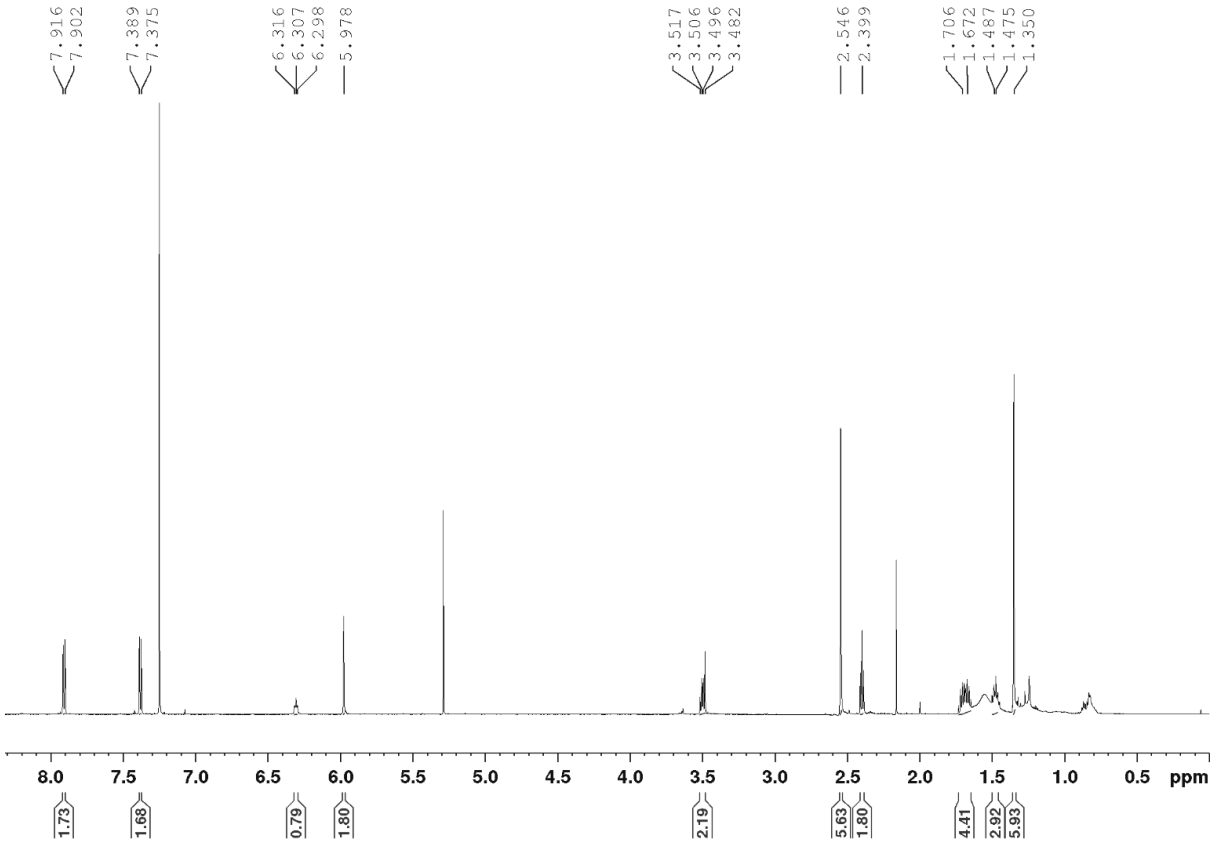

Figure S3.10 ^{1}H NMR (600 MHz) of **5** in $CDCl_3$.

Single Mass Analysis
Tolerance = 5.0 PPM / DBE: min = -1.5, max = 70.0
Isotope cluster parameters: Separation = 1.0 Abundance = 1.0%

Monoisotopic Mass, Odd and Even Electron Ions
52 formula(e) evaluated with 1 results within limits (all results (up to 1000) for each mass)

External Client
DCU_TK_DOC_1-BODIPY-Ar-Ahx-OH 16 (0.527) AM (Cen,5, 80.00, Ar,1.0,556.28,0.70,LS 1); Sm (Mn, 4x4.00); Sb (16,20.00); Cm (15:34) 1: TOF MS ES+ 796

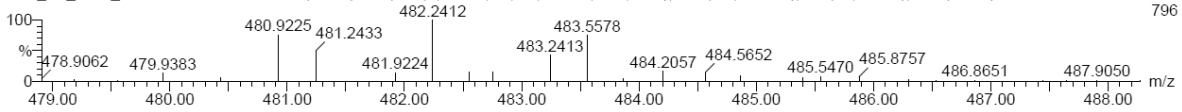

Minimum:				-1.5		
Maximum:		200.0	5.0	70.0		
Mass	Calc. Mass	mDa	PPM	DBE	Score	Formula
482.2412	482.2427	-1.5	-3.0	12.5	1	C26 H31 B N3 O3 F2

Figure S3.11 HR-MS (ESI-QTOF): Single Mass Analysis of **2** indicating [M]+

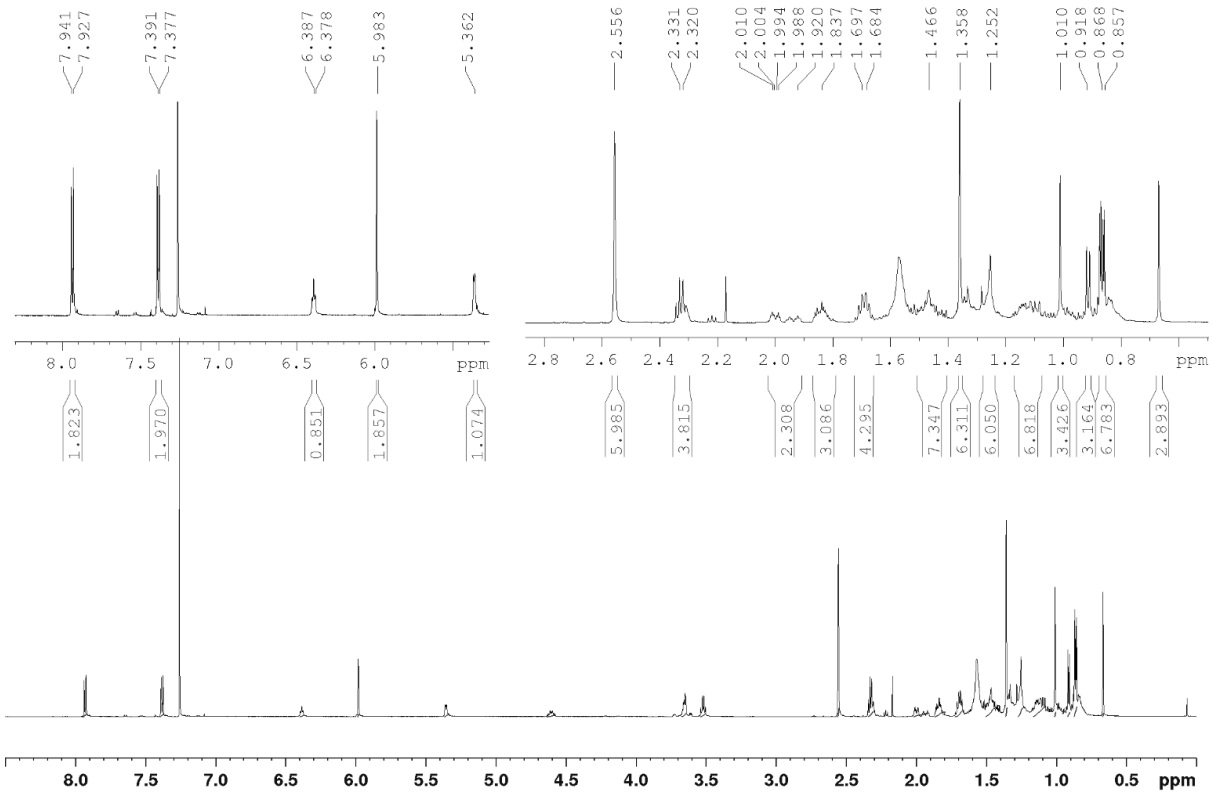

Figure S3.12 ^{1}H NMR (600 MHz) of **6** in $CDCl_3$.

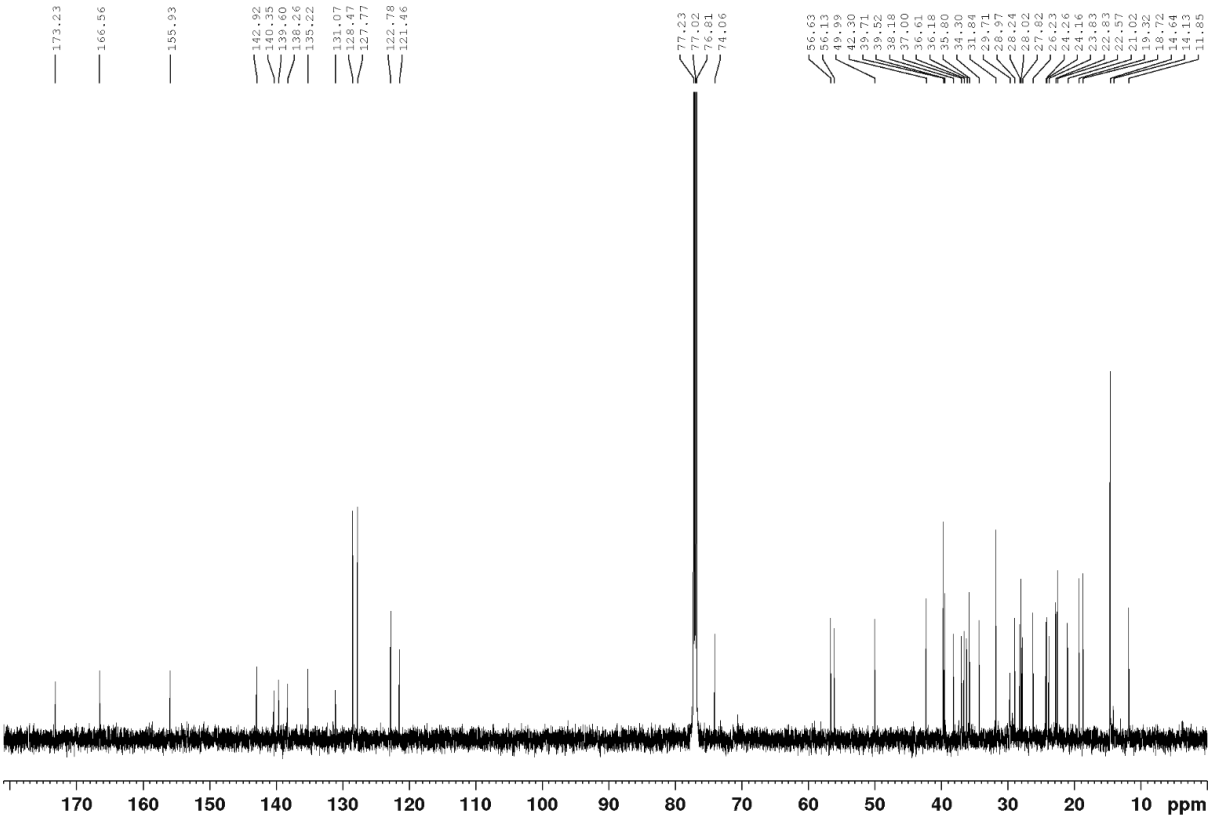

Figure S3.13 ^{13}C NMR (150 MHz) of **6** in $CDCl_3$.

Elemental Composition Report **Page 1**

Single Mass Analysis
Tolerance = 5.0 PPM / DBE: min = -1.5, max = 70.0
Isotope cluster parameters: Separation = 1.0 Abundance = 1.0%

Monoisotopic Mass, Odd and Even Electron Ions
92 formula(e) evaluated with 1 results within limits (all results (up to 1000) for each mass)

DCU - Tia KEyes
DCU_TK_DOC_BODIPY-Ar-Ahx-Chol-BAAC_20171003 13 (0.269) AM (Cen,5, 80.00, Ar,1.0,556.28,0.70,LS 1); Sm (SG, 4x4.00); Sb (16,20.00); Cm (8:13)

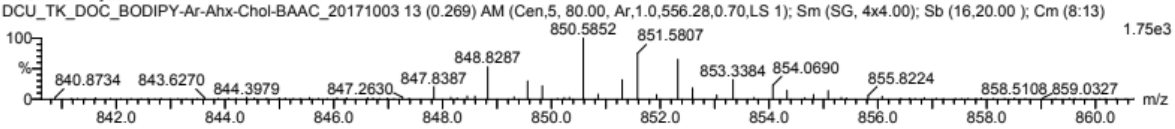

Minimum:				-1.5		
Maximum:		200.0	5.0	70.0		
Mass	Calc. Mass	mDa	PPM	DBE	Score	Formula
850.5852	850.5870	-1.8	-2.1	17.5	1	C53 H75 B N3 O3 F2

Figure S3.14 HR-MS (ESI-QTOF): Single Mass Analysis of **6** indicating $[M + H]^+$.

S3.3. Additional Photophysical Data

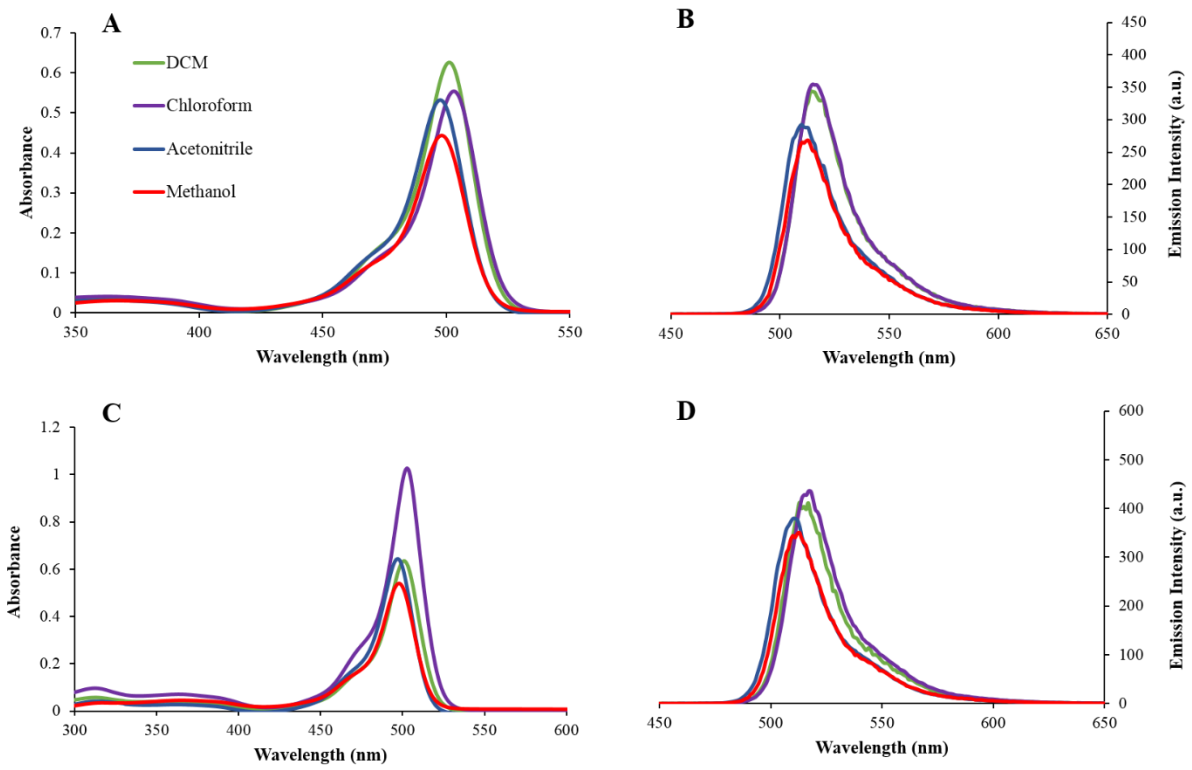

Figure S3.15 (a) Solvent dependent absorbance curves for 2 (10 μM). (b) Solvent dependent emission curves for 2 (10 μM, slit widths; 2.5 nm). (c) Solvent dependent absorbance curves for 6 (10 μM). (d) Solvent dependent emission curves for 6 (10 μM, slit widths; 2.5 nm).

Quantum yield determination: The quantum yields for **2** and **6** in a range of solvents was calculated using fluorescein as a reference. Fluorescein (in 0.1 M NaOH) (φ =0.90)[3]. Solutions were prepared, and absorbance matched, and the optimal excitation was taken as wavelength of intersection. Fluorescence emission spectra were obtained using slit widths 2.5 nm and the following equation was used to calculate the quantum yields.

$$\phi_x = \phi_{st} * (Area_x/Area_{st}) * (\eta^2_x/\eta^2_{st})$$

where the ϕ_x and ϕ_{st} refer to the fluorescence quantum yield of the sample and fluorescein standard, respectively. $Area_x$ and $Area_{st}$ are the integrated emission intensities for the sample and fluorescein standard, respectively. η_x and η_{st} is the refractive index of the solvent for the sample and fluorescein standard, respectively.

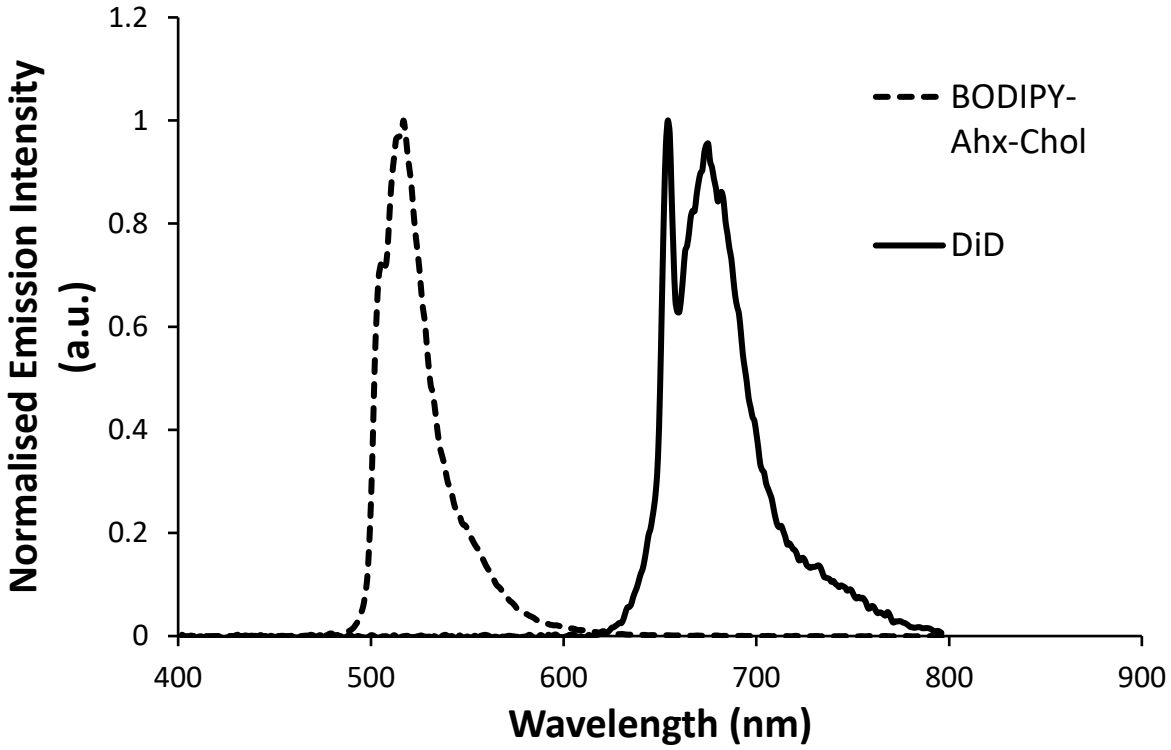

Figure S3.16 Normalised emission spectra of a mixed solution of chloroform containing both BODIPY-Ahx-Chol (5 μM) (**6**) and DiD (5 μM). BODIPY-Ahx-Chol and DiD have emission maxima of 516 nm and 675 nm respectively. This shows that there is no crosstalk between dyes when used in GUV experiments, using emission filters as stated in experimental sections. For the spectrum of BODIPY-Ahx-Chol, the sample was excited at 503 nm using an excitation slit width of 2.5 nm and an emission slit width of 5 nm. For the spectrum of DiD, the sample was excited at 503 nm using an excitation slit width of 2.5 nm and an emission slit width of 5 nm.

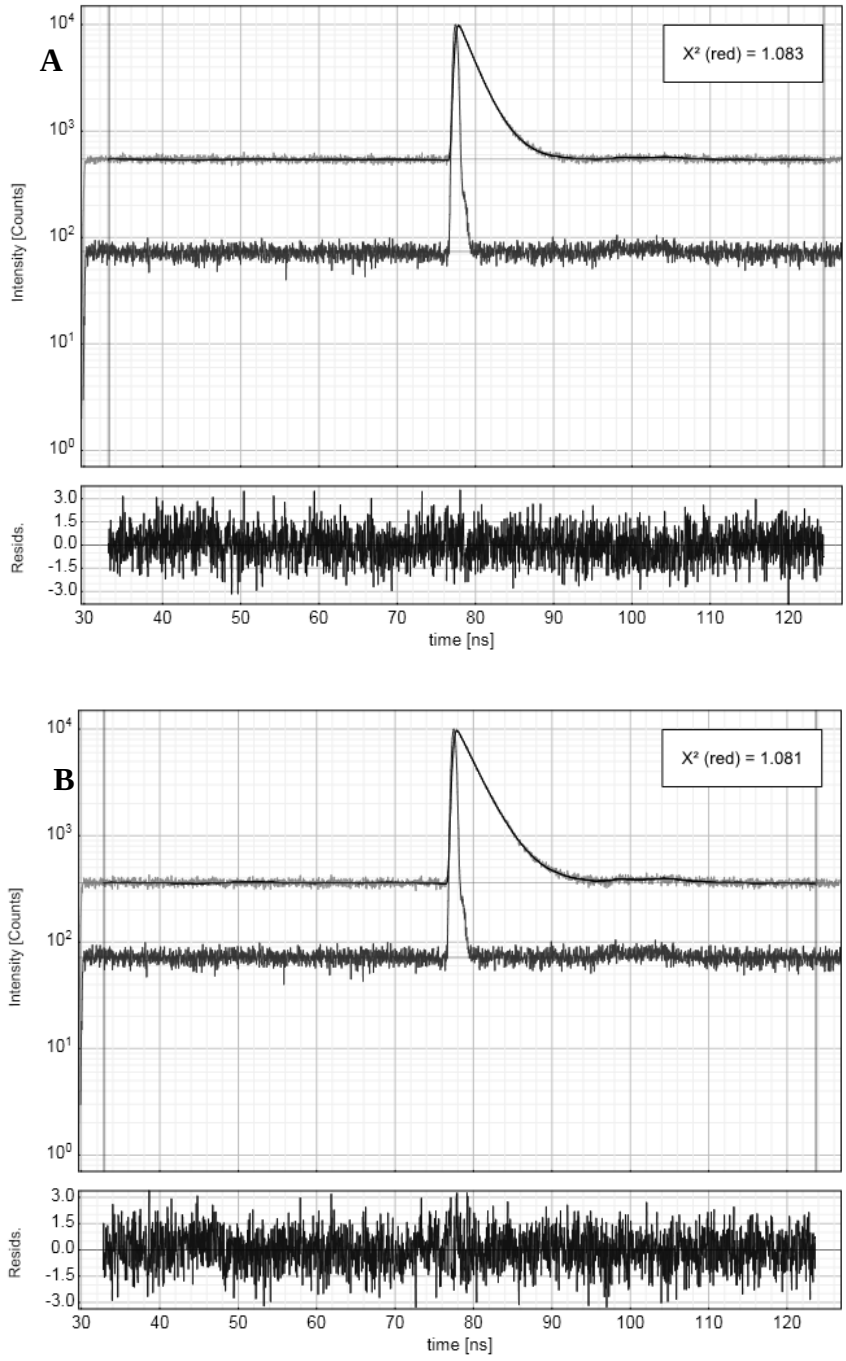

Figure S3.17 Time correlated single photon counting trace for BODIPY-Ar-Chol (**2**) in methanol (10 µM) with IRF (red) at room temperature (**A**) and for BODIPY-Ar-Ahx-Chol (**6)** in methanol (10 µM) with IRF (red) at room temperature (**B**).

S3.4 Cell Imaging

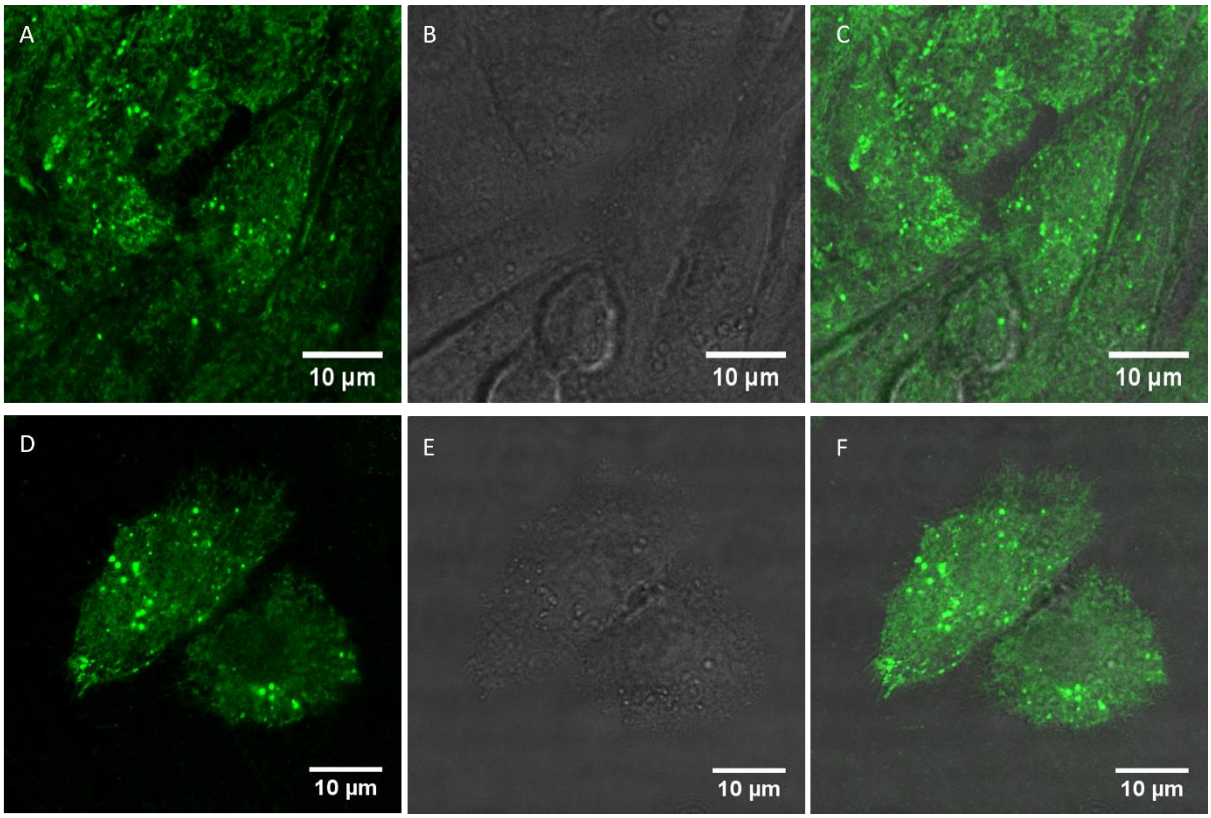

Figure S3.18 CHO cells stained with BODIPY-Ahx-Chol (5 µM, 2h), showing a group of CHO cells (A-C) and a second cluster of cells (D-F). A, D – BODIPY channel. B, E – overlay of BODIPY channel and background channel. C, F – background channel.

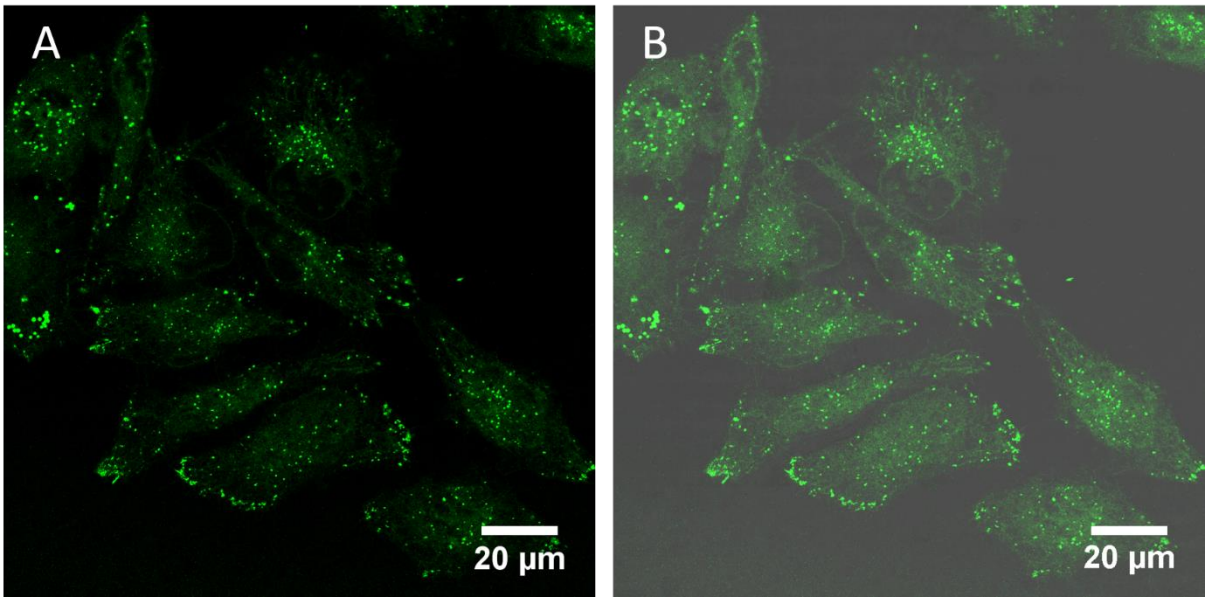

Figure S3.19 Confocal imaging of live HeLa cells stained with BODIPY-Ar-Chol (5 µM, 37 °C, 3 h).

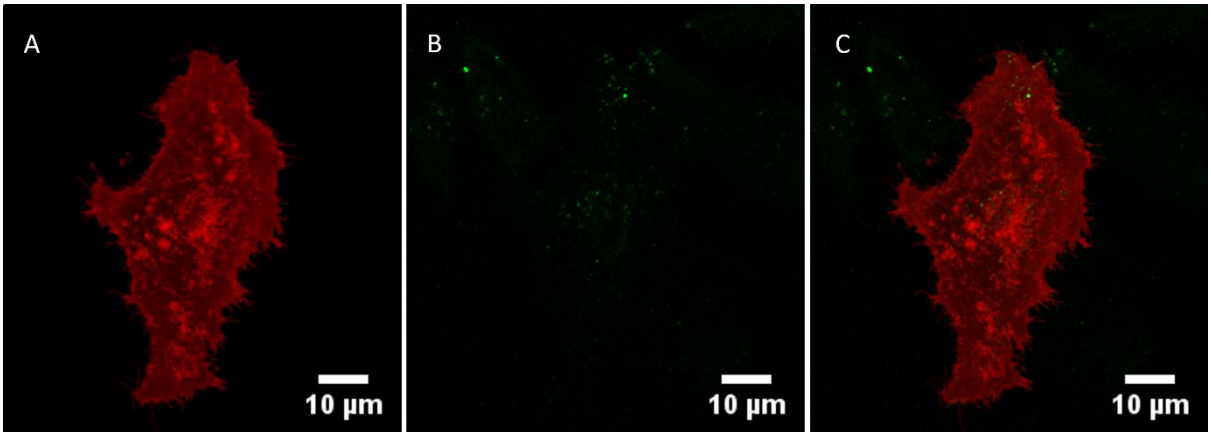

Figure S3.20 Confocal imaging of live HeLa cell co-stained with DiD (800 nM) (A), BODIPY-Ar-Chol (5 µM) (B), and the overlay of both channels (C). Emission from the BODIPY-Ar-Chol channel is low as the focus is on the cell membrane, where it does not localise.

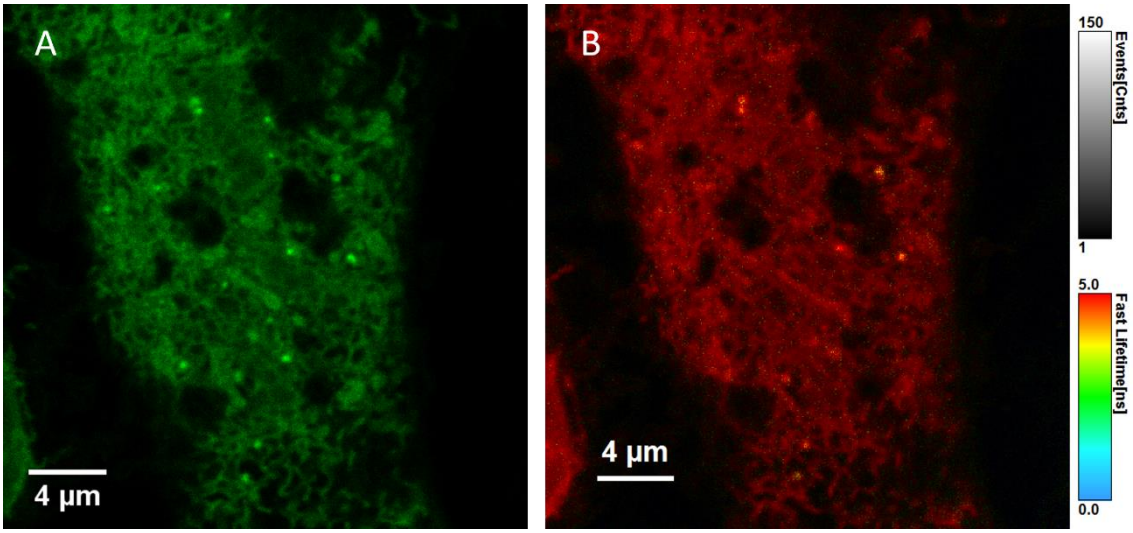

Figure S3.21 Confocal image of a live HeLa cell stained with BODIPY-Ahx-Chol, focused at the membrane of the cell (A), and the corresponding FLIM lifetime distribution image (B). FLIM was acquired by exciting at 497 nm for 2 minutes.

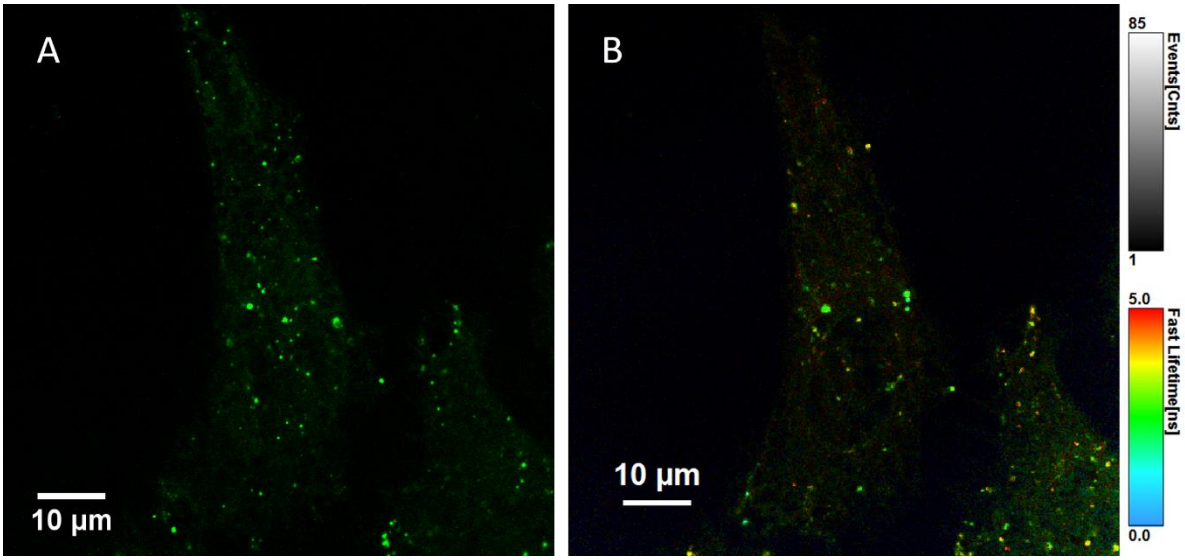

Figure S3.22 Confocal image of a live HeLa cell stained with BODIPY-Ar-Chol, focused at the membrane of the cell (A), and the corresponding FLIM lifetime distribution image (B). FLIM was acquired by exciting at 497 nm for 2 minutes.

S3.5 Giant Unilamellar Vesicle (GUV) Studies

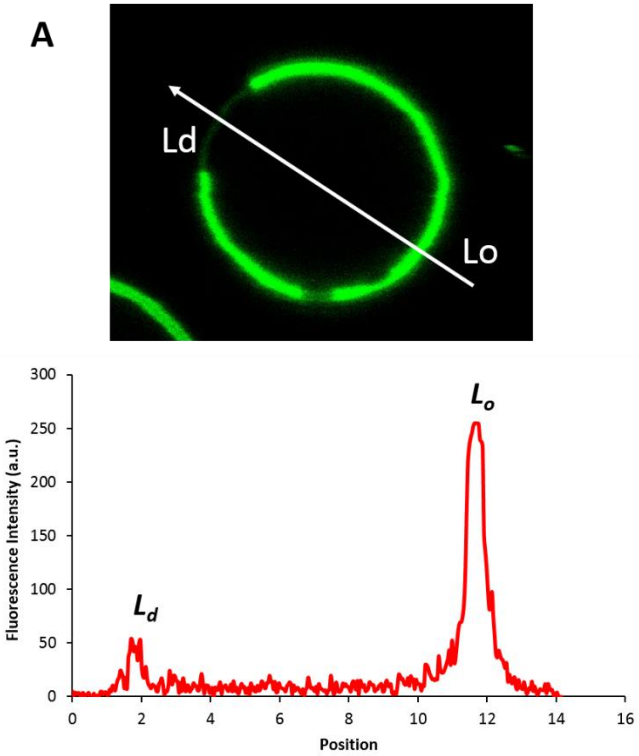

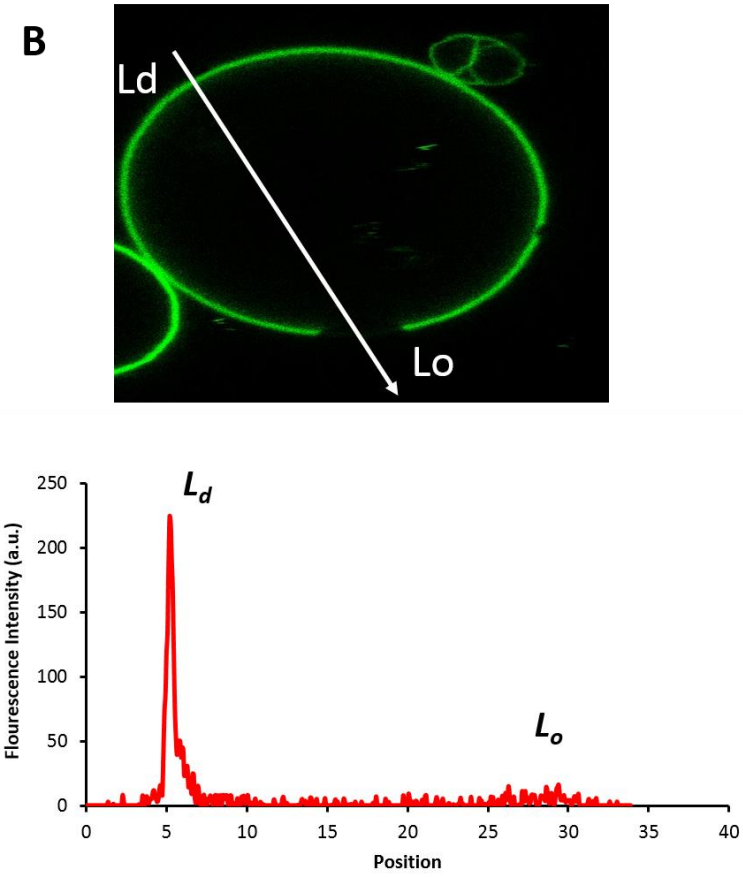

$$\%L_o = \frac{F(L_o)}{F(L_o) + F(L_d)}\ x\ 100$$

Figure S3.23 Calculation of Lo% and Ld% was carried out using intensity profiles through scanning confocal fluorescence images as given by the examples above. Representative scanning confocal fluorescence images of phase were obtained of separated GUVS labelled with BODIPY-Ahx-Chol (A) BODIPY-Ar-Chol (B) respectively. The distribution of these molecules is revealed by the fluorescence intensity (green). The fluorescence intensities of the Lo and Ld phases, F(Lo) and F(Ld) respectively, were determined from the peak maxima of the line scan, where the different phases were identified by the Ld phase markers DiD (fluorescence not shown).

Table S3.1 Fluorescent lifetimes of BODIPY-Ahx-Chol in live HeLa and CHO cells, with and without treatment using MβCD (10 mM, 4 h)

	HeLa cells		**CHO cells**	
	τ (ns)	**τ_{Amp}** (%)	**τ** (ns)	**τ_{Amp}** (%)
Control	$\tau_1 = 5.85 \pm 0.15$ $\tau_2 = 2.31 \pm 0.37$	67.6 32.5	$\tau_1 = 5.3 \pm 0.01$ $\tau_2 = 2.4 \pm 0.05$	63.8 29.3
MβCD	$\tau_1 = 5.35 \pm 0.25$ $\tau_2 = 2.23 \pm 0.17$	63.6 36.5	$\tau_1 = 5.85 \pm 0.05$ $\tau_2 = 2.89 \pm 0.21$	68.3 32.7

Table S3.2 Fluorescent lifetimes of BODIPY-Ar-Chol in live HeLa

	HeLa Cells	
	τ (ns)	**τ_{Amp}** (%)
BODIPY-Ar-Chol	$\tau_1 = 5.26 \pm 0.09$ $\tau_2 = 1.65 \pm 0.14$	63.5 37.5

Appendix C

Supporting information associated with Chapter 4.

S4.1 Experimental Section

S4.1.1Materials

All chemical reagents were purchased from Sigma Aldrich (Ireland) and used without further purification unless otherwise stated. 1,2-dioleoyl-sn-glycero-3-phosphocholine (DOPC), brain sphingomyelin (BSM), cholesterol (Chol) and N-heptadecanoyl-D-erythro-sphingosine C_{17} Ceramide were obtained from Avanti Polar Lipids (Alabaster, AL, USA). Nile Red technical grade was purchased from Sigma Aldrich (Ireland).

S4.1.2 Instrumentation

^{1}H and ^{13}C NMR spectra were recorded on a 400 MHz or 600 MHz Bruker spectrometer respectively and the solvent stated. The spectra were processed using Bruker Topspin NMR software. High Resolution Mass Spectrometry (HR-MS) was carried out at the Mass Spectrometry facility, University College Dublin. MALDI-ToF mass spectrometry was performed on MALDI-Q-ToF Premier instrument at Trinity College Dublin. Elemental analysis was carried out using an Exeter Analytical CE 440 elemental analyser at the Microanalytical Laboratory, University College Dublin. Analytical HPLC was performed on a Varian 940-LC Liquid Chromatograph using an Agilent C18 column (4.6 250 mm) and the solvent system stated. Flow rates were kept at 1.6 mL/min and run times were 20 minutes. PDAD was used for peak detection and the analysis was followed by monitoring 280 nm and 430 nm channels. UV – Vis absorption spectra were recorded on Varian Cary 50 spectrometer. Samples were analysed in Hellma quartz fluorescence cuvettes, with a path length of 1 cm, and spectral range of 330 – 800 nm unless otherwise stated. Background measurements were carried out at room temperature prior to each measurement. Emission Spectra were recorded on a Varian Cary Eclipse fluorescence spectrophotometer with excitation and emission slit widths stated. All analyses were carried out using quartz cuvettes and background correction was applied prior to measurement. Fluorescence lifetime measurements were carried out using a PicoQuant FluoTime 100 Compact FLS TCSPC

system using a 450 nm pulsed laser source generated from a PicoQuant PDL800-B box. The instrument response function was determined using Ludox colloidal silica solution. Lifetime decay plots were analysed using PicoQuant TimeHarp software. The goodness of each fit to exponential decay kinetics was assessed from chi – squared values (where χ^2 <1.3) and visual inspection of residuals.

S4.1.3 Preparation of Supported Lipid Bilayers

The lipid bilayers were prepared by a hybrid method using Langmuir-Blodgett – Vesicle Fusion methods inspired by Basit et al[1]. The lipid bottom layer is formed by transferring a lipid monolayer by Langmuir-Blodgett technique (KSV Nema). The surface pressure was controlled by a Wilherm platinum balance. Lipid solution was spread at the sub-phase surface (MiliQ water, pH 7.4) and left to evaporate for about 15 min. The lipid monolayer was transferred at 32mN/m. To prepare liposomes lipids dissolved in chloroform were mixed to PyLa-C_{17}Cer at ratio of 5000:1 mol and dried gently against nitrogen flow. Dried lipids were suspended in PBS buffer by vortex agitation, then liposomes were prepared by lipid extrusion (Avanti Lipids) with 0.1um PC membrane. Liposomes composed of raft composition were extruded at 50^{o}C and kept at this temperature to assure proper lipid fluidity. After liposomes introduction to the microfluidic chamber vesicle's solution were left to react for 30 min. To remove any residual liposomes, the vesicle solution is purged with PBS buffer.

S4.1.4 Fluorescence Lifetime Correlation Spectroscopy

Diffusion coefficients for labelled supported lipid bilayers were obtained using fluorescence lifetime correlation spectroscopy, FLCS performed on a Microtime 200 system (Picoquant GmBH, Berlin, Germany). The system consists of an inverted microscope model Olympus X1-71 with an Olympus UPlanSApo 60x/1.2 water immersion objective. The fluorophores were excited with a 440 nm PicoTA from Toptica (Picoquant). The laser was directed onto 440/532rpc dichroic mirror and focused on the aforementioned objective. The sample fluorescence was collected through the same objective and filtered by the dichroic mirror and by a 460 nm interference filter. The sample fluorescence was passed through a 50 µM pinhole onto a Single Photon Avalanche Diode (SPAD). The autocorrelation functions (ACFs) were fit using SymphoTime 2.3 software (Picoquant GmBH, Berlin, Germany) to the following equation (S4.1):

$$G(\tau) = \frac{1}{N(1-T)}\left[1 - T + Te^{\left(-\frac{\tau}{\tau_T}\right)}\right]\left[1 + \left(\frac{\tau}{\tau_D}\right)^{\alpha}\right]^{-1} \quad \text{(Equation S4.1)}$$

Where G(τ) is the autocorrelation function of fluorescence fluctuations; N is the average number of diffusing fluorophores in the effective volume; τ is the delay time; T is the fraction of molecules in the triplet state; α is the anomalous parameter; τD is the diffusion time of the molecules and τ_T is the decay time for the triplet state. The bilayer was located by scanning the microscope along the z-axis to identify peak fluorescence intensity. A minimum of nine measurements were taken and any outliers were disregarded. Autocorrelation curves were fit to a 2D model to determine the diffusion coefficients. All lipid bilayers used in the FLCS experiments were labelled with PyLa-C_{17}Cer at a concentration of 10 nM. The confocal volume was determined by prior calibration using Atto 425, fitting the resulting autocorrelation function using the known diffusion coefficient of the dye at 20 °C. The free diffusion of Atto 425 was calculated with equation S4.2 following the water viscosity correction[2]:

$$D(T) = D(25℃)\frac{T}{298.15K}\frac{8.9.10^{-4}\ Pa.s}{\eta(T)} \quad \text{(Equation S4.2)}$$

Where D is the dye diffusion and η is the viscosity of water.

S4.1.5 Fluorescence Lifetime Imaging (FLIM) of Supported Lipid Bilayers

Fluorescence lifetime imaging was carried out using a PicoQuant 100 system attached to Leica TSP inverted (DMi8) confocal microscope using a 100x oil immersion objective. Each sample was acquired for 120 s with a 512 x 512 resolution. A 405 nm pulsed laser was used to excite the dyes in supported lipid bilayers and in live cell samples. Data was analysed using PicoQuant Symphotime software.

S4.1.6 Cell Culture

HeLa cells, a cervical cancer cell line, were cultured. The media used to culture the cells was MEM media supplemented with 2% L-glutamine, 1% MEM non-essential amino acid solution, 10% foetal bovine serum and 1% penicillin-streptomycin and grown at 37°C with

5% CO_2. Cells were harvested or split at 90% confluency using 0.25% trypsin for 5 minutes at 37°C.

S4.1.7 Confocal Microscopy for Cell Imaging

HeLa cells were seeded at 1.5 x 10^5 cells in 2 mL culture media on poly-L-lysine coated, #1.5 coverslips in a 6-well plate and left for 48 h at 37°C under 5% CO_2. PyLa and PyLa-C_{17}Cer were added to the wells in cell media to give a final concentration of 2 μM (final DMSO concentration of 0.5%) and were incubated for 2 h at 37°C with 5% CO_2. Prior to imaging, the compounds were removed, and the cells were washed once with PBS supplemented with 1.1 mM $MgCl_2$ and 0.9 mM $CaCl_2$. The cells were imaged live using a Leica TSP DMi8 confocal microscope with a 100X oil immersion objective lens. A heated box covered the stage to keep the temperature at 37°C. A 405 nm laser was used to excite the compounds, and a 520-620 nm filter was used to collect the emission.

For real-time imaging, cells were seeded at 1.5 x 10^5 cells in 2 mL culture media on 35 mm high precision glass-bottom dishes (Ibidi, Germany) as described previously. PyLa and PyLa-C_{17}Cer were added to Leibovitz media to give a final concentration of 2 μM and was added to live cells and imaged immediately using Time Series mode to capture images every 1 minute over a 25-minute period. To assess the mode of uptake, cells were prepared as mentioned above and incubated with the compounds at 4°C for 4 h. Cells were washed with PBS (supplemented with 1.1 mM $MgCl_2$ and 0.9 mM $CaCl_2$) and imaged immediately.

To induce lipid droplet production, HeLa cells were seeded and incubated as described previously. TNF-α (Bio-techne Ltd) was added to the cells to give a final concentration of 10 ng/mL in Hela media, and cells were incubated for 16 h in the absence of light at 37°C and 5% CO_2. PyLa-C_{17}Cer (2 μM) was added to the cells for 2 h prior to imaging.

S4.1.8 Phototoxicity

Phototoxicity HeLa cells were seeded at 1.5 x 105 on 35 mm glass bottom culture dishes and incubated for 48 h. The media was removed, and cells were washed with PBS supplemented with 1.1 mM MgCl2 and 0.9 mM CaCl2 and transferred to a 37°C heated stage. 2 μM of PyLa-C_{17}Cer in HeLa media for 2 h. Prior to imaging, the dye was removed, cells were washed with supplemented PBS, and DRAQ 7 (1:100) was added to the live cells. The Time

Series mode on a Leica TSP DMi8 confocal microscope was used. DRAQ 7, which stains the nucleus of dead cells, was excited at 633 nm and collected between 635 -720 nm. Cells were scanned continuously using the PyLa-C_{17}Cer settings (0.06 mW/cm2) for 5-minute intervals, imaging with the DRAQ 7 settings between intervals to assess viability. For the control, cells were set up as described above, and DRAQ 7 (1:100) in HeLa media was added to the live cells. They were scanned continuously using the Pyrene settings and imaged after each interval to assess for DRAQ 7 uptake.

S4.1.9 Cytotoxicity Studies

Cytotoxicity Studies HeLa cells were seeded in 96-well plates (Sarstedt flat-bottom cell+ culture plate) at 1 × 104 in 100 μL media for 24 h at 37°C with 5 % CO2. PyLa and PyLa-C_{17}Cer were added for 20 hours at 37°C with 5 % CO2. Final dye concentrations were 100, 50, 20, 10, 5 and 1 μM. The Alamar blue assay (Promocell GmbH) was used to measure cell viability by the addition of 10 μL resazurin reagent and cells were incubated for 7 h at 37°C in the dark. Absorbance was measured using a Tecan 96-well plate reader at 570 nm and 600 nm (corrected for background subtraction).

S4.1.10 FLIM of Live HeLa Cells

HeLa cells were prepared and stained as described for confocal imaging. Live FLIM images were acquired using SymphoTime 200, Picoquant, attached to a Leica TSP DMi8 confocal microscope using a 100x oil immersion objective and heated stage set to 37°C. Each FLIM image was acquired for 2 minutes with 512 x 512 resolution. A 405 nm laser was used to excite the sample, and emission collected using a 520-620 nm filter. The data was analysed using PicoQuant Symphotime software. Lifetimes were fit to a mono-exponential decay for PyLa, and bi-exponential decay for PyLa-C_{17}Cer, until a X^2 value of 0.9-1.1 was achieved.

S4.1.11 STED Imaging of Live HeLa cells

HeLa cells were seeded at 1.5 x 10^5 cells in 2 mL culture media on poly-L-lysine coated, #1.5 coverslips in a 6-well plate and left for 24 h at 37°C under 5 % CO_2. TNF-α was added to the cells to give a final concentration of 10 ng/mL in Hela media, and cells were incubated for 16 h in the absence of light at 37°C and 5% CO_2. PyLa-C_{17}Cer (2 μM) was added to the cells for 2 h prior to imaging. The dye was removed, and the cells were washed x2 for 2 minutes with supplemented PBS. To acquire STED images, a Leica DMI8 confocal system

with STED lasers was used. A 405 nm laser (PicoQuant) was used to excite PyLa-C_{17}Cer, collecting the emission between 520-620 nm, using a 100X oil immersion objective. Images were scanned at 2408 x 2408 resolutions, using a scan speed of 0.032 frame/s. A line accumulation of 6 was used to eliminate as much background as possible. A time gating system was used to remove any autofluorescence and was set to 1.5-12 ns. A 660 nm depletion laser was used to acquire the live cell STED images. Images were deconvolved using Huygens Professional software. All data and FWHM analysis were carried out on raw images before deconvolution process using Image J and OriginPro.

S4.1.12 Photostability

HeLa cells were prepped for STED as described above and stained with either PyLa-C_{17}Cer (2 μM) or Nile Red (1 ng/mL). The samples were imaged using the optimum STED settings. A 405 nm laser was used to excite Pyla-C_{17}Cer, collecting the emission between 520-620 nm, and a 560 nm white light laser was used to excite Nile Red collecting the emission between 580-670 nm with a 100X oil immersion objective. The STED 660 nm at 0.05 W was used for both samples. The images were acquired at 1024 x 1024 resolutions every 1 minutes for 30 minutes at a pixel dwell time of 2.43 μs. The emission intensity of a selected area in both samples was measured at each time interval over the 20 minutes and plot to show stability over time.

S4.1.13 Computational Studies

The quantum chemical calculations were undertaken using the Gaussian 16 programme suite.[3] The B3LYP hybrid functional was used with a range of basis sets as indicated.[4-5] Initial structures were obtained from molecular mechanics methods. The polarisable continuum model[6-7] was used to mimic the solvent environment. GaussView 3.0[8] was used to visualise the electron density difference maps and the AOMix package was used to simulate the UV/visible spectra.[9-10] Band structures used Gaussian functions with a width at half height of 3000 cm^{-1}.

S4.2 Synthesis and Structural Characterisation

S4.2.1 Synthesis of pyrene-1-carboxylic acid (2) Synthesised according to a reported method.[43] Yield: brown solid, 0.671 g, (2.51 mmol, 57 %).

^{1}H NMR (400 MHz, DMSO-d^6) (ppm): 9.23 (d, J = 9.4 Hz, 1H); 8.62 (d, J = 8.2 Hz, 1H); 8.41 (dd, J = 8.1 Hz, 1.7, 2H); 8.37-8.33 (m, 3H); 8.26 (d, J = 9 Hz, 1H); 8.16 (t, J = 7.6 Hz, 1H).

S4.2.2 Synthesis of 3,6,8-(4-(dimethylamino)phenyl)pyrene-1-carboxylic acid (PyLa) (4)

Over a period of 15 min bromine (1.32 g, 8.2 mmol) was added dropwise to a solution of pyrene-1-carboxylic acid **(2)** (0.517 g, 2.1 mmol) in nitrobenzene (40 mL) at 160 °C under vigorous stirring. The reaction mixture was kept at 160 °C for 5 h, after which it was allowed to cool to room temperature. The precipitate was filtered off and washed with EtOH and dried under vacuum overnight. The reaction afforded 3,6,8-tris-bromopyrene-1-carboxylic acid **(2)** as a yellow powder (0.852 g, 1.76 mmol, 84 %). Due to its low solubility, the product was used in the next step without further purification or characterisation. Following this, **(2)** (0.169 g, 0.35 mmol), 4-(dimethylaminophenyl) boronic acid (0.348 g, 2.11 mmol), $Pd(PPh_3)_4$ (0.070 g, 0.061 mmol) and K_2CO_3 (0.5 g, 3.6 mmol) were added to a nitrogen saturated mixture of toluene (10 mL) and ethanol (5 mL). The reaction mixture was then heated to reflux under nitrogen for 24 h. After the mixture was allowed to cool to room temperature, diluted with dichloromethane (150 mL) and was then washed with water (3 x 50 mL). The precipitate was collected by filtration and purified on silica gel by column chromatography using dichloromethane/methanol (9:1) to afford PyLa **(4)** as an orange powder (0.091 g, 0.2 mmol, 57 %).

^{1}H NMR (600 MHz, DMSO-d$_6$) (ppm): 13.30 (s, 1H); 9.12 (d, J = 9.6 Hz, 1H); 8.45 (s, 1H); 8.34 (d, J = 9.6 Hz, 1H); 8.28 (d, J = 9.4 Hz, 1H); 8.17 (d, J = 9.4 Hz, 1H); 7.93 (s, 1H); 7.56-7.49 (m, 6H); 6.94 (q, J = 6.6 Hz , 6H); 3.02 (s, 6 H); 3.018 (s, 6 H); 3.00 (s, 6 H).

^{13}C NMR (150 MHz, DMSO-d$_6$): 171.76, 150.09, 149.95, 136.93, 136.72, 136.52, 129.19, 128.97, 128.80, 128.59, 128.55, 127.56, 127.35, 127.18, 127.13, 126.43, 126.08, 124.99, 124.45, 123.47, 112.85, 112.83, 112.81

HR-MS (ESI-TOF) m/z: calculated for $C_{41}H_{37}N_3O_2$ 604.2964 found 604.2964 ([M^+])

S4.2.3 Synthesis of 3,6,8-tris-(4-(dimethylamino)phenyl)pyrene-1-C_{17}-Ceramide (PyLa-C_{17}Cer) (5)

To a stirred solution of PyLa **(4)** (27 mg, 0.045 mmol,) and 4-(dimethylaminopyridine) (0.55 mg, 0.0045 mmol) in DCM (2 mL), a solution of C_{17} ceramide (50 mg, 0.09 mmol) in DCM (2 mL) was added. The reaction mixture was stirred for 5 min at room temperature. A solution of DCC (10.22 mg, 0.049 mmol) in DCM (2 mL) was added and the mixture was stirred at room temperature overnight. The crude mixture was concentrated to dryness via vacuum. The crude product was purified by chromatography on preparative silica TLC using DCM/MeOH (9:1) to afford a yellow powder (6.7 mg, 0.005 mmol, 8.6 %).

^{1}H NMR (600 MHz, $CDCl_3$) (ppm): 9.11 (d, J = 11 Hz, 1H); 8.54 (s, 1H); 8.44 (d, J = 10.5 Hz, 1 H); 8.34 (d, J = 10.3 Hz, 1H); 8.20 (d, J = 6.8 Hz, 1H); 8.05 (s, 1H); 7.58-7.51 (m, 6H); 6.91 (q, J = 6.6 Hz , 6H); 6.07 (d, J = 7.92 Hz, 1H); 5.79-5.74 (m, 1H); 5.58-5.54 (m, 1H); 4.76 (q, J = 6.4 Hz, 1 H); 4.53 (dd, J = 11.6, 4.7 Hz, 1H); 4.47-4.43 (m, 1H); 4.31-4.25 (s, 1H); 3.02 (s, 6 H); 3.016 (s, 6 H); 3.00 (s, 6 H); 2.2-2.17 (m, 2H); 2.02-1.95 (m, 2H); 1.29-1.17 (m, 48H); 0.88-0.84 (m, 7H).

MALDI TOF MS LD+ calculated for $C_{75}H_{101}N_4O_4$: 1136.8082 found 1136.8058 ([M^+])

S4.2.4. Characterisation Data

S4.2.4.1 Pyrene-1-carboxylic acid (2).

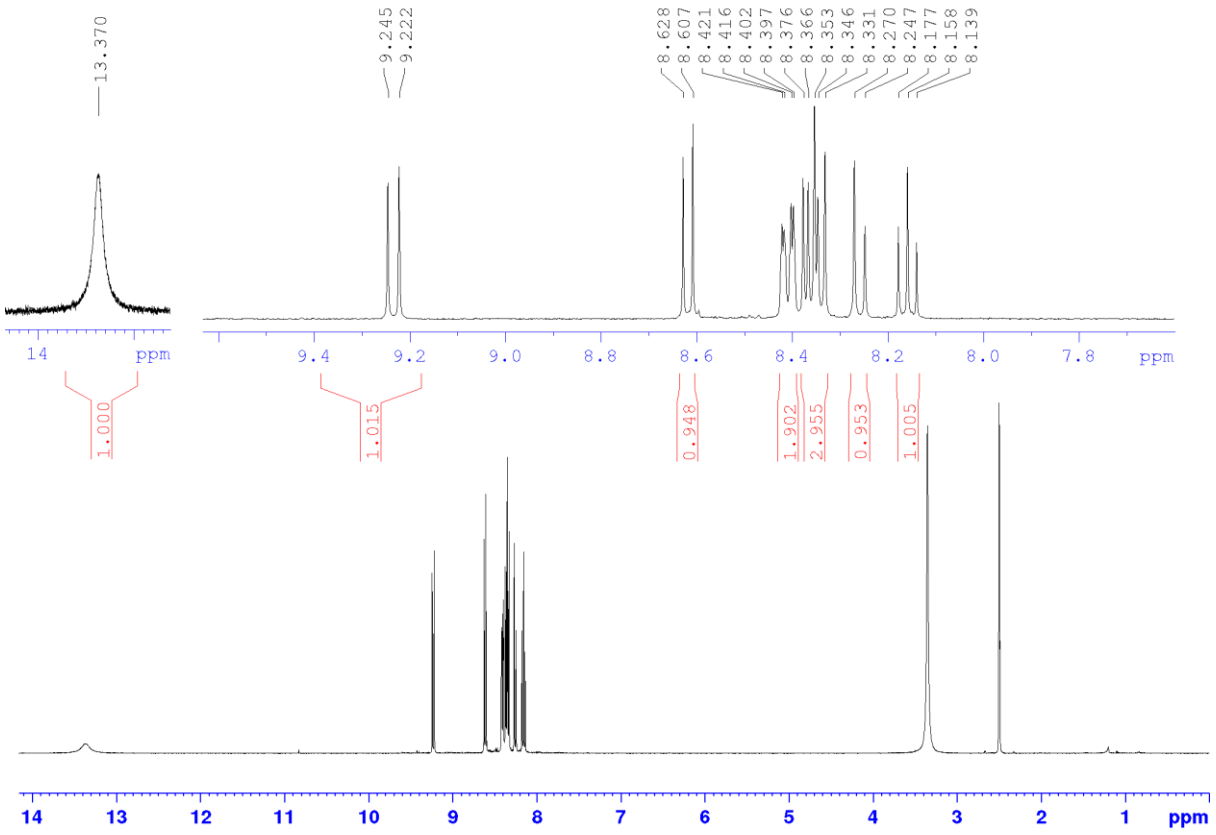

Figure S4.1 ^{1}H NMR Spectrum (400 MHz) of (**2)** in DMSO-d^{6}.

S4.2.4.2 3,6,8-tris-(4-(dimethylamino)phenyl)pyrene-1-carboxylic acid (PyLa) (4)

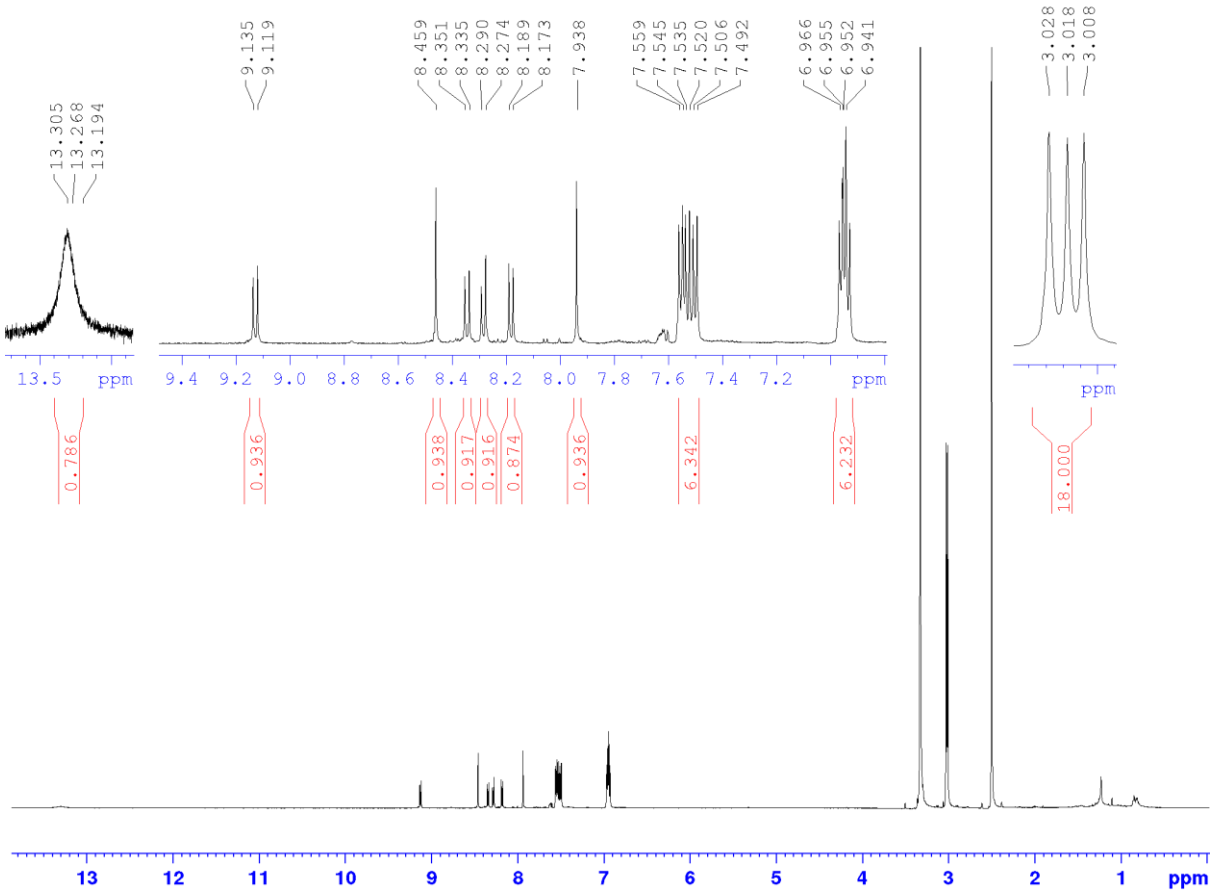

Figure S4.2 ^{1}H NMR Spectrum (600 MHz) of (**4)** in DMSO-d^{6}.

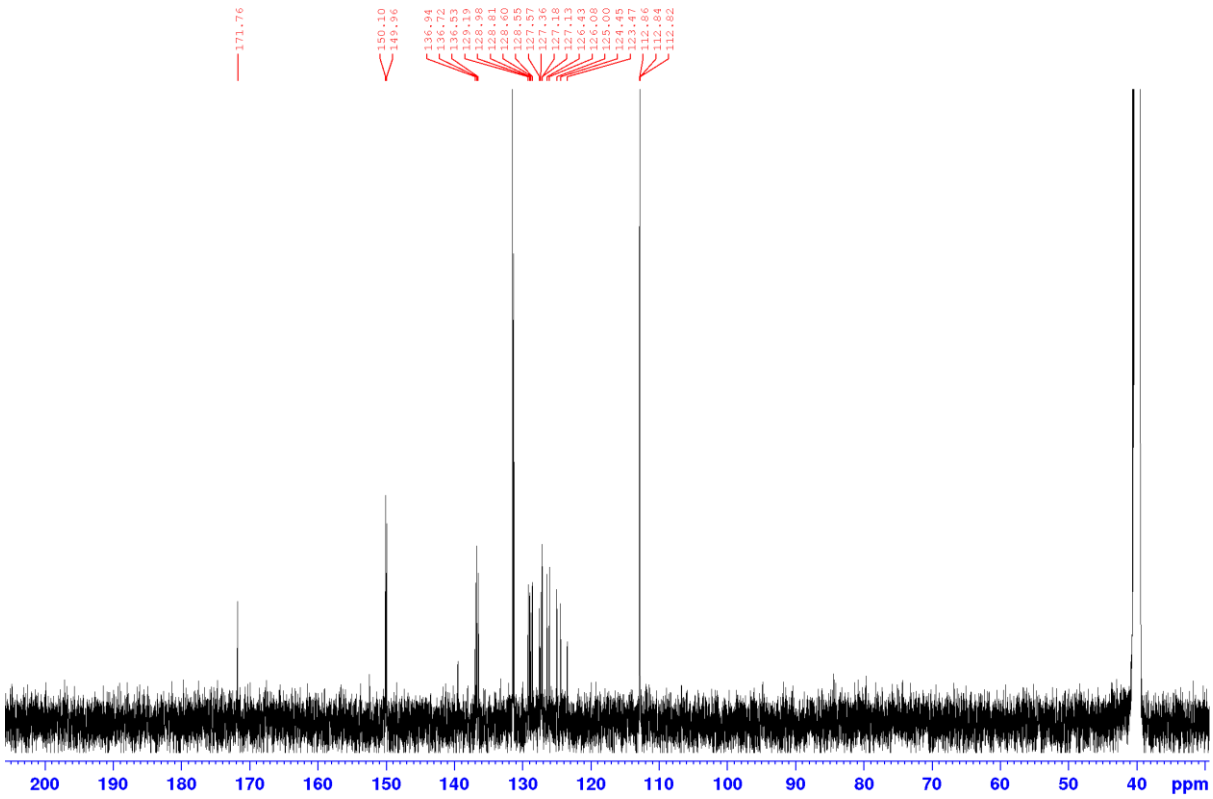

Figure S4.3 ^{13}C NMR Spectrum (150 MHz) of (**4)** in DMSO-d^{6}.

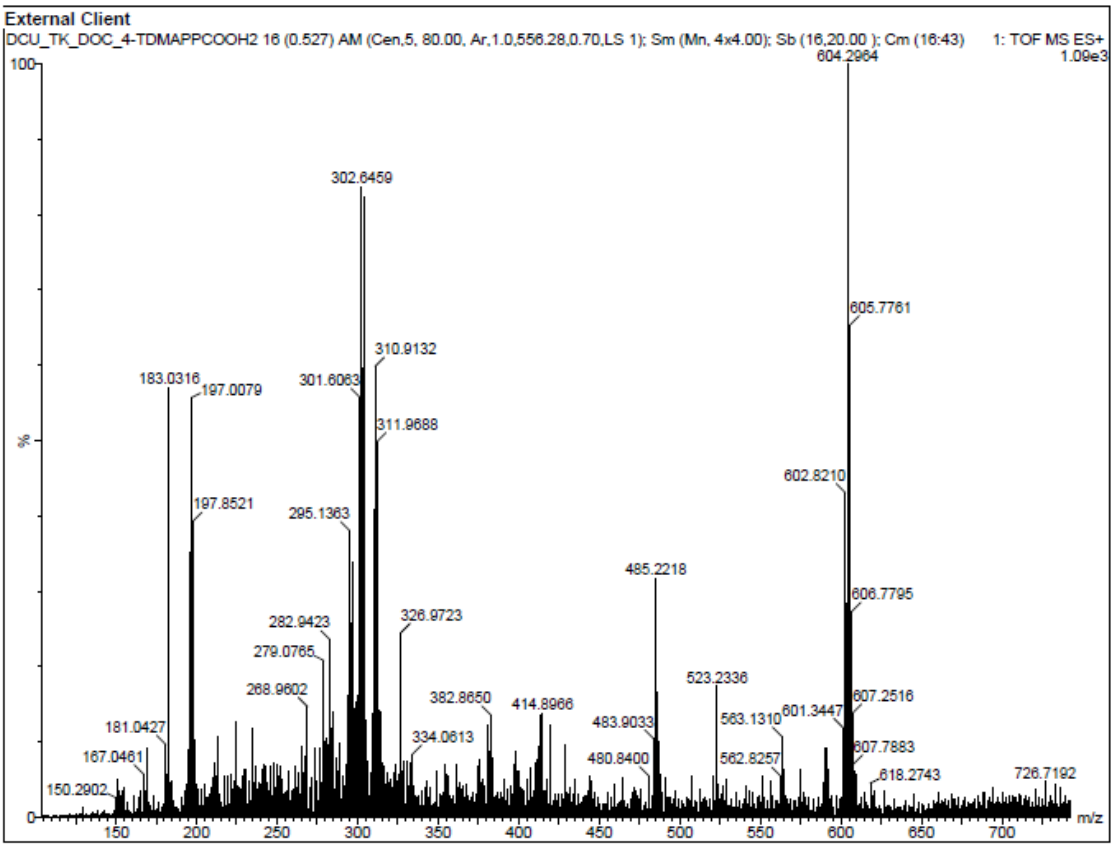

Figure S4.4 HR-MS (ESI-QTOF): Single Mass Analysis of **(4)** indicating [M]+

Elemental Composition Report **Page 1**

Single Mass Analysis
Tolerance = 5.0 PPM / DBE: min = -1.5, max = 70.0
Isotope cluster parameters: Separation = 1.0 Abundance = 1.0%

Monoisotopic Mass, Odd and Even Electron Ions
4 formula(e) evaluated with 1 results within limits (all results (up to 1000) for each mass)

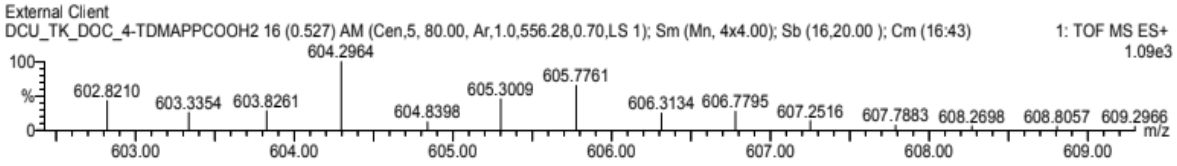

Minimum:				-1.5		
Maximum:		200.0	5.0	70.0		
Mass	Calc. Mass	mDa	PPM	DBE	Score	Formula
604.2964	604.2964	0.0	0.0	24.5	1	C41 H38 N3 O2

Figure S5 HR-MS (ESI-QTOF): Single Mass Analysis of **(4)** indicating [M]+.

S4.2.4.3 3,6,8-tris-(4-(dimethylamino)phenyl)pyrene-1-C_{17}-Ceramide (PyLa-C_{17}Cer) (5)

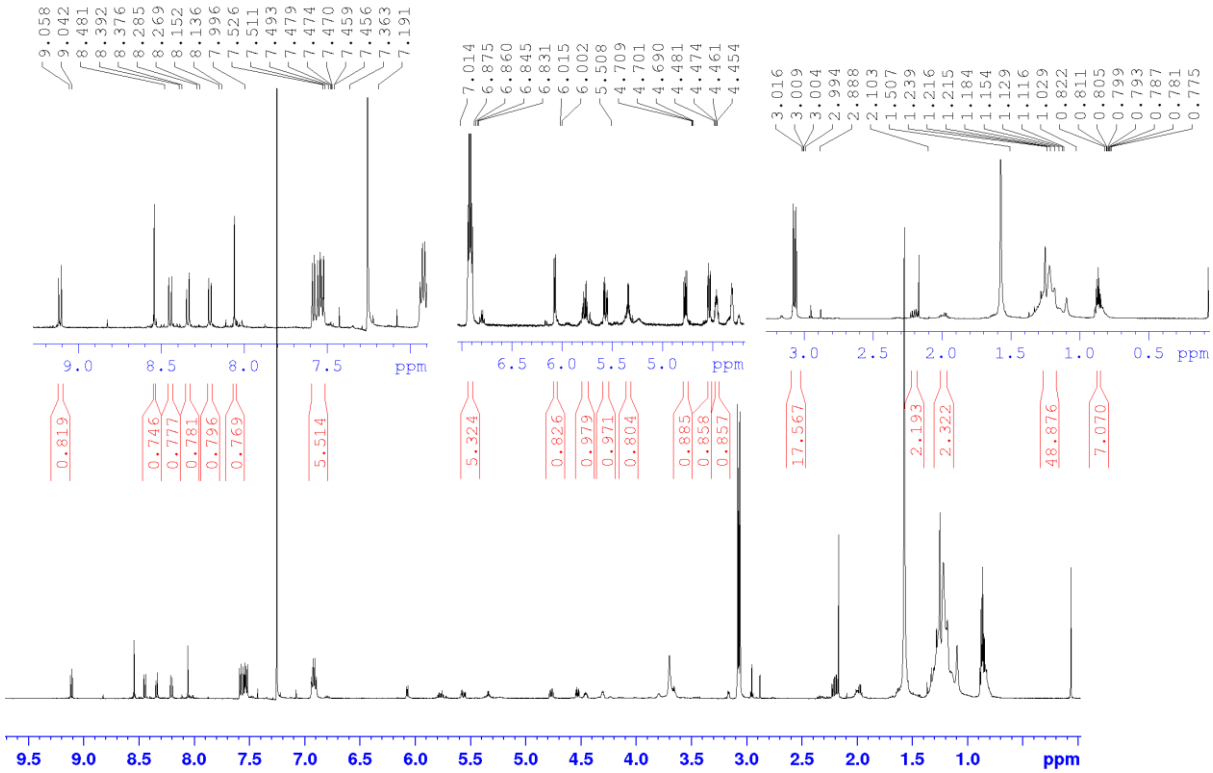

Figure S4.6 ^{1}H NMR Spectrum (600 MHz) of (**5)** in $CDCl_3$.

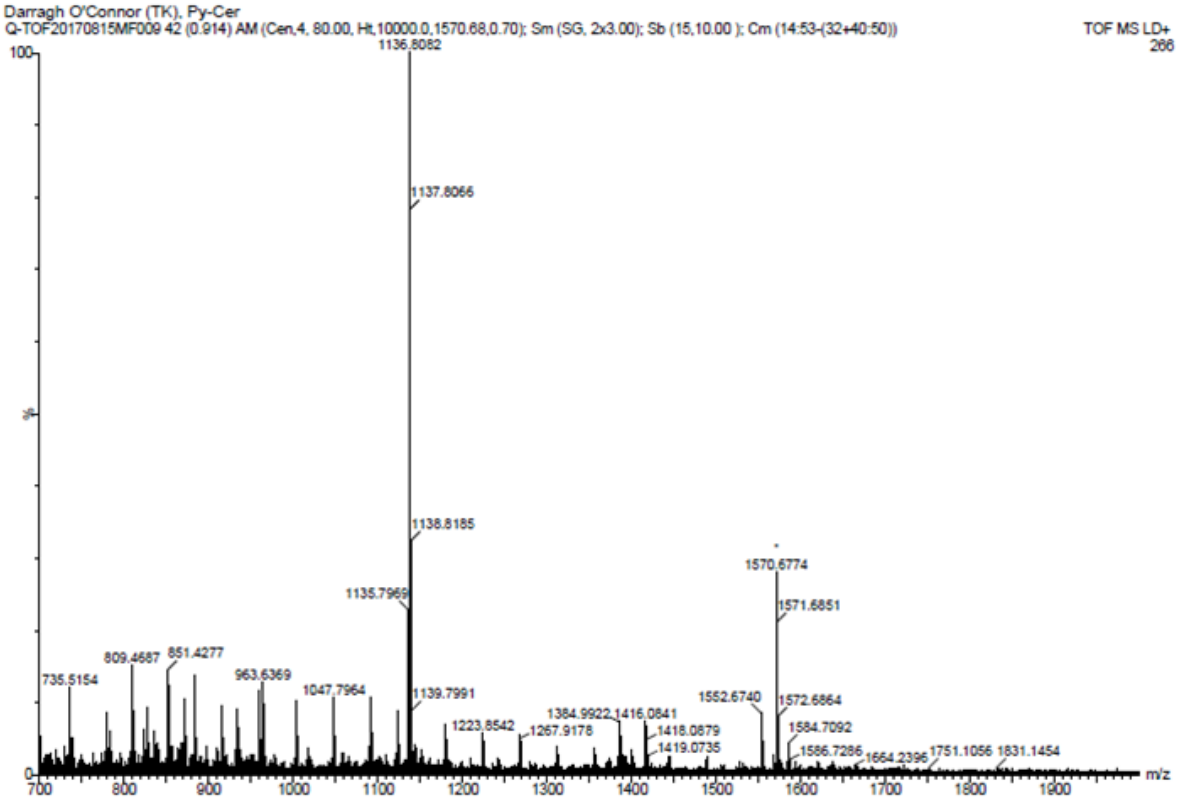

Figure S4.7 MALDI-TOF: Single Mass Analysis of **(5)** indicating [M]+.

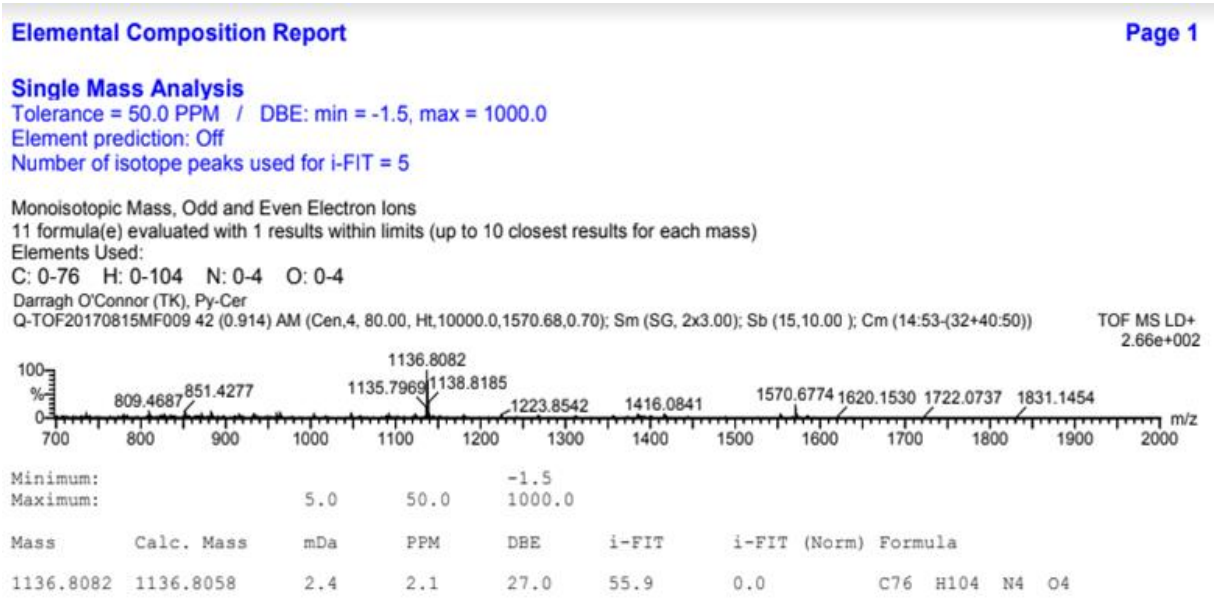

Elemental Composition Report **Page 1**

Single Mass Analysis
Tolerance = 50.0 PPM / DBE: min = -1.5, max = 1000.0
Element prediction: Off
Number of isotope peaks used for i-FIT = 5

Monoisotopic Mass, Odd and Even Electron Ions
11 formula(e) evaluated with 1 results within limits (up to 10 closest results for each mass)
Elements Used:
C: 0-76 H: 0-104 N: 0-4 O: 0-4

Darragh O'Connor (TK), Py-Cer
Q-TOF20170815MF009 42 (0.914) AM (Cen,4, 80.00, Ht,10000.0,1570.68,0.70); Sm (SG, 2x3.00); Sb (15,10.00); Cm (14:53-(32+40:50))
TOF MS LD+
2.66e+002

Minimum:				-1.5			
Maximum:		5.0	50.0	1000.0			
Mass	Calc. Mass	mDa	PPM	DBE	i-FIT	i-FIT (Norm)	Formula
1136.8082	1136.8058	2.4	2.1	27.0	55.9	0.0	C76 H104 N4 O4

Figure S4.8 MALDI-TOF: Single Mass Analysis of **(5)** indicating [M]+.

S4.2.4 HPLC Analysis

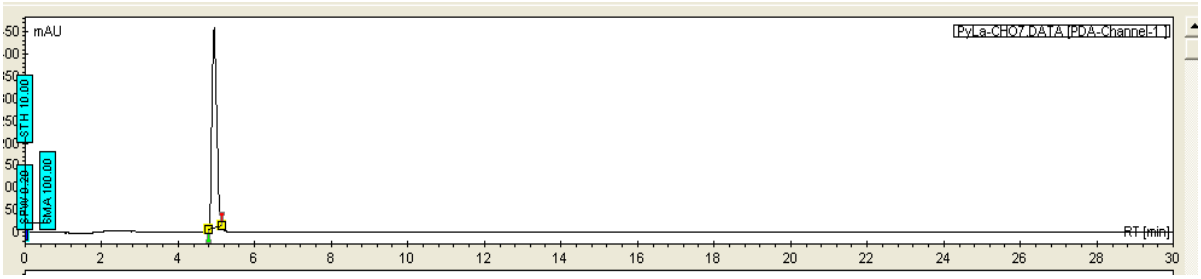

Figure S4.9 HPLC of reference compound **(1)** using C_{18} reverse phase column, flow rate 1.0 mL/min, run time 30 min. Wavelengths 394 nm and 430 nm. Solvent ACN TFA 0.1 %.

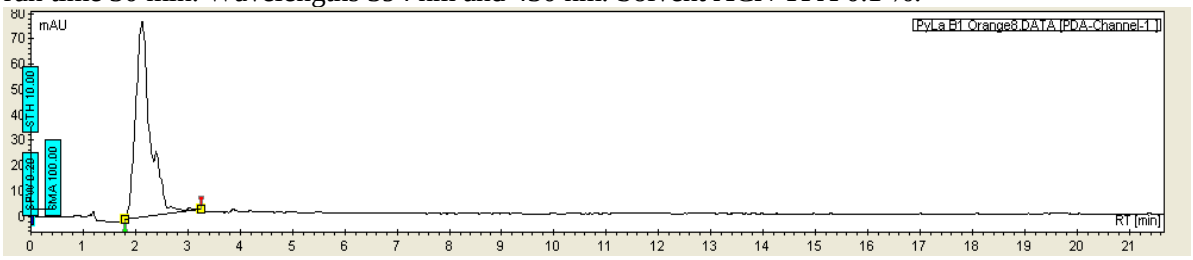

Figure S4.10 HPLC of **(3)** using C_{18} reverse phase column, flow rate 1.0 mL/min, run time 20 min. Wavelengths 394 nm and 430 nm. Solvent ACN TFA 0.1 %.

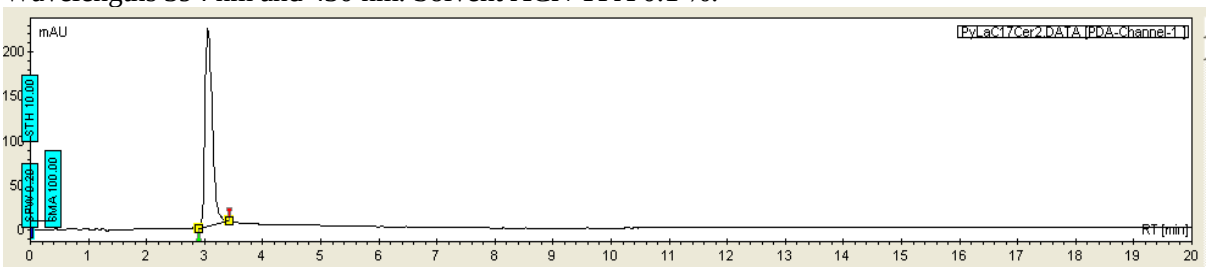

Figure S4.11 HPLC of **(5)** using C_{18} reverse phase column, flow rate 1.0 mL/min, run time 20 min. Wavelengths 394 nm and 430 nm. Solvent ACN 100 %.

S4.3 Photophysical Characterisation

Table S4.1 Summary of photophysical data

Compound	ϕ_{fl}	Solvent	λ_{abs} (nm) (ε = x 10^3 M^{-1} cm^{-1})	λ_{em} (nm) (ε_r)*	τ_{lum} (ns) ± SD
PyLa	0.40	DCM	431 (20.55)	552 (9.08)	4.42 ± 0.01
	[a]	Acetone	426 (12.57)	580 (20.7)	3.34 ± 0.02
	[a]	MeOH	396 (23.38)	525 (33.0)	3.54 ± 0.01
	0.49	Acetonitrile	399 (28.19)	520 (37.50)	3.85 ± 0.04
	[a]	H_2O	413 (0.79)	557 (78.54)	0.38 ± 0.01
PyLa-C17Cer	0.10	DCM	427 (13.74)	562 (9.08)	4.34 ± 0.00
	[a]	Acetone	428 (4.61)	592 (20.7)	2.66 ± 0.17
	[a]	MeOH	416 (4.70)	510 (33.0)	2.60 ± 0.28
	0.08	Acetonitrile	423 (9.60)	582 (37.50)	2.98 ± 0.02
	[a]	H_2O	417 (0.76)	557 (78.54)	0.84 ± 0.006

Solutions of PyLa and PyLa-C_{17}Cer were were absorbance matched at 0.4 (a.u.) and emission spectra were obtained using excitation slit width 5 nm and emission slit width 2.5 nm. Lifetime data was recorded in triplicate at concentrations of (10 μM) and curves conformed to tailfit criteria of $\chi^2 < 1.3$. Quantum yields were obtained using Atto 425 in water (ϕ_{fl} = 0.90) with slit widths 2.5 nm as a standard. [a]Not measured. *Dielectric constants of solvents at 20 °C.

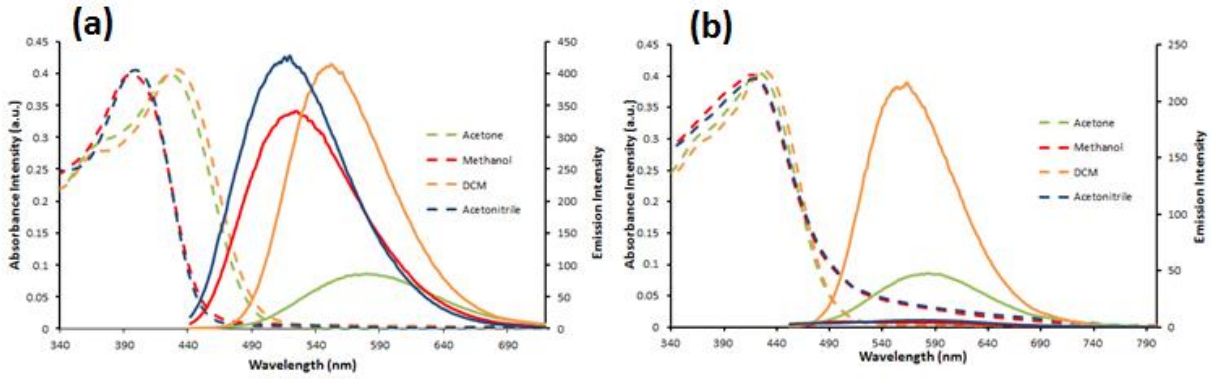

Figure S4.12 (a) Solvent dependence absorbance and emission spectra for PyLa (absorbance matched at 0.4 a.u. excitation slit width 5 nm, emission slit width 2.5 nm). (b) Solvent dependence absorbance and emission spectra for PyLa-C_{17}Cer (absorbance matched at 0.4 a.u. excitation slit width 5 nm, emission slit width 2.5 nm).

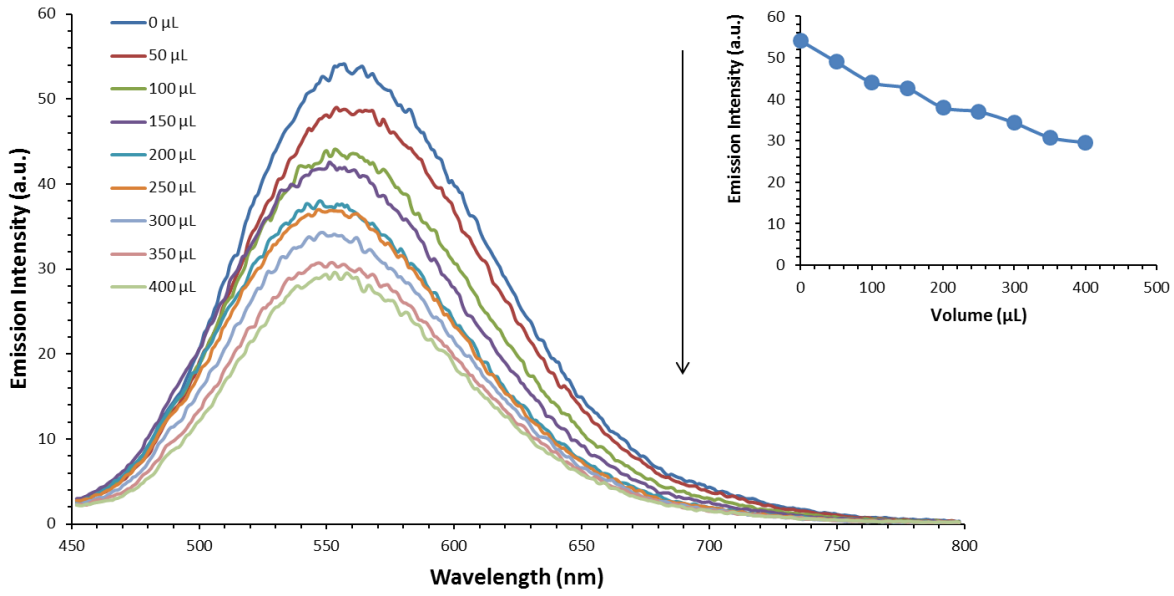

Figure S4.13 Emission spectra of PyLa **(4)** (50 µM) in MeOH with the addition of 50 µL water titrations. Excitation slit width 5 nm and emission slit width 2.5 nm were used for emission intensity measurements. Emission intensity decreases by 45 % following addition of water (21 mol % water to MeOH). Inset shows maximum emission versus volume of water added.

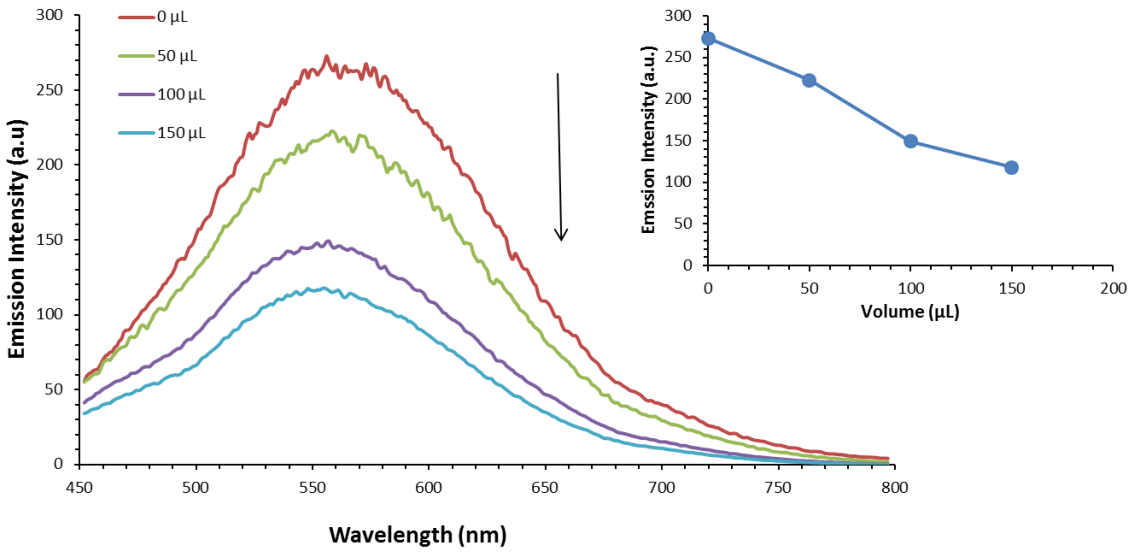

Figure S4.14 Emission spectra of PyLa-C_{17}Cer **(5)** (50 µM) in MeOH with the addition of 50 µL water titrations. Excitation and emission slit widths 10 nm were used for emission intensity measurements. Emission intensity decreases by 58 % following addition of water (11.36 mol % water to MeOH). Inset shows maximum emission versus volume of water added.

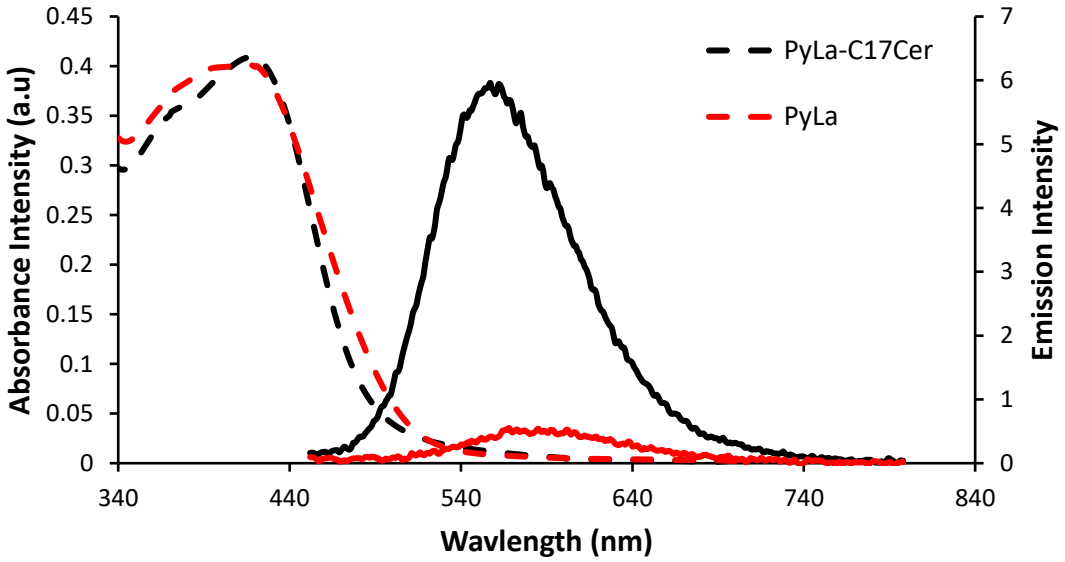

Figure S4.15 Absorbance and emission spectra of PyLa **(4)** and PyLa-C_{17}Cer **(5)** in water absorbance matched at 0.4 absorbance intensity. Emission spectra were obtained with excitation slits widths set to 5 nm and emission slit widths set to 2.5 nm. Emission spectra show both dyes exhibit extremely weak emission in aqueous media.

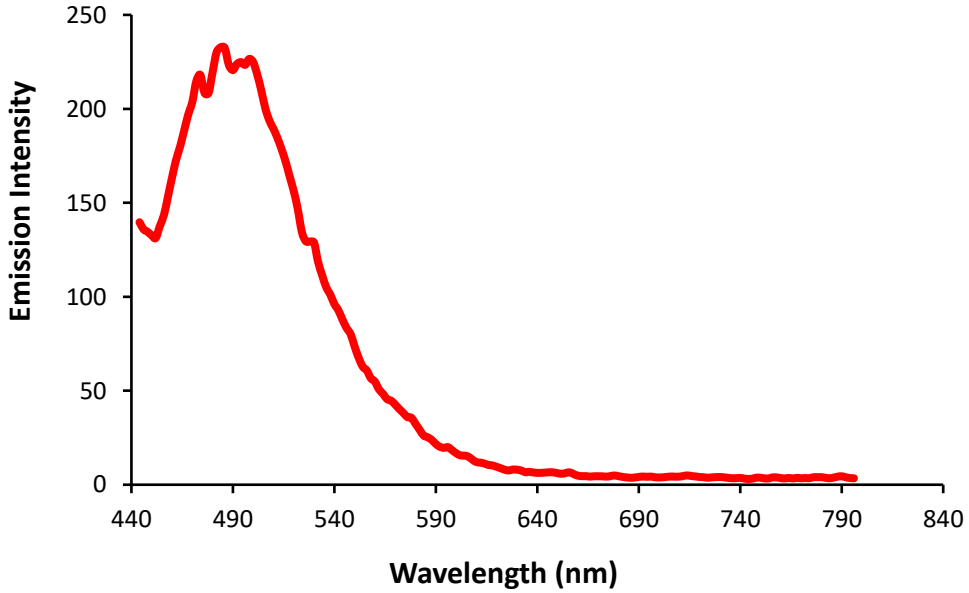

Figure S4.16 77K emission spectrum of PyLa **(4)** in butyronitrile 1 μM. Sample was excited at 420 nm using an excitation slit width of 5 nm and an emission slit width of 10 nm.

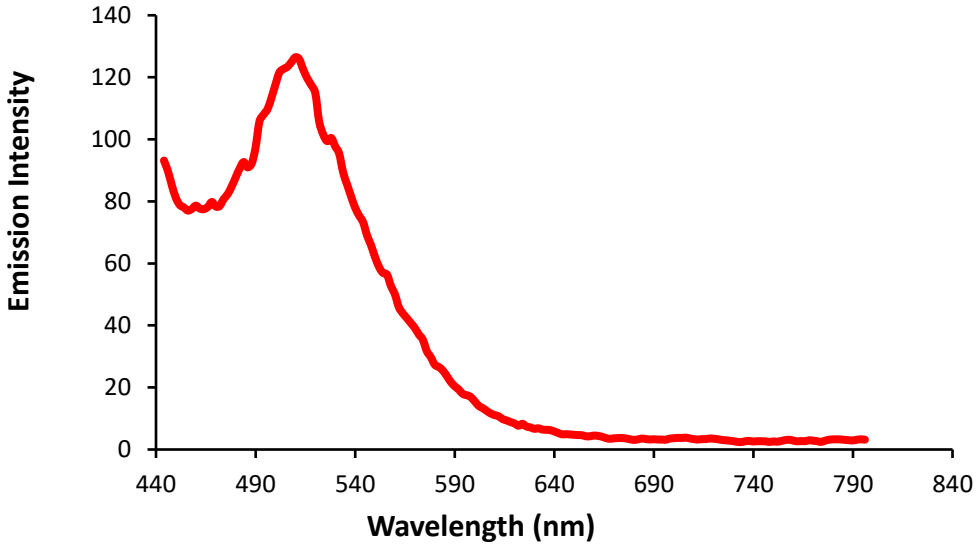

Figure S4.17 77K emission spectrum of PyLa-C_{17}Cer **(5)** in butyronitrile 1 μM. Sample was excited at 420 nm using an excitation slit width of 5 nm and an emission slit width of 10 nm.

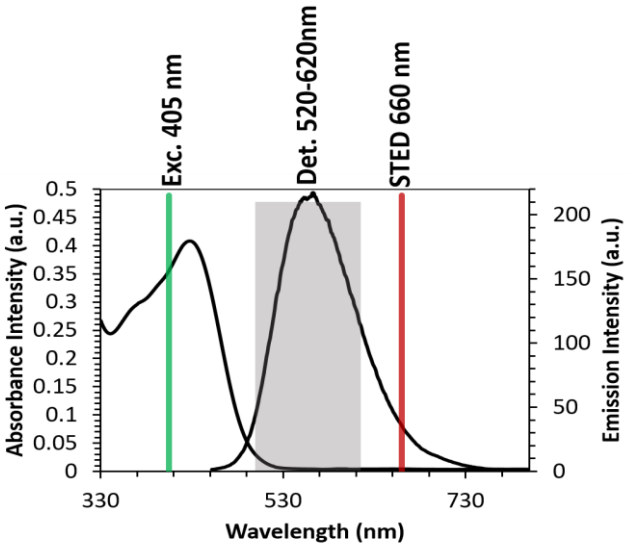

Figure S4.18 Absorbance and emission spectra of PyLa-C_{17}Cer in DCM. The confocal excitation 405 nm (—) and STED 660 depletion laser (—).

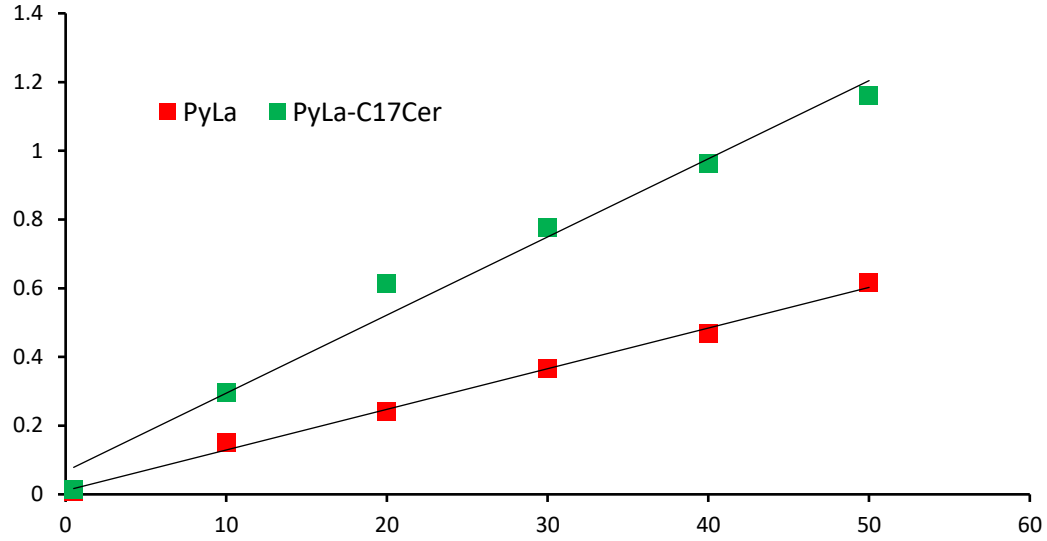

Figure S4.19 Concentration dependent absorption of PyLa (-) and PyLa-C_{17}Cer (-) in dichloromethane using concentrations ranging between 0.5-50 µM. The graph shows that PyLa **(4)** and PyLa-C_{17}Cer **(5)** does not exhibit any aggregation up to concentrations of 25 times greater than imaging concentration (2 µM).

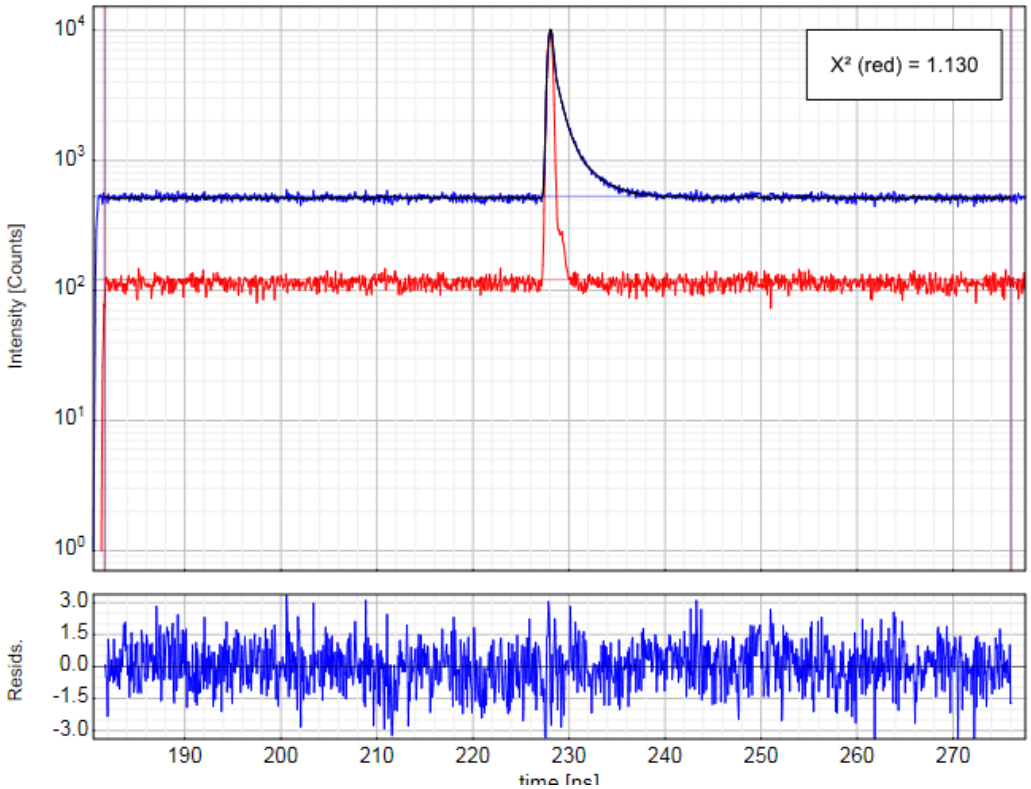

Figure S4.20 Time correlated Single Photon counting trace for PyLa-C_{17}Cer in Acetonitrile (10 µM) with IRF (red) at room temperature.

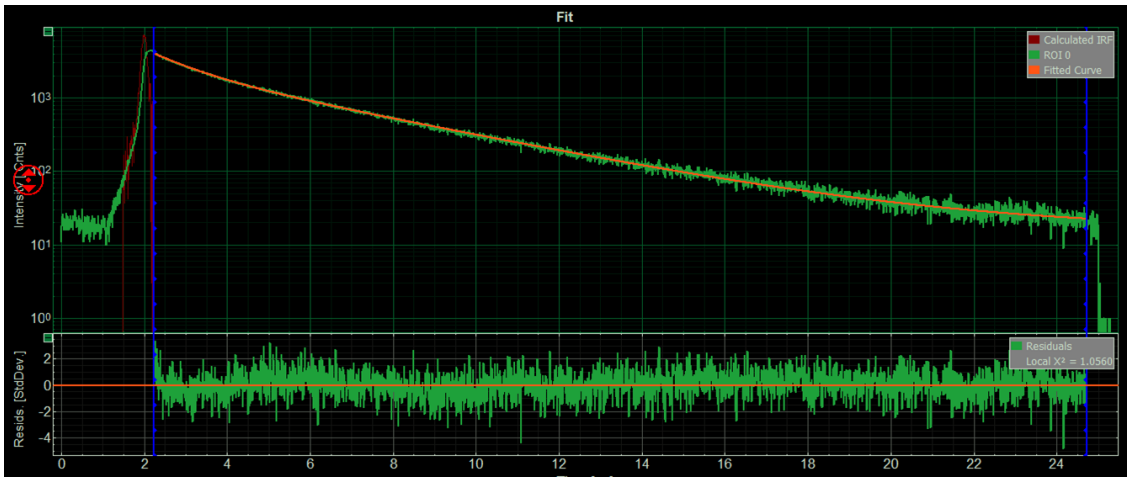

Figure S4.21 Fluorescent lifetime imaging decay for PyLa in lipid bilayers of composition DOPC/SM/Chol 4:4:2 mol % (10 µM).

S4.4 Cell Studies

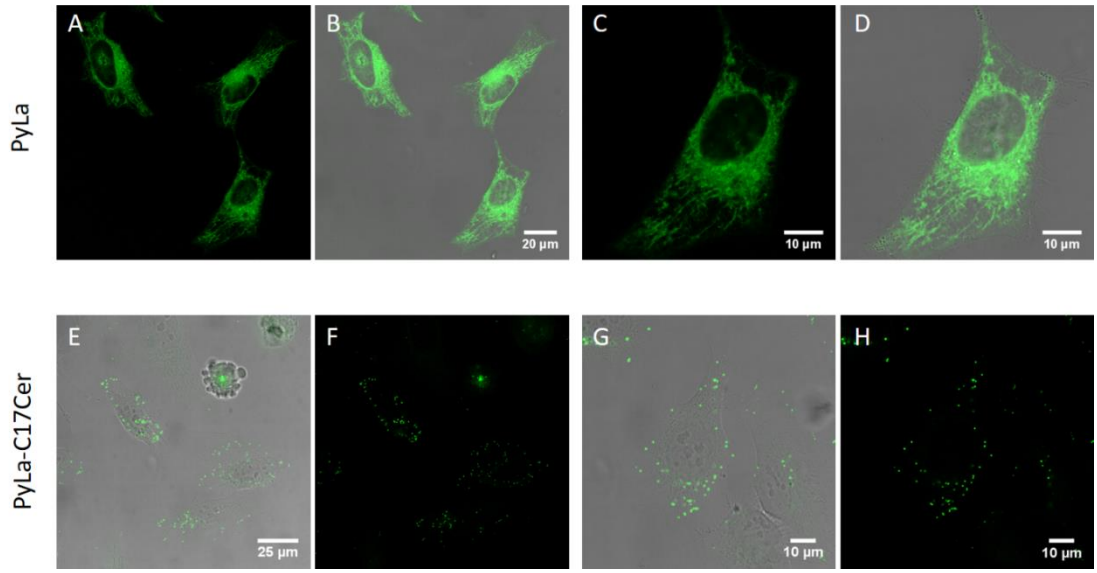

Figure S4.22 Live HeLa cells incubated with 2 µM PyLa(D) and PyLA-C_{17}Cer (E-H) for 1 h, where A, B, E, F show a group of cells, and C,D,G,H show a single cell, showing the distribution. Ex 405 nm, Em 520-620 nm.

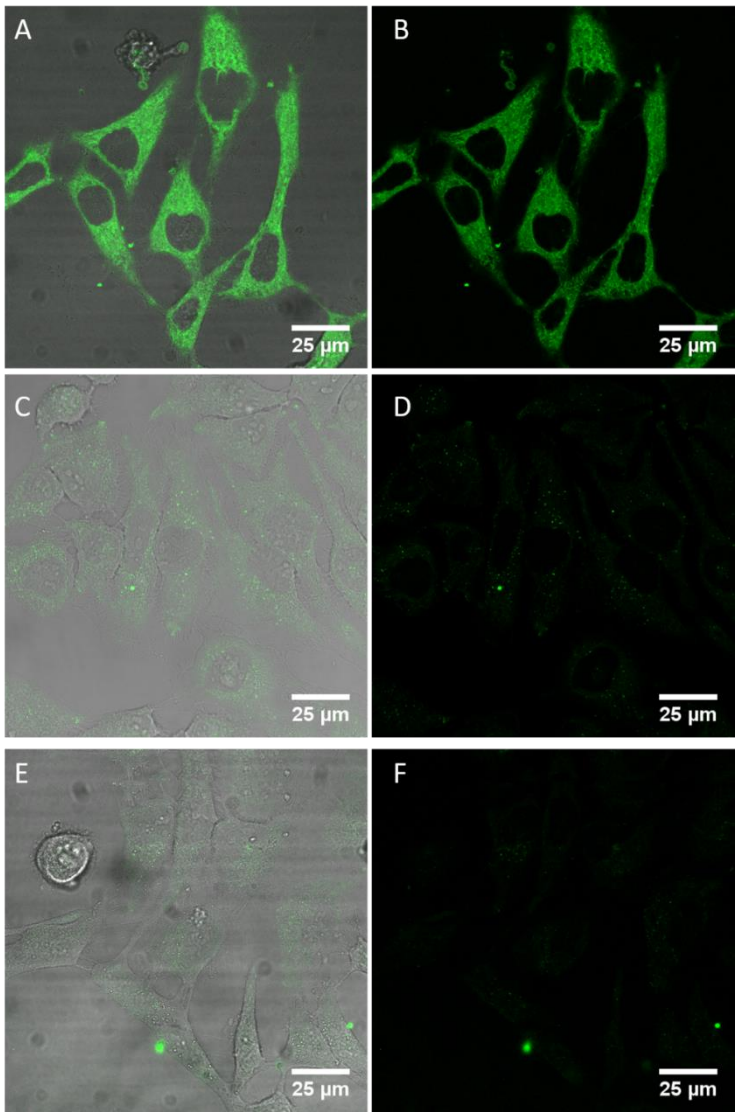

Figure S4.23 Uptake at 4 °C in live HeLa cells. Cells were incubated at 4 °C for 1 h, then 2 µM PyLa (A,B) and PyLa-C_{17}Cer (C,D) was added and incubated at 4 °C for 4 h prior to imaging. HeLa cells were treated with TNF-a for 16 h, then incubated at 4 °C with PyLa-C_{17}Cer (E,F).

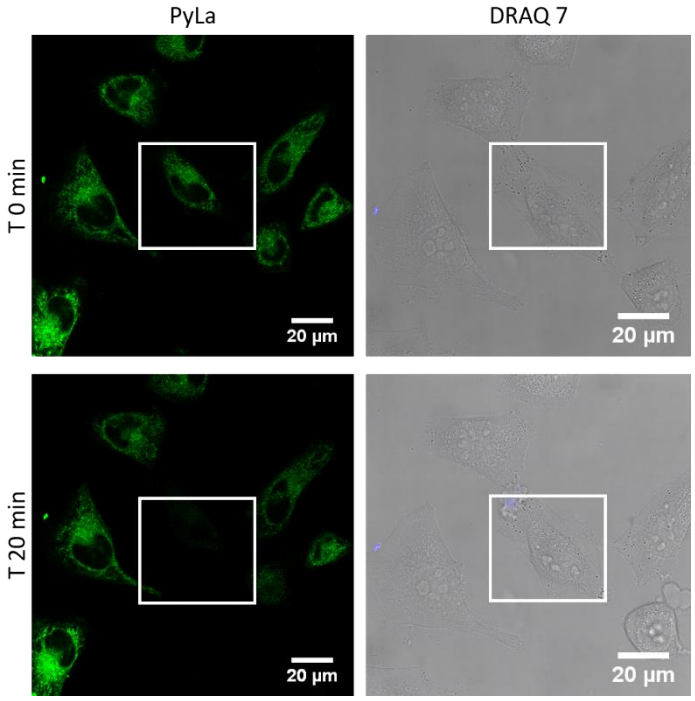

Figure S4.24 Phototoxicity of PyLa in live Hela cells. Cells were stained with PyLa (2 µM, 2 h). The cell highlighted in the white box was continuously scanned for 5 minutes exciting at 405 nm (0.06 mW/cm^2) then imaged using the DRAQ7 settings (Ex 633 nm, Em 635-720 nm) to determine viability for a total of 20 minutes. An overlay of the four channels and DRAQ 7 channel at T 0 minutes and T 20 minutes shows the distribution of the dyes in the cells.

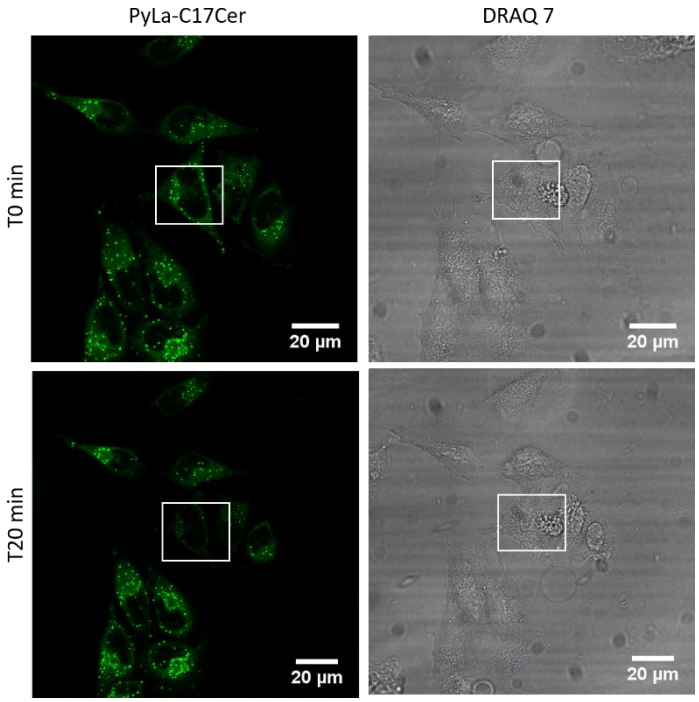

Figure S4.25 Phototoxicity of PyLa-C_{17}Cer in live Hela cells. Cells were stained with (2 µM, 2 h). The cell highlighted in the white box was continuously scanned for 5 minutes exciting at 405 nm (0.06 mW/cm^2), then imaged using the DRAQ7 settings (Ex 633 nm, Em 635-720 nm) to determine viability for a total of 30 minutes. An overlay of the PyLa-C_{17}Cer channel and DRAQ 7 channel at T 0 minutes and T 20 minutes shows the distribution of the dyes in the cells.

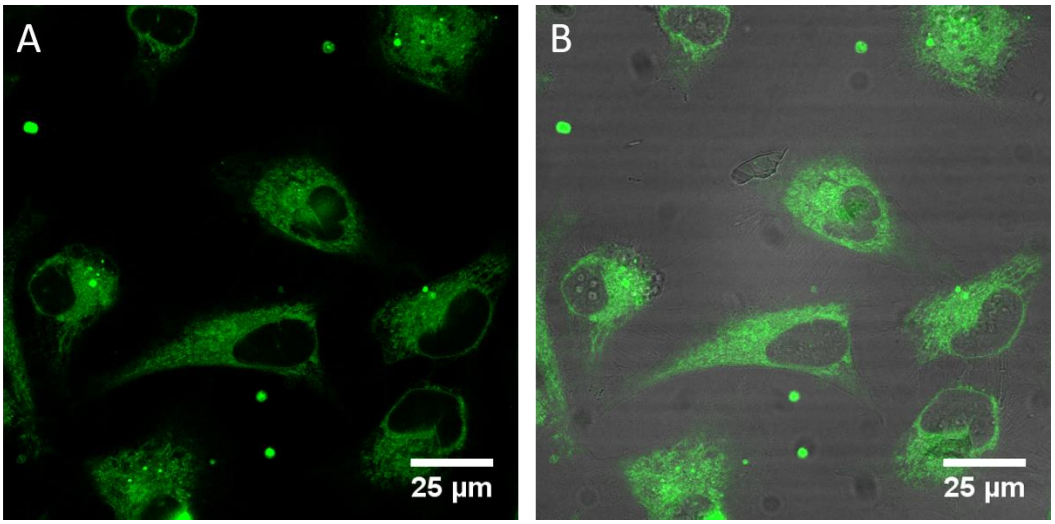

Figure S4.26 Live Hela cells treated with TNF-α for 16 h. PyLA (2 µM) was added to cells and incubated for 2 h at 37 °C. Cells were washed and imaged using at 405 nm laser to excite PyLa, and the emission was collected at 520-620 nm. PyLa does not enter and stain LDs.

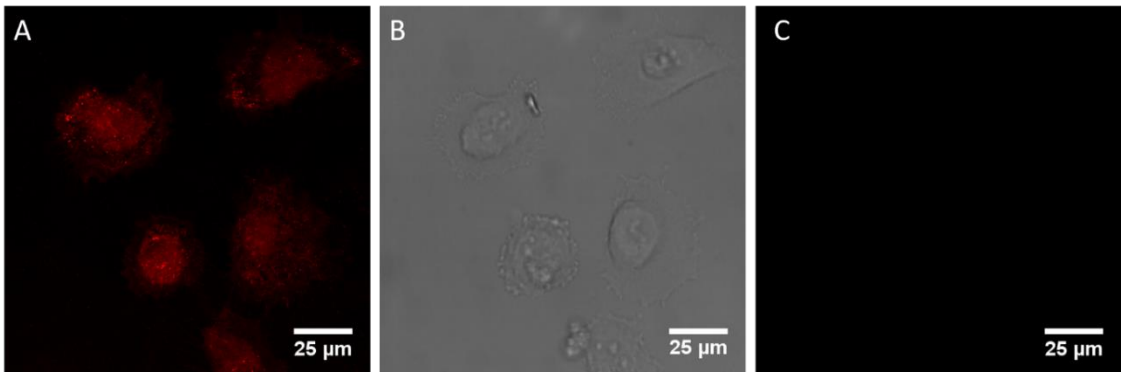

Figure S4.27 Control HeLa cells stained with Nile Red only (1 ng/mL, 20 minutes and washed) (A) (Ex 552, Em 560–700 nm), and imaged using Pyrene settings (Ex 405, Em 520-620 nm), to confirm no cross-talk was occurring between the 2 dyes, shown in (B) and (C) where no emission was recorded at the Pyrene settings.

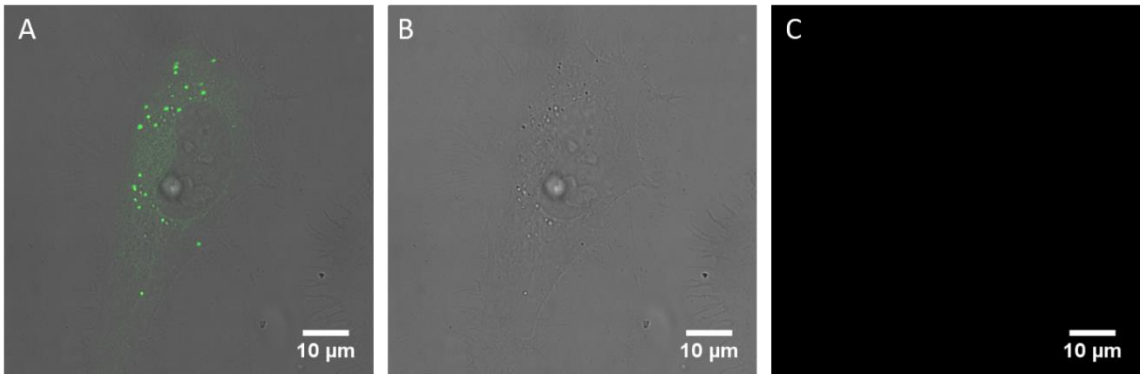

Figure S4.28 Control HeLa cells stained with PyLa-C_{17}Cer (2 µM, 2 h and washed) (A) (Ex 405, Em 520-620 nm), and imaged using Nile Red settings (Ex 552, Em 560–700 nm), to show no cross talk between the 2 dyes, shown in (B) and (C) where no emission was recorded at the Pyrene settings.

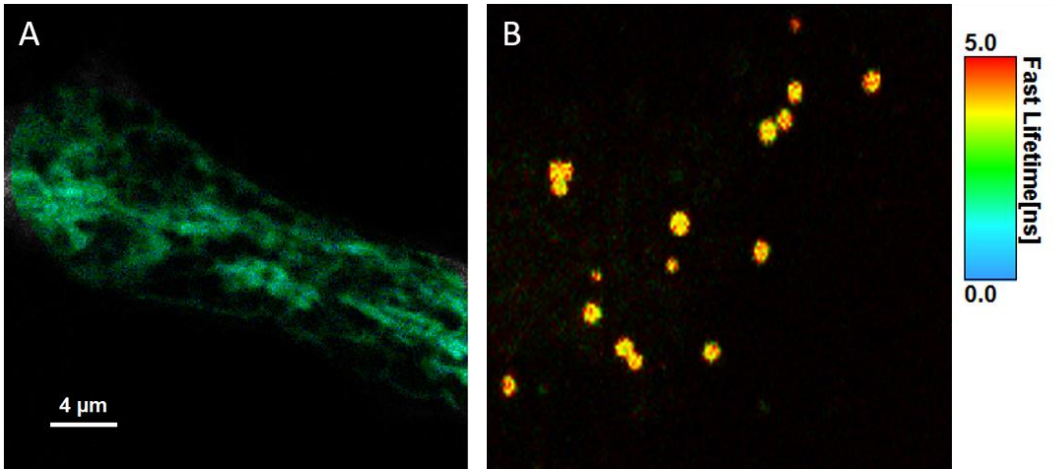

Figure S4.29 False-colour FLIM of a region of the cytoplasm stained with PyLa (A) and a group of lipid droplets in a live HeLa cell stained with PyLa-C_{17}Cer (B). Cells were incubated with 2 µM PyLa (A) or PyLa-C_{17}Cer (B) for 2 h, then washed with PBS before carrying out FLIM. (Ex 405, Em 520-620 nM).

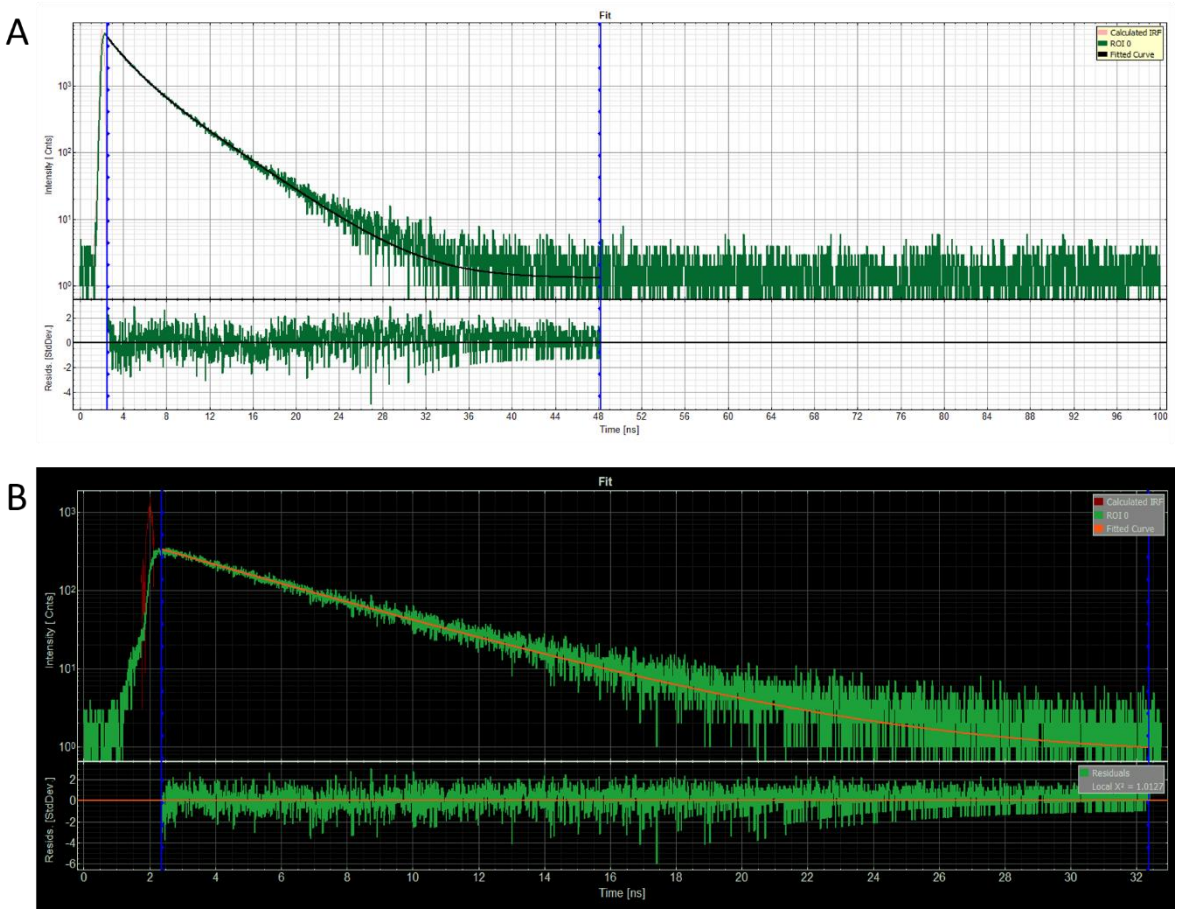

Figure S4.30 FLIM lifetime decays for PyLa (A) and PyLa-C_{17}Cer (B) in live HeLa cells. Ex 405, Em 520-620 nm.

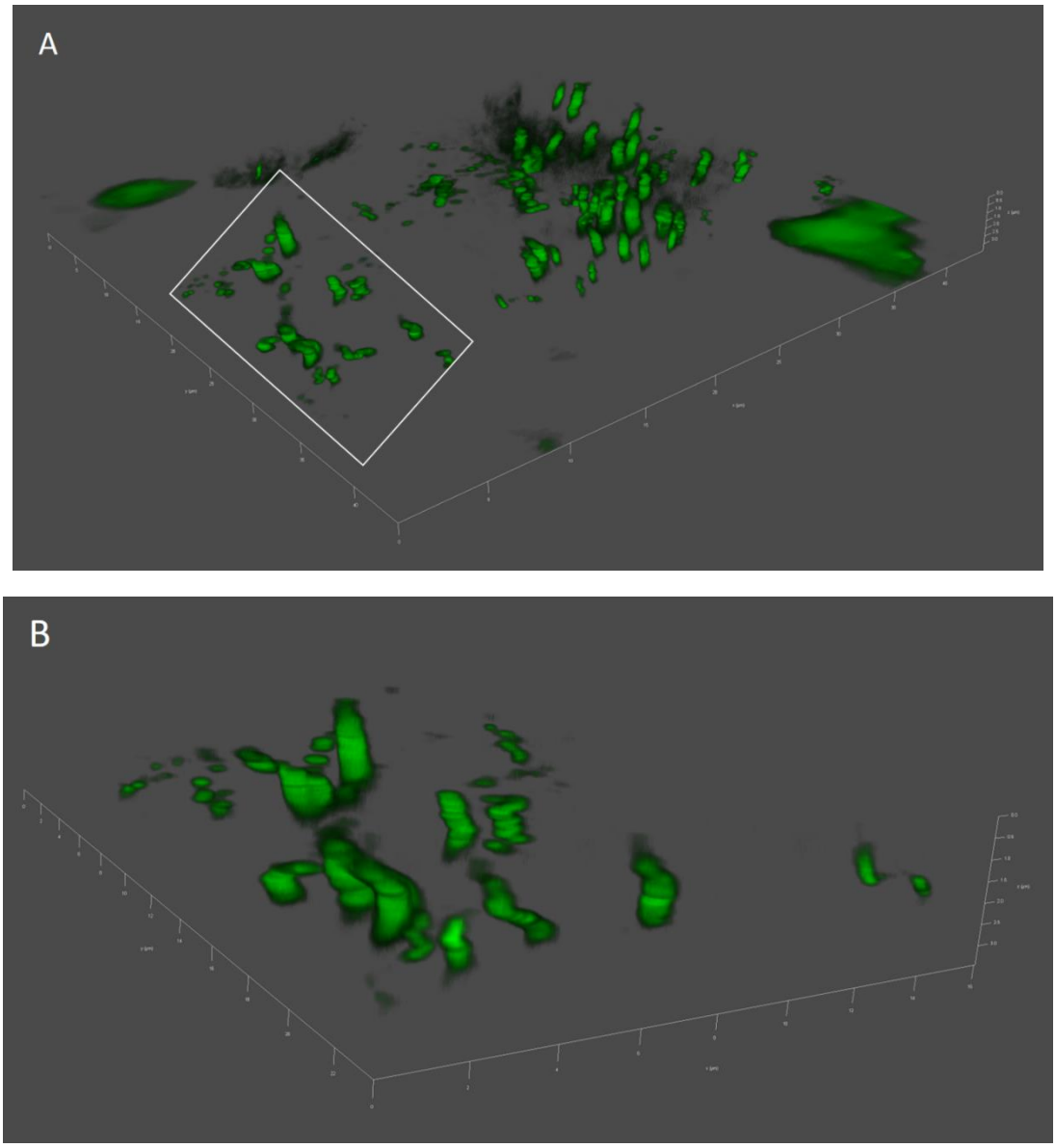

Figure S4.31 Corresponding 3D confocal z-stack of PyLa-C_{17}Cer in live HeLa cells to the 3D FLIM z-stack video/image. The distribution of PyLa-C_{17}Cer throughout a single HeLa cell (A), and the region of droplets chosen for 3D FLIM (B) shown in Figure 5 (C) in the main text.

ROI	Confocal	STED
1	0.435	0.383
	0.440	0.383
2	0.864	0.339
		0.385
3	0.474	0.426
	0.372	0.294
4	0.455	0.411
5	0.522	0.422
	0.425	0.405
6	0.423	0.345
7	0.460	0.424
	0.477	0.408
8	0.522	0.422
	0.457	0.405
9	0.932	0.385
		0.446
10	0.659	0.366
		0.331
11	0.468	0.415
12	0.476	0.449
13	0.409	0.347
14	0.560	0.435
	0.492	0.427
15	0.453	0.382
	0.548	0.424
16	0.518	0.409
17	0.556	0.465
18	0.556	0.336
		0.405
		0.352
19	0.962	0.399
		0.479

20	0.702	0.308
	0.292	0.338
		0.307
21	0.446	0.421
	0.411	0.384
22	0.464	0.411
	0.410	0.411
Average	0.516	0.396
Standard Deviation (±)	0.144	0.044

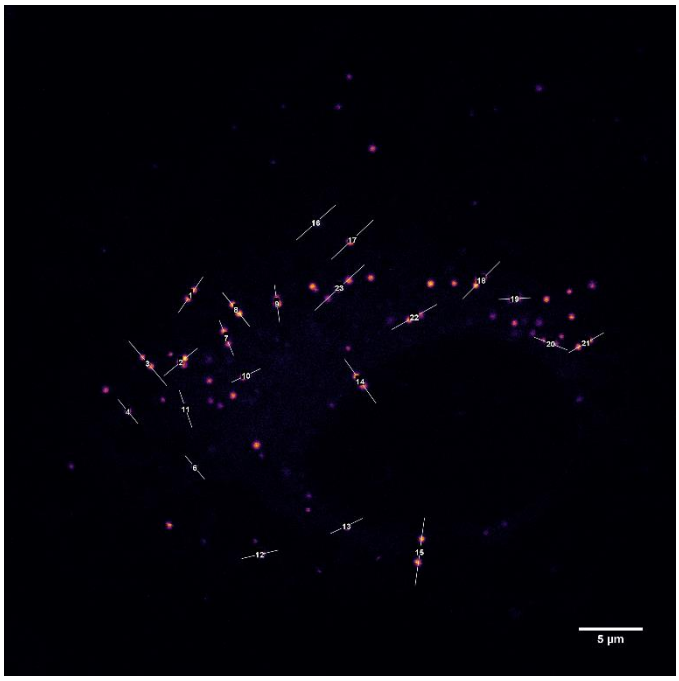

Figure S4.32 Cell. 1 Raw data full width half maxima (FWHM) values of a live Hela cell stained with PyLa-C_{17}Cer (2 µM, 2 h), where region of interest (ROI) is a lipid droplet, and the FWHM value for confocal and STED of each lipid droplet. Data was obtained using Image J, and FWHM was worked out using Origin Pro 2016 on a STED image before deconvolution.

ROI	Confocal	STED
1	0.802	0.341
		0.450
2	0.088	0.048
	0.719	0.283
3	0.645	0.275
	0.412	0.475
4	0.559	0.378
5	0.512	0.319
6	0.515	0.404
7	0.861	0.389
		0.328
8	0.582	0.313
9	0.591	0.358
10	0.458	0.341
11	0.518	0.421
12	0.520	0.430
13	0.608	0.315
14	0.608	0.450
15	0.530	0.448
16	0.782	0.383
		0.376
17	0.723	0.421
18	0.508	0.360
19	0.413	0.355
20	0.61	0.405
21	0.584	0.372
22	0.485	0.358
Average	0.561	0.365

Standard Deviation (±)	0.152	0.080

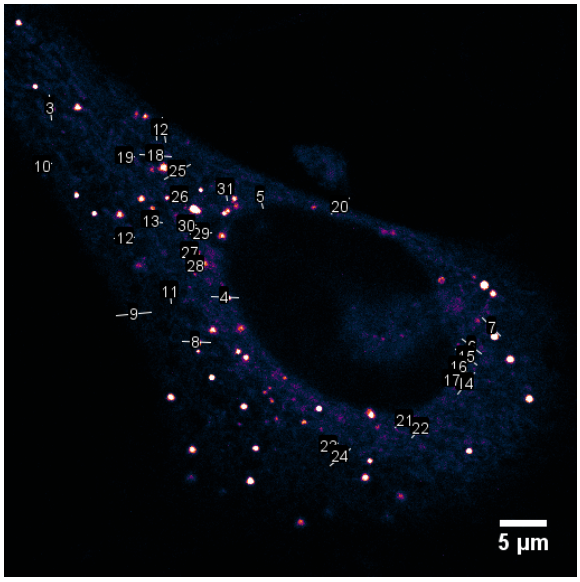

Figure S4.33 Cell 2 Raw data full width half maxima (FWHM) values of a live Hela cell stained with PyLa-C_{17}Cer (2 µM, 2 h) and the corresponding cell, where region of interest (ROI) is a lipid droplet, and the FWHM value for confocal and STED of each lipid droplet. Data was obtained using Image J, and FWHM was worked out using Origin Pro 2016 on a STED image before deconvolution.

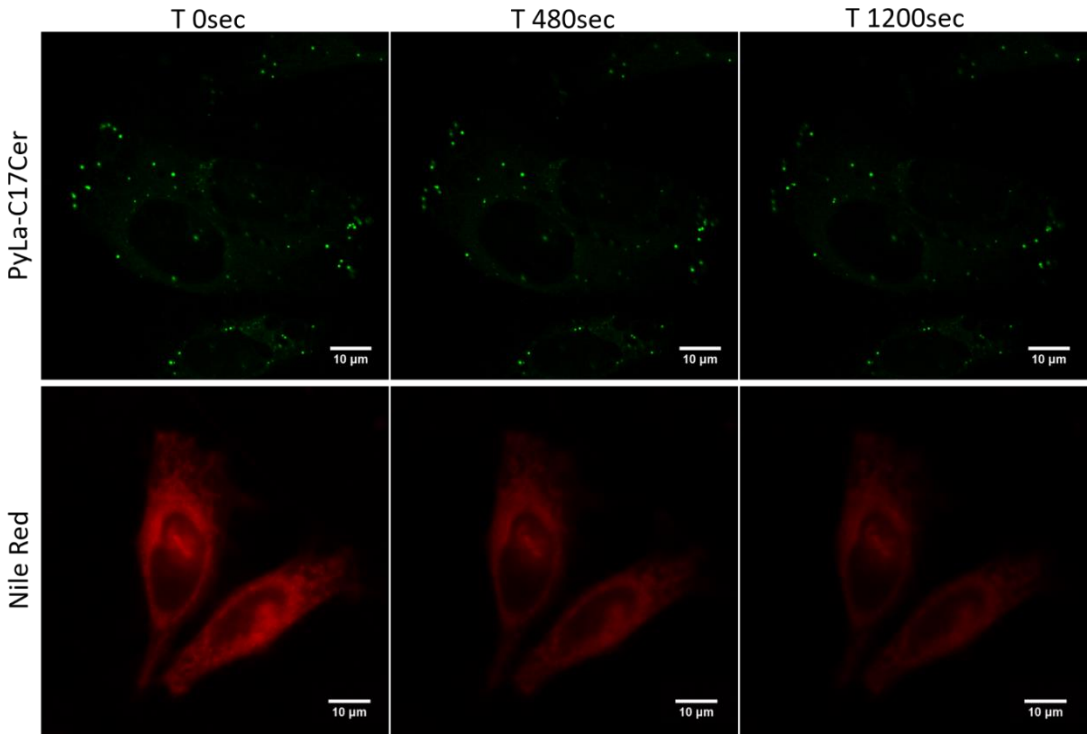

Figure S4.34 STED photostability of live HeLa cells stained with PyLa-C_{17}Cer, and Nile Red. A 405 nm laser was used to excite PyLa-C_{17}Cer, collecting the emission between 520-620 nm, and a 560 nm white light laser was used to excite Nile Red collecting the emission between 580-670 nm. The STED 660 nm at 0.03 W/cm^2 was used for both samples. The images were acquired at 1024 x 1024 resolutions every 1 minutes for 30 minutes at a pixel dwell time of 2.43 µs. The emission intensity of a selected area in both samples was measured at each time interval over the 20 minutes and plot to show stability over time.

Appendix D

Supporting information associated with Chapter 5.

S5.1 Experimental Section

S5.1.1 Materials and Instrumentation

All chemical reagents were purchased from Sigma Aldrich (Ireland) and used without further purification unless otherwise stated.

S5.1.2 Instrumentation

^{1}H and ^{13}C NMR spectra were recorded on a 400 MHz or 600 MHz Bruker spectrometer respectively and the solvent stated. The spectra were processed using Bruker Topspin NMR software. High Resolution Mass Spectrometry (HR-MS) was carried out at the Mass Spectrometry facility, University College Dublin. MALDI-ToF mass spectrometry was performed on MALDI-Q-ToF Premier instrument at Trinity College Dublin. Elemental analysis was carried out using an Exeter Analytical CE 440 elemental analyser at the Microanalytical Laboratory, University College Dublin. Analytical HPLC was performed on a Varian 940-LC Liquid Chromatograph using an Agilent Pursuit XRs 5C-C18 column (4.6x250 mm) and the solvent system stated. Flow rates were kept at 1.6 mL/min and run times were 20 minutes. PDAD was used for peak detection and the analysis was followed by monitoring 280 nm and 430 nm channels. UV-Vis absorption spectra were recorded on Varian Cary 50 spectrometer. Samples were analysed in Hellma quartz fluorescence cuvettes, with a path length of 1 cm, and spectral range of 330 – 800 nm unless otherwise stated. Background measurements were carried out at room temperature prior to each measurement. Emission Spectra were recorded on a Varian Cary Eclipse fluorescence spectrophotometer with excitation and emission slit widths stated. All analyses were carried out using quartz cuvettes and background correction was applied prior to measurement. Fluorescence lifetime measurements were carried out using a PicoQuant FluoTime 100 Compact FLS TCSPC system using a 450 nm pulsed laser source generated from a PicoQuant PDL800-B box. The instrument response function was determined using Ludox colloidal silica solution. Lifetime decay plots were analysed using PicoQuant TimeHarp software. The goodness of each fit to exponential decay kinetics was assessed from chi-squared values (where χ^2 <1.3) and visual inspection of residuals.

S5.1.3 Absorption and Fluorescence Measurements

UV-Vis spectra were recorded on a Varian Cary 50 spectrometer. Samples were analysed in Hellma quartz fluorescence cuvettes, with a path length of 1 cm, and spectral range of 280–800 nm unless otherwise stated. Background measurements were carried out at room temperature prior to each measurement. Emission Spectra were recorded on a Varian Cary Eclipse fluorescence spectrophotometer with excitation and emission slit widths stated. All analyses were carried out using quartz cuvettes and background correction was applied prior to measurement. 77 K emission spectra were obtained a Varian Cary Eclipse fluorescence spectrophotometer using concentrations of 1 μM using excitation slit widths 5 nm and emission slit widths 10 nm over a spectral range of 440-800 nm. For pH-dependent experiments in solution, aqueous samples were prepared using phosphate buffer solution (PBS) with sample concentrations 100 μM, and they were titrated by successive of small volumes (in the order of microliters) of HCl and NaOH solutions (1 M) to an initial volume of 5 mL for negligible changes to concentration and volume of the sample. pH of the samples was then measured using an EDT microprocessor pH meter.

For pH-dependent experiments in organic solution, samples in acetonitrile were prepared with sample concentrations 50 μM, and they were titrated by successive small volumes (in the order of microliters) of perchloric acid and triethylamine solutions of differing concentrations (0.5-1 M) to an initial volume of 5 mL for negligible changes to concentration and volume of the sample. pH of the samples was then calculated to obtain an apparent pH in organic solution. Prior to use ITO was cleaned using warm soapy water and cotton wool, followed by deionised water and ethanol wash and sonication. For absorption and fluorescence measurements of PyLa on ITO glass, the fluorophore in ethanol (1 mM) was deposited onto an ITO glass slide and left to evaporate over 24 h in an enclosed petri dish. The newly formed film was then washed with ethanol and then used for pH measurements. The ITO slide was placed inverted onto a glass slide and a mother PBS solution of known pH was deposited between the ITO and coverslip glass slide. This solution was then added back into the mother solution and the pH was adjusted using small microliter volumes of HCl and NaOH. Fluorescence spectral scans were then carried out at different pH using a Leica TSP inverted (DMi8) confocal microscope, using 100 x oil objective with a 405 nm excitation laser. For fluorescence measurements of PyLaOT bound to flat gold, an Olympus confocal microscope attached to a Horiba Jobin-

Y Labram HR 1000 spectrometer with a 50× long distance magnification objective (NA 0.55) was used. The excitation light of 457 nm was delivered by a diode laser (Horiba Jobin-Y Labram HR 1000). The quantum yields of the samples ϕ_x were measured in solutions applying a standard reference of fluorescein in EtOH (ϕ_s = 0.79) and using equation S5.1,

$$\Phi_x = \Phi_s . \frac{I_x}{I_s} . \frac{A_s}{A_x} . \frac{\eta_x^2}{\eta_s^2} \qquad \text{(Equation S5.1)}$$

where *I* is the integrated emission, *A* is the absorbance at the excitation wavelength and the subscripts *x* and *s* are the sample and standard, respectively. The refractive index of is given by η. The excitation and emission slit widths were both set to 5 nm.

S5.1.4 Self-assembled Monolayer Formation of PyLaOT on Gold Electrode

Prior to self-assembled monolayer (SAM) modification, electrochemical cleaning procedure was carried out in 0.5 M H_2SO_4 from -0.2 to +1.6 V at 50 mV s-1 until reproducible voltammograms were obtained. Next, the electrode was rinsed with de-ionised (DI) water and finally dried by high pure stream of N_2. For the SAM modification, the electrode was immersed in the freshly prepared 1 mM PyLaOT in ethanolic solution for 48 hours. Upon removal, the electrode was washed with a copious amount of ethanol followed by DI water, and immediately transferred to the electrochemical cell for measurement.

S5.1.5 Electrochemical Measurements

Cyclic voltammetry was carried out using a conventional three-electrode cell using 1 mM $[Fe(CN)_6]^{3-/4-}$ as an internal redox probe in 0.1 M KCl electrolyte solution in PBS buffer with an applied potential in the range of -0.2 to +0.8 V at a scan rate of 50 mV s^{-1}. The electrodes are gold (working electrode), Ag/AgCl (reference electrode) and platinum wire (counter electrode). Electrochemical impedance measurements were performed on a CHI 760B bipotentiostat (CH Instruments Inc., Austin, TX) in a three-electrode cell. The EIS recording was performed in the frequency region between 104 and 0.01 Hz with a bias potential of 0.26 V vs Ag/AgCl when redox probe is used and a bias potential of 0 V vs Ag/AgCl without the redox probe i.e., only on PBS buffer. The EIS data were fit to equivalent circuit using Z view (v. 3.4e, Scribner Associates, Inc.)

S5.1.6 Computation

The structural and electronic data of the pyrene derivatives (PyLa and its mono-, di- and triple protonated species) were obtained from quantum chemistry calculations performed with the Gaussian09 program.[1] The optimised equilibrium geometries and vibrational frequencies of the ground state were calculated by means of DFT with the hybrid-functional B3LYP[2,3] in cooperation with the triple-ζ-valence-polarisation (TZVP) basis set.[4–6] Subsequent vibrational analysis confirmed that all obtained optimised structures correspond to a minimum on the potential energy hypersurface. The vertical excitation energies and oscillator strengths within the Franck-Condon region were obtained from TDDFT calculations by means of the 20 lowest singlet excited states. The TDDFT calculations were performed with four functionals, which include different amounts of Hartree-Fock exchange: B3LYP (20%), PBE0 (25%)[7–9], M06-2X (54%)[10] and CAM-B3LYP (19-65%)[11]; in cooperation with the TZVP basis set. The effects of solvation (Acetonitrile: ε=35.69, n=1.3442) on the ground and excited state properties were considered based on the integral equation formalism of the polarizable continuum model.[12] In order to describe the influence of different mono- and di-protonated species of PyLa (*e.g.* first protonation in either the 3-, 6- or 8-position of the pyrene) on the absorption properties (as a mixture of several single or double-protonated forms can be present at room temperature) the oscillator strengths were statistically weighted using the Boltzmann distribution,

$$p_i = \exp\left(-\frac{E_i}{\mathrm{k_B}T}\right) \cdot \left[\sum_i^4 \exp\left(-\frac{E_i}{\mathrm{k_B}T}\right)\right]^{-1}$$

where p_i is the weight and E_i the energy of a species *i* contributing to the absorption properties, k_B the Boltzmann constant and T the temperature.

S5.2 Synthesis and Structural Characterisation

S5.2.1 Synthesis of PyLa (1)

Was synthesised as previously reported[13].

S5.2.2 Synthesis of PyLaOT (2)

DMF (5 mL) was purged with nitrogen for 20 minutes. To a reaction mixture of PyLa (**1**) (50 mg, 0.083 mmol), PyBOP (86 mg, 0.166 mmol) and DIPEA (60 uL), 8-

aminooctanethiol hydrochloride (32 mg, 0.166 mmol) in 1 mL DMF was added slowly to the reaction mixture under nitrogen over a period of 30 minutes after which point the reaction mixture was allowed to stir at room temperature under nitrogen overnight. Following this the reaction mixture was precipitated using ice-cold water, collected under vacuum filtration and rinsed with ice-cold water (2 x 50 mL) and ice-cold MeOH (2 x 100 mL). The crude product was purified on silica gel by column chromatography eluent: Diethyl ether/DCM (80:20), dried over anhydrous Na_2SO_4 and concentrated to dryness under vacuum. Following this the compound was triturated using hot $CHCl_3$ and ice-cold MeOH to give the product. Yield: yellow-brown solid, 32.8 mg (0.043 mmol, 53 %).

^{1}H NMR (600 MHz, $CDCl_3$) (ppm): 8.45 (d, J = 9.5, 1H); 8.35 (d, J=9.5, 1H); 8.27 (d, J = 10, 1H); 8.16 (d, J =9.5, 1H); 8.03 (d, J = 2, 2H); 7.57-7.51(m, 6H); 6.91-6.89 (m, 6H); 6.13 (t, J = 5.5, 1H); 3.59 (q, J =11.5, 7.2, 2H); 3.069 (s, 6H); 3.057 (s, 6H); 3.050 (s, 6H); 2.50 (q, J=16.5, 8, 2H); 1.71-1.66 (m, 2H); 1.62-1.57 (m, 2H); 1.46-1.27 (m, 11H).

^{13}C NMR (150 MHz, $CDCl_3$) (ppm): 170.35, 149.87, 138.26, 138.05, 136.77, 131.49, 131.31, 130.46, 129.89, 129.04, 128.69, 127.63, 127.38, 126.65, 126.60, 126.23, 126.03, 124.56, 123.51, 112.40, 40.67, 40.28, 34.02, 31.45, 30.21, 29.79, 29.71, 29.19, 28.98, 28.30m 26.96, 24.63, 14.13.

MADLI-TOF) m/z: calculated for $C_{49}H_{54}N_4OS$ 747.3998 found 746.4018.

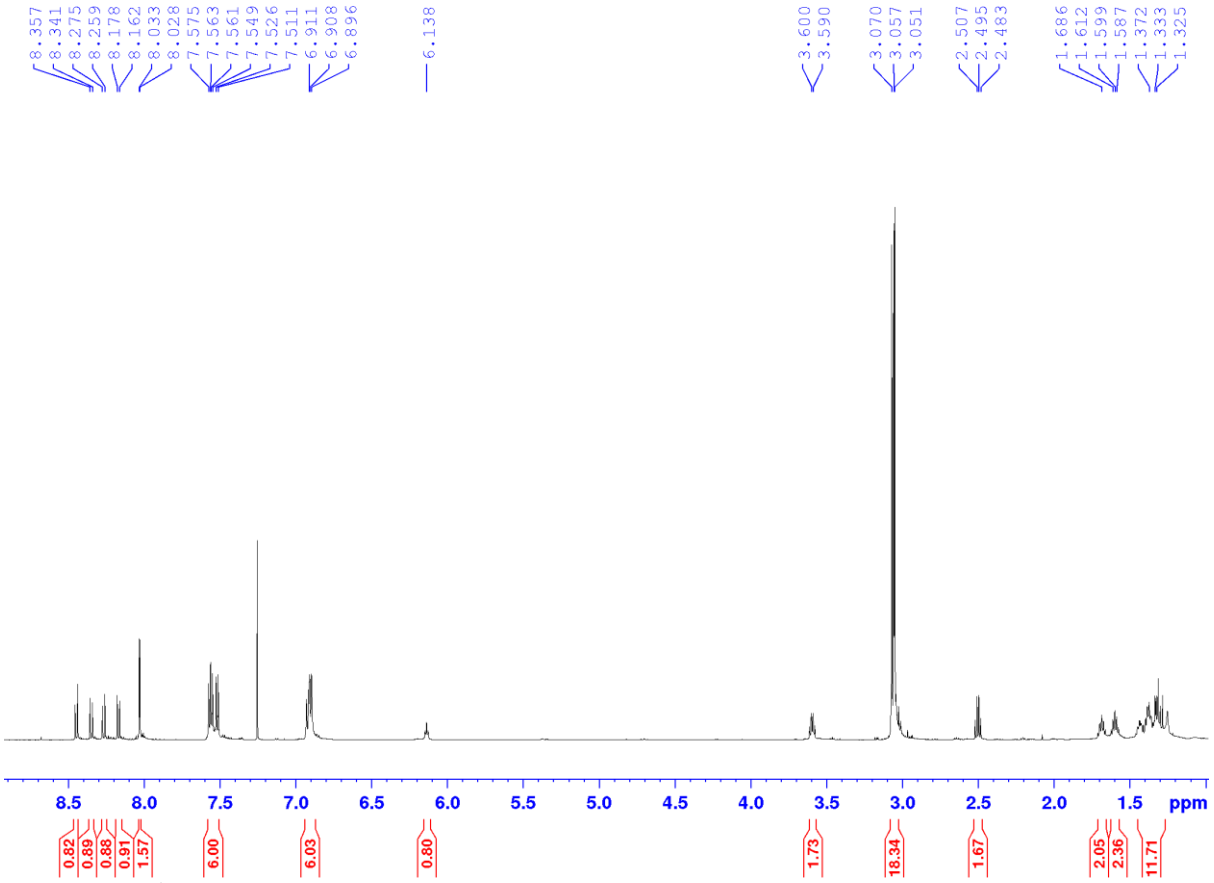

Figure S5.1 ^{1}HNMR (600 MHz) of PyLaOT (**2**) in $CDCl_3$.

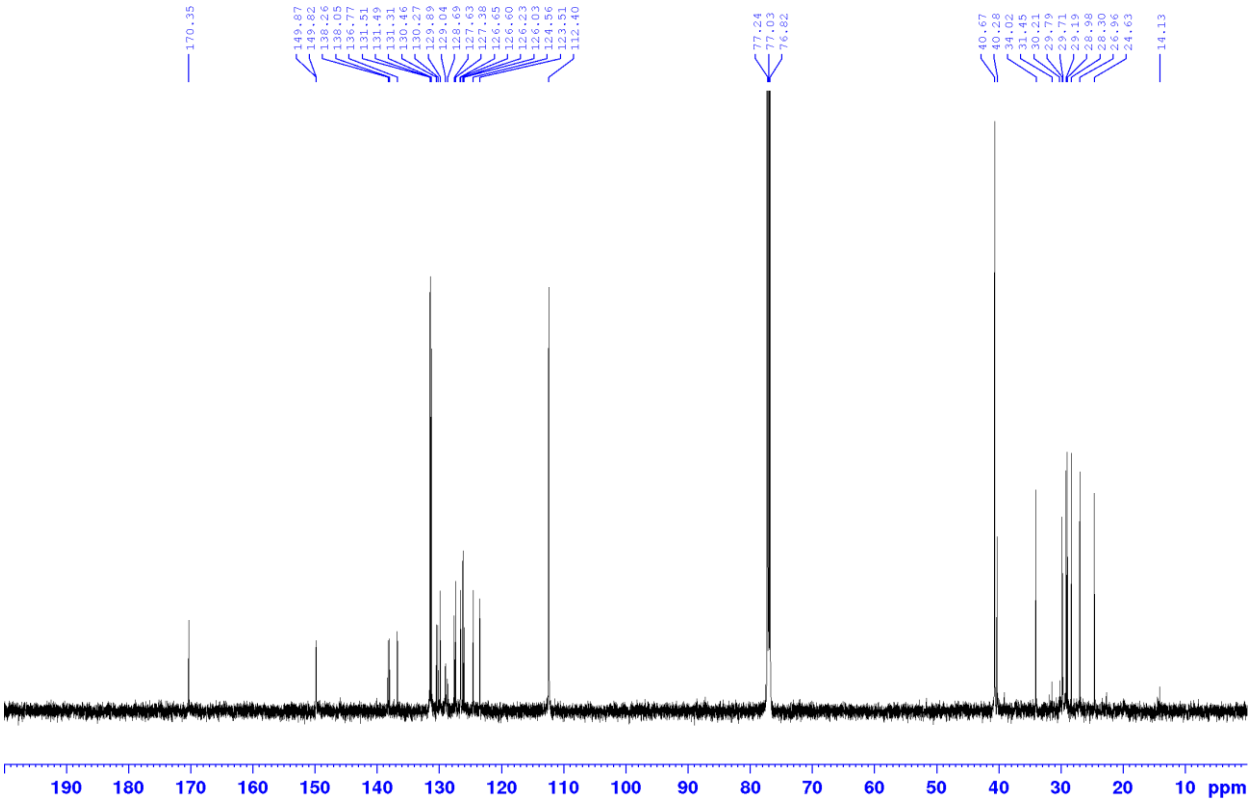

Figure S5.2 ^{13}CNMR (150 MHz) of PyLaOT (**2**) in $CDCl_3$.

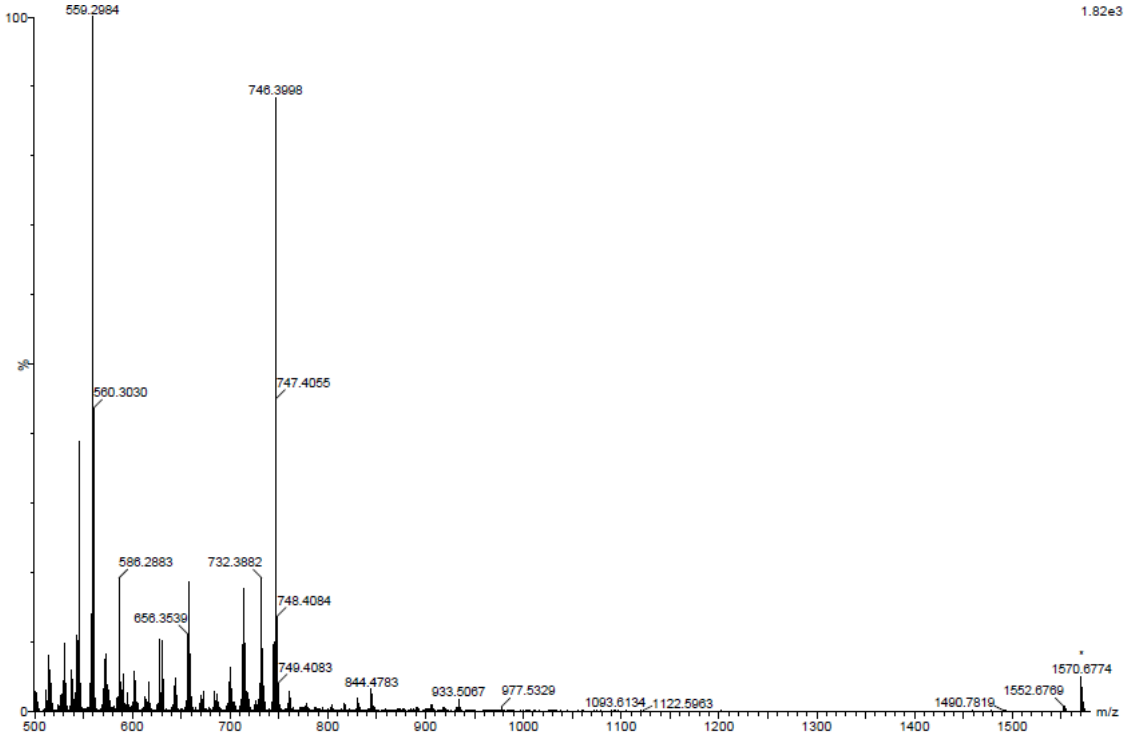

Figure S5.3 HR-MS (ESI-QTOF): Single Mass Analysis of PyLaOT indicating [M]+.

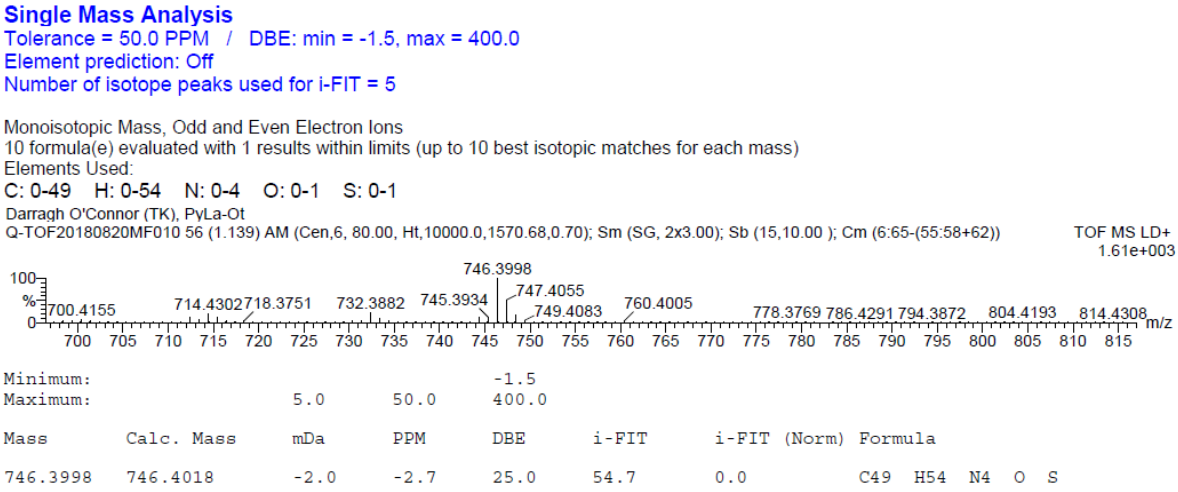

Figure S5.4 HR-MS (ESI-QTOF): Single Mass Analysis of PyLaOT indicating [M]+.

S5.3 Computational Studies

Table S5.1 Electronic character, vertical excitation energies and oscillator strengths of the bright singlet excitations contributing to the UV-vis absorption properties of PyLa obtained at TD-DFT level of theory (CAM-B3LYP/TZVP) including the solvent effects of acetonitrile based on the integral equation formalism of the polarizable continuum model.

State	Transition	P in %	E in eV	λ in nm	f	λ^{exp} in nm
S_1	$\pi_{8,py}$ (160) $\rightarrow \pi^*_{9,py} + \pi^*_{COO}$(161)	91	2.99	415	1.062	429

S_2	$\pi_{3,ph(2)}$ (159) $\rightarrow \pi^*_{9,py} + \pi^*_{COO}$(161) $\pi_{6,py}$ (156) $\rightarrow \pi^*_{9,py} + \pi^*_{COO}$(161)	45 21	3.57	347	0.131	370
S_4	$\pi_{8,py}$ (160) $\rightarrow \pi^*_{10,py} + \pi^*_{COO}$(162) $\pi_{3,ph(2)}$ (159) $\rightarrow \pi^*_{9,py} + \pi^*_{COO}$(161)	36 32	3.85	322	0.540	300
S_7	$\pi_{6,ph(2)}$ (156) $\rightarrow \pi^*_{9,py} + \pi^*_{COO}$(161) $\pi_{8,py}$ (160) $\rightarrow \pi^*_{10,py} + \pi^*_{COO}$(162)	39 22	4.49	276	0.467	265

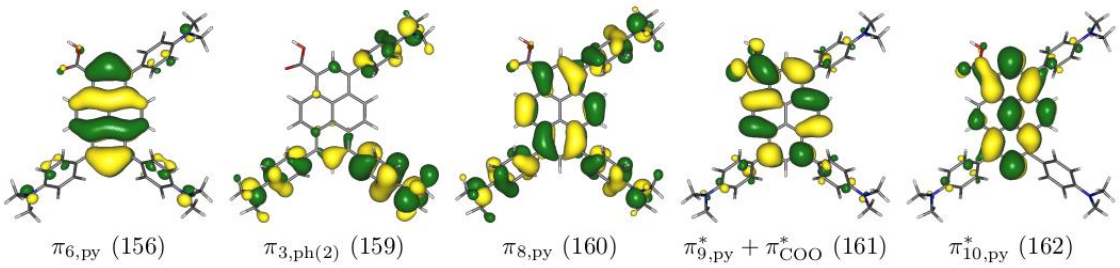

Figure S5.5 Isocontour representations (ρ = ±0.02) of the Kohn-Sham orbitals involved in the main configurations of the low-lying energetic states of PyLa, which are responsible for the ground state absorption properties.

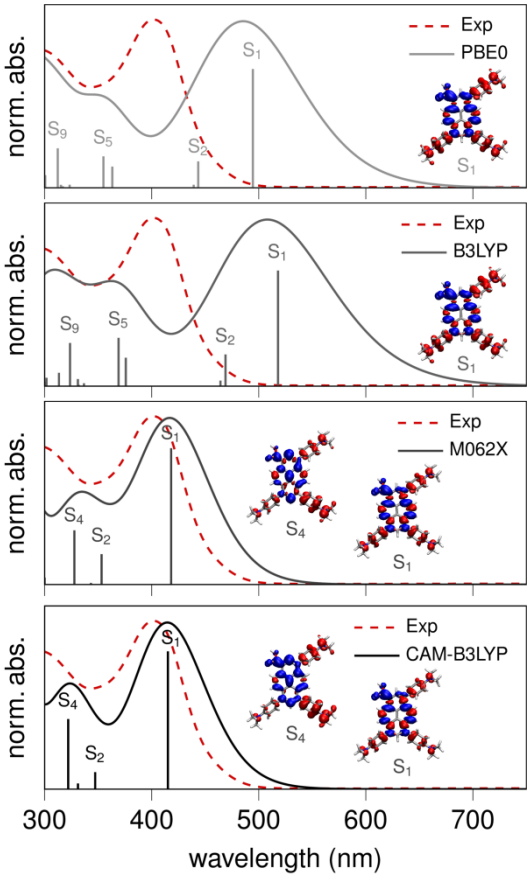

Figure S5.6 Experimental and simulated absorption spectra of PyLa. The vertical excitation energies are obtained via TD-DFT simulations on CAM-B3LYP/TZVP, M062X/TZVP, B3LYP/TZVP and PBE0/TZVP level of theory using a DFT (B3LYP/TZVP) optimised structure of the ground state. Some charge density differences of low-lying energetic states obtained for the different computational levels are depicted in the graphs (The excitation is from red ($\rho = -0.005$) to blue ($\rho = +0.005$).).

Table S5.2 Calculated ground state energies (B3LYP/TZVP) of three different mono- (PyLa13, PyLa16 and PyLa18) and di-protonated forms (PyLa236, PyLa238 and PyLa268) of PyLa and their corresponding Boltzmann factors at room temperature.

Species	Relative energy	Boltzmann factor
Mono-protonated PyLa		
Py13	0.00 kJ/mol	0.369
Py16	0.55 kJ/mol	0.296
Py18	0.24 kJ/mol	0.335
Di-protonated PyLa		
Py236	1.08 kJ/mol	0.287
Py238	1.26 kJ/mol	0.268
Py268	0.00 kJ/mol	0.445

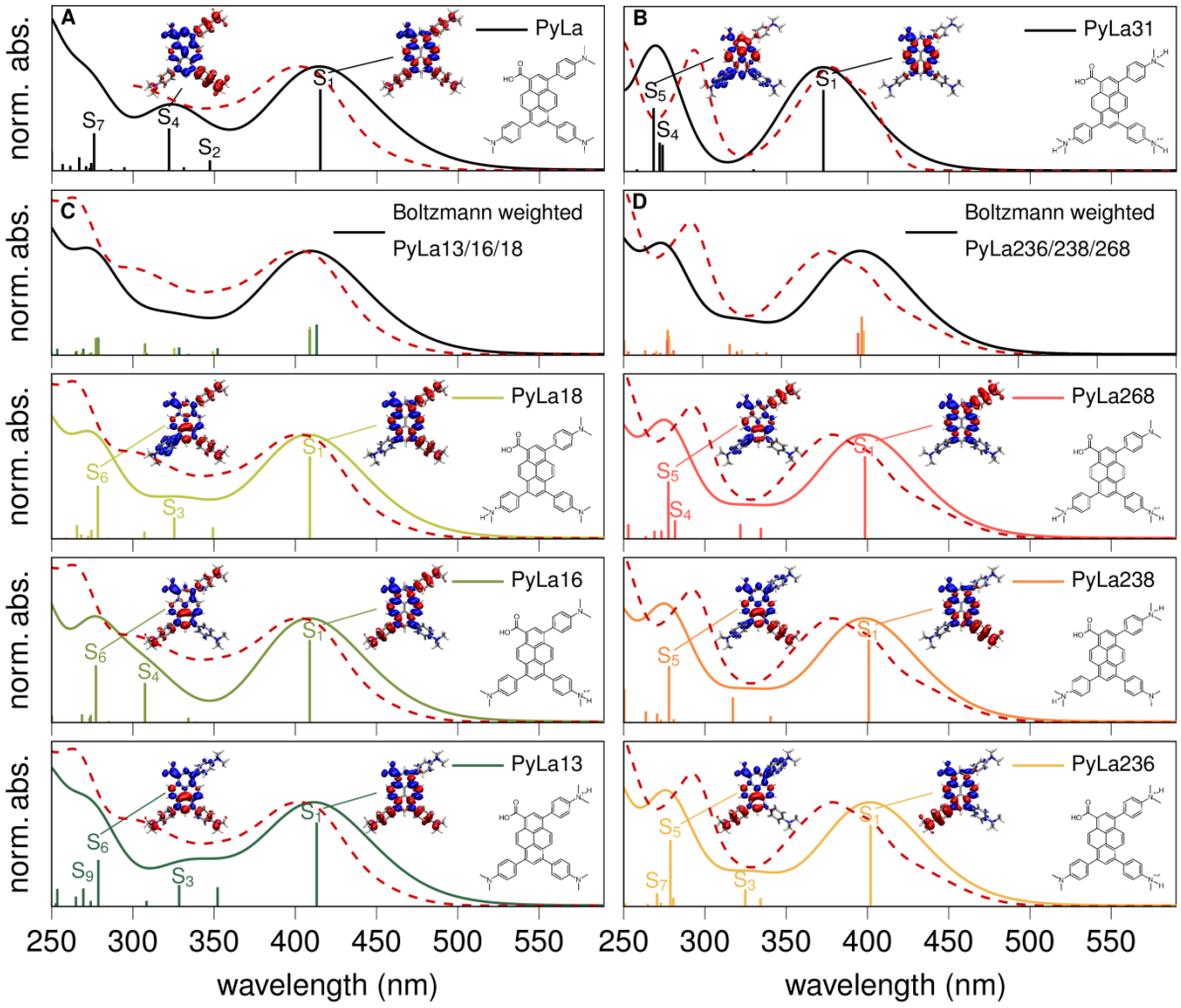

Figure S5.7 Experimental (red, dashed) and simulated (TD-CAM-B3LYP/TZVP) absorption spectra of PyLa (**A**) and three of its mono- (**C**: PyLa13, PyLa16, PyLa18) and di-protonated forms (**D**: PyLa236, PyLa238, PyLa268) as well as its tris-protonated species (PyLa31, **B**). Some charge density differences ($\rho = \pm 0.005$) of low-lying energetic states obtained for the different protonated species are depicted as inset (excitation from red to blue). For the mono- and di-protonated species the Boltzmann weighted absorption spectra are depicted in **C** and **D**.

Table S5.3 Calculated vertical excitation energies (E), oscillator strengths (f) and main single-excited configurations of the main excited states of the neutral PyLa species atB3LYP/TZVP//CAM-B3LYP/TZVP (IEFPCM of acetonitrile) as level of theory and experimental absorption maxima.

S_n	transition			p	E	λ	f	$\lambda^{\mathrm{Exp.}}$
				in %	in eV	in nm		in nm
			PyLa					
S_1	$\pi_{8,\mathrm{py}}$ (160)	$\rightarrow$	$\pi^*_{9,\mathrm{py}} + \pi^*_{\mathrm{COO}}$ (161)	91	2.99	415	1.062	429
S_4	$\pi_{8,\mathrm{py}}$ (160)	$\rightarrow$	$\pi^*_{10,\mathrm{py}} + \pi^*_{\mathrm{COO}}$ (162)	36	3.85	322	0.540	300
	$\pi_{3,\mathrm{DMA(2)}}$ (159)	$\rightarrow$	$\pi^*_{9,\mathrm{py}} + \pi^*_{\mathrm{COO}}$ (161)	32				
S_7	$\pi_{6,\mathrm{py}}$ (156)	$\rightarrow$	$\pi^*_{9,\mathrm{py}} + \pi^*_{\mathrm{COO}}$ (161)	39	4.49	276	0.467	265
	$\pi_{8,\mathrm{py}}$ (160)	$\rightarrow$	$\pi^*_{10,\mathrm{py}} + \pi^*_{\mathrm{COO}}$ (162)	22				
			PyLa03					
S_1	$\pi_{8,\mathrm{py}}$ (160)	$\rightarrow$	$\pi^*_{9,\mathrm{py}} + \pi^*_{4,\mathrm{DMA(3)}}$ (161)	90	3.28	378	1.092	360
S_3	$\pi_{3,\mathrm{DMA(6,8)}}$ (159)	$\rightarrow$	$\pi^*_{9,\mathrm{py}} + \pi^*_{4,\mathrm{DMA(3)}}$ (161)	71	4.06	306	0.686	300
S_6	$\pi_{8,\mathrm{py}}$ (160)	$\rightarrow$	$\pi^*_{4,\mathrm{DMA(3)}}$ (162)	15	4.52	275	0.234	265
	$\pi_{3,\mathrm{DMA(6,8)}}$ (159)	$\rightarrow$	$\pi^*_{4,\mathrm{DMA(6,8)}}$ (166)	13				
	$\pi_{8,\mathrm{py}}$ (160)	$\rightarrow$	$\pi^*_{4,\mathrm{DMA(6,8)}}$ (166)	12				
			PyLa06					
S_1	$\pi_{8,\mathrm{py}}$ (160)	$\rightarrow$	$\pi^*_{9,\mathrm{py}} + \pi^*_{4,\mathrm{DMA(6)}}$ (161)	91	3.27	379	1.165	360
S_4	$\pi_{3,\mathrm{DMA(3,8)}}$ (158)	$\rightarrow$	$\pi^*_{9,\mathrm{py}} + \pi^*_{4,\mathrm{DMA(6)}}$ (161)	45	4.22	294	0.649	300
	$\pi_{8,\mathrm{py}}$ (160)	$\rightarrow$	$\pi^*_{4,\mathrm{DMA(6)}}$ (162)	26				
S_5	$\pi_{8,\mathrm{py}}$ (160)	$\rightarrow$	$\pi^*_{4,\mathrm{DMA(3,8)}}$ (165)	29	4.32	287	0.179	265
	$\pi_{3,\mathrm{DMA(3,8)}}$ (158)	$\rightarrow$	$\pi^*_{9,\mathrm{py}} + \pi^*_{4,\mathrm{DMA(6)}}$ (161)	22				
	$\pi_{8,\mathrm{py}}$ (160)	$\rightarrow$	$\pi^*_{4,\mathrm{DMA(6)}}$ (164)	21				
			PyLa08					
S_1	$\pi_{8,\mathrm{py}}$ (160)	$\rightarrow$	$\pi^*_{9,\mathrm{py}} + \pi^*_{4,\mathrm{DMA(8)}}$ (161)	91	3.28	378	1.095	360
S_3	$\pi_{3,\mathrm{DMA(3,6)}}$ (159)	$\rightarrow$	$\pi^*_{9,\mathrm{py}} + \pi^*_{4,\mathrm{DMA(8)}}$ (161)	73	4.07	304	0.649	300
S_8	$\pi_{6,\mathrm{py}}$ (157)	$\rightarrow$	$\pi^*_{9,\mathrm{py}} + \pi^*_{4,\mathrm{DMA(8)}}$ (161)	19	4.59	270	0.225	265
	$\pi_{8,\mathrm{py}}$ (160)	$\rightarrow$	$\pi^*_{5,\mathrm{DMA(3,6)}}$ (168)	18				
	$\pi_{7,\mathrm{py}} + \pi_{3,\mathrm{DMA(3,6)}}$ (158)	$\rightarrow$	$\pi^*_{10,\mathrm{py}}$ (165)	9				
	$\pi_{3,\mathrm{DMA(3,6)}}$ (159)	$\rightarrow$	$\pi^*_{4,\mathrm{DMA(3,6)}}$ (166)	9				

Table S5.4 Calculated vertical excitation energies (E), oscillator strengths (f) and main single-excited configurations of the main excited states of the mono-protonated forms of PyLa at B3LYP/TZVP//CAM-B3LYP/TZVP (IEFPCM of acetonitrile) as level of theory and experimental absorption maxima.

S_n	transition			p	E	λ	f	$\lambda^{\mathrm{Exp.}}$
				in %	in eV	in nm		in nm
			PyLa13					
S_1	$\pi_{8,\mathrm{py}}$ (160)	$\rightarrow$	$\pi^*_{9,\mathrm{py}}$ (161)	89	3.00	413	0.981	417
S_3	$\pi_{8,\mathrm{py}}$ (160)	$\rightarrow$	$\pi^*_{4,\mathrm{DMA(3)}}$ (162)	33	3.77	329	0.250	300
	$\pi_{3,\mathrm{DMA(6,8)}}$ (159)	$\rightarrow$	$\pi^*_{9,\mathrm{py}}$ (161)	23				
	$\pi_{7,\mathrm{py}}$ (157)	$\rightarrow$	$\pi^*_{9,\mathrm{py}}$ (161)	19				
S_6	$\pi_{7,\mathrm{py}}$ (157)	$\rightarrow$	$\pi^*_{9,\mathrm{py}}$ (161)	42	4.45	279	0.545	265
	$\pi_{8,\mathrm{py}}$ (160)	$\rightarrow$	$\pi^*_{4,\mathrm{DMA(3)}}$ (162)	25				
			PyLa16					
S_1	$\pi_{8,\mathrm{py}}$ (160)	$\rightarrow$	$\pi^*_{9,\mathrm{py}}$ (161)	90	3.03	409	1.027	417
S_4	$\pi_{3,\mathrm{DMA(3,8)}}$ (158)	$\rightarrow$	$\pi^*_{9,\mathrm{py}}$ (161)	74	4.03	308	0.474	300
S_6	$\pi_{7,\mathrm{py}}$ (157)	$\rightarrow$	$\pi^*_{9,\mathrm{py}}$ (161)	42	4.47	277	0.632	265
	$\pi_{8,\mathrm{py}}$ (160)	$\rightarrow$	$\pi^*_{4,\mathrm{DMA(6)}}$ (162)	32				
			PyLa18					
S_1	$\pi_{8,\mathrm{py}}$ (160)	$\rightarrow$	$\pi^*_{9,\mathrm{py}}$ (161)	89	3.03	409	1.002	417
S_3	$\pi_{3,\mathrm{DMA(3,6)}}$ (159)	$\rightarrow$	$\pi^*_{9,\mathrm{py}}$ (161)	32	3.81	325	0.255	300
	$\pi_{8,\mathrm{py}}$ (160)	$\rightarrow$	$\pi^*_{4,\mathrm{DMA(8)}}$ (162)	27				
	$\pi_{7,\mathrm{py}}$ (157)	$\rightarrow$	$\pi^*_{9,\mathrm{py}}$ (161)	16				
S_6	$\pi_{7,\mathrm{py}}$ (157)	$\rightarrow$	$\pi^*_{9,\mathrm{py}}$ (161)	48	4.45	279	0.632	265
	$\pi_{8,\mathrm{py}}$ (160)	$\rightarrow$	$\pi^*_{4,\mathrm{DMA(8)}}$ (162)	38				
			PyLa136					
S_1	$\pi_{8,\mathrm{py}}$ (160)	$\rightarrow$	$\pi^*_{9,\mathrm{py}}$ (161)	87	3.32	374	1.046	386
S_3	$\pi_{3,\mathrm{DMA(3,6)}}$ (159)	$\rightarrow$	$\pi^*_{9,\mathrm{py}}$ (161)	74	4.11	302	0.301	300
S_6	$\pi_{8,\mathrm{py}}$ (160)	$\rightarrow$	$\pi^*_{4,\mathrm{DMA(8)}}$ (162)	43	4.50	276	0.480	265
	$\pi_{7,\mathrm{py}}$ (158)	$\rightarrow$	$\pi^*_{9,\mathrm{py}}$ (161)	20				
			PyLa138					
S_1	$\pi_{8,\mathrm{py}}$ (160)	$\rightarrow$	$\pi^*_{9,\mathrm{py}}$ (161)	88	3.32	373	0.999	386
S_3	$\pi_{3,\mathrm{DMA(3,8)}}$ (159)	$\rightarrow$	$\pi^*_{9,\mathrm{py}}$ (161)	76	4.12	301	0.352	300
S_6	$\pi_{7,\mathrm{py}}$ (158)	$\rightarrow$	$\pi^*_{9,\mathrm{py}}$ (161)	38	4.52	274	0.649	265
	$\pi_{8,\mathrm{py}}$ (160)	$\rightarrow$	$\pi^*_{4,\mathrm{DMA(6)}}$ (163)	22				
			PyLa168					
S_1	$\pi_{8,\mathrm{py}}$ (160)	$\rightarrow$	$\pi^*_{9,\mathrm{py}}$ (161)	87	3.29	377	1.055	386
S_3	$\pi_{3,\mathrm{DMA(6,8)}}$ (159)	$\rightarrow$	$\pi^*_{9,\mathrm{py}}$ (161)	66	4.09	303	0.344	300
S_6	$\pi_{8,\mathrm{py}}$ (160)	$\rightarrow$	$\pi^*_{4,\mathrm{DMA(3)}}$ (164)	17	4.63	268	0.382	265
	$\pi_{7,\mathrm{py}}$ (157)	$\rightarrow$	$\pi^*_{9,\mathrm{py}}$ (161)	17				

Table S5.5 Calculated vertical excitation energies (E), oscillator strengths (f) and main single-excited configurations of the main excited states of the di-protonated forms of PyLa at B3LYP/TZVP//CAM-B3LYP/TZVP (IEFPCM of acetonitrile) as level of theory and experimental absorption maxima.

S_n	transition			p	E	λ	f	$\lambda^{\text{Exp.}}$
				in %	in eV	in nm		in nm
			PyLa236					
S_1	$\pi_{8,\text{py}}$ (160)	$\rightarrow$	$\pi^*_{9,\text{py}}$ (161)	83	3.08	402	0.929	417
S_3	$\pi_{3,\text{DMA(8)}}$ (159)	$\rightarrow$	$\pi^*_{9,\text{py}}$ (161)	61	3.82	325	0.202	370
S_5	$\pi_{7,\text{py}}$ (158)	$\rightarrow$	$\pi^*_{9,\text{py}}$ (161)	42	4.45	279	0.721	265
	$\pi_{8,\text{py}}$ (160)	$\rightarrow$	$\pi^*_{4,\text{DMA(3,6)}}$ (162)	37				
			PyLa238					
S_1	$\pi_{8,\text{py}}$ (160)	$\rightarrow$	$\pi^*_{9,\text{py}}$ (161)	84	3.09	401	0.942	417
S_3	$\pi_{3,\text{DMA(6)}}$ (159)	$\rightarrow$	$\pi^*_{9,\text{py}} + \pi^*_{\text{COO}}$ (161)	49	3.91	317	0.272	370
	$\pi_{8,\text{py}}$ (160)	$\rightarrow$	$\pi^*_{4,\text{DMA(3,8)}}$ (162)	14				
S_5	$\pi_{7,\text{py}}$ (158)	$\rightarrow$	$\pi^*_{9,\text{py}}$ (161)	45	4.46	278	0.614	265
	$\pi_{8,\text{py}}$ (160)	$\rightarrow$	$\pi^*_{4,\text{DMA(3,8)}}$ (162)	39				
			PyLa268					
S_1	$\pi_{8,\text{py}}$ (160)	$\rightarrow$	$\pi^*_{9,\text{py}}$ (161)	84	3.11	399	0.905	417
S_3	$\pi_{3,\text{DMA(3)}}$ (159)	$\rightarrow$	$\pi^*_{9,\text{py}}$ (161)	58	3.85	322	0.157	370
S_5	$\pi_{8,\text{py}}$ (160)	$\rightarrow$	$\pi^*_{4,\text{DMA(6,8)}}$ (162)	36	4.47	278	0.609	265
	$\pi_{7,\text{py}}$ (158)	$\rightarrow$	$\pi^*_{9,\text{py}}$ (161)	34				

Table S5.6 Calculated vertical excitation energies (E), oscillator strengths (f) and main single-excited configurations of the tri-protonated forms of PyLa at B3LYP/TZVP//CAM-B3LYP/TZVP (IEFPCM of acetonitrile) as level of theory and experimental absorption maxima.

S_n	transition			p	E	λ	f	$\lambda^{\text{Exp.}}$
				in %	in eV	in nm		in nm
			PyLa31					
S_1	$\pi_{8,\text{py}}$ (160)	$\rightarrow$	$\pi^*_{9,\text{py}}$ (161)	95	3.33	373	0.967	370
S_3	$\pi_{5,\text{py}}$ (157)	$\rightarrow$	$\pi^*_{9,\text{py}}$ (161)	55	4.53	274	0.258	300
S_4	$\pi_{8,\text{py}}$ (160)	$\rightarrow$	$\pi^*_{4,\text{DMA(3,6,8)}}$ (163)	48	4.56	272	0.279	265
	$\pi_{8,\text{py}}$ (160)	$\rightarrow$	$\pi^*_{11,\text{py}}$ (169)	15				
S_5	$\pi_{8,\text{py}}$ (160)	$\rightarrow$	$\pi^*_{10,\text{py}}$ (162)	26	4.62	268	0.614	265
	$\pi_{5,\text{py}}$ (157)	$\rightarrow$	$\pi^*_{9,\text{py}}$ (161)	23				
	$\pi_{7,\text{py}}$ (159)	$\rightarrow$	$\pi^*_{9,\text{py}}$ (161)	18				

S5.4 Additional Photophysical Characterisation

Table S5.7 Photophysical data including UV-Vis absorption maxima (λ_{abs} nm), emission maxima (λ_{em} nm), full width half maximum of emission intensity profile (FWHM), quantum fluorescence yield of the charge-transfer emission (ϕ_{fl}) and luminescent lifetime (τ_{lum} ns) of PyLa and PyLaOT in a range of different solvents. [a]Previously reported in literature.

	Solvent	λ_{abs} (nm)	λ_{em} (nm)	FWHM (cm^{-1})	ϕ_{fl}	τ_{lum} (ns)
	1-butanol	397	487	3226	0.11	2.7
	2-propanol	396	486	4676	0.27	2.4
	Chloroform	437	537	2674	0.88	3.1
	Ethanol	396	500	3471	0.82	3.2
PyLa	Tetrahydrofuran	419	501	4290	0.88	3.1
	Methanol	396[a]	525 [a]	3696	0.55	3.5 [a]
	Acetone	426 [a]	580 [a]	3338	0.97	2.6 [a]
	Acetonitrile	399 [a]	520 [a]	3620	0.49 [a]	3.8 [a]
	Dichloromethane	431 [a]	552 [a]	2965	0.40 [a]	4.4 [a]
	1-butanol	404	523	3652	0.15	2.7
	2-propanol	404	524	3699	0.89	2.1
	Chloroform	394	510	3001	-	2.5
	Ethanol	404	530	3913	-	2.5
PyLaOT	Tetrahydrofuran	407	508	3393	0.12	2.6
	Methanol	398	550	3767	0.67	2.2
	Acetone	411	530	3728	-	-
	Acetonitrile	416	552	3660	0.31	4.6
	Dichloromethane	410	515	3136	0.73	2.6

Table S5.8 Photophysical data (λ_{abs} nm), emission maxima (λ_{em} nm) and luminescent lifetime (τ ns) of PyLa and PyLaOT in PBS and acetonitrile at isolated pH. *EDT microprocessor pH meter was used to measure pH in PBS samples with changes in pH due to HCl and NaOH titrations. In acetonitrile we refer to pH approximation; pH -log[$HClO_4$] as perchloric acid and triethylamine was used to determine apparent pH.

		pH 7.4 (Neutral Species)			pH 5.5 (Mono-)			pH 4.4 (Di-)			pH 1.5 (Tris-)			pH Reversal (Addition of base)		
	Solvent	λ_{abs} (nm)	λ_{em} (nm)	τ (ns)	λ_{abs} (nm)	λ_{em} (nm)	τ (ns)	λ_{abs} (nm)	λ_{em} (nm)	τ (ns)	λ_{abs} (nm)	λ_{em} (nm)	τ (ns)	λ_{abs} (nm)	λ_{em} (nm)	τ (ns)
PyLa	PBS	417	577	2.74±0.10	434	575	2.46 ± 0.10	444	575	2.28 ± 0.11	380	450	2.20±0.06	420	552	2.5 ± 0.05
	ACN	404	518	3.79 ±0.02	408	518	3.77 ± 0.05	380	433	1.51 ± 0.01	379	433	2.69 ± 0.1	413	565	1.52±0.01
PyLaOT	PBS	434	544	3.80 ±0.15	438	542	3.33 ±0.14	438	544	2.79 ± 0.06	378	428	2.25±0.01	434	532	2.65±0.07
	ACN	418	550	4.67 ± 0.05	418	520	5.44 ± 0.06	384	430	4.74 ± 0.01	378	430	2.77±0.01	418	560	3.95±0.01

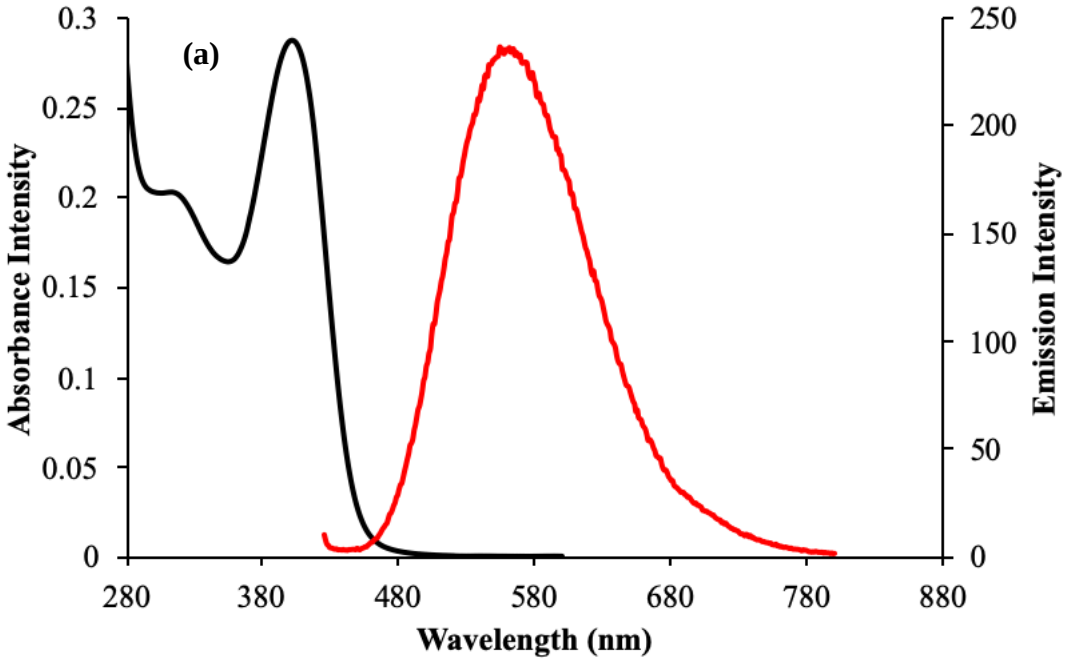

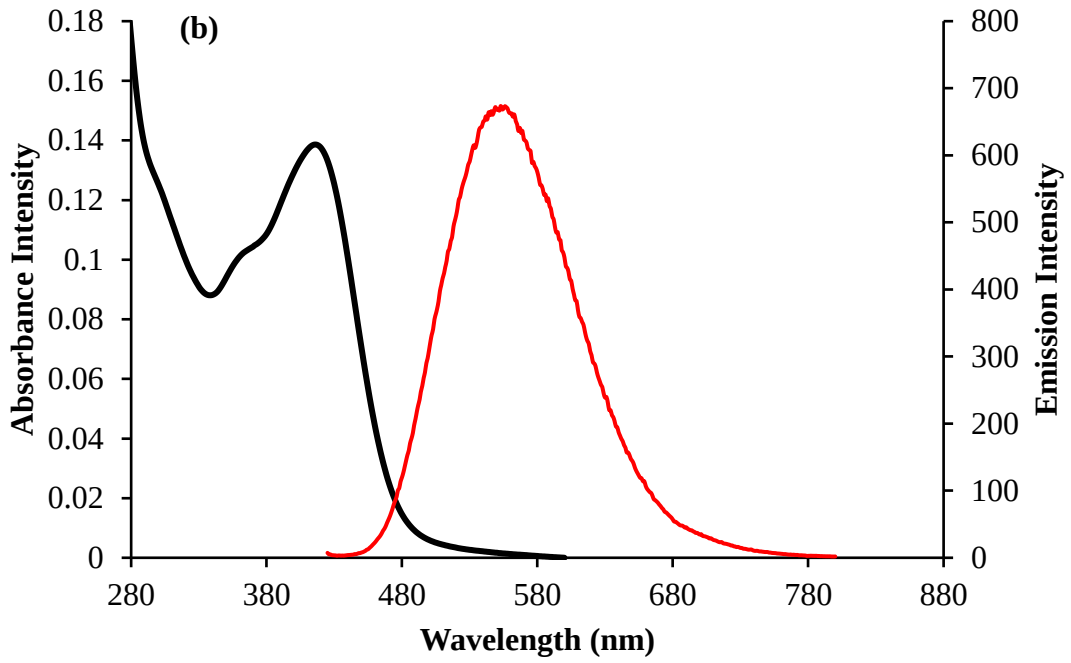

Figure S5.8 Absorbance and emission spectra of PyLa **(a)** and PyLaOT **(b)** in acetonitrile (sample concentration 20 μM). Emission spectra were obtained using slit widths of 5 nm.

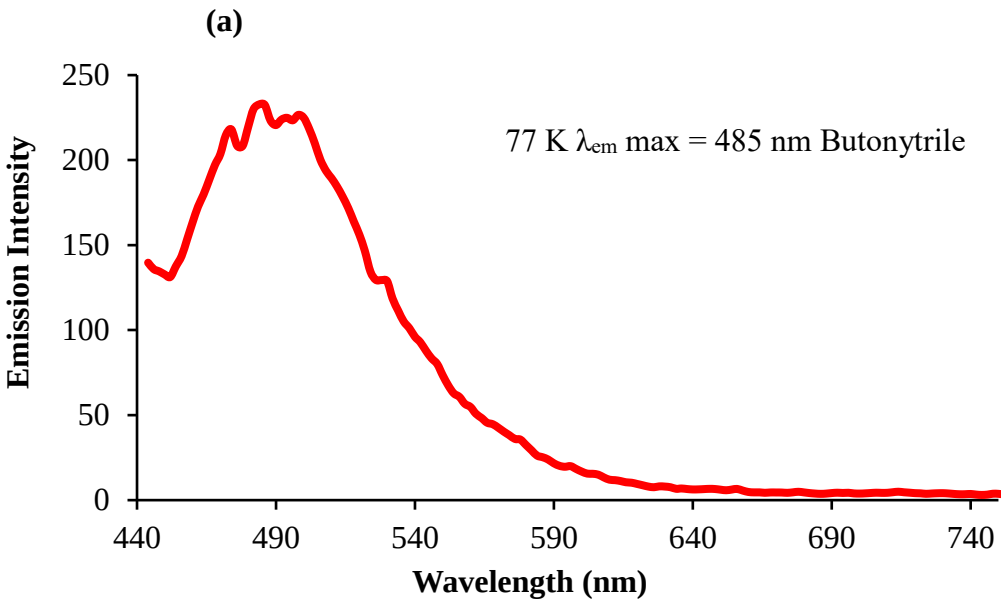

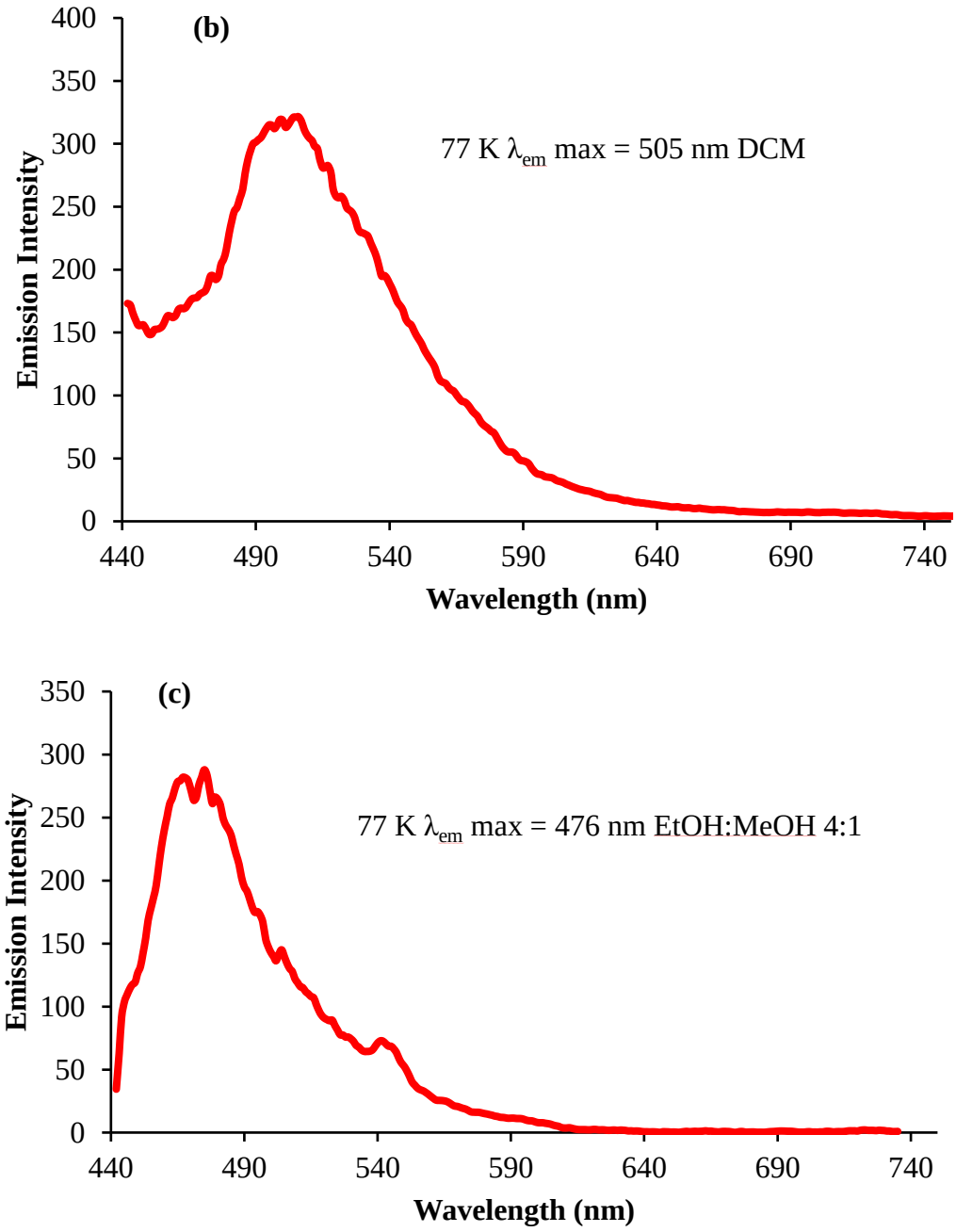

Figure S5.9 77 K emission spectra of PyLa in butonytrile **(a)**, dichloromethane **(b)** and ethanol:methanol 4:1: **(c)** (sample concentration 1 μM). Emission spectra were obtained using an excitation slit width of 5 nm and emission slit width of 10 nm.

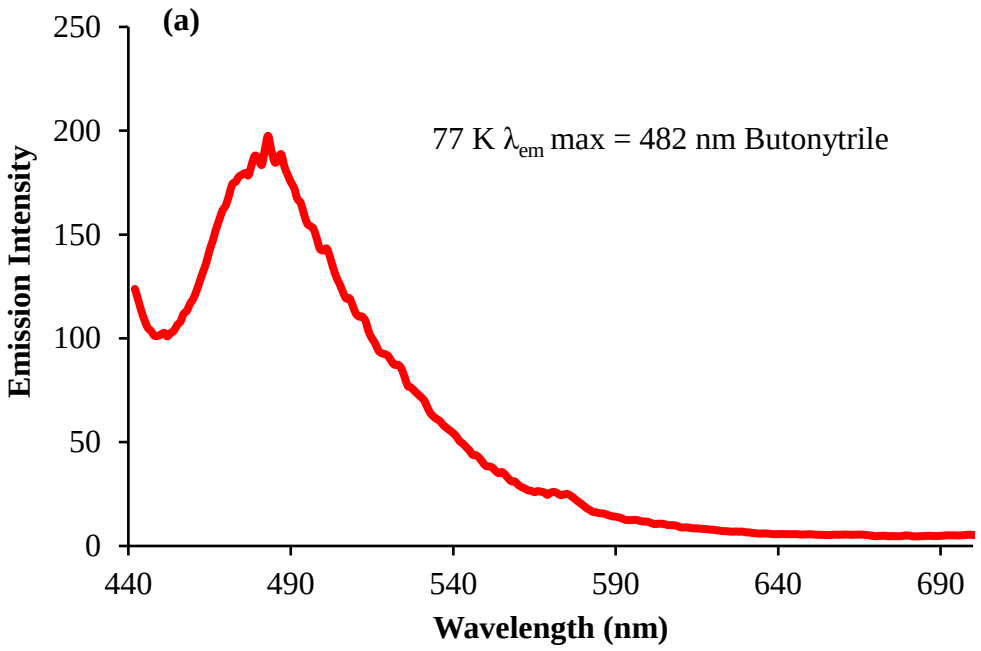
(a)
77 K λem max = 482 nm Butonytrile
Emission Intensity
250
200
150
100
50
0
440
490
540
590
640
690
Wavelength (nm)

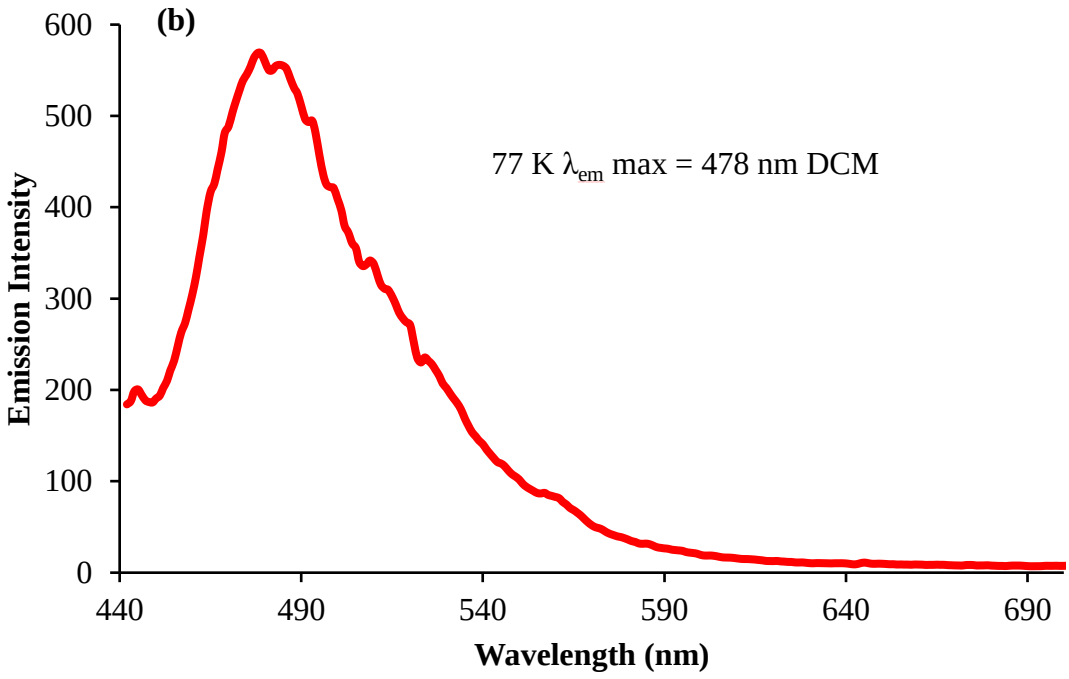
(b)
77 K λem max = 478 nm DCM
Emission Intensity
600
500
400
300
200
100
0
440
490
540
590
640
690
Wavelength (nm)

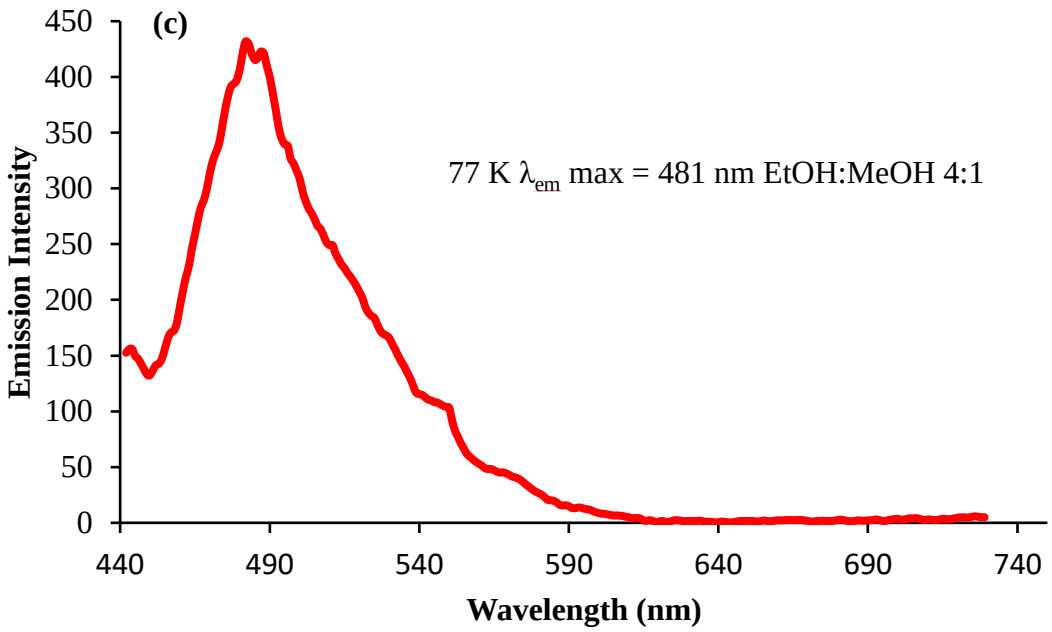

Figure S5.10 77 K emission spectra of PyLaOT in butonytrile **(a)**, dichloromethane **(b)** and ethanol:methanol 4:1: **(c)** (sample concentration 1 μM). Emission spectra were obtained using an excitation slit width of 5 nm and emission slit width of 10 nm.

pKa determination: Ground state pKas were obtained for PyLa and PyLaOT by plotting absorbance versus pH as seen in Figure S5.11 below.

Using equation: $pKa = pH_x + \log [(A_{HB}^{+} - A_x)/ (A_x - A_B)]$

A_{HB}^{+} = absolute acid absorbance

A_x = absorbance at pH

A_B = absolute base form absorbance

PyLaOT PBS GS pKa = 7.2 pKa = 3.1

PyLa PBS GS pKa = 6.6 pKa = 3.7

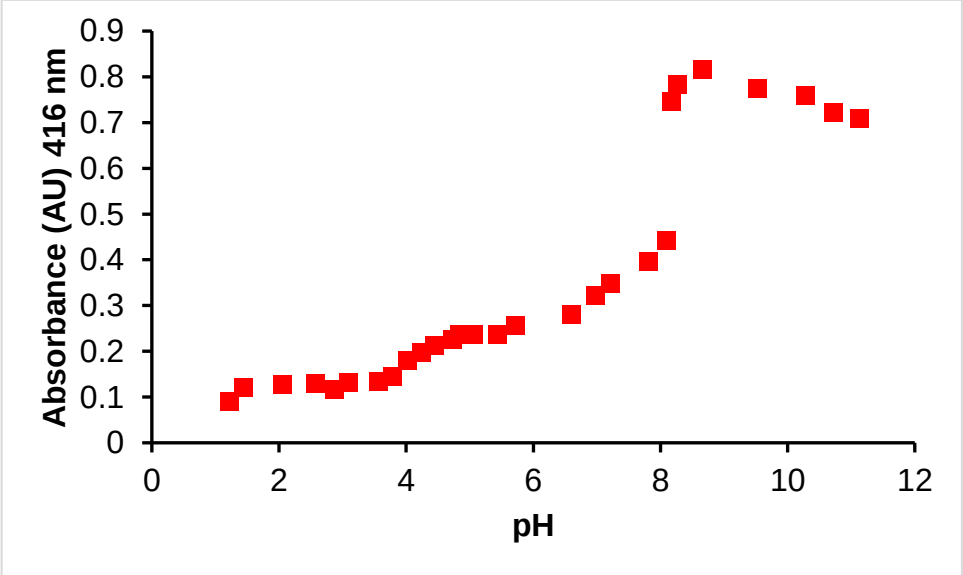

Figure S5.11 Plot of absorbance versus pH of PyLaOT (**2**) (100 μM PBS) at 416 nm.

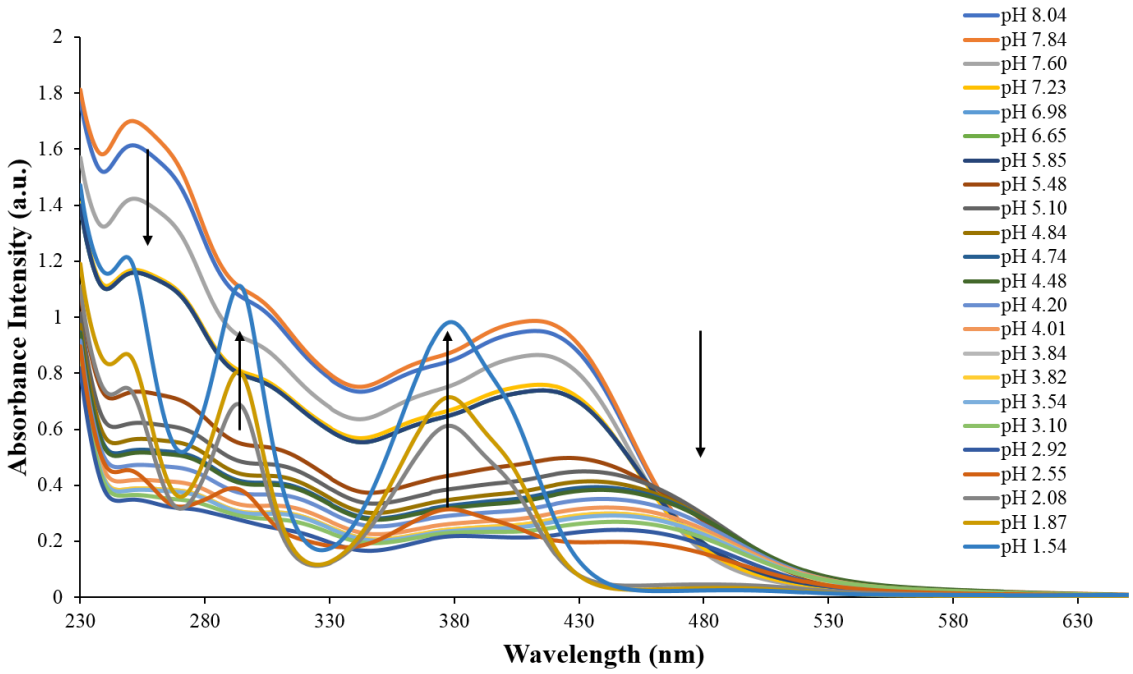

Figure S5.12 Absorption spectra of PyLa at decreasing pH values (c = 100 µM) in PBS. Spectra shows decrease in absorbance max and red-shift at approximately 428 nm with decreasing pH. Disappearance of this absorbance shoulder is observed below pH 3 with the formation of a pyrene like absorbance max at approximately 380 nm which then increases in intensity with decreasing pH.

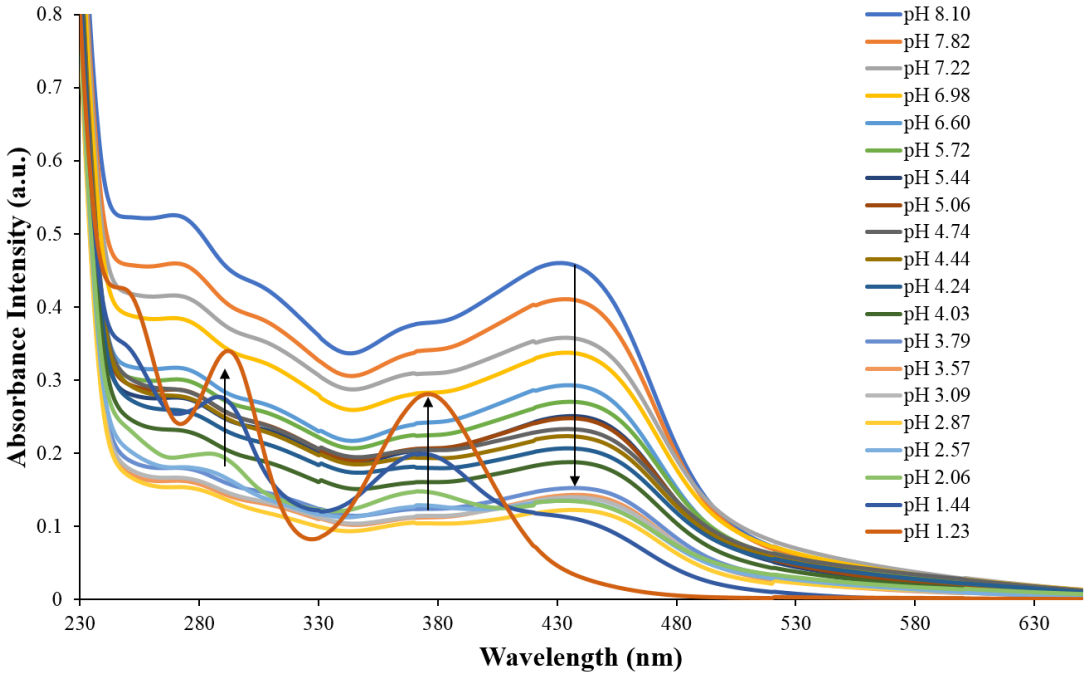

Figure S5.13 Absorption spectra of PyLaOT at decreasing pH values (c = 100 µM) in PBS. Spectra shows decrease in absorbance max and red-shift at approximately 434 nm with decreasing pH. Disappearance of this absorbance shoulder is observed below pH 3 with the formation of a pyrene like absorbance max at approximately 380 nm which then increases in intensity with decreasing pH.

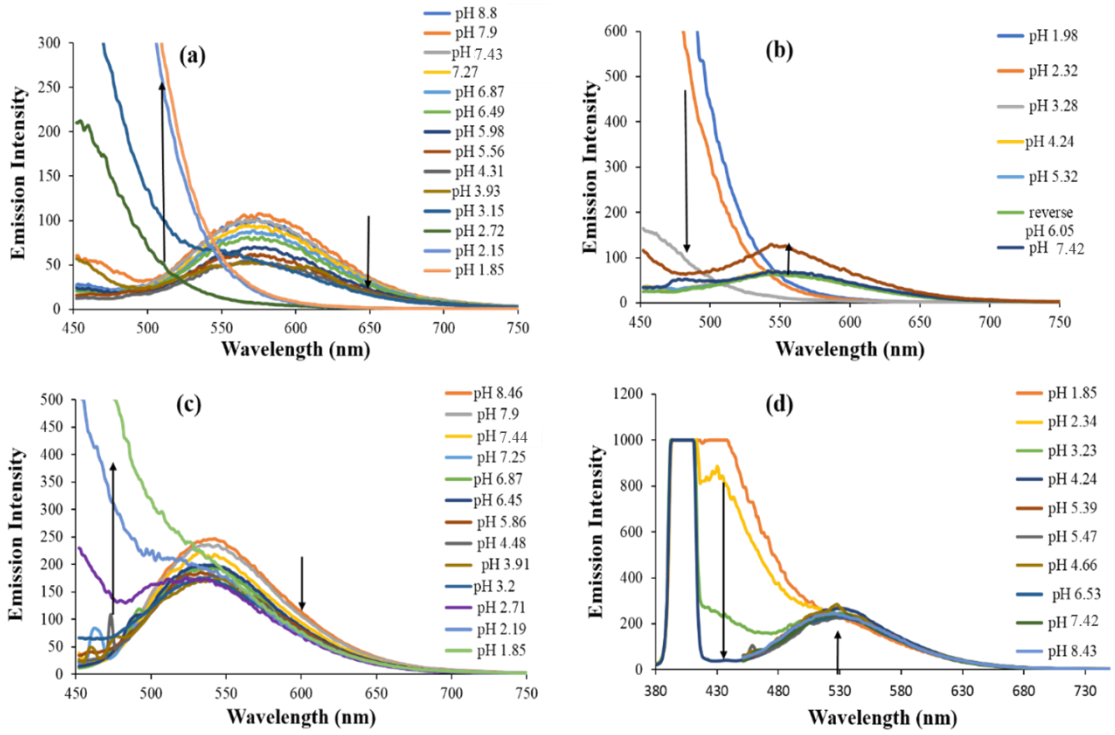

Figure S5.14 (a) Emission spectra of PyLa at decreasing pH values (c = 100 µM) in PBS. (b) Emission spectra of PyLa at increasing pH values (c = 100 µM) in PBS. (c) Emission spectra of PyLaOT at decreasing pH values (c = 100 µM) in PBS (d) Emission spectra of PyLaOT at increasing pH values (c = 100 µM) in PBS. PyLa = λ_{Ex} 384 nm, PyLaOT = λ_{Ex} 398 nm.

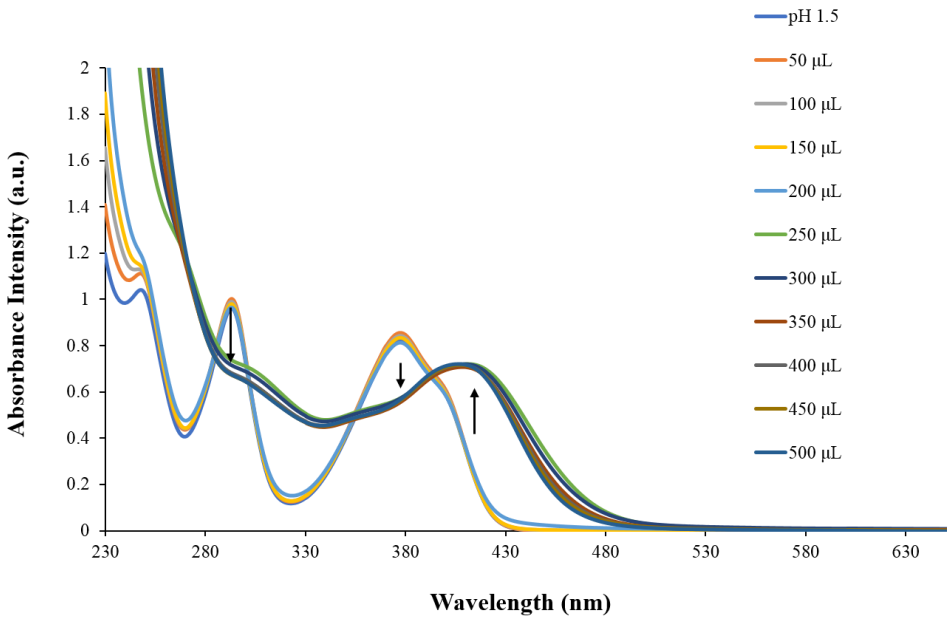

Figure S5.15 Absorption spectra of PyLa at increasing pH values (c = 50 µM) in acetonitrile using titrations of triethylamine. At pH 1.5 the absorbance max of PyLa is approximately 378 nm. This absorbance max slightly decreases with addition of triethylamine until the addition of 250 µL, at which point the normal absorbance max of approximately 420 nm is restored.

.

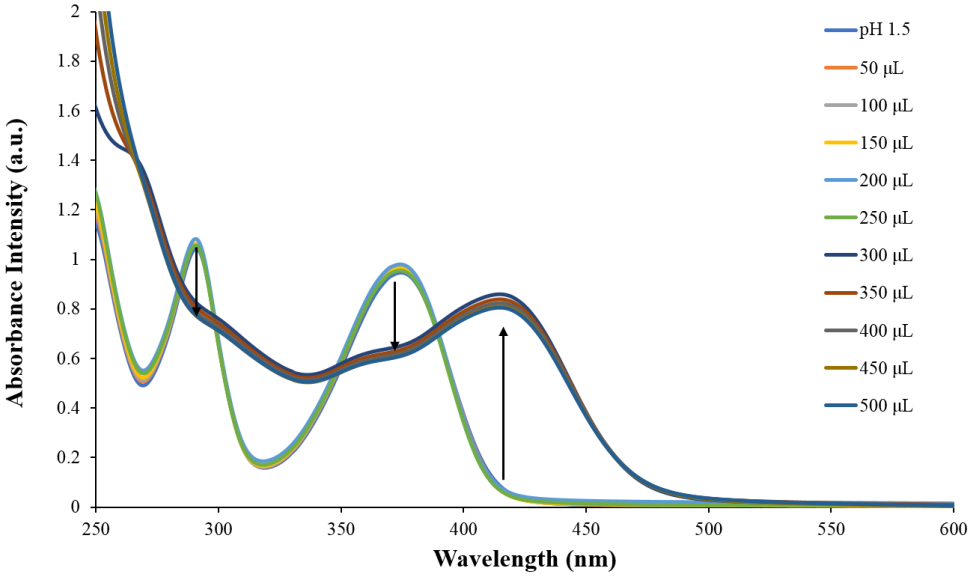

Figure S5.16 Absorption spectra of PyLa at increasing pH values (c = 50 µM) in acetonitrile using titrations of triethylamine. At pH 1.5 the absorbance max of PyLa is approximately 376 nm. This absorbance max slightly decreases with addition of triethylamine until the addition of 300 µL, at which point the normal absorbance max of approximately 418 nm is restored.

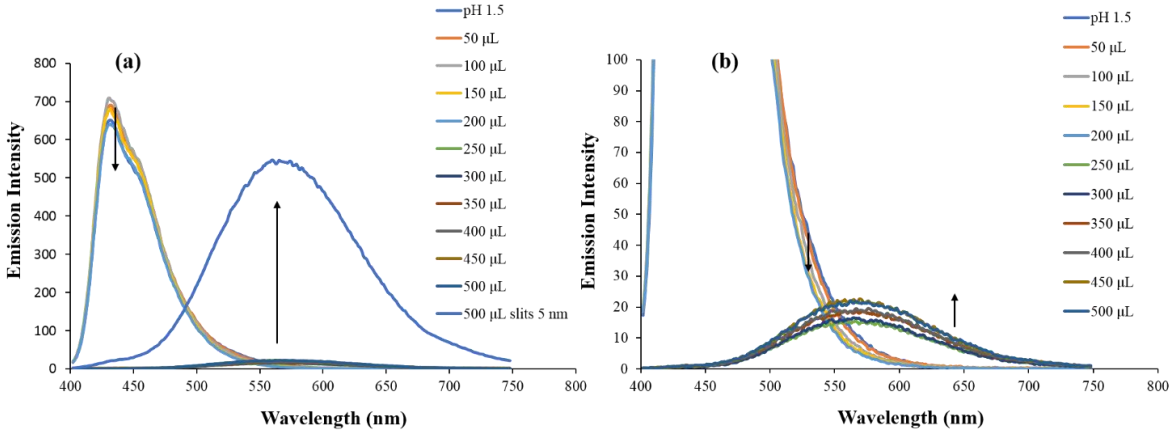

Figure S5.17 (a) Emission spectra of PyLa at increasing pH values (c = 50 µM) in acetonitrile using titrations of triethylamine, excited at 384 nm. At pH 1.5 the emission maxima of PyLa is approximately 430 nm. This decreases in intensity with increasing pH. After the addition of 250 µL of triethylamine the charge-transfer emission band at 520 nm is restored and increases slightly with increasing pH. Excitation slit width was 2.5 nm and emission slit width was 5 nm. and the emission is show after the addition of 500 µL with excitation and emission slit widths set to 5 nm also. (b) Inset of the appearance of the charge-transfer emission band at 520 nm after the addition of 250 µL and the slight increase in emission intensity with the addition of triethylamine.

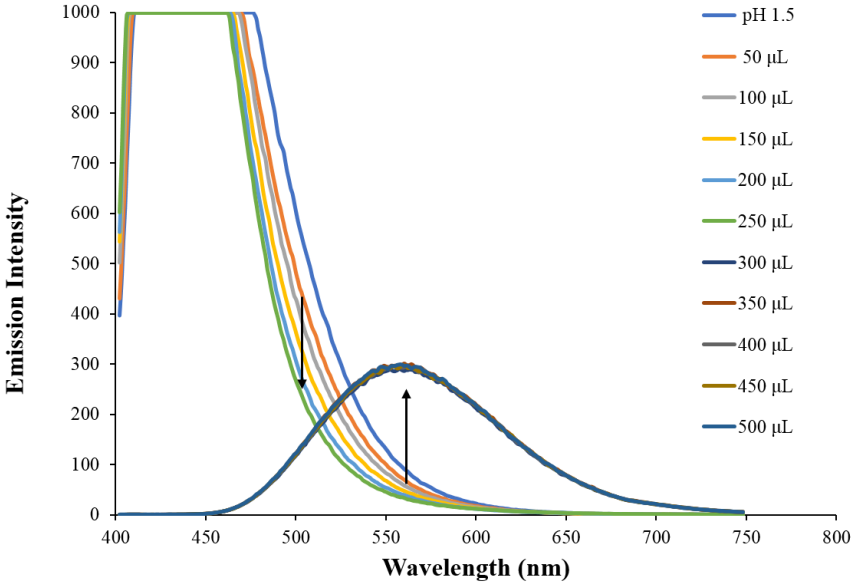

Figure S5.18 (a) Emission spectra of PyLaOT at increasing pH values (c = 50 µM) in acetonitrile on addition of triethylamine, exciting at 392 nm. At pH 1.5 the emission maxima of PyLaOT is approximately 426 nm. This decreases in intensity with increasing pH. After the addition of 300 µL of triethylamine the charge-transfer emission band at 552 nm is restored. Excitation and emission slit widths were 2.5 nm and 5 nm respectively.

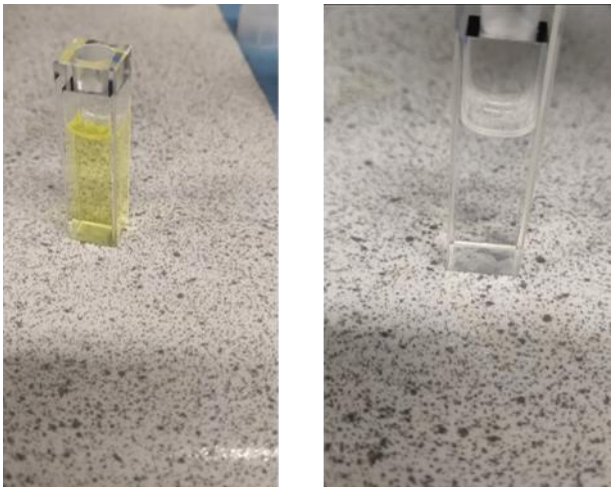

Figure S5.19 (a) Solution of PyLa (c = 50 µM) in acetonitrile (luminescent yellow). (b) Solution of PyLa (c = 50 µM) in acetonitrile upon addition of triethylamine (pH > 3) (colourless). The colour of the solution changes from luminescent yellow to colourless. This reversible colour change occurs for both PyLa and PyLaOT in both PBS and acetonitrile.

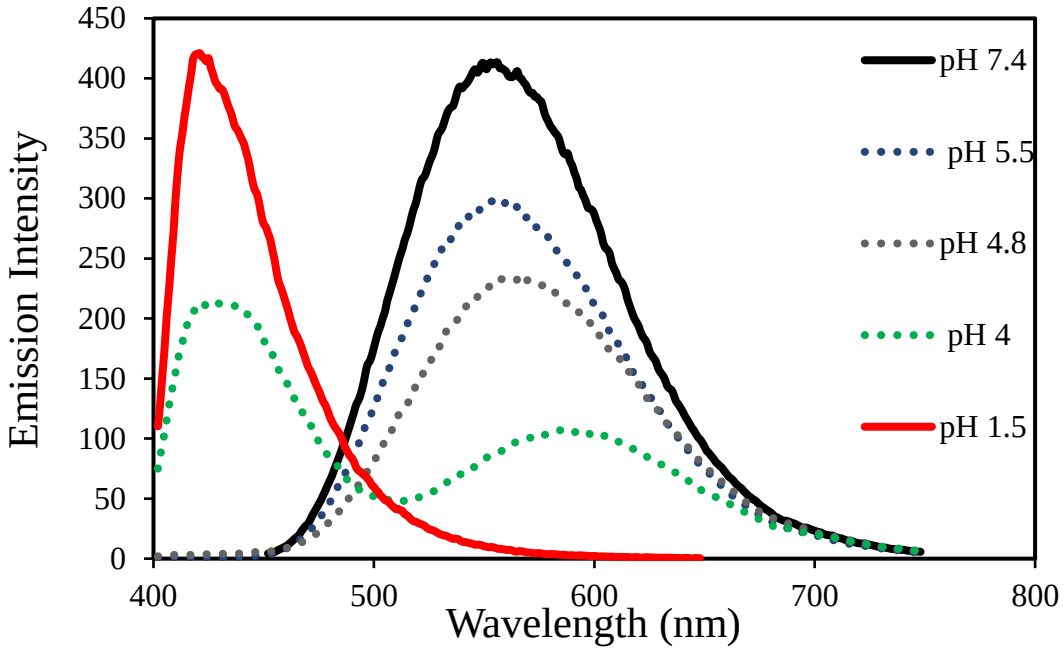

Figure S5.20 Emission spectra of PyLaOT (c = 50 μM) in acetonitrile. pH (7.5-4) were excited into the absorbance max at approximately 409 nm using excitation and emission slit widths of 5 nm and 2.5 nm respectively. pH 1.5 was excited into the absorbance max at approximately 378 nm and slit widths were reduced to 2.5 nm in order show full emission profile without saturating the detector.

S5.5 References

(1) M. J. Frisch, G. W. Trucks, H. B. Schlegel, G. E. Scuseria, M. A. Robb, G. Scalmani, V. Barone, B. Mennucci, G. A. Petersson, and et al. Gaussian 09 Revision E.01. Gaussian Inc. Wallingford CT 2009.

(2) A. D. Becke, *J. Chem. Phys.*, 1993, 98, 5648–5652.

(3) C. Lee, W. Yang and R. G. Parr, *Phys. Rev. B*, 1988, 37, 785–789.

(4) T. H. Dunning, *J. Chem. Phys.*, 1971, 55, 716–723.

(5) A. Schäfer, H. Horn and R. Ahlrichs, *J. Chem. Phys.*, 1992, 97, 2571–2577.

(6) A. Schäfer, C. Huber and R. Ahlrichs, *J. Chem. Phys.*, 1994, 100, 5829–5835.

(7) J. P. Perdew, K. Burke and M. Ernzerhof, *Phys. Rev. Lett.*, 1996, 77, 3865–3868.

(9) (a) J. P. Perdew, K. Burke and M. Ernzerhof, *Phys. Rev. Lett.*, 1997, 78, 1396–1396. (b) C. Adamo and V. Barone, *J. Chem. Phys.*, 1999, 110, 6158–6170.

(10) Y. Zhao and D. G. Truhlar, *Theor. Chem. Acc.*, 2008, 120, 215–241.

(11) T. Yanai, D. P. Tew and N. C. Handy, *Chem. Phys. Lett.*, 2004, 393, 51–57.

(12) B. Mennucci, C. Cappelli, C. A. Guido, R. Cammi and J. Tomasi, *J. Phys. Chem. A*, 2009, 113, 3009–3020.

(13) D. O. Connor, A. Byrne, G. B. Berselli, C. Long and T. E. Keyes, *Analyst*, 2019, 144, 1608–1621.